University of Alberta

AC Frequency-based Cyclical Electrical Stimulation of Hydrogel Microactuators

by

Joseph Ryan Charles Saunders

A thesis submitted to the Faculty of Graduate Studies and Research
in partial fulfillment of the requirements for the degree of

Doctor of Philosophy

Department of Mechanical Engineering

©Joseph Ryan Charles Saunders
Fall 2013
Edmonton, Alberta

Dedications

To the diligent search for deeper knowledge and wisdom

To those who came before me, setting the stage

To my loved family and friends

"Furious activity is no substitute for understanding"

- H. H. Williams

"Every accomplishment starts with the decision to try"

- Gail Devers

Abstract

The continuing interest in Lab-on-a-Chip technologies and Point-of-Care diagnostics systems is driving the development of supporting components for microfluidic regulation. Optimally the microfluidic regulation components would operate cyclically with a minimum input power, could be precisely controlled in specific locations, and wouldn't require bulky external components. One potential microactuator that could satisfy these requirements is an electrically stimulated hydrogel microactuator to provide a swelling and deswelling response. A hydrogel's temporal performance is also enhanced at reduced length scales, its fabrication is amenable to mass fabrication processes, and knowledge exists for macroscale cyclical bending. However, electrical stimulation at the microscale in a closed system would need to overcome electrolyte electrolysis effects and electrochemical reactions at electrodes.

In this thesis, several aspects of an electrically stimulated hydrogel microactuator that undergoes cyclical swelling have been analyzed. Firstly, the chemical and electrical field dynamics were numerically investigated through application of a yet uninvestigated cycling polarity electrical field, which highlighted the need for increased applied electric fields, and reduced hydrogel dimensions and modulus. Secondly, the hydrogel's dynamic mechanical properties were investigated to ascertain the straining frequency's

effect on the hydrogel's viscoelastic state, and quantifiable moduli were identified with appropriate mechanical stiffness for microactuation. These two studies provided system design parameters to maximize performance.

Thirdly, to overcome electrolysis and electrochemical reactions a dielectric layer was introduced over the electrodes. This system modification required the unprecedented use of AC frequencies for stimulation and necessitated an analysis, both analytically and experimentally, of the characteristic AC frequency needed to successfully demonstrate and maximize hydrogel microactuation. The system's frequency-varying capacitance, impedance, and apparent power were also investigated.

Lastly, the hydrogel microactuator's operation under cyclical electrical stimulation, achieved through pulse width modification, was successfully demonstrated and investigated for up to three cycles of actuation. The system was subjected to increasing electric fields to demonstrate a maximum true strain of ~27% with response times <10 seconds, and the electrically induced osmotic pressure throughout the analysis was analytically calculated. Furthermore, the system employing dielectric coated electrodes was compared to a stable system without dielectrics, highlighting the further performance enhancements available with continued optimization.

Acknowledgments

The time I've spent at the University of Alberta during my graduate studies has been a life changing journey. I have grown enormously during this period in my life, both intellectually and socially, to a degree that will only become known with time's hindsight. The University of Alberta community; its students, professors, and staff, will always be a part of my extended family.

I would like to thank my Ph.D. supervisor, Dr. Walied Moussa, who gave an ambitious and eager young undergraduate a chance to immerse himself in the world of micro and nanotechnology. He allowed me to pursue many avenues of academic research, provided me with resources to investigate promising opportunities, and helped me navigate the waters of academia. I'd also like to thank my supervisory committee members, Dr. Alidad Amirfazli and Dr. Subir Bhattacharjee, who posed compelling questions that motivated me to seek out the answers, and who also patiently responded to queries.

I would also like to thank my research group, who were my academic community throughout my degree. I thank you all for your time spent listening to my presentations, asking questions, and just generally being available to have scientific debates and discussions. A special thanks to Jon Lueke, David Benfield, Suzan Elshaer, Mehdi Rezaei, Noor Al Quddus, Mohamed El Gowini, and Hossam Gharib.

I am also very thankful for the help and guidance given to me by the NanoFab staff. They helped train me on countless pieces of equipment and processes, had enough confidence in my skills to give me afterhours access to expedite my work, and withstood the waves of questions I asked along the way. Specifically, Les Schowalter, Stephanie Bozic, Melissa Hawrelechko, Glenn Elaschuk, Keith Franklin, Dr. Eric Flaim, and Aruna Kroetch.

I am grateful to all the Mechanical Engineering department office staff, graduate coordinators and assistants, machine shop staff, and

Table of Contents

List of Tables

List of Figures

Nomenclature

%wt	percent weight, %
A_{Eff}	effective area of electrodes, m^2
A_{InEff}	ineffective area of electrodes, m^2
b	body forces, N
c_F	fixed ions, mol/m^3 or mol/L
c_k	electrolyte concentration of the kth ion inside the hydrogel, mol/m^3 or mol/L
$c_k{}^o$	electrolyte concentration of the kth ion outside the hydrogel, mol/m^3 or mol/L
c_∞	bulk electrolyte concentration, mol/m^3 or mol/L
c_M	mobile ions, mol/m^3 or mol/L
C	capacitance, F
C_j	capacitance of the jth parameter, F
C_{D1}	capacitance through the dielectric between electrodes, F
C_{EDLH}	capacitance of the hydrogel's electric double layer, F
C_{EINT}	capacitance of interface over effective electrode areas, F
C_H	capacitance of the hydrogel, F
C_{M2}	capacitance of media in effective electrode areas, F
C_{M3}	capacitance of the media in ineffective electrode areas, F
C_{Teq1}	capacitive pathway through hydrogel, F
C_{Teq2}	capacitive pathway through electrolyte, F
C_{Top}	capacitance of the microchannel top, F
C_{Total}	total capacitance of the system, F
C_{xeq11}	cross-sectional capacitive pathway through dielectric layer, F
C_{xeq12}	cross-sectional capacitive pathway through the microchannel, F
C_{xeq13}	cross-sectional capacitive pathway through the microchannel top, F
d	hydrogel's final diameter, m
d_o	hydrogel's initial diameter, m
d_p	diameter of the interior post, m
D	duty cycle of applied electrical signal, %
D_k	ionic diffusivity of kth ionic species, m^2/s
$\overline{E}$	electric field, V/m

E	Young's modulus, Pa
E'	storage modulus, Pa
E_o'	storage modulus at an initial state, Pa
E_j'	storage modulus of the jth parameter, Pa
E"	loss modulus, Pa
E*	complex modulus, Pa
ET	exposure time, s
E_w	electrode width, m
E_g	electrode gap, m
f	viscous damping parameter, N s/m
f	frequency, Hz
f_{app}	frequency of the applied electrical signal, Hz
f_c	characteristic AC frequency to minimize electrostatic shielding, Hz
F	Faraday constant, C/mol
G	shear modulus, Pa
G_p	admittance, S
h_{chan}	height of the microchannel, m
H	hydrogel hydration
H_o	hydrogel hydration at an initial state
H_j	hydrogel hydration at the jth state
k	hydraulic permeability, m^{-2}
M	longitudinal modulus, Pa
P	apparent power, V A
$P_{osmotic}$	osmotic pressure, Pa
$P_{osmotic, j}$	osmotic pressure at the jth state, Pa
PI	polymerization intensity at sample, W/cm^2
Q_m	weight degree of swelling
r	radius, m
r_j	radius of the jth parameter, m
R	universal gas constant, J mol^{-1} K^{-1}
R_{M2}	electrolyte resistance over effective electrode areas, Ohms
t	time, s
t_D	thickness of dielectric layer over electrodes, m
t_j	thickness of jth parameter, m
t_{JA}	hydrogel jacket thickness, m
t_{JAo}	initial hydrogel jacket thickness, m
T	absolute temperature, K
u	displacement, m

V_{app}	electric potential applied across the electrodes, V
V_{ave}	average electric potential of applied electrical signal, V
V_{DC}	direct current component of applied electrical signal, V
V_{max}	maximum electric potential of applied electrical signal, V
V_{min}	minimum electric potential of applied electrical signal, V
V_M	electric potential across the electrolyte media, V
V_{off}	offset voltage, V
V_{pk-pk}	peak to peak electric potential of applied electrical signal, V
V_{rms}	root mean square voltage of applied electrical signal, V
$V_{threashold}$	electric potential threshold above which actuation occurs, V
w_d	weight of the dry hydrogel, kg
w_{Eff}	effective width of electrodes, m
w_H	hydrogel width, m
w_{InEff}	ineffective width of electrodes, m
w_s	weight of the swollen hydrogel, kg
x	rectilinear coordinates in the x-direction, m
y	rectilinear coordinates in the y-direction, m
z_k	valence of kth ionic species
Z	impedance, Ohms

Greek Symbols

δ	phase angle, rad
ε	strain or true strain
ε_e	effective relative dielectric permittivity of hydrogel
ε_{Max}	maximum applied strain
ε_j	relative dielectric permittivity of jth parameter
ε_r	relative dielectric permittivity of electrolyte
ε_M	relative dielectric permittivity of media
ε_p	relative dielectric permittivity of the polymer chains
ε_o	dielectric permittivity of free space, $C^2N^{-1}m^{-2}$
i	unit imaginary number
κ	inverse Debye length, m^{-1}
μ_k	ionic mobility of kth ionic species, $m^2V^{-1}s^{-1}$
ρ	density of the hydrogel, kg/m^3
σ	stress, Pa
σ_{Max}	maximum measured stress, Pa
σ_M	conductivity of electrolyte, S/m
σ_H	conductivity of hydrogel, S/m

τ	shear stress, Pa
τ_{dr}	diffusion reaction time constant, s
τ_{edr}	electrodiffusion reaction time constant, s
τ_{EINT}	time constant of the electrode interface, s
τ_{mech}	mechanical response time constant, s
υ	Poisson's ratio
ψ	electric potential, V
ψ_s	true surface electric potential, V
ψ_d	electric potential at Stern plane, V
ω	angular testing frequency, rad/s

Subscripts (for symbols above with subscript *j*)

FAB	as fabricated
HCL	within hydrochloric acid
0.5 M KOH	within 0.5 M potassium hydroxide
1 mM KOH	within 1 mM potassium hydroxide
anode, Elec	at the anode side during electrical stimulation
Elec	electrical stimulation
x	x-component
y	y-component
D2	dielectric layer over effective electrode areas
S2	Stern layer over effective electrode areas
DL2	Debye layer over effective electrode areas
D3	dielectric layer over ineffective electrode areas
S3	Stern layer over ineffective electrode areas
DL3	Debye layer over ineffective electrode areas

Abbreviations

AA	acrylic acid
AC	alternating current
ALE	arbitrary Langrangian-Eulerian
CAD	computer aided design
COC	cyclicolefin copolymer
DC	direct current
DMA	dynamic mechanical analysis
DMP	dynamic mechanical properties
DMPA	2,2-dimethoxy-2-phenylacetophenone
DMSO	dimethylsulfoxide
DRT	diffusion reaction time constant
EAP	electroactive polymers

EDL	electric double layer
EDRT	electrodiffusion reaction time constant
EFSH	electric field sensitive hydrogels
EGDMA	ethylene glycol dimethacrylate
EHOD	electrical hydrogels on dielectrics
HEMA	hydroxyethyl methacrylate
HCl	hydrochloric acid
IBA	isobornyl acrylate
IMPC	ionic polymer-metal composites
IPA	isopropanol
KOH	potassium hydroxide
LCST	lower critical solution temperature
LOC	Lab-on-a-Chip
MEMS	microelectromechanical systems
NP	Nernst-Planck
P	Poisson's Equation
PDMS	polydimethyl siloxane
POC	Point-of-Care
PMMA	polymethacrylic acid
RF	radio frequency
RIE	reactive ion etching
RP	rapid prototype
SEM	scanning electron microscopy
SRH	stimuli responsive hydrogel
SSH	stimuli sensitive hydrogels
TEGDMA	tetraethylene glycol dimethacrylate
UV	ultra violet

Chapter 1

Introduction

1.1 Motivation

Presently and over the past decades, microfluidic chip systems have been the focus of research for the development of Lab-on-a-Chip (LOC) and portable Point-of-Care (POC) diagnostic tests; however, significant progress towards comprehensive systems has been hampered by the integration of microfluidic regulation components [1]. These LOC and POC technologies have demonstrated advantages over traditional laboratory tests, such as a shorter sample processing time, smaller reagent quantities are required, and their potential for portability, among others [2, 3]. Specific microfluidic chip systems each have their own layout and function, but in general, systems can perform sample preparation, separation, and sensing or detection [4]. Throughout these systems the integration of microfluidic regulation components are necessary for fluidic movement and manipulation. Microfluidic regulation systems contain two main components: micropumps and microvalves.

Various micropumping schemes have been proposed, such as passive capillary pumping, active non-mechanical electroosmotic pumping, or active mechanical pneumatic peristaltic pumping [4, 5]. Several microvalving configurations have also been proposed with differing actuation methods, such as: pneumatic [6], electrostatic [7], and electromagnetic [8], among others. Certain microactuation systems initially developed for microvalving have also been extended for sequential operation in peristaltic micropumping configurations or alternatively

1

micropumping actuators have been reconfigured for microvalving. It is unclear which micropumping scheme dominates LOC and POC applications, as a method's applicability depends on the microchip configuration; however, it is clear that an easily controllable active on-off microvalve is needed for complex LOC and POC systems. Towards the fulfillment of this microvalving need, various microactuation systems are under development which are presently employed as microvalves or which can be extended to perform as microvalves.

The development of microactuation methods for applications in microvalving has been ongoing for over two decades [9]; however, difficulties integrating microvalves within LOC and POC systems still remain. For example, the popular pneumatic air membrane-based microvalve first developed by Unger *et al.* [6] requires external and bulky vacuum/pressure pumps to provide the necessary pneumatic actuation, drawing high power and hindering portability. Another popular example are embedded electrostatic microvalves that use parallel plate electrodes above and below the microchannel [7]. While they are integrated without bulky external equipment they can also require 50-300 V for operation which hinders their utility in a POC system. Microvalving configurations avoiding these drawbacks, such as an electromagnetically actuated system, can also require complex expensive microfabrication processes and incorporate moving components susceptible to wear [8].

The integration of microvalves that are easy to fabricate and do not require complex external control systems remains a critical challenge to the large scale integration of microvalving technologies within LOC and POC systems [4, 10, 11]. Furthermore, for POC diagnostics the microvalving power requirements must be at a minimum to facilitate long-term battery operation [1].

1.2 Proposed Approach

Electrically actuated hydrogels offer some interesting advantages over other microactuation methods, they: have relatively low power consumption when actuated, allow precise electrical control of the actuator response and the response location, are amenable to inexpensive mass fabrication processes, and their temporal performance is enhanced at reduced length scales. In the past decades electrically actuated hydrogels have been extensively studied [12-14], but in systems with macroscale geometries and configurations intended for artificial muscle applications [15, 16]. These macroscale works provided a knowledgebase for understanding actuation kinetics and rough performance capabilities, investigated the use of various materials, and studied many different systems configurations. However, few researchers have investigated microscale electrical swelling of hydrogel microactuators with intended applications in microfluidics, which is the primary goal of the current research.

Work with microscale hydrogels has been largely catalyzed by Beebe *et al.*'s demonstration in the year 2000 of photopolymerizable microscale hydrogels, which were employed as pH responsive microvalves [17]. Bassetti *et al.* extended this work and was among the few examples of literature that have examined microscale electrically stimulated hydrogels, which demonstrated the swelling of a cylindrical microscale hydrogel under an applied electric field [18]. Their study showed an increased swelling response with increased applied electric potential, and that this response could be step-wise increased by modifying an applied duty cycle. However, their work did not examine the electrical deswelling of a hydrogel and thus did not perform cyclical stimulation of a hydrogel microactuator. Cyclical hydrogel swelling and deswelling, or cyclical stimulation/actuation, would be highly advantageous to produce a microvalve that can be actively turned on and off repeatedly. Examining the cycling of stimulation would be necessary to

3

understand potential opening and closing kinetic responses, and any behaviors associated with cyclical actuation. Two other microscale works by Kwon *et al.* demonstrated the electrically induced bending of a rectangular prismatic hydrogel, specifically for the applications of cell sorting [19] or micropumping [20]. The latter configuration for micropumping cyclically bent the hydrogel approximately 6 million times over 6 months, highlighting the repeatable nature of electrical actuation. However, hydrogel bending is difficult to apply to many configurations for microfluidic regulation. Swelling can be applied to regulation easier than bending, especially for out-of-plane microvalving configurations, but studies examining electrically induced hydrogel swelling are rare. Both the works of Bassetti *et al.* and Kwon *et al.* also suffered from the effects of electrolyte electrolysis and electrochemical reactions at the electrodes. Bassetti *et al.* needed to continuously flush the channel with electrolyte to wash away bubbles, which would significantly hinder the system's utility within a complicated microfluidic chip. Kwon *et al.* was forced to apply electric potentials <1.2 V to avoid these crippling effects, which limited the system's performance. In addition, neither of these systems examined the initial chemical or induced electrical osmotic pressure responsible for hydrogel actuation, as this would require knowledge of the hydrogel's mechanical properties and state of swelling. Nor did they investigate the underlying electrical and chemical field dynamics responsible for inducing the hydrogel's osmotic pressure.

The current research adopts a cylindrical microscale hydrogel configuration to develop a cyclically operating microactuator, without the negative effects of electrolyte electrolysis and electrochemical reactions. The system incorporates dielectric coated electrodes to overcome these negative effects which allow examination of the primary research *objective*: to cyclically actuate a cylindrical hydrogel using pulse width modulation to study microactuation performance. Understanding the behavior and performance of a hydrogel microactuator would be

4

necessary to further employ this material in a microvalving configuration. This main objective is aided by an analytical and experimental examination of the characteristic AC frequency needed to overcome electrostatic shielding effects, initially caused by incorporating dielectric coated electrodes. To better understand the underlying electric and chemical field dynamics responsible for cyclical electrical actuation a preliminary system will be studied through the development of a numerical model. In addition, to understand the effects of cyclical actuation on the hydrogel's elastic restoring force the dynamic mechanical properties will be investigated and quantified for a range of testing and fabrication parameters.

1.3   Research Objectives

The following are the overall research objectives of the current research, presented in the chronological order of investigation:

1. Numerical Modeling. Investigation of the cyclic deformation behavior through numerical modeling of a hydrogel actuator macroscale system under a reversed polarity electric field. This numerical study also allows for an examination of the underlying electric field and chemical field dynamics under both chemical and electric stimulus, and their overall effect on displacement. This examination helps identify an appropriate range of mechanical properties and electric field magnitudes needed for further experimental studies.

2. Prototype Microfabrication. Prototype a microfluidic chip that incorporates the necessary components for *in-situ* electrical stimulation of a hydrogel microactuator. This objective involves the development of a microfabrication process flow utilizing microfabrication techniques and resources available within the University of Alberta's NanoFab and the MEMS/NEMS Advanced Design Laboratory (ADL). An evolution of prototypes will be needed

to systematically incorporate all necessary components, with the desired geometries and critical dimensions. The final prototyped chip will then be used to perform experimental studies which aim to mimic potential operational environments found in LOC systems.

3. Mechanical Characterization. Perform a systematic determination of a photopolymerizable hydrogel's dynamic mechanical properties under different electrolyte concentrations, cyclical testing frequencies, and various fabrication conditions. This characterization also studies the relationship between elastic and viscous contributions within the hydrogel during deformation. Once the dynamic mechanical properties are known, a specific set of fabrication conditions can be identified which will produce hydrogels that can satisfy the range needed for actuation. In addition, these quantitative values can be further incorporated into analytical expressions to calculate the initial chemical and electrically induced osmotic pressure in deforming hydrogels.

4. Analytical Modeling. Develop a theoretical model for prediction of the characteristic AC frequency required to overcome all electrostatic shielding effects. This model will analyze the capacitances found within the hydrogel-electrolyte-dielectric system, focusing on capacitances over the electrodes. This model will then be compared to experimental measurements of capacitance. In parallel the system impedance will be experimentally measured to allow calculation of the apparent power consumption of the system.

5. Frequency-based Microactuation. Experimentally actuate hydrogels electrically using AC frequencies both above and below the predicted characteristic frequency, and contrast the resulting deformation and response times achieved. This study performs the first electrical actuation of a hydrogel with AC frequencies and no

external pumping equipment, and verifies that maximum displacement occurs above the predicted frequency.

6. Cyclical Microactuation. Explore the AC electrically induced cyclical actuation of hydrogels by implementing pulse width modification to control the applied electric field magnitude and hence the actuation response. This study also examines the effect of increasing electric field magnitudes on the induced deformation and response times, and the overall peak-to-trough deformation response. Furthermore, combining the previously determined mechanical properties with the observed deformation the hydrogel's electrically induced osmotic pressure can be calculated. Lastly, this system can be compared to a similar system without dielectric coated electrodes, but needing external pumping, to examine the potential for future performance enhancements.

1.4 Thesis Outline

This thesis provides a detailed description of an electrically stimulated hydrogel microactuator's development through numerical modeling, prototype microfabrication, hydrogel characterization, and experimental electrical microactuation. The thesis is divided into 8 chapters, where the following paragraphs describe the areas covered in each of the chapters.

Chapter 1 provided a brief introduction and overview of the investigated research and highlights the motivation behind the current research and the methodology for its study. Chapter 2 provides a review of the literature pertaining to microactuators in microfluidics, stimuli sensitive hydrogels, electrically actuated hydrogels, the theoretical equation systems for numerical modeling, and methods for characterization of a hydrogel's mechanical properties. It briefly overviews systems that electrically bend hydrogel macroscale rectangular prisms,

and highlights the few studies that have investigated electrically actuated microscale hydrogels.

Chapter 3 presents the coupled chemo-electro-mechanical transport-based equations for numerical simulation of electrical hydrogel actuation. It then illustrates a system under a chemical equilibrium that is electrically deformed, which is cycled by reversing the electrical polarity to reverse the induced deformation. The numerical model also overviews the electric and chemical field dynamics that occur during cyclical hydrogel actuation.

Chapter 4 examines the details of the microfabrication processes conducted to prototype two major hydrogel based systems: one with dielectric coated electrodes and one without dielectric coated electrodes. The latter system represents an earlier evolution of the former, and both systems are used to experimentally test hydrogel microactuation. The chapter also presents the testing system used to apply electrical signals and the methodology implemented to optically characterize hydrogel deformation.

Chapter 5 presents an experimental study of a hydrogel's dynamic mechanical properties as measured through dynamic mechanical analysis. The chapter quantifies the hydrogel's storage and loss modulus at different electrolyte concentrations, cyclic testing frequencies, photopolymerization intensities and exposure times, and with varying crosslinker concentration. Through these parameters the effects of hydrogel swelling and polymer network structure on the relationship between storage modulus and loss modulus were studied.

Chapter 6 presents an analytical capacitance model for prediction of the system's characteristic AC frequency needed to overcome electrostatic shielding, and provides predicted frequencies for varying electrolyte concentrations and dielectric thicknesses. The analytical model was then compared to the experimental measurements of system capacitance. In addition, experimental measurements of impedance as a function of frequency and concentration are presented to calculate the

apparent power of the system at the maximum experimentally applied electric potential. The chapter also presents the first experimentally observed AC-frequency based electrical actuation of hydrogels, which examines actuation at increasing frequencies, two different electrolyte concentrations and increasing electric field magnitudes.

Chapter 7 presents the first demonstration of experimental cyclical microactuation of electrically stimulated hydrogels by employing AC frequencies and pulse width modulation. The experiments examine the effect of an increased electric field on the deformation and temporal responses, while cycling the hydrogel through at least three swollen-deswollen states. The experiments also compare systems with and without dielectric coated electrodes to contrast performance, and provide an outlook for potential system enhancements. Analytically the initial chemical and electrically induced osmotic pressures are calculated using the previously quantified dynamic mechanical properties to provide a measure of the maximum actuation pressure generated.

Each chapter provides learning experiences to influence and improve the primary research objective. The four research chapters are intertwined, whereby knowledge gained from the earlier chapters impacted later chapters, as depicted in Figure 1.1. The outcomes from Chapter 3 showed the need for improved actuator response through larger electric fields, a smaller scale hydrogel, and a lower elastic modulus hydrogel. In addition, it showed that a cylindrical hydrogel would be better for characterization, as it would have a singular point of maximum deflection and would not experience torsion the way an imbalanced square might. Chapter 5 provided quantification of the dynamic mechanical properties which would be used later in Chapter 7 for calculation of hydrogel osmotic pressure. It also provided crucial fabrication parameters needed for hydrogel fabrication within Chapter 4's prototyping, and Chapter 6's and 7's experimental research. Chapter 6 demonstrated prototyping success, proving the manufacturing process was complete and adequate for further

electrical actuation studies. In addition, it predicted the characteristic AC frequencies needed to overcome electrostatic shielding and confirmed a viable range of electric field magnitudes that would cause actuation. All the aforementioned experience culminated in Chapter 7 to demonstrate the cyclical electrically induced hydrogel microactuation, with a large strain response and response times on the order of seconds.
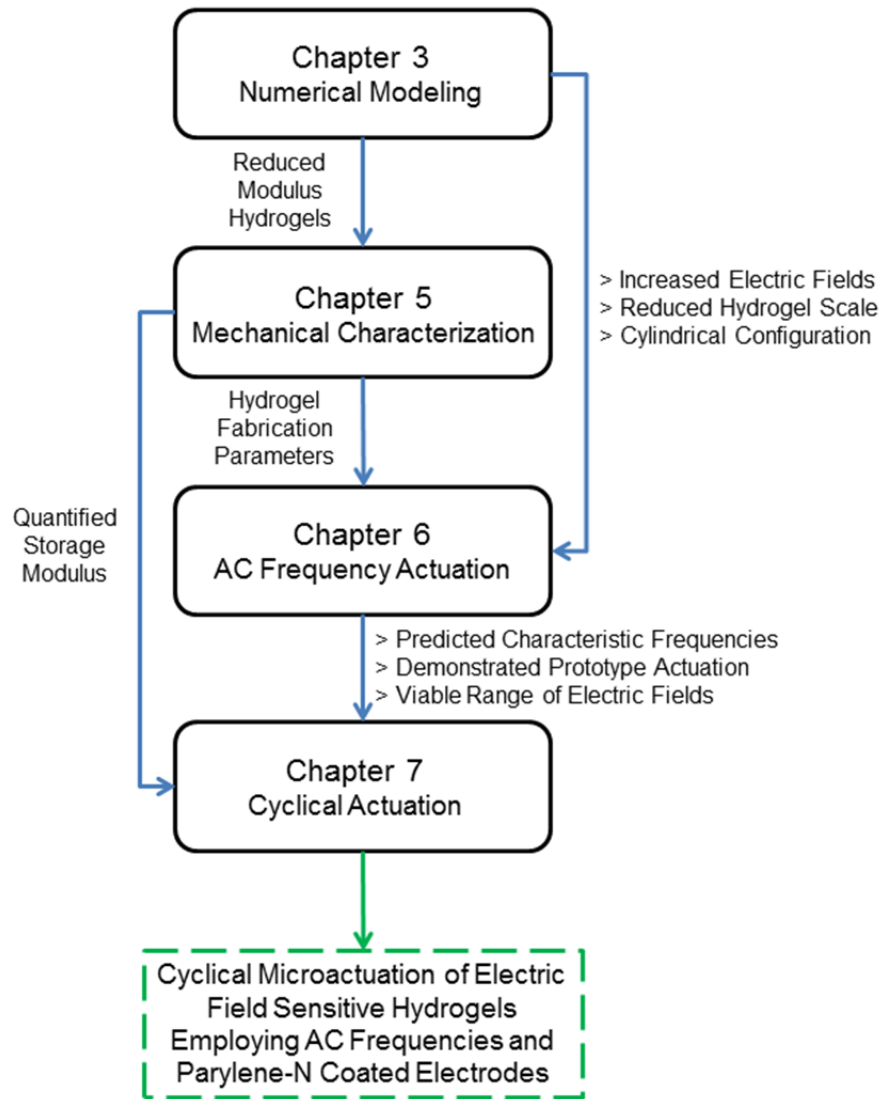
Figure 1.1: Relationships between research chapters within this thesis, and how earlier chapters influenced the primary research objective investigated in Chapter 7.

References

[1]   C. D. Chin, V. Linder, and S. K. Sia, "Commercialization of microfluidic point-of-care diagnostic devices," *Lab on a Chip,* vol. 12, pp. 2118-2134, 2012.

[2]   M. J. Cima, "Microsystem Technologies for Medical Applications," *Annual Review of Chemical and Biomolecular Engineering, Vol 2,* vol. 2, pp. 355-378, 2011.

[3]   L. Gervais, N. de Rooij, and E. Delamarche, "Microfluidic Chips for Point-of-Care Immunodiagnostics," *Advanced Materials,* vol. 23, pp. H151-H176, Jun 24 2011.

[4]   P. N. Nge, C. I. Rogers, and A. T. Woolley, "Advances in Microfluidic Materials, Functions, Integration, and Applications," *Chemical Reviews,* vol. 113, pp. 2550-2583, 2013/04/10 2013.

[5]   N. T. Nguyen, X. Y. Huang, and T. K. Chuan, "MEMS-micropumps: A review," *Journal of Fluids Engineering-Transactions of the Asme,* vol. 124, pp. 384-392, Jun 2002.

[6]   M. A. Unger, H. P. Chou, T. Thorsen, A. Scherer, and S. R. Quake, "Monolithic microfabricated valves and pumps by multilayer soft lithography," *Science,* vol. 288, pp. 113-116, Apr 7 2000.

[7]   A. V. Desai, J. D. Tice, C. A. Apblett, and P. J. A. Kenis, "Design considerations for electrostatic microvalves with applications in poly(dimethylsiloxane)-based microfluidics," *Lab on a Chip,* vol. 12, pp. 1078-1088, 2012.

[8]   M. Capanu, J. G. Boyd, and P. J. Hesketh, "Design, fabrication, and testing of a bistable electromagnetically actuated microvalve," *Journal of Microelectromechanical Systems,* vol. 9, pp. 181-189, Jun 2000.

[9]   S. Shoji and M. Esashi, "Microflow Devices and Systems," *Journal of Micromechanics and Microengineering,* vol. 4, pp. 157-171, Dec 1994.

[10]   T. Thorsen, S. J. Maerkl, and S. R. Quake, "Microfluidic large-scale integration," *Science,* vol. 298, pp. 580-584, Oct 18 2002.

[11]   P. Mitchell, "Microfluidics - downsizing large-scale biology," *Nature Biotechnology,* vol. 19, pp. 717-721, Aug 2001.

[12]   T. Tanaka, I. Nishio, S. T. Sun, and S. Uenonishio, "Collapse of Gels in an Electric-Field," *Science,* vol. 218, pp. 467-469, 1982.

[13]   T. Shiga and T. Kurauchi, "Deformation of Polyelectrolyte Gels under the Influence of Electric-Field," *Journal of Applied Polymer Science,* vol. 39, pp. 2305-2320, Jun 5 1990.

[14]   G. Q. Liu and X. P. Zhao, "Electroresponsive behavior of gelatin/alginate semi-interpenetrating polymer network membranes under direct-current electric field," *Journal of Macromolecular Science-Pure and Applied Chemistry,* vol. A43, pp. 345-354, 2006.

[15]   E. A. Moschou, S. F. Peteu, L. G. Bachas, M. J. Madou, and S. Daunert, "Artificial muscle material with fast electroactuation under neutral pH conditions," *Chemistry of Materials,* vol. 16, pp. 2499-2502, Jun 15 2004.

[16]   H. B. Schreyer, N. Gebhart, K. J. Kim, and M. Shahinpoor, "Electrical activation of artificial muscles containing polyacrylonitrile gel fibers," *Biomacromolecules,* vol. 1, pp. 642-647, 2000.

[17]   D. J. Beebe, J. S. Moore, J. M. Bauer, Q. Yu, R. H. Liu, C. Devadoss*, et al.*, "Functional hydrogel structures for autonomous flow control inside microfluidic channels," *Nature,* vol. 404, pp. 588-590, Apr 6 2000.

[18]   M. J. Bassetti, A. N. Chatterjee, N. R. Aluru, and D. J. Beebe, "Development and modeling of electrically triggered hydrogels for microfluidic applications," *Journal of Microelectromechanical Systems,* vol. 14, pp. 1198-1207, Oct 2005.

[19]   G. H. Kwon, Y. Y. Choi, J. Y. Park, D. H. Woo, K. B. Lee, J. H. Kim*, et al.*, "Electrically-driven hydrogel actuators in microfluidic channels: fabrication, characterization, and biological application," *Lab on a Chip,* vol. 10, pp. 1604-1610, 2010.

[20]   G. H. Kwon, G. S. Jeong, J. Y. Park, J. H. Moon, and S. H. Lee, "A low-energy-consumption electroactive valveless hydrogel micropump for long-term biomedical applications," *Lab on a Chip,* vol. 11, pp. 2910-2915, 2011.

Chapter 2

Literature Review

2.1   Introduction

Relevant experimental, theoretical, and characterization literature is discussed. Electrically stimulated hydrogel microactuators fall within the realm of three major research areas: microactuators for microfluidics, electrically activated polymers, and stimuli-sensitive hydrogels, shown in Figure 2.1. These three areas are briefly reviewed, focusing on stimuli-sensitive hydrogels and the stimulation mechanisms which cause actuation. Within the realm of stimuli sensitive hydrogels the chronological investigation of macroscale and microscale electrically activated hydrogels is overviewed, highlighting examples related to the development of this work. Following this a description of equation systems for numerical modeling are reviewed, and evaluated for their applicability to model the system examined within this work. The closing section examines the techniques available to characterize a hydrogel's mechanical properties, specifically the hydrogel's tensile dynamic mechanical properties, and briefly overviews literature that have previously measured a hydrogel's mechanical properties.
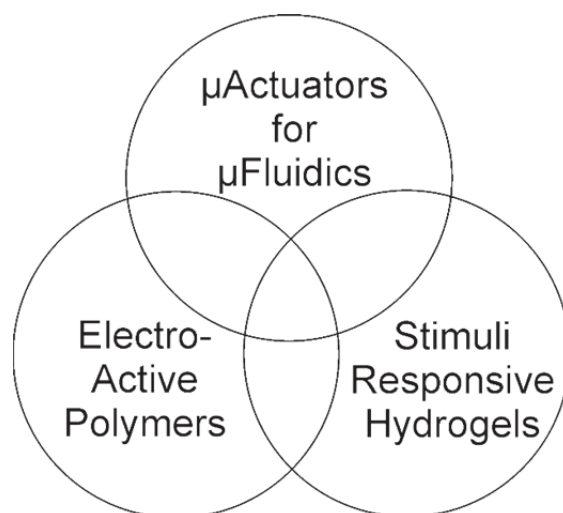
Figure 2.1: Electrically stimulated hydrogel actuators for microfluidic applications fall in the realm between microactuators for microfluidics, electrically actuated polymers, and stimuli-sensitive hydrogels.

2.2   Microactuators in Microfluidic Systems

The use of microactuators for microfluidic regulation has received significant attention from researchers. While passive microvalving [1] and micropumping [2] techniques do exist, the use of active microactuator-based systems offers more control for the automation and integration of complex microfluidic systems. In microelectromechanical systems (MEMS) there are a wide array of applications for microactuators [3], but for microfluidic systems they are generally employed for either microvalving or micropumping, or both, as seen in Figure 2.2.

Two- and three-dimensional microvalving designs cover a wide range of configurations [4, 5], with the final design depending on the intended application and components required for use. Microvalves have been shown to incorporate microactuators within a wide variety of stimulation methods, including: pneumatic [6], electrostatic [7, 8], magnetic [9], electromagnetic [10], bimetallic [11], electroactive polymers [12], and stimuli-sensitive hydrogels [13]. New developments evolve microactuators to decrease response times, reduce complex external components, hold higher pressures, enhance operational utility, and reduce the overall device size.

Micropumping systems have also been developed to incorporate microactuators, typically implementing a deformable membrane and one or two check valves. The integration of micropumping is required for more complex flow movement throughout a microfluidic chip, with thorough reviews previously published on MEMS-based systems [14, 15]. Micropumping has been shown to be actuated using: pneumatics [6], thermopnuematics [16], shape-memory alloys [17], piezoelectrics [18], magnetic materials [19], electroactive polymers [20], and stimuli-sensitive hydrogels [21].

Electrically-stimulated hydrogel microactuators are well suited for microvalving and micropumping applications because their performance scales with reduced size, they do not require extensive external components, they can have a large actuating stroke, and can be operated under low power. In addition, the fabrication of hydrogels using photopolymerization techniques allows for large arrays of microactuators to be fabricated simultaneously without complicated and costly microfabrication processes. However, further research is required to understand the response kinetics and osmotic pressure performance of electric field sensitive hydrogels (EFSH) under varying and cyclical electrical stimulation.

2.3   Electroactive polymers

Electroactive polymers (EAP) are electrically responsive materials that undergo deformation when stimulated by a suitable electrical stimulus, and can have characteristics in common with natural muscles [22]. Compared to some of the competing actuating technologies outlined in Section 2.2, they can undergo large strains without failure, have improved temporal performance with reduced scale, can be structurally simple, and have a high power density [23].
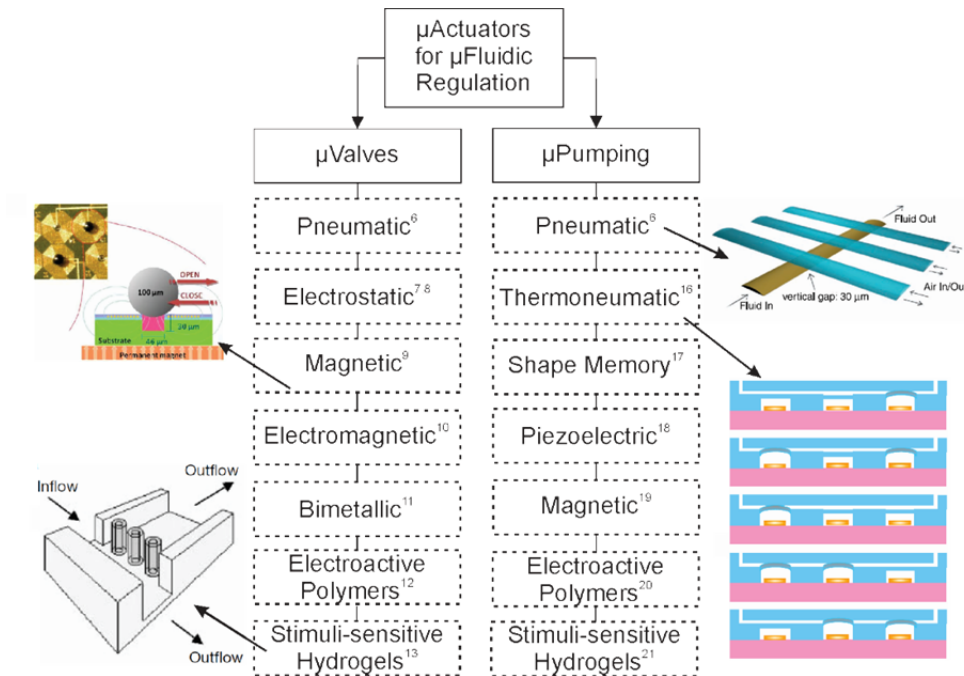
Figure 2.2: Microactuators utilizing various mechanisms for microfluidic flow regulation through microvalving or micropumping applications.

EAP can be classified into two main categories: electronic EAPs and ionic EAPs, as seen in Figure 2.3. Electronic EAPs are governed by electrostatic forces, while ionic EAPs are governed by the electrically induced migration of ionic species. Electronic EAPs can be divided into four main categories: piezoelectric polymers [24], electrostrictive polymers [25], dielectric elastomers [26, 27], and liquid crystal elastomers [12]. Generally electronic EAPs have large actuation strains and stresses, fast response times, and long lifetimes, but also require relatively large driving electric potentials (up to 1 kV) to provide these advantages.

Ionic EAPs can be divided into four categories: polymer hydrogels [28, 29], ionic polymer-metal composites (IMPC) [30-33], conjugated polymers [34, 35], and carbon nanotubes [36, 37]. Their main advantage is signified by their responsiveness at relatively low electric potentials (1-50 V); however, they can be limited by shorter lifetimes and higher relative response times. The shorter lifetimes can be caused by material and electrode degradation with repeated cycles, due to electrochemical effects at the electrodes. The longer response times are due to the

16

electrodiffusion of mobile ionic species, which can be enhanced by reducing the critical length scale to decrease diffusion pathways.

To date, EAPs are generally employed for applications as artificial muscles [23, 27, 31, 34] or as actuators in a broader system [26]. They have also been employed in microfluidic applications as microactuators [29], microvalves [12], and micropumps [33]. These systems take advantage of the specific polymer's ability to turn electrical energy into mechanical work. Electric field sensitive polymer hydrogels, a type of ionic EAP, have the particular advantages of relatively low actuation voltages; they're capable of mass fabrication at the microscale, and have the potential for repeated use without significant polymer degradation.
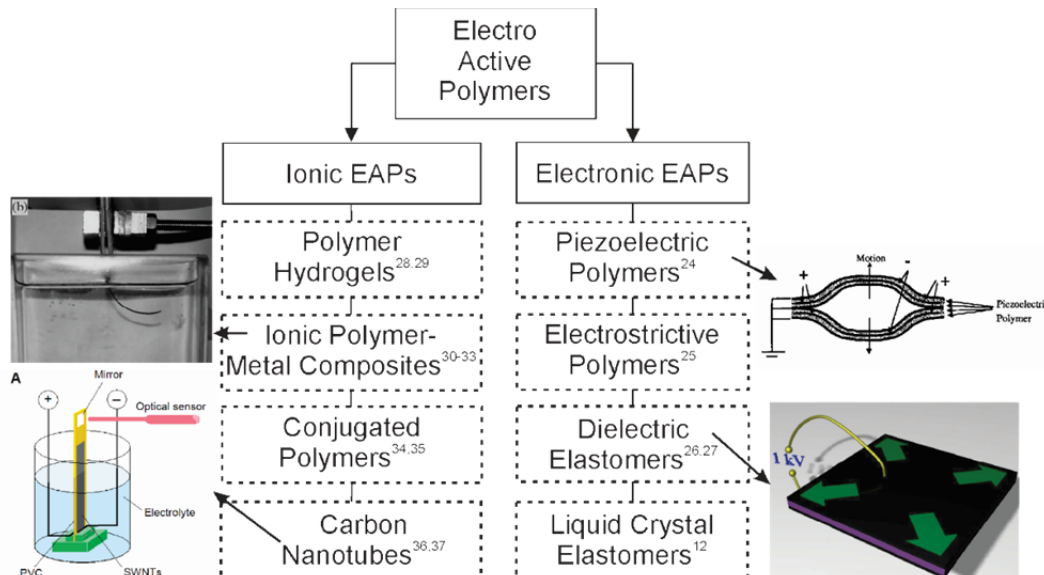
Figure 2.3: Electroactive polymers, classified as fundamentally governed through either ionic or electronic processes.

2.4   Stimuli Sensitive Hydrogels

Stimuli sensitive hydrogels (SSH) are functional polymers that are fabricated as part of a system to produce a deformation, sense a compound or deliver a drug. They have also been referred to as intelligent polymers, stimuli responsive polymers, smart polymers, or polyelectrolyte hydrogels.

17

Hydrogels are cross-linked networks of hydrophobic and/or hydrophilic polymer chains that can be highly swollen with water or other appropriate solvents. They have been shown to respond to a wide variety of environmental stimulus, which can manipulate their volume, shape, pore size; and optical, mechanical, or electrical properties. Many SSHs have shown a reversible response of these properties upon removal of stimulus, a characteristic required for repeated microactuator use. A number of review papers [38-46] have detailed SSH discussing their applications as microactuators, sensors, remote controlled biomaterials, and their operational fundamentals.

Stimuli sensitive hydrogels have been shown to respond to biological stimuli (glucose [47, 48], antigens [49, 50], proteins [51], and enzymes [52]), chemical stimuli (pH [13, 53, 54] and/or electrolytes [54]), and physical stimuli (magnetic fields [55, 56], light [57-61], temperature [62-68], and electric fields [29, 69-71]), as outlined in Figure 2.4. These hydrogels respond to stimulus with a volume transition and/or deformation. The exact mechanism behind their individual responses is unique, but some stimulation methods also share the same underlying mechanism behind actuation. Below their mechanisms will be discussed, except for chemical and electrical stimuli as they will be discussed in greater detail in the following sections.

Various biological stimuli affect the hydrogel differently. Second generation glucose sensitive hydrogels become swollen by glucose, when glucose causes an increase in the charged boronic groups which induces an osmotic pressure [48]. Antigen responsive hydrogels have both an antibody and antigen graphed on the polymer network. Introduction of a free antigen causes competitive binding which breaks the non-covalent crosslinks and induces swelling in the hydrogel [49]. Protein responsive hydrogels have a network whereby the presence of the protein EGTA removes Ca^{2+} from functional groups bound to the polymer backbone, which induces an osmotic pressure and causes swelling [51]. An enzyme-

responsive hydrogel's amine groups are functionalized with neutral zwitterion peptide linkers. The target enzyme catalyzes hydrolysis of these linkers which charges the hydrogel's backbone, and induces osmotic pressure based swelling [52]. Hydrogels responding to biological stimulus are typically employed in systems for sensing of the particular biological marker. Three of the four biological stimuli rely on an osmotic pressure to develop for swelling to occur, a process which will be discussed in detail later.

A type of physically stimulated hydrogels are magnetic field sensitive hydrogels that can either be swollen by a ferrofluid [55] or the polymer network can be a nanocomposite with embedded magnetic nanoparticles [56]. In the first case the ferrofluid interacts with a nonuniform external magnetic field causing an extension, but not a volume transition [55]. In the second case, an alternating magnetic field causes an increase in the temperature of the iron oxide nanoparticles, which induces a subsequent increase in temperature and temperature-based deswelling of the hydrogel [56]. These nanocomposite magnetically sensitive hydrogels have been applied as actuators in microvalves, but suffer from response times on the order of minutes and need an external system to produce the magnetic field [56]. No magnetic system to date relies on an osmotic pressure to develop for actuation.

Light sensitive hydrogels can be stimulated using three main methods, light induced: direct or indirect heating of the polymer network for temperature-based stimulation [57, 58], proton dissociation for pH-based stimulation [59, 60], and proton pumping for pH-based stimulation [61]. Heating of the polymer networks was caused by either directly applying visible light to the gel [57] or heating a gold-colloid nanocomposite gel [58]. The gold-colloid nanocomposite gel was applied as a two-dimensional microvalve, which opened in 40 minutes time. Light induced proton dissociation was enabled by modifying the hydrogel with photoresponsive spirobenzopyran [59, 60], which was subsequently

19

applied for on-demand microvalves opening/closing in minutes [60]. A new design has seen an anionic hydrogel undergoing pH-based actuation when a separate sheet coated with photosensitive bacteriorhodopsin and porous anodic alumnia acted as a proton pump allowing diffusion towards the hydrogel [61]. Light sensitive hydrogels rely on either pH-induced osmotic pressure based actuation or temperature induced actuation, the two most common actuation mechanisms.

Temperature sensitive hydrogels are a popular form of stimuli sensitive hydrogels. Their volume transition actuation mechanism has been previously discussed by many researchers [72-74]. As hydrogels are a three-dimensional polymer network composed of hydrophobic and hydrophilic side chains, it is the energy balance between these chains responsible for volume transition. The equilibrium state can be disturbed by the addition or removal of a thermal load on the system. Below the gel's lower critical solution temperature (LCST) the gels is swollen, and the hydrophobic chains have water molecules hydrogen-bonded to them. At temperatures above the LCST two main mechanisms cause deswelling: a decrease in the bond strength between hydrophobic chains and water molecules, and a natural increase of hydrophobic interactions. The LCST has been demonstrated to be variable, depending on the ratio of hydrophobic to hydrophilic chains within the hydrogel structure. Generally hydrogels deswell with a thermal load, but compositions have been fabricated that swell at high temperatures [75]. In some cases hydrogels have been synthesized to be both temperature and pH sensitive [76], to allow for flexibility of stimulation. Temperature sensitive hydrogels have been applied in microfluidic systems as microvalves [64, 65], micropumps [63], and micromixers [66]. They have also been applied for drug delivery [75, 77], microlenses [78], reversible 'smart' surfaces [79], linear springs and coils [67], and high-resolution tactile displays [68].

Each stimulation method can find niche uses within specific applications, providing a diverse portfolio of applications for SSHs.

20

However, some systems require complex and/or bulky external stimulation components to produce actuation. Response times can also vary drastically across stimulation methods, from under a second to hours. Furthermore, the magnitude of actuation can vary drastically as well, ranging from 1-2 % strain for some biological stimulation methods to >50 % strain for some chemical and physical stimuli. Hydrogels subjected to the physical electric field stimuli show the most opportunity to minimize response time and maximize actuation strain, while keeping the required stimulation components to a minimum. Electrical stimulation does however require preliminary application of a chemical stimulus to initialize the system and ready it for further actuation, necessitating an understanding of pH and ionic sensitive hydrogels.
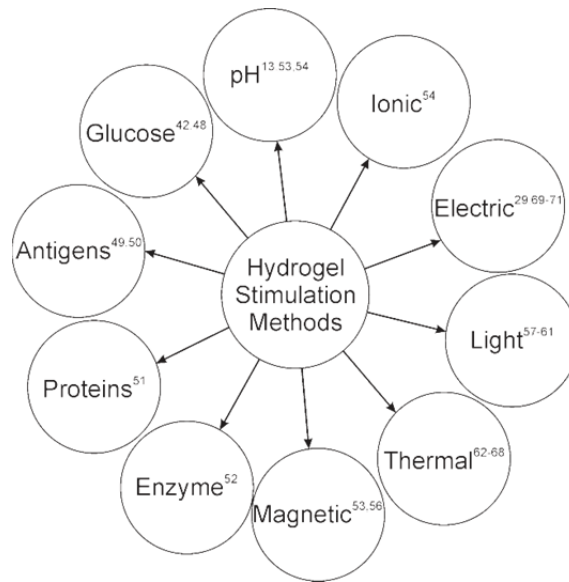
Figure 2.4: Hydrogel stimulation methods through chemical processes, physical fields, or biological molecules.

2.5 pH and Ionic Sensitive Hydrogels

pH and ionic sensitive hydrogels are a broadly researched class of stimuli sensitive hydrogels. A thorough understanding of the underlying mechanisms for pH-based swelling and deswelling is a prerequisite for those looking to further examine electrical swelling. The final equilibrium state of pH/ionic hydrogel swelling becomes the initial condition for electrical swelling; it provides the baseline pressure and deformation prior

21

to further electrical stimulation. Moreover some historical demonstrations of electrically induced actuation are actually employing pH-based swelling or bending through generation of protons and hydroxide at the electrodes. pH sensitive hydrogels have a long history of research, and with the knowledge gained of their deformation mechanisms and kinetics they have been employed in a variety of applications.

Early work on pH sensitive hydrogels by Kuhn *et al.* in the 1950s examined the cyclical dilation and contraction of macroscale hydrogel strips subjected to alkaline and acid solutions, respectively [53]. This demonstrated the reversible nature of hydrogels under pH cycling. By 1994 this work had evolved into the bundling of an array of hydrogel fibers together with a fluid irrigation system to dispense acidic and basic solutions, towards the application of a linear actuator for artificial muscles [80]. Large actuation strains were achieved, but its applicability was questionable due to response times of minutes and the need for irrigation systems to apply the needed chemical stimulus. During this time it was also being shown experimentally that hydrogels respond differently to varying electrolyte concentrations, swelling to a greater extend in weaker acidic or basic solutions depending on the hydrogel type [81].

Applications as actuators in microfluidics weren't thoroughly developed until the year 2000 when Beebe *et al.* demonstrated the *in-situ* photopolymerization of pH-sensitive hydrogels within microchannels [13]. Hydrogel response times decrease with a decreased scale, thus the development of hydrogels at the microscale catalyzed an explosion in applications, which included: microvalves [82-87], micropumps [88], micromixers [89], micropistons [90], microlenses [91], sensors [40, 92-94], and drug delivery systems [95, 96], as shown in Figure 2.5. For these purposes they are generally fabricated as solid cylinders, spheres, or rectangular prisms; however, in some cases for sensing they have been fabricated as inverse opal structures [97, 98] or as a composite with a crystalline colloidal array [99].
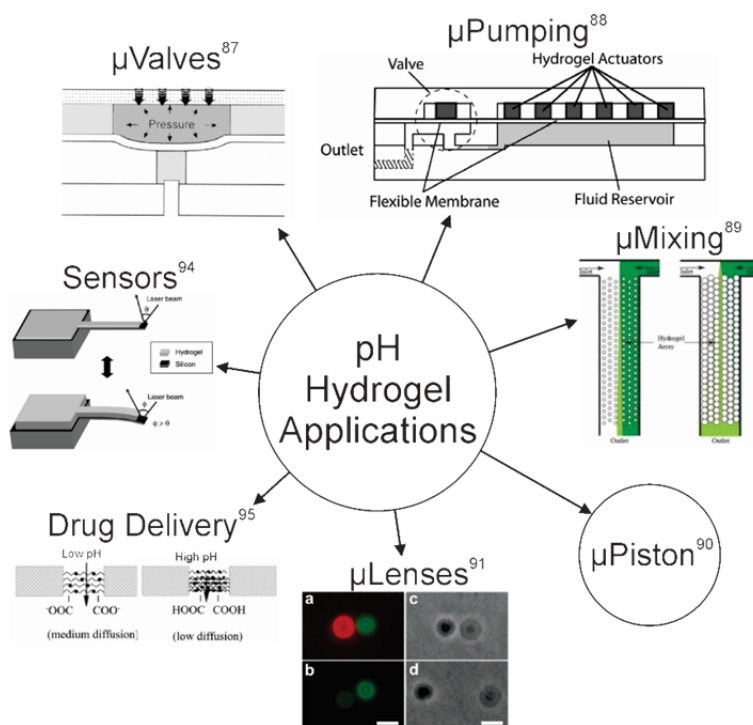
Figure 2.5: Applications of pH stimulated hydrogels in microscale systems

This work focuses on a pH and electrically sensitive hydrogel that is composed of hydroxyethyl methacrylate (HEMA) copolymerized with acrylic acid (AA), which has functional carboxyl groups on the polymer backbone. This structural composition is visualized in Figure 2.6. Overall the hydrogel structure has three-dimensional randomly oriented polymer chains with covalently bound crosslinks. When hydrated in an alkaline electrolyte the carboxyl groups are deprotonated and negatively charged, and mobile cations and anions are found throughout the matrix together with water molecules.

The pH stimulation mechanism relies on the presence of the bound carboxyl groups. Within acid solutions, at a pH below the carboxyl group's dissociation constant, the carboxyl group is protonated and has a neutral charge. At this state any hydration is due to the mixing energy between solvent and the polymer network, which is minor for HEMA-AA and water due to low polymer-solvent interaction. When immersed in an alkaline electrolyte, above the carboxyl group dissociation constant, the carboxyl group deprotonates and becomes negatively charged.

23

$$RCOOH \rightleftharpoons RCOO^- + H^+ \qquad pKa = 5.3 \qquad \text{(2-1)}$$
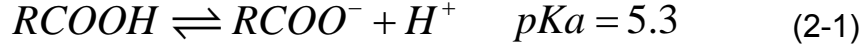
To preserve electroneutrality mobile cations from the surrounding electrolyte diffuse into the hydrogel, dragging water molecules with them and driving swelling of the hydrogel. In addition, the deprotonated protons also bond with mobile hydroxide ions generating added water to cause swelling. This process establishes an osmotic pressure between the hydrogel and surrounding electrolyte solution, with a magnitude equal to the concentration gradient at the hydrogel-electrolyte interface [100].

$$P_{osmotic} = RT\sum_{k=1}^{n}(c_k - c_k^0)$$

$$\text{(2-2)}$$

where R is the universal gas constant, T is temperature, c_k is the concentration of the kth ion inside the hydrogel, and c_k^0 is the concentration of the kth ion outside the hydrogel. Calculation of the osmotic pressure is visualized in Figure 2.7, whereby the mobile anion and cations within and surrounding the hydrogel must be known. Final ionic magnitudes rely strongly on the concentration of the fixed ions on the hydrogel's polymer backbone. In pH stimulation hydrogen diffusion and migration drives the mechanism, and when a buffered electrolyte is used an additional pathway for proton diffusion is added [54]. The hydrogen can diffuse into the hydrogel bonded with the buffer, and as it moves into a location of low hydrogen concentration it can dissociate to influence the electrochemical balance.

The ionic stimulation mechanism relies on the presence of an established osmotic pressure, thus for hydrogels considered here the hydrogel must already be immersed in an alkaline solution. Upon the application of a weaker alkaline ionic concentration, the hydrogel will swell to a greater extent. This is due to a larger concentration gradient being generated between the hydrogel and electrolyte, as the concentration within the hydrogel remains relatively the same but the concentration outside is reduced.
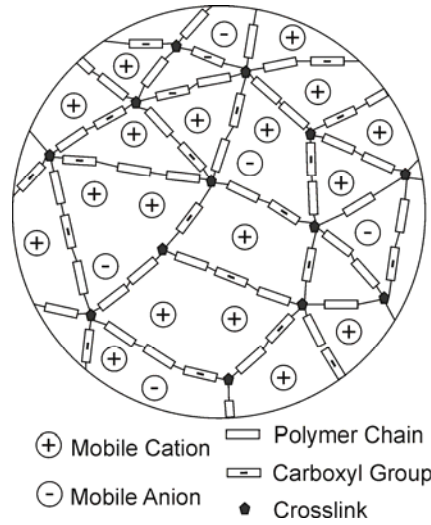
Figure 2.6: Composition of pH-sensitive hydrogel with bound carboxyl groups and interstitial mobile ions, as swollen in an alkaline electrolyte.
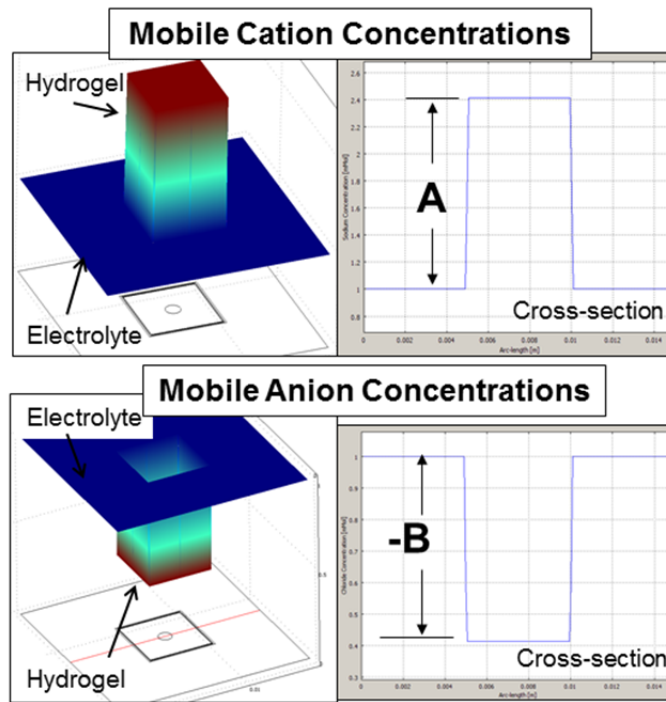
$$A > B \quad \text{for Hydrogel's with Fixed Negative Charges (Anionic)}$$

$$P_{osmotic} = RT \sum_{k=1}^{n} \left(c_k - c_k^0 \right) = RT(A - B)$$

Figure 2.7: Chemically induced osmotic pressure, and the corresponding mobile ion concentrations responsible for osmotic pressures. For chemically induced swelling the deformation is symmetric around the hydrogel.

Significant effort has been made to understand the complex chemical, electrical, and structural interactions that govern hydrogel swelling and deswelling. A wide array of numerical modeling techniques have been employed to examine different aspects governing overall deformation [54, 101-104]. The hydration/dehydration that occurs with swelling/deswelling can have a significant impact on the hydrogel's porosity, stiffness, fixed ion density, and interstitial diffusion rates. The outcomes and impacts of these models will be reviewed in a later section, when the coupled interaction between Poisson's equation, Nernst-Planck equation, and the equations of motion are discussed.

The response time for pH and ionic stimulation of hydrogels is governed by diffusion of molecules into the hydrogel, and equilibrium can be achieved within minutes to hours. As the hydrogel's size scales to microscale dimensions the response times of hydrogels decrease, as diffusion pathways are reduced; however, the response times are still longer than desired for microactuator applications. In addition, the mechanisms causing volume transition requires external system components to pump alkaline or acid solutions into the system containing the hydrogels. This greatly reduces the hydrogels overall utility in complex microfluidic systems. To overcome these drawbacks researchers have looked towards electrically activated hydrogels. Electrically activated hydrogels swelling is governed by both diffusion and migration of ions, providing faster response times on the order of seconds. In addition, the only external equipment required to induce volume transformation are microelectrodes and electrical equipment. Electrically controlling hydrogels also enables high locational selectivity, which is advantageous when regulating a complex microfluidic system.

2.6   Electric Field Sensitive Hydrogels

Electric field sensitive hydrogels (EFSH) are the main focus of this work. They are advantageous over some other microactuators in

microfluidics and SSHs for several main reasons: they can convert electrical energy into mechanical energy, they allow precise locational and performance control through the applied electric field, they have a faster actuation response than thermal or pH stimulus, and they respond faster at smaller length scales.

Research into electric field sensitive hydrogels began in the 1960s with Hamlen *et al.* who examined one cycle of contraction and expansion for a macroscale high aspect ratio rectangular prismatic hydrogel under electrical stimulus (both an electric potential and current was applied) [105]. This work was followed a decade later by Grodzinky and Shoenfeld who provided a theoretical explanation of the observed phenomena and further experimentally examined the tensile force of contraction [106]. Soon after, designs and further investigations for electrically activated artificial sphincters were reported [107]. However, it was the seminal experimental works of Tanaka *et al.* [108] and Shiga and Kurauchi [109] that systematically studied a macroscale hydrogel's deswelling, swelling, and bending under an applied electric field. They found that a hydrogel's position relative to the electrodes (middle/touching and parallel/perpendicular) and configuration of the hydrogel (low or high aspect rectangular prisms) determined the resultant volume transition mechanism and final deformed state. This work was also paralleled by Grimshaw *et al.* who was examining electrically actuated hydrogels for transport of solutes through their porous structure, and produced informative experimental [110] and theoretical [111] works. Through these works it was shown the hydrogels can be repeatedly and cyclically bent [109] or swollen [110] through controlled application of an electrical signal. This repeatable bending mechanism was quickly demonstrated in a hydrogel-based ratcheting mechanism mimicking a worm-like motion [112].

The deformation mechanism behind EFSH bending, swelling, or deswelling stems from two main effects 1) electric field based

manipulation of the chemical equilibrium osmotic pressure 2) pH- and/or ionic-based manipulation of the hydrogel composition itself and/or chemical equilibrium osmotic pressure, respectively. The second pH-based mechanism occurs due to electrochemical reactions on the anode and cathode generating protons and hydroxide, respectively, which diffuse towards the hydrogel. The half reaction that occurs at the anode is (where E^o is the oxidization or reduction potential):

$$2H_2O \rightarrow O_2 + 4H^+ + 4e^- \qquad E^o = -1.23V \qquad \text{(2-3)}$$

The half reaction that occurs at the cathode is:

$$2H_2O + 2e^- \rightarrow H_2 + 2OH^- \qquad E^o = -0.83V \qquad \text{(2-4)}$$

Once in contact with the hydrogel the protons bond with the backbone carboxyl groups (or similar functional group) and neutralize its charge, causing drastic deswelling on the anode side of the hydrogel. Depending on the equilibrium concentration hydroxide ions can also cause swelling, further inducing bending, or a slight deswelling, countering bending: however, these ionic manipulations of the osmotic pressure are less dominant than proton-based deswelling. This is the same osmotic pressure mechanism outlined in Section 2.5, but protons and hydroxide ions come from electrochemical reactions at the electrodes. This pH/ionic mechanism was shown for many EFSH studies that used open well containers to vent bubbles from electrolysis [108, 109], but overall this mechanism does not afford precise control of actuation and has slower response kinetics than pure electric field manipulation. While early studies combined electric field and pH/ionic mechanisms, works eventually emerged that focused on pure electric field manipulation of hydrogels [29, 70, 71]. The mechanism for electric field manipulation relies on the migration of mobile ions to rearrange the concentration gradient at the hydrogel-electrolyte interface, modifying the osmotic pressure, as shown in Figure 2.8. Mobile cations are attracted towards the anode and vice

versa for anions, thus mobile ions redistribute according to the electric potential gradient over the hydrogel and electrolyte domains.

Over the next two decades the seminal works of Tanaka *et al.* [108] and Shiga and Kurauchi [109] catalyzed a large number of studies examining the stimulation of EFSH [29, 69, 70, 113-150], either in bending, swelling, or deswelling configurations. A summary of this large body of work can be seen in Table 1 and 2, which highlights the compositions studied, fabrication methods, type of hydrogel employed, number of electrical cycles performed, electric field or current applied, hydrogel configuration, and hydrogel critical dimension. Major trends within the field of EFSH can be distinguished from these tables.

The majority of hydrogels investigated are anionic, and of these anionic hydrogels carboxyl groups are the dominant functional group.

$$P_{osmotic,Anode} = RT\sum_{k=1}^{n}\left(c_k - c_k^0\right) = RT(B - D)$$

$$P_{osmotic,Cathode} = RT\sum_{k=1}^{n}\left(c_k - c_k^0\right) = RT(A - C)$$

$$P_{osmotic,Anode} > P_{osmotic,Cathode}$$
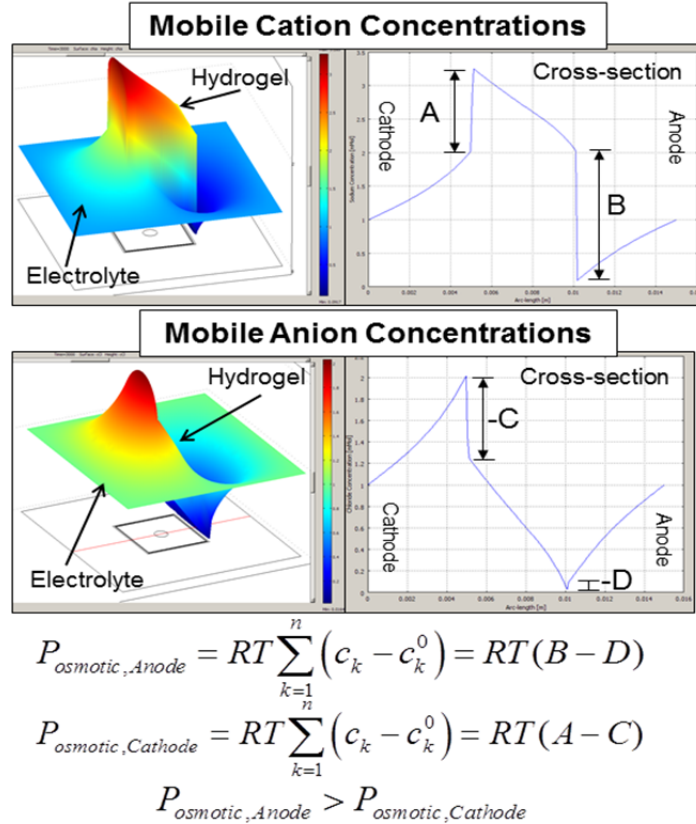
Figure 2.8: Electrically induced osmotic pressure, and the corresponding mobile ion concentration distributions responsible for the induced osmotic pressure. For electrically induced swelling the deformation is asymmetric towards the anode.

Cationic and amphoteric hydrogel types have also been investigated, which allows the hydrogels to be electrically actuated in acidic electrolytes or both acidic and basic electrolytes, respectively. Although no hydrogel monomer composition significantly dominates the investigations, typically the most chronologically recent compositions examined are those that can be photopolymerized at the microscale. Notably within the works shown in Tables 1 and 2, S. J. Kim and his colleagues produced 20 works examining different hydrogel compositions, and consistently showed the repeatable nature of macroscale EFSH cyclical actuation [118-125, 127-133, 136, 139, 151-153]. However, the bulk of these investigations were focused on the bending of macroscale high aspect ratio rectangular prisms, and appeared to be motivated to prove that the composition could be electrically actuated rather than investigate deformation dynamics for a specific application. In addition, a significant number of interpenetrating network polymer compositions have been investigated, as seen in Table 2, generally with motivations to increase the mechanical strength of gels, combine stimuli sensitive properties, or blend together synthetic and natural polymer complexes. The composition chosen for this work was the synthetic copolymer HEMA-AA, the same composition studied by Bassetti *et al.* [29] and within various pH-stimulation based systems [13, 54, 86]. This composition was chosen because it can be UV photopolymerized *in-situ*, has functional carboxyl groups, and the monomer HEMA has been the focus of many research studies [81, 154-160]. A large existing body of work with HEMA and HEMA-AA provides a good background, and also allows the work performed here to add value to this body of knowledge.

Bending was the dominant EFSH configuration tested, whereby a high aspect ratio rectangular prism was placed parallel to parallel-plate electrodes. These electrodes were spaced far enough apart to allow for bending of the hydrogel, and were generally immersed in an open-air container to allow bubbles from electrolysis to escape. Early work into EFSH tested systems was performed under extension and contraction, but

this configuration was largely replaced by bending configurations with little work into extension and contraction in recent years. Bending was widely examined due to the system's intended application as artificial muscles; however, bubbles generated during electrolysis and the dominant pH-induced bending hinder these systems direct application. Two works have been performed that overcome these drawbacks by bending hydrogels operating in air [161, 162]. One system employed PVA-PSA hydrogels, but required the hydrogel rod be coated with an electrolyte charged PVA film which makes manufacturing difficult [161]. The other system used a PVA hydrogel swollen with dimethylsulfoxide (DMSO), but needed a very high 470 kV/m to generate actuation which limits its operational utility [162]. Overall more research is needed to enhance the operational utility of bending hydrogels for artificial muscle applications, although other applications are possible for bending configurations as will be discussed later.

Configurations of hydrogels that examined swelling and deswelling were scarce and when performed were focused on changes in the out-of-plane thickness of the hydrogel. Only recently has in-plane swelling been gaining more attention for their applications as microactuators [29, 69, 149]. In this work in-plane swelling and deswelling will be investigated to close a major gap examining the microscale cyclical swelling-deswelling of hydrogels. The in-plane swelling-deswelling configuration lends itself to thorough investigation, as it allows for simplified examination of the system's characteristics which can then later be exploited for out-of-plane actuation.

Hydrogel fabrication for microsystems requires the precise control of geometries and dimensions, thus UV photolithography is advantageous over alternative fabrication methods to polymerize hydrogels at the microscale. *In-situ p*hotopolymerization also means the hydrogels don't have to be handled or cut after fabrication, which removes any handling-induced errors. Traditional methods of fabrication macroscale hydrogels

include: thermal polymerization, free-radical polymerization, and freeze-thawing. These techniques have been used to fabricate a wide array of hydrogel compositions. For interpenetrating networks fabrication techniques can be combined with each other to generate the desired network structure. Other non-standard fabrication techniques have also been employed, such as electro-wet-spinning of chitosan fibers which produced 10 μm diameter fibers that could be electrically stimulated [140]. Composite hydrogel structures have also been fabricated through grafting [143], doping [150], and rolling [161].

Within the field of EFSH generally only 3-5 cycles of electrical actuation have been undertaken to demonstrate the cyclical deformation response. Some works only examine one cycle of actuation, just to ensure the deformation mechanism is initially reversible. A portion of works have gone beyond this standard of 3-5 cycles to investigate deformation degradation with repeated cycling. Notably Kwon *et al.* operated 10 micropumps continuously for 6 months and the actuators underwent over 6 million cycles of actuation, and they noted no significant degradation in actuation stroke [70]. To ensure that reversible cycling can be performed, this work will subject systems to 3-5 cycles of actuation and studies the system's underlying dynamics of cycling in detail. The fundamental ability to cycle a system is highly advantageous for a variety of applications; micropumping would require continuous operation of the microactuator and microvalving would require active on/off capabilities to influence flow when needed.

A fabricated hydrogel's critical dimension strongly governs its temporal deformation dynamics. Its critical dimension is defined as the dimension that is perpendicular to the electrodes or parallel to the applied electric field. For all configurations mobile ion diffusion and migration must traverse this critical dimension to reach equilibrium, and smaller dimensions afford shorter pathways to traverse. For bending configurations this critical dimension in conjunction with the rectangular

prism's length dictates the magnitude of bending and its kinetic response. For swelling-deswelling configurations this critical dimension dictates response times, but also controls the actuation stroke. For thicker swelling hydrogels the magnitude of deformation will be larger than thinner hydrogels (experiencing equal strain); however, response times will be slower. These opposing effects would have to be balanced according to the end-use application of the microactuator. Examining Table 1 and Table 2 the critical dimensions for hydrogel's have varied from work to work, with anywhere between 6 μm to 5 mm being tested. Studies also do not have the same critical dimension, which makes performance comparison harder; however, their intended applications are different as well. Common among these works was that the critical dimension directly influenced or was the independent variable being measured to determine overall performance.

The pressure induced to cause deformation is proportional to the magnitude of the applied electric field. For the body of works examined in Tables 1 and 2 the magnitude of electric field varied significantly, from 62 V/m [108] to 470 kV/m [162]. For works that use electrochemical reactions at electrodes to generate pH-gradients, lower electric fields are needed with electric potentials just large enough to generate sufficient protons and hydroxide ions. For works that use pure electric field based actuation the applied electric fields must be stronger to generate enough osmotic pressure to cause sufficient actuation. For bending configurations these electric fields are on the 500 V/m to 1kV/m range, as geometric aspect ratios allow for bending under moderate electric fields. For swelling and deswelling based actuation the electric fields applied must be larger, as they must generate significant osmotic pressure to cause sufficient actuation. The two previous systems examining swelling-based actuation used either electrodes spaced 200 μm together with a 1.25 kV/m field [69] or electrode spacing of 2 mm with a maximum 12.5 kV/m [29]. When bending in air was investigated that the maximum electric field of 470

kV/m was applied [162]. This work will examine swelling-deswelling based actuation, thus it will require electric fields on the order of 12.5 kV/m for sufficient actuation. Also, the applied electric potential across electrodes must be large enough to account for losses through any dielectric layer over the electrodes; therefore, the applied electric potentials will be larger than previous swelling-deswelling actuation work.

In addition to artificial muscle applications the electrical stimulation of hydrogels has been employed in a variety of systems, as seen in Figure 2.9, such as drug delivery [163-166], electrochromism [167], biomimetic locomotion [168], cell sorting [71], microactuators [29], and micropumping [70]. Electroresponsive drug delivery results from the ejection of a drug from a hydrogel as it becomes swollen and more porous [163], or electric field degradation of a hydrogel for drug release [166]. Structural color changes under reflection spectroscopy were induced with electrochromatic inverse opal hydrogels that were electrically deswollen using electrostatic forces acting on the charged backbone molecules. This electrochromatic system employed a salt-free organic solvent with a wide electrochemical potential window to avoid electrolysis effects [167]. Biomimetic locomotion was achieved with microdevices that utilize the cyclical bending of EFSH beam to induce forward motion, either through 'swimming' or 'crawling'. However, it's unclear in these systems how electrolysis and electrochemical reactions were avoided, if at all. Cell sorting was the first microfluidic device demonstrated that utilized EFSH beam bending, which was employed to switch cell flow from one channel to another [71]. Due to electrolysis and electrochemical effects Kwon *et al.* was forced to apply voltages below 1.2 V. Kwon *et al.* also employed this same EFSH beam-based system to generate a microfluidic pump, but was still limited to a maximum voltage of 1.2 V [70]. Development of a system that overcomes both electrolysis and electrochemical effects could provide research pathways for these EFSH applications to expand both their utility and performance.

Table 2.1: Copolymer hydrogel compositions that have been electrically stimulated either through bending, shrinking, or swelling.

Classification	Acronym	Name	Fabrication	Type	# Cycles	Electric Field and/or Current	Configuration	Critical Dimension
Synthetic	PVA-PAA [105], [107]	poly(vinyl alcohol - polyacrylic acid)	TP	A	1, No	5V/40mA, 100 V/m	C	?
	HPAM [108], [137]	hydrolized polyacrylamide	FRP	A	No, 5	62.5 V/m, 650 V/m	DS;B	4 mm, 2 mm
	PSA-PAAm [109]	poly sodium acrylate - polyacrylamide	FRP	A	5	2 kV/m	B	?
	PMAA [110]	polymethacrylic acid	FRP	A	3	400 A/m²	S-DS	266 µm
	PAMPS [112], [115]	poly(2-acrylamido-2-methyl propane) sulphonic acid	FRP	A	No, 4	2 kV/m, 500 V/m	B	1 mm
	PVA-PSA [179], [180]	poly(vinyl alcohol) - poly(sodium acrylate)	FT	A	1, No	3 kV/m, 1.5 kV/m	B	1.1 mm
	PAMPS-BMA [113]	poly(2-acrylamido-2-methyl propane) sulphonic acid - n-butylmethacrylate	FRP	A	2	650 V/m	B	1 mm
	PAN [117]	polyacrylonitrile	MAS	A	2	10V + 250 mA	C-E	6.4 µm
	PAAc-PVSA [128], [132], 138]	poly(acrylic acid) - poly(vinyl sulfonic acid)	TP	A	4, 1/2, 4	100 V/m, 125 V/m, 100 V/m	C-E, DS., C-E	5 mm, 2 mm, 5 mm
	HEMA-AA [29]	2-hydroxyethyl methacylate - acrylic acid	UVP	A	1/2	12.5 kV/m	S	300 µm
	PVA [162]	poly(vinyl alcohol)	TP+FT	A	1/2	470 kV/m	B/L	500 µm
	HBA-AAc [71], [70]	4-hydroxybutyl acrylate - acrylic acid	UVP	A	?, 6 mil	1.5 kV/m, 1.5 kV/m + 1.25 mA	B	100 µm, 50 µm
	PF127-BMA-DMAEMA [149], [69]	pluronic F127 - bis methacrylate - dimethylaminoethyl methacrylate	UVP	C	1, 17	4 kV/m, 6.8 kV/m	S-DS	100 µm
Natural	CA [106]	collagen	ECP	C	1/2	3 mA/cm²	C	4.5 mm
	GA [135]	gelatin	TP	Amp	4	320 V/m	B	500 µm
	CS [140]	chitosan	EWS	C	5	1 kV/m	C-E	10 µm
	SPI [148]	soy protein isolate	TP	Amp	6	800 V/m	B	135 µm
Blend	HACC [147]	2-hydroxypropyltrimethyl ammonium chloride chitosan	TP	C	7	667 V/m	B	160 µm
Composite	PVA-PSA + SC [161]	poly(vinyl alcohol) - poly(sodium acrylate) + sodium carbonate	FT+R	A	1	15 kV/m	B	3 mm
	SA-g-PAAc [143]	sodium alginate - graft- poly(acrylic acid)	RGC	A	8	400 V/m	B	1 mm
	PVI-PNIMA-d-CdTe [150]	poly(N-vinylimidazole) - poly(N-methylidacrylamide) -doped- Cadmium Telluride	TP	C	4	30 V	B	3 mm

TP = Thermal Polymerization ; FRP = Free-Radical Polymerization ; FT = Freeze-Thawing ; UVP = UV Photopolymerization

MAS = Manufacturing + Annealing + Saponification ; ECP = Extrusion Cast + Plasticized ; EWS = Electro-wet-spinning ; RGC = Radical Graph Copolymerization ; R = Rolling

A = Anionic ; C = Cationic ; Amp = Amphoteric

C = Contraction ; E = Expansion ; B = Bending ; S = Swelling ; DS = Deswelling ; L = Locomotion ; / = both demonstrated

Table 2.2: Interpenetrating network hydrogel compositions that have been electrically stimulated either through bending, shrinking, or swelling.

Type	Acronym	Name	Fabrication	Type	# Cycles	Electric Field and/or Current	Configuration	Critical Dimension
Synthetic	HSMA/PVA [114]	hydrolized styrene-maleic anhydride/poly(vinyl alcohol)	FRP	A	1	385 V/m	B/S	?
	PVA/PAAc [116], [144]	poly(vinyl alcohol)/poly(acrylic acid)	UVP+FT	A	3, 1	20 V, 333 V/m	B	2 mm, 5 mm
	PVA/PNIPAAm [120]	poly(vinyl alcohol)/poly(N-isopropylacrylamide)	FRP	A	3	667 V/m	B	200 μm
	SA/PDADMAC [122]	alginate/poly(dialyldimethylammonium chloride) sodium	FRP	Amp	3	500 V/m	B	5 mm
	PPG/PAAc [123]	poly(propylene glycol)/poly(acrylic acid)	TP+UVP	A	3	750 V/m	B	2 mm
	PAAc/PAN [131]	poly(acrylic acid)/polyacrylonitrile	UVP	A	3	667 V/m	B	200 μm
	PDADMAC/PAAc-PVA [134]	poly(dialyldimethylammonium chloride)/poly(acrylic acid) - poly(vinyl alcohol)	FRP	A	2	500 V/m	B	400 μm
	PVA/PEI [145]	poly(vinyl alcohol)/polyethyleneimine	TP+FRP	A	3	10 V	B	2mm
Natural	CS/HA [119]	chitosan/hyaluronic acid	TP	A	3	500 V/m	B	200 μm
	GA/AG [138]	gelatin/alginate	TP	Amp	5	469 V/m	B	400 μm
	CS/CMC [142]	chitosan/carboxymethyl cellulose	TP+FRP	Amp	5	300 V/m	B	2mm
Blend	CS/PAAy [118]	chitosan/polyallylamine	TP	A	3	233 V/m	B	200 μm
	CS/PAN [121]	chitosan/polyacrylonitrile	FRP	C	3	750 V/m	B	2 mm
	HA/PVA [124], [133]	hyaluronic acid/poly(vinyl alcohol)	TP+FRP	A	5, 3	15 V, 500 V/m	DS-S, B	?, 200 μm
	CS/PDADMAC [125]	chitosan/poly(dialyldimethylammonium chloride)	FRP	A	3	500 V/m	B	300 μm
	CS/PHEMA [127]	chitosan/poly(hydroyethyl methacrylate)	TP	C	1	300 V/m	B	140 μm
	SA/PMAAc [129]	sodium alginate/poly(methacrylic acid)	FRP	A	3	500 V/m	B	400 μm
	HA/PAMPS [130]	hyaluronic acid/poly(2-acrylamindo-2methylpropane sulfonic acid)	TP+FRP	A	5	500 V/m	DS-S	?
	CS/PAN [139]	chitosan/polyaniline	TP+FT	A	1/2	10 V	B	2mm
	HACC/PVA [148]	2-hydroxypropyltrimethyl ammonium chloride chitosan/poly(vinyl alcohol)	TP+FRP	C	7	667 V/m	B	310 μm
Composite	PAAc/PAAm+PPy/CB [126], [141]	poly(acrylic acid/polyacrylamide+polypyrrole/carbon black	TP	A	24, 5	150 V/m, 300 V/m	B	2 mm, 4 mm

TP = Thermal Polymerization ; FRP = Free-Radical Polymerization ; FT = Freeze-Thawing ; UVP = UV Photopolymerization

MAS = Manufacturing + Annealing + Saponification ; ECP = Extrusion Cast + Plasticized ; EWS = Electro-wet-spinning ; RGC = Radical Graph Copolymerization ; R = Rolling

A = Anionic ; C = Cationic ; Amp = Amphoteric

C = Contraction ; E = Expansion ; B = Bending ; S = Swelling ; DS = Deswelling ; L = Locomotion ; / = both demonstrated
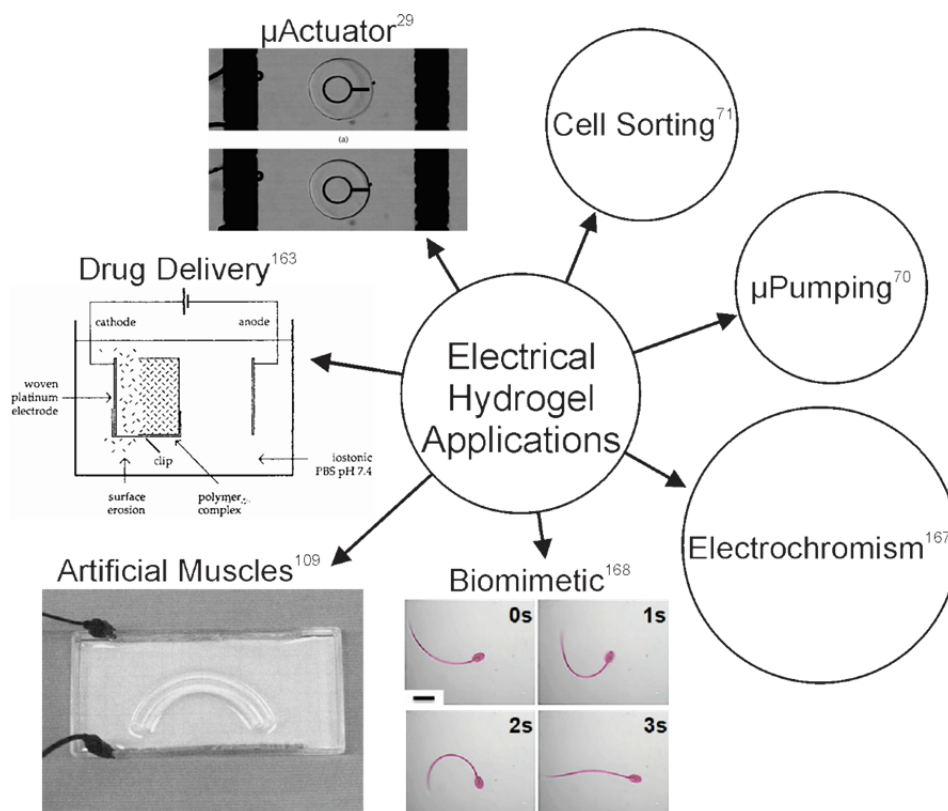
Figure 2.9: Electrically stimulated hydrogel applications for microactuation, micropumping, artificial muscles, drug delivery, and cell sorting.

2.6.1 AC Electrical Actuation

To overcome the negative effects of electrolysis and electrochemical reactions on EFSH system's performance and operational utility, the system in this work utilized a dielectric thin film over electrodes. The incorporation of this dielectric layer complicated the system's operation by inducing electrostatic shielding effects over the electrodes, which necessitated the use of AC-based electrical signals.

In this system electrostatic shielding occurred when a DC electric potential was applied between electrodes and mobile ions built up to form an electric double layer (EDL) on top of the electrodes, as seen in Figure 2.10. This EDL effectively reduced or eliminated the applied electric potential over its thickness, as seen in Figure 2.10. The thickness of the Debye length (κ^{-1}) layer is a function of concentration, shown in Eq. 2-5, and has a thickness that ranges from <1 nm to >10 nm. This EDL thickness was orders of magnitude smaller than the proposed critical

37

dimensions for the hydrogels in this work, thus any electrostatic shielding would effectively eliminate all applied electric potential across the hydrogel and thus any actuator displacement.

$$\kappa^{-1} = \sqrt{\frac{\varepsilon_r \varepsilon_o RT}{2F^2 c_\infty}}$$

(2-5)

where ε_r is the dielectric permittivity of electrolyte, ε_o is the dielectric permittivity of free space, R is the universal gas constant, T is temperature, F is Faraday's constant, and c_∞ is the bulk electrolyte concentration.

Electrostatic shielding can be prevented by driving the EFSH actuator using AC square waves with a sufficiently high frequency. Above a certain characteristic frequency the system's mobile ions do not have enough time to accumulate over electrodes and form an electric double layer. Therefore, the applied electric field will be uniform and actuation will be undisturbed. Determining the system's characteristic frequency requires analysis of the capacitive interactions primarily influenced by electrolyte concentration and dielectric film thickness.

The use of AC electrical signals to overcome electrostatic shielding has previously been implemented by those investigating: comb-drive actuators in conducting liquid media [169-172], parallel plate electrostatic actuators [172, 173], dielectrophoretic liquid actuation [174, 175], and electrowetting-on-dielectric [176-178]. Each of these systems had different dielectric layer thicknesses, electrolyte conductivities, electrode gap spacing, and required varying magnitudes of electric potential; however, each system was able to overcome electrostatic shielding. Characteristic frequencies for these systems range from 10^2 to 10^7 Hz, depending dominantly on the electrolyte concentrations and dielectric layer thicknesses.

Previously EFSH systems in bending configurations were examined under the effect of an AC sinusoidally oscillating electric field [179, 180].

However, these two systems applied electric potentials that were symmetric about 0V, with no DC offset. These systems also did not have dielectric coated electrodes and the research intention was more to investigate bending mode shapes. As the frequency increased above 5 Hz it was found that the hydrogel actuation tended towards zero. This was due to the lack of an effective applied electric field, and the electrically-induced osmotic pressure tended towards zero as well.

To induce EFSH actuation using AC frequencies, and still obtain actuation, an electrical signal with a DC offset must be employed, shown in Figure 2.11. The duty cycle of the square wave signal can be modified to control the average electric potential applied without modifying the maximum or minimum potentials. Using this duty cycle modulation could afford control of the hydrogel actuation and easy cycling between two actuation states.
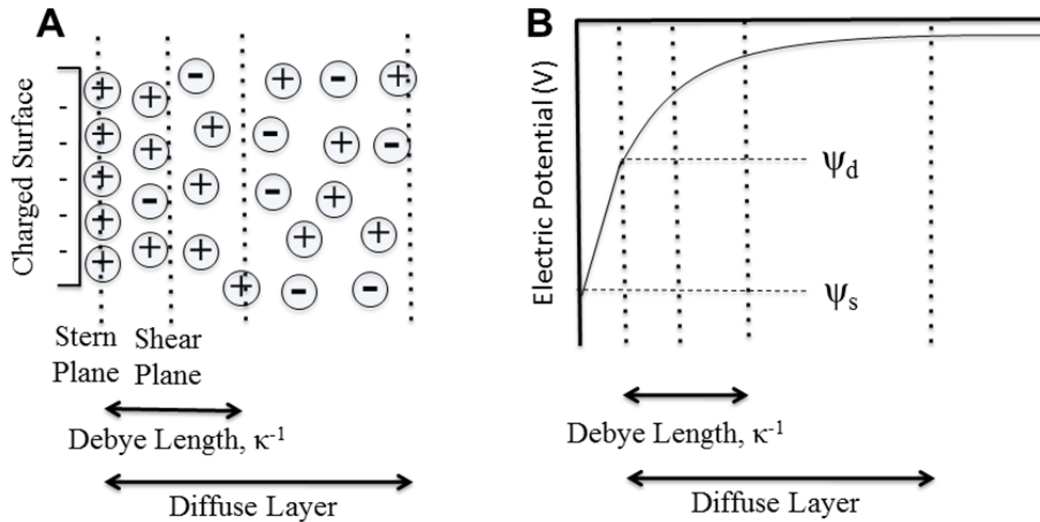
Figure 2.10: (A) Structure and (B) electric potential decay across the Debye length and diffuse layer, as dictated by mobile ions in electrolyte. Here ψ_s is the surface electric potential and ψ_d is the Stern plane electric potential. Adapted from [181].
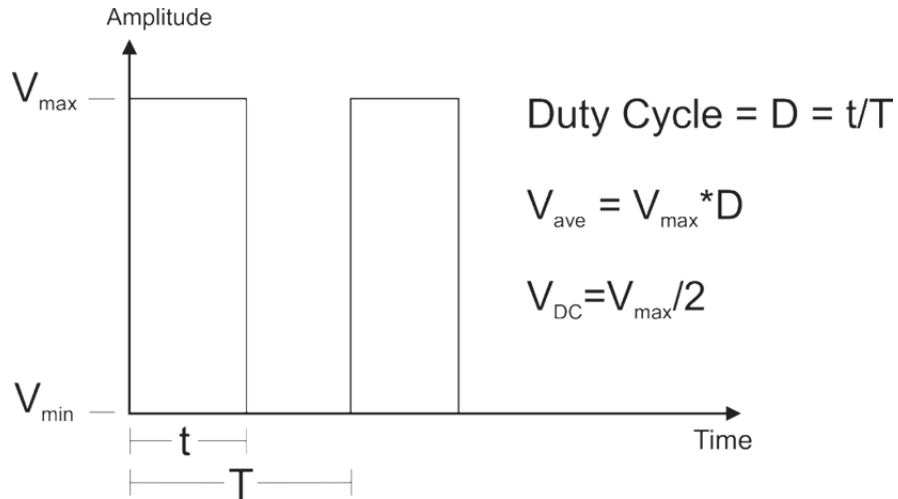
Figure 2.11: Square wave electrical signal applied to electric field sensitive hydrogels

2.7   Modeling of Electrical Stimulation

Numerical modeling of a hydrogel's response under electrical stimulation is of great interest to researchers experimentally or theoretically investigating these systems. Modeling gives researchers the ability to decompose the complex physical system into a solvable set of governing and supplementary equations that can predict the EFSH system's response. This can help researchers understand the underlying phenomenon that causes EFSH actuation, and further optimize their systems to maximize application specific performance. It's important to remember throughout the evaluation of different governing equation systems that pH stimulation sets the initial condition for electrical stimulation, thus models should have a demonstrated capability to accurately predict actuation under both pH and electrical stimulation methods.

Three distinct governing equation systems have been developed to numerically model EFSH hydrogel actuation: thermodynamic models, multiphasic mixture theory, and transport models. In addition, molecular simulations have been developed but generally model hydrogel monomer strands at scales orders of magnitude smaller than of interest to this work. The desired numerical model would be one that can: both qualitatively and quantitatively predict EFSH actuation, model equilibrium and transiently

deforming systems, have the ability to model large deformations, and have been proven to work at the microscale. Each of the three main models has their own advantages, disadvantages, and similarities. The following will discuss these models briefly, while more comprehensive reviews are available for further reading [182-184].

2.7.1 Thermodynamic Models

Thermodynamic models were the first equation system proposed to predict the swelling and deswelling response of ionic hydrogel polymers, although initially these models just targeted polymer-solvent systems and neglected any ionic contributions. Models are based on the total free energy of the polymer-solvent system, composed of: mixing, elastic, and ionic free energies. The theoretical basis, and its ongoing evolution, can be largely attributed to Flory [100, 185-187] who described the three contributions to total free energy in detail and their supplementary equations, such as the important polymer-solvent interaction parameter (which needs to be empirically determined for each different polymer/solvent system, e.g. [188]). The thermodynamic equation system has been previously implemented to model pH [81] and temperature [189] based hydrogel actuation, but no examples of EFSH systems have been found.

Thermodynamic models employ relatively simple governing equations that provide good qualitative trends, but do not always show good quantitative agreement with experiments (although some experimental verification has been shown [190]). The parameters used within thermodynamic models are empirically determined, estimated, or taken as adjustable parameters to obtain agreement between models and experiments, which significantly limits their predictive capabilities. Moreover, the Gaussian chain model was employed to formulate the elastic free energy contribution [100], thus the models do not inherently have the capability to simulate large deformation actuation responses observed for hydrogels. The models also do not consider transient

41

analysis and focus solely on equilibrium responses, which significantly limit the information that can be synthesized from simulations. Therefore, thermodynamic models were considered a poor candidate for EFSH hydrogel modeling.

2.7.2 Multiphasic Mixture Theory

Multiphasic mixture theory proposes that physical systems can be broken down into two or more phases, with separate governing equations for each phase. Initially biphasic mixture theory was developed to model articular cartilage [191], which did not include an ionic phase. Biphasic models examined a variety of system parameters [192, 193], but didn't allow for changes in ionic concentration within the articular cartilage tissue. Thus, Lai *et al.* expanded upon biphasic models to develop triphasic models which incorporated contributions from an incompressible solid, an incompressible liquid, and an ionic phase (whether fixed and/or mobile cations/anions) [194, 195]. This expansion to a triphasic system was initially applied to articular cartilage; however, the triphasic system was an ideal candidate for modeling stimuli sensitive hydrogels and was further implemented for this purpose. This early triphasic model was built upon by Gu *et al.* [196, 197], Sun *et al.* [198], and Zhou *et al.* [199]. However, it was Li *et al.* who composed a comprehensive triphasic mixture theory incorporating all the individual contributions into one overall model [200].

The governing equations are formulated by beginning with a saturation condition to account for the separate volume fractions of the three phases, and generally infinitesimal deformation is assumed to relate solid and liquid phases. The continuity and momentum equations are then applied to solid, liquid, and fixed ion phases. The liquid and ionic phases are further defined by the system's osmotic pressure, any induced convection or migration through the diffusion equation, and the electric potential distribution through Poisson's Equation. It is important to note that these equations are coupled, and overall deformation can change

42

significantly when one parameter is altered. Multiphasic models have been shown to provide both good qualitative and quantitative agreement with experiments, as shown through verification studies by Sun *et al.* [198] and Gu *et al.* [197]. For the purpose of EFSH triphasic models have been implemented to examine bending under an electric field at equilibrium [199].

The triphasic theory was augmented by Chen *et al.* in 2006 to account for large deformations when simulating articular cartilage [201]. A version of this theory was also implemented for biphasic modeling of thermosensitive hydrogels [74], but to date no pH or electric field sensitive hydrogel has been modeled to account for large material deformations. Tied together with large deformation models are variations in the properties of the hydrogel with changing hydration, which to date has also not been incorporated into the modeling theory. Lastly, no researchers to date have implemented triphasic models to examine microscale systems.

2.7.3 Transport Models

Transport models presume that actuation of an ionic hydrogel is driven by diffusion and migration of mobile ions into and out of the hydrogel. Early work towards developing a comprehensive transport model to simulate hydrogel systems was performed by Nussbaum and Grodzinsky [202], and Grimshaw *et al.* [110, 111] who were examining pH or electrical solute transport across swelling and deswelling membranes. This was later followed by Chu *et al.* who focused on the transient response kinetics of pH-based swelling and deswelling [81].

After these works the ongoing development and application of these models can be segmented into three major groups of researchers. One group, composed of Wallmersperger *et al.* and Ballhause *et al.*, examined a number of millimeter scale hydrogels responding to either pH [101, 104, 203] or electrical stimulus [204-206]. These works studied a variety of chemical bath conditions, hydrogel geometries, and electric field magnitudes. All works by this group implement numerical modeling using

43

finite element methods, and verified their models based on the experimental work by Gulch *et al.* [207] in a bending configuration. For EFSH simulations, one work did not examine any deformation at all [204], while another examined bending of a fiber [205] and the last work examined swelling of a square hydrogel [206]. This last work had a similar configuration to the numerical modeling performed within Chapter 3 [208]; however, in that work Wallmersperger *et al.* did not communicate transient electric or chemical field profiles, nor did he consider a rigid core for structural stability. Lastly, Wallmersperger considered a linearly increasing cyclical potential rather than a sharp transient reversal of the electric field, as Chapter 3 considers and which would be more relevant to microactuator applications.

Another major body of work has been spearheaded by Li *et al.* and Luo *et al.* who modeled hydrogel stimulation from pH [103, 209-218] and electrical fields [214, 217, 218]. All works by this group were solved numerically by implementing a meshless Hermite-Cloud method, except one [212] which used a meshless point weighted least-squares method. The EFSH simulations were verified against the experiments by Sun *et al.* [219] and Kim *et al.* [153], which examined the bending of a hydrogel fiber. This research group also developed a hybrid transport-multiphasic model [220], which was initially based on a multiphasic system. It was employed to eliminate the use of the electroneutrality condition allowing for the direct simulation of electric potential distributions within the hydrogel using Poisson's Equation and the Nernst-Plank Equation. The hybrid system has been implemented extensively by Li *et al.* and Lou *et al.* to simulate EFSH bending [220-228], and evolved to be primarily based on transport models. As the hybrid model evolved the continuity equation which was initially used to solve for fluidic pressure [222], was replaced by, the now traditional, equations for osmotic pressure [224]. The only other difference between the hybrid system and the transport system is the use of the fluidic and solid volume fraction for calculation of the hydration, and

44

subsequently the fixed ion concentration, instead of a strain-based hydration equation. It's unclear which method is more accurate, as both equation sets agree with the experimental systems they simulate. A number of the hybrid systems have also incorporated large deformation equations based off the total Lagrangian description using the second Piola-Kirchhoff stress tensor [221, 223-228], which significantly enhances this equation sets ability to model nonlinear deforming EFSH systems. All the hybrid systems examined were solved using the meshless Hermit-Cloud methods. They were experimentally verified against works by Kim *et al.* [153], Sun *et al.* [219], Ali *et al.* [229], and Shiga and Kurauchi [109], all examining bending configurations.

The last major research group was composed of De *et al.* and Bassetti *et al.* who examined both pH [54, 102] and electrical stimulation [29]. The geometries and scale examined are directly applicable to the work performed here. However, simplification of this complicated equation system would be required for initial numerical modeling as they incorporate a significant amount of coupled supplementary equations. For both pH and electrical swelling the numerical systems were implemented using a meshless finite cloud method. For EFSH Bassetti *et al.* implemented linear elastic equations of motion, but accounted for large deformation effects by incorporating of analytical expressions for a nonlinear Young's modulus [230] and shear modulus [231]. With these additions the model accurately predicted deformations for strains of ~20 %, but this model could be expanded in the future to account for large deformations by incorporating the second Piola-Kirchhoff stress tensor similar to that used by the aforementioned hybrid systems. These models were successful in simulating the large deformation that occurs during pH-based stimulation, and modeled the large concentration gradients that occur for EFSH stimulation. However, these models are unclear regarding how they calculated osmotic pressure, as the meshless method only considered the hydrogel domain and did not include electrolyte domains.

45

While not an extensive body of work, De *et al.* and Bassetti *et al.* produced the only numerical modeling of microscale hydrogels using transport equations and examined pH-based swelling and deswelling of cylindrical geometries which is directly applicable to this work.

Transport models themselves are, at their core, composed of Poisson's Equation (P) to model the electric field distribution, the Nernst-Planck (NP) Equation to model the transient flux of mobile ion species, and the equations of motion to determine the structural displacement of the hydrogel polymer network. These equations are highly coupled, as the P-NP equations both contain mobile ion and electric field terms. The applied osmotic pressure is calculated from the mobile ion distribution, which then influences the hydrogel's displacement through the equations of motion. Moreover, as the hydrogel undergoes large deformations the density of fixed ions changes which further affects the mobile ions' distribution. In addition, a number of supplementary equations are required to fully define the equation system, which include: changes in relative permeability due to hydration [232], changes in the fixed ion distribution due to hydration or protons [233], changes in intermembrane diffusivity due to hydration [234], non-linear changes in Young's Modulus due to hydration [230], and relating the ionic mobility to diffusivity [235]. Four of these crucial supplementary equations depend on the hydration state of the hydrogel, which is representative of the amount of deformation experienced by the hydrogel. Thus, for large deformations this system becomes highly coupled and non-linear, and appropriate initial conditions, time steps, and discretization is required to achieve solution convergence. The exact equations used for numerical modeling in Chapter 3 will be presented in more detail within that chapter.

None of the transport models examined a cyclically actuated hydrogel system. In theory the system would be fully reversible, but no modeling has been performed to examine how an EFSH system (bending or swelling) would respond to a step change in electric field polarity or

46

magnitude. As more hydrogel systems incorporate cyclical actuation into their operational mechanics there will be a strong need to transiently simulate system to optimize performance.

2.8   Hydrogel Swelling

Hydrogels swell upon exposure to environmental stimuli, and this observed swelling is dependent on the hydrogel's geometry, composition, the surrounding system, and the strength of the stimulus. This is a complex and interconnected system, and as the previous section on numerical analysis outlines, can involve complicated modeling to fully define dynamics. However, more simplified experimental and numerical studies focused on examining hydrogel swelling have occurred. A portion of these studies have been tied with broader studies investigating hydrogel actuation [113, 127, 134, 148], whereby the weight degree of swelling is a measurement taken alongside actuation measurements. Other studies have directly investigated swelling, and those we will discuss further with specific focus on hydrogels responding to pH swelling.

Before hydrogel electrical actuation, the hydrogel goes through a series of pH and ionic induced chemical equilibrium states. These states serve as the initial conditions to electrical actuation. In general, various configurations of hydrogel swelling exist, including: free swelling of any geometry [156, 236], free swelling of spherical or cylindrical gels with rigid cores of the same geometry [237, 238], a rectangular prism bonded to a rigid base [237, 239], or swelling with the gel constrained by a rigid base and top [239]. The hydrogel in this work was cylindrical with a rigid cylindrical core that had out-of-plane deformation constrained, allowing for only in-plane deformation. This system represents two cases of swelling; one with a rigid base and top representing a plane strain system and another case of cylindrical swelling with a rigid core.

The incorporation of a rigid core inside the hydrogel created an inhomogeneous equilibrium state through the hydrogel. At the exterior of

the equilibrated gel the radial and circumferential stresses would be negligible [240]. However, assuming a perfectly bonded gel-core, the stresses in the immediate neighborhood of the core have been shown to be non-zero [240, 241]. When the ratio between the core's and hydrogel's radius remains small these stresses remain near the gel-core interface. However, when this ratio becomes larger these stresses become apparent throughout the hydrogel, with the threshold ratio a function of hydrogel stiffness [241]. Thus, the core to equilibrated hydrogel ratio should be minimized to reduce stresses within the hydrogel that could cause rupture.

Perfect bonding between the hydrogel and core was assumed; however, the bonding state was not explicitly tested. Imperfect bonding, while not visually apparent, could have occurred and would result in lower stresses throughout the hydrogel. This would not significantly affect actuation; however, if delamination occurred actuation would be affected. The hydrogel-core bonding state could be tested by fabricating a high aspect ratio rectangular prism at a 45 degree angle to the microchannel and around a cylindrical core. Flowing liquid down the microchannel to apply a pressure to the fiber and observing either rigid body rotation or a bending of the hydrogel could be performed to investigate the bonding.

The hydrogels considered within this work are depicted in Figure 2.12, and have 4 distinct states before electrical actuation: as fabricated, deswollen in acidic electrolytes, swollen in strong basic electrolytes, and continual swelling in weaker and weaker basic electrolytes. There is some minimum basic electrolyte concentration after which continued swelling will not occur and deswelling will start to occur [239]; however, that was not experienced in this work as the minimum electrolyte concentration used here was 1 mM KOH. The deformation in all of these four cases is radially symmetric. It was observed in this work that the core and hydrogel always remained bonded together; however, numerical models have been developed to simulate constrained swelling when no bonding between the core-hydrogel occurs [242].

When the hydrogels were fabricated they had a certain radius, modulus, and unbound fixed ions. In this as-fabricated state they also had no hydration, mobile ions, or osmotic pressure. Upon immersion in a strong basic environment (e.g. 500 mM KOH) the hydrogel experiences radial deformation and a change in system characteristics. The hydration, osmotic pressure, and mobile ions were all larger than the as-fabricated state; however, the modulus was decreased. Immersing the hydrogel in a dilute basic solution (e.g. 1 mM KOH) resulted in even more radial deformation, and increased hydration, mobile ions, and osmotic pressure. However, the modulus was further decreased when immersed in dilute basic solution. Throughout all the states within a basic electrolyte the fixed ions within the hydrogels remain constant, and can only be modified through immersion in an acidic environment. Upon electrical stimulation the swelling regions would experience increased hydration, mobile ions, and osmotic pressure; while experiencing a decreased modulus. If a hydrogel property needed to be modified to increase deformation or reduce response times during electrical actuation, it would have to be made by altering the as-fabricated state. Thus we will investigate how the fabrication parameters influence the hydrogel's properties in Chapter 5.

As Fabricated	1-500 mM HCL	500 mM KOH	1 mM KOH	Electrically Stimulated
Radius $(r)=r_{FAB}$	$r_{HCL}>r_{FAB}$	$r_{0.5M\,KOH}>r_{HCL}$	$r_{1mM\,KOH}>r_{0.5M\,KOH}$	$r_{Anode,Elec}>r_{1mM\,KOH}$
Hydration $(H)=0$	$H_{HCL}>0$	$H_{0.5M\,KOH}>H_{HCL}$	$H_{1mM\,KOH}>H_{0.5M\,KOH}$	$H_{Elec}>H_{1mM\,KOH}$
Osmotic Pressure $(P_{os})=0$	$P_{os}=0$	$P_{os}>0$	$P_{os,1mM\,KOH}>P_{os,0.5M\,KOH}$	$P_{Elec}>P_{os,1mM\,KOH}$
Modulus$=E_{FAB}$	$E_{HCL}<E_{fab}$	$E_{0.5M\,KOH}<E_{HCL}$	$E_{1mM\,KOH}<E_{0.5M\,KOH}$	$E_{Elec}<E_{1mM\,KOH}$
Mobile Ions $(c_M)=0$	$C_M=0$	$C_{M,0.5M\,KOH}>0$	$C_{M,1mM\,KOH}>C_{M,0.5M\,KOH}$	$C_{Elec}>C_{M,1mM\,KOH}$
Unbound Fixed Ions $(c_F)=c_{F,FAB}$	$c_F=0$	$c_{F,0.5M\,KOH}=c_{F,FAB}$	$c_{F,0.5M\,KOH}=c_{F,FAB}$	$c_{F,Elec}=c_{F,FAB}$

Figure 2.12: Swelling states of hydrogels from as-fabricated to electrically stimulated, overviewing the changes in deformation, material properties, and ionic species.

49

2.9 Mechanical Properties

Hydrogels are porous polymer structures swollen with a solvent, and thus contain both a solid and liquid phase. A hydrogel responds to an external force like an elastic solid due to the polymer network, but can also transport matter due to the solvent's mobility through the porous structure. A perfect elastic solid under an imposed load would undergo near instantaneous stress and strain; however, in perfect Newtonian liquids the strain-rate affects the stress distribution. These effects lead to two main phenomena that can describe a hydrogel's mechanical properties: poroelasticity and viscoelasticity.

Poroelasticity describes the concurrent processes of polymer network deformation and transport of solvent through the porous structure due to this deformation [243]. Linear poroelasticity assumes a linear elastic polymer network with superimposed Newtonian liquid, and is generally characterized using uniaxial compression [244] and indentation [245, 246]. This characterization can yield material properties such as: modulus, Poisson's ratio, and permittivity of the hydrogel. They have been implemented to characterize various compositions, including poly(N-isopropylacrylamide) [243], alginate [244], gelatin [245], and poly(acrylamide) [246]. The use of poroelastic techniques to characterize hydrogels has only been applied within the last decade, and to date no tension based experiments have performed. The poroelastic phenomena will be watched for; however, not explicitly measured, as the effects of viscoelasticity on the hydrogel dynamics are more dominant for the hydrogel composition examined in this work.

Viscoelasticity is a measure of the elastic effects of the polymer network and the viscous effects of the interstitial solvent [247]. Viscoelasticity must be considered for systems that will undergo cyclical actuation, such as the electrically actuated system examined in this work. It can be measured by applying a sinusoidally oscillating deformation and measuring the resultant stress in the material, a process which will be

described later. But, these measurements do not yield the Poisson's ratio of the material, which must be measured separately.

Poisson's ratio is one of the most important mechanical properties of a system, and is commonly measured for polymer gels by examining the transverse strain compared to the axial strain [54]. A newer technique employs an embedded rod, whereby upon application of an external force the rigid body motion of the rod is measured magnetically [248]. Poisson's ratio has been measured for stimuli sensitive hydrogel compositions such as polyacrylamide [249, 250], poly(N-isopropylacylamide) [251], and hydroxyethyl methacrylate –co- acrylic acid [54]. This work focuses on the composition HEMA-AA, which has previously had its Poisson's ratio characterized yielding a value of 0.43 [54]. For a swollen hydrogel this value for Poisson's ratio has some error, ±0.06 at a pH of 9, but the results are consistent with values of other gel compositions, such as 0.457 for polyacrylamide [250]. Poisson's ratio can be combined with the Young's (or Storage) modulus of the hydrogel to fully define the material properties needed within the equations of motion (note that inertia effects are generally neglected, thus density is not required).

Polymer gels that are capable of large deformations require non-linear elastic theories to be extensively analyzed and fully defined, thus theories of finite elasticity can be employed. Two extensive reviews of finite elasticity with examples are given by M. F. Beatty [252] and R. W. Ogden [253]. However, linear elastic theories combined with supplementary equations have met with significant success in describing reasonably large deformations [29, 54, 102]. Thus any measurements of viscoelastic mechanical properties will be made in the linear regime, and analytically employed in equation systems using linear theories of elasticity, together with appropriate supplementary equations.

While tensile viscoelastic properties remain the focus of this work, as hydrogels in this work always experience tensile strains, a range of methods are available to measure different moduli of a hydrogel. Major

techniques are compression testing to determine the compressive modulus and shear modulus, and traditional tensile testing to determine the Young's modulus. These techniques will be reviewed briefly below to illustrate the hydrogel compositions previously tested, the range of properties characterized, and related pieces of literature.

2.9.1 Compression and Shear

Swollen hydrogels have gained attention as a replacement material for articular cartilage as its material properties can be matched by engineering hydrogels [254]. The mechanical properties of interest for this application, or any other application requiring the hydrogel to bear a compressive load, are compressive modulus and shear modulus.

Measurement of compressive modulus is performed by applying a uniaxial load on a hydrogel in confined compression. The resultant force caused by a prescribed deformation is measured, and the compressive modulus can be calculated given the area of the sample [255]. In addition, the shear modulus can be related back to the compressive modulus should the stress-strain isotherms fit an appropriate theory, as demonstrated by Horkay *et al.* for a Mooney-Rivlin relation [256].

Using these techniques a variety of hydrogel compositions have been investigated, including: semi interpenetrating networks containing poly(acrylamide) [255], hydroxypropyl methacrylate–co-N,N-dimethylaminoethyl methacrylate [256], poly(vinyl alcohol) [257], poly(ethylene glycol) dimethacrylate [258], poly(N-isopropylacrylamide) [259], and poly(hydroxyethyl methacrylate) [260]. Of note is the HEMA composition which had a measured compressive modulus between 310-960 kPa [260], which shows that they are mechanically strong enough for the intended application but the range is quite large and depends significantly on the tested solvent composition.

Dynamic measurements can also be performed to measure the complex compressive modulus or the complex shear modulus. The complex moduli are a combination of the storage modulus (elastic

components) and the loss modulus (viscous component). These measurements examine the viscoelasticity of the hydrogel in a compression configuration. These tests have been previously performed for HEMA-AA for compression [261] and shear behavior [254]. The compressive complex modulus ranged from 1-1.4 MPa [261] while the complex shear modulus ranged from 0.24-2.3 MPa [254]. It's apparent from these quantities that elastic effects are not always dominant over viscous effects and depend significantly on the composition fabricated.

2.9.2 Tensile Testing

Stimuli sensitive hydrogels that swell upon stimulation require that their mechanical properties be measured in tension to mimic the actuation application. These hydrogels have found a variety of applications for their actuation capabilities, including: pH-sensitive microfluidic valves [54, 262], electrically activated artificial muscles [230, 263-265], and thermally stimulated bioprosthetic heart valve stents [266], among others. A repeatable and quantifiable measure of mechanical properties that balance this actuation is necessary to adequately design and optimize these applications.

The use of tensile testing for stimuli sensitive hydrogels traditionally applies a deformation of a known rate while the resultant opposing force is measured with a load cell. Measuring the cross-section of dumbbell shaped samples allows for the generation of a stress-strain curve. Applying linear Hooke's Law, the Young's modulus of the sample can then be determined from the slope of the stress-strain curve. Tensile testing can also be implemented to measure the ultimate tensile strength of hydrogels [262], the percent elongation of the gel at fracture [262], the transition from linear to nonlinear responses [160], and changes in the Young's modulus as the SSH is being actuated (deswollen to swollen, or vice versa) [267].

Traditionally tensile testing uses an automated system that measures stress and applies strain. However, polymer gels do not always

lend themselves to this technique due to their low mechanical stiffness or a lack of available equipment. Thus alternative methods have been experimented with that apply loads and observe deformation through a CCD camera [263, 264, 268]. Deformation has been observed by placing graphite particles on the surface [264], ink markers on the surface [263], or incorporating glass beads or fluorescent seed particles inside the hydrogel [268]. These methods have apparent disadvantages though. The markers on the surface are prone to being dissolved in the solution surrounding the hydrogel samples, blurring the marker or washing it away entirely [263, 264]. The particles inside the hydrogel also hamper accuracy due the hydrogel's fundamental swelling behavior. When fabricated the hydrogel-particle composite is in a deswollen state, and upon swelling the hydrogel to a testing state the particles have a non-uniform region formed around them [268]. This region has either decreased hydrogel mechanical strength or is a void, allowing the particles to move around which decreases the measurement accuracy. The more swollen the hydrogel is, the larger these inaccuracies become. More work needs to be performed to develop a technique that can consistently and accurately measure tensile properties, should the use of these non-traditional techniques continue.

Various stimuli sensitive compositions and property ranges have been tested and achieved through tensile testing methods. For electric field sensitive compositions; 2-acrylamido-2-methylpropane sulfonic acid sodium salt with moduli between 1-5 kPa [230], poly(acrylonitrile) with moduli between 7-24 kPa [264] or a maximum of 2.4 MPa [265], poly(vinyl alcohol)-poly(acrylic acid) with moduli between 240-300 kPa [263], and poly(vinyl alcohol) with moduli between 10-900 kPa [266]. A unique hybrid of poly(vinyl alcohol) and carbon nanotubes was also examined, with moduli between 320-570 kPa [269]. In addition, thermosensitive compositions of poly(N-isopropylacrylamide) [267], N-vinyl caprolactam [270], and hydroxypropylcellulose [270] have been tested with moduli

ranges of 2-60 kPa, 30-940 kPa, and 67-765 kPa, respectively. Both the electric field sensitive and thermally sensitive hydrogels have similar requirements for mechanical properties, and can have a very small minimum moduli. It's clear that a wide range of mechanical properties can be achieved, depending on the composition employed, and the hydrogel's environmental and fabrication conditions.

Of direct interest to this work are tensile tested compositions of either HEMA or HEMA-AA. The latter being a neutral hydrogel, generally employed for biomedical applications but provides the basis for later compositional variations. The former being a pH and electric field sensitive hydrogel, which is also the composition of choice for this work and can be photopolymerized *in-situ*. Early work examining the Young's modulus of HEMA achieved moduli between 1-10 kPa, depending on the solvent employed [271]. This mechanical range was expanded considerably to 98-588 kPa when researchers began photopolymerizing HEMA and experimented with different photoinitiators [272]. HEMA with photoinitiator Irgacure-651 produced hydrogels with the strongest tear strength, but also the weakest moduli. Since high tear strength promotes high fatigue resistance and/or rupture during actuation, alternative methods to increase moduli were employed. The most influential method was to vary the crosslinker percentage in the monomer solution. This was tested for HEMA as various crosslinkers were employed to achieve a broad range of moduli between 0.08-1.1 MPa (although this test did not employ photopolymerization) [273].

The most relevant body of work was produced by Johnson *et al.* [262, 268, 274] and De *et al.* [54], who examined the tensile properties of pH and electric field sensitive photopolymerized HEMA-AA. Initially they measured the Young's modulus of the hydrogel at various pHs [54, 274], showing that there is a semi-plateau in modulus at either the expanded or contracted state (with constant degree of swelling), ranging from 230 kPa to 290 kPa, respectively. Johnson *et al.* also provided a thorough analysis

of mechanical properties as affected by the solution pH (swollen and contracted states), percent weight crosslinker, and photopolymerization time [262]. A broad range of moduli were found from between 0.2-4 MPa, largely affected by the percent weight crosslinker included in the precursor mixture.

These works provide an excellent basis for tensile testing of HEMA-AA hydrogels. However, these works did not examine the influence of varying electrolyte concentration which can significantly alter the modulus of the hydrogel, only testing at one buffer concentration of 0.2 M. In addition, the effect of the photopolymerization intensity was not explored. Most critically for the application of cyclically actuated hydrogels, the dynamic mechanical properties were not explored to specifically examine the relationship between the elastic and viscous moduli of a deforming hydrogel.

2.9.3 Dynamic Mechanical Analysis

Dynamic mechanical analysis (DMA) is a powerful mechanical and thermal analysis technique, employed to detect a polymer's fundamental viscoelastic mechanical properties and phase transition points, respectively [275]. For phase transitions DMA is employed to measure the glass transition temperature of a polymer by measuring internal damping as a function of increasing temperature or frequency [276]; however, this is not the focus here. The fundamental viscoelastic mechanical properties are of importance to this work, especially those measured in tension.

Within a linear viscoelastic system the polymer phase can be considered a perfect elastic solid experiencing instantaneous stress and strain, while the solvent phase is a perfect Newtonian liquid that experiences stress dependent on the strain rate [275]. The two measured dynamic mechanical properties (DMP) are the storage modulus (elastic) and loss modulus (viscous), which can be combined to calculate the complex modulus and tangent delta (internal friction based damping).

Nonlinear viscoelastic systems are more complex, and require the investigation of stress induced creep or strain induced relaxation [277]. These two nonlinear effects are often coupled and a function of both material and geometric origins. These effects should be incorporated within an appropriate nonlinear model defining the constitutive behavior. However, this complex investigation is beyond the scope of this work, as linear elastic constitutive behavior has been shown previously to agree with experiments when used with appropriate supplementary equations [29, 54, 102].

The technique of dynamic mechanical analysis can be employed to measure compressive, tensile or shear dynamic mechanical properties. Each measurement would generate a respective storage and loss moduli, e.g. for shear DMA a shear storage modulus and shear loss modulus. Shear-based DMA employs a parallel plate oscillatory shear rheometer, and has been employed for polymers of chitosan-xanthan [278], poly(vinyl alcohol)-hyaluonan [279], and hydroxyethylcellulose [280]. Compressive and tensile DMA is typically performed with the same equipment, but through application of forces in opposing directions. Compressive DMA has previously measured dextran methacrylate polymers, under both controlled force (applying stress) and multi-strain methods (applying displacement) [281].

The hydrogel's tensile dynamic mechanical properties are the main interest of this work. The elastic and viscous components can be decoupled by studying a specimen's response to a sinusoidally oscillating strain (or stress), as depicted in Figure 2.13. To obtain these properties a hydrated sample is mounted between two grips. A known sinusoidal strain is applied at a specific frequency, as in Eq. 2-6, and the resulting stress can be measured, as in Eq. 2-6. The stress response would also be sinusoidal in nature, and would be neither perfectly in phase (as a perfect elastic solid) nor 90° out of phase (for a perfect viscous fluid). Thus stress lags at a measurable phase angle. This phase angle in

combination with the known frequency, measured stress, and applied strain is used to determine the storage and loss modulus of the hydrogel, as calculated using Eq. 2-7. The storage and loss modulus can be combined to determine the complex modulus of the system, which is a combination of the real storage modulus and the imaginary loss modulus, shown in Eq. 2-8.

$$\varepsilon = \varepsilon_{Max} \sin(\omega t) \qquad \sigma = \sigma_{Max} \sin(\omega t) \qquad (2\text{-}6)$$

where ε is the sample strain, ε_o is the maximum applied strain, σ is the sample stress, σ_o is the maximum measured stress, ω is the angular testing frequency, and t is time.

$$E' = \frac{\sigma_{Max}}{\varepsilon_{Max}} \cos\delta \qquad E'' = \frac{\sigma_{Max}}{\varepsilon_{Max}} \sin\delta \qquad \tan\delta = \frac{E''}{E'} \qquad (2\text{-}7)$$

where E' is the storage modulus, E" is the loss modulus, and δ is the phase angle between storage and loss modulus.

$$E^* = E' + iE'' \qquad (2\text{-}8)$$

where E* is the complex modulus, and i is the unit imaginary number.
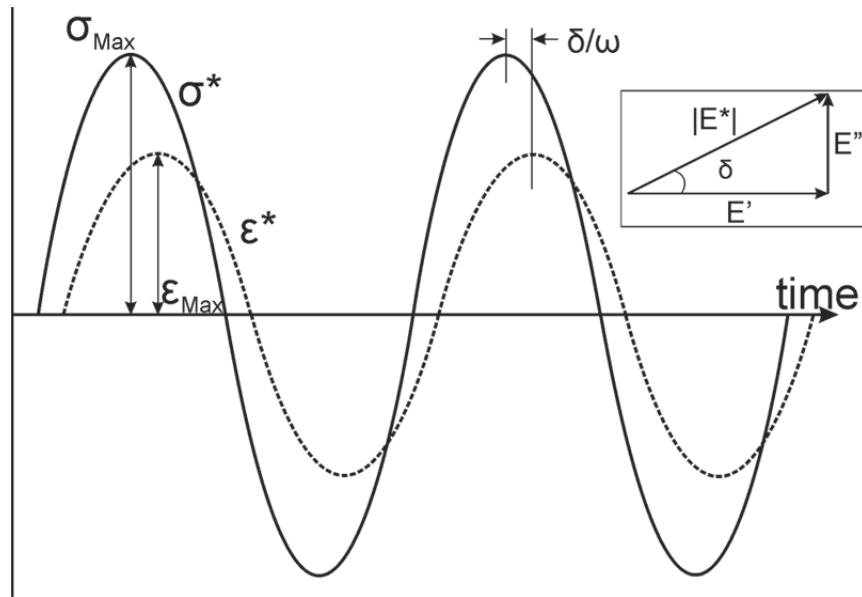
Figure 2.13: Dynamic mechanical analysis through the application of a sinusoidal strain to determine the dynamic mechanical properties of storage and loss modulus.

The measurement of tensile DMP has been employed for electric field sensitive polymers of poly(vinyl alcohol-vinyl acetate)-poly(acrylic acid) (PAA-PVAA) [282], gelatin [283], poly(vinyl alcohol) [283], and collagen-poly(vinyl alcohol) [283]. These studies all measured the storage modulus and tangent delta as a function of increasing temperature, focusing on measuring the glass transition temperature. In addition, for PAA-PVAA all DMP were measured, with storage and loss modulus ranging from 2.7-25 MPa and 2.3-14.5 MPa. These values were relatively large, and showed how elastic effects are not always dominant over viscous effects.

Of particular interest to this work are HEMA and HEMA-AA composition. No literature has performed DMA with HEMA-AA, thus this composition's viscoelastic properties remain unknown. However, previous work has investigated the DMP of HEMA. Early work by Nakamura and Nakagawa measured the DMP while varying the water content of hydrogels, but within a low frequency range of 0.006 to 0.6 Hz [284]. Over this frequency range the storage modulus varied from 398 kPa to 4 MPa, highlighting the effect of frequency on the system. But, investigation at higher frequencies in the range of 0.1 to 10 Hz would be necessary for hydrogels being cyclically actuated in the range of 10 to 0.1 s per cycle. Another work by Marco et $al.$ examined HEMA over a larger frequency range from 0.3-30 Hz, but the focus was on changes in tensile storage modulus with varying temperature [285]. Over the temperature range of $27^{o}C$ to $175^{o}C$ the storage modulus varied from 1.5 GPa to 5 MPa, respectively. The frequency regime and low temperature measurements are somewhat relevant to the system in this work; however, the hydrogel was order of magnitudes stiffer than applicable for hydrogel actuation.

As mentioned previously no literature has studied the DMP of a HEMA-AA composition. Thus, when applying a HEMA-AA composition in a cyclically actuating system, as performed in Chapter 5, the DMP must be thoroughly investigated to examine the relationship between storage modulus and loss modulus. In addition, tensile testing studies have shown

that the inclusion of AA into the polymeric structure can have a significant influence on the mechanical properties [159, 160], varying Young's modulus from 0.4 to 1.8 MPa for AA weight percentages from 5 % to 25 %, respectively [159]. To accurately compare and contrast developed experimental systems with those in literature the concentration of AA within the hydrogel will have to be kept constant, eliminating the potential for varying DMP. Fabrication parameters that can be examined would be the crosslinker weight percentage, polymerization intensity, and exposure time. Testing parameters that could be modified to better mimic the applied system would be the cyclical testing frequency and swelling state of the hydrogel, as governed by the electrolyte concentration. Performing these studies for tensile dynamic mechanical properties would provide a resource for those applying HEMA-AA within active systems, and begin the experimental examination of this compositions viscoelastic properties.

References

[1]   N. L. Jeon, D. T. Chiu, C. J. Wargo, H. K. Wu, I. S. Choi, J. R. Anderson*, et al.*, "Design and fabrication of integrated passive valves and pumps for flexible polymer 3-dimensional microfluidic systems," *Biomedical Microdevices,* vol. 4, pp. 117-121, May 2002.

[2]   G. M. Walker and D. J. Beebe, "A passive pumping method for microfluidic devices," *Lab on a Chip,* vol. 2, pp. 131-134, 2002.

[3]   E. Thielicke and E. Obermeier, "Microactuators and their technologies," *Mechatronics,* vol. 10, pp. 431-455, Jun-Aug 2000.

[4]   K. W. Oh and C. H. Ahn, "A review of microvalves," *Journal of Micromechanics and Microengineering,* vol. 16, pp. R13-R39, May 2006.

[5]   M. S. Groen, D. M. Brouwer, R. J. Wiegerink, and J. C. Lötters, "Design Considerations for a Micromachined Proportional Control Valve," *Micromachines,* vol. 3, pp. 396-412, 2012.

[6]   M. A. Unger, H. P. Chou, T. Thorsen, A. Scherer, and S. R. Quake, "Monolithic microfabricated valves and pumps by multilayer soft lithography," *Science,* vol. 288, pp. 113-116, Apr 7 2000.

[7]   D. Anjewierden, G. A. Liddiard, and B. K. Gale, "An electrostatic microvalve for pneumatic control of microfluidic systems," *Journal of Micromechanics and Microengineering,* vol. 22, pp. 025019-9, Feb 2012.

[8]   A. V. Desai, J. D. Tice, C. A. Apblett, and P. J. A. Kenis, "Design considerations for electrostatic microvalves with applications in poly(dimethylsiloxane)-based microfluidics," *Lab on a Chip,* vol. 12, pp. 1078-1088, 2012.

[9]   P. J. Chang, K. Yung-Yuan, C. Mei-Lin, M. Megens, and D. A. Horsley, "Low-power magnetically-actuated microvalves for highly parallel microfluidic automation," in *Sensors, 2012 IEEE*, 2012, pp. 1-4.

[10]   M. Capanu, J. G. Boyd, and P. J. Hesketh, "Design, fabrication, and testing of a bistable electromagnetically actuated microvalve," *Journal of Microelectromechanical Systems,* vol. 9, pp. 181-189, Jun 2000.

[11]   H. Jerman, "Electrically-Activated, Normally-Closed Diaphragm Valves," *Journal of Micromechanics and Microengineering,* vol. 4, pp. 210-216, Dec 1994.

[12]   A. Sanchez-Ferrer, T. Fischl, M. Stubenrauch, A. Albrecht, H. Wurmus, M. Hoffmann*, et al.*, "Liquid-Crystalline Elastomer Microvalve for Microfluidics," *Advanced Materials,* vol. 23, pp. 4526-4530, Oct 18 2011.

[13]   D. J. Beebe, J. S. Moore, J. M. Bauer, Q. Yu, R. H. Liu, C. Devadoss*, et al.*, "Functional hydrogel structures for autonomous flow control inside microfluidic channels," *Nature,* vol. 404, pp. 588-590, Apr 6 2000.

[14]   N. T. Nguyen, X. Y. Huang, and T. K. Chuan, "MEMS-micropumps: A review," *Journal of Fluids Engineering-Transactions of the Asme,* vol. 124, pp. 384-392, Jun 2002.

[15]   B. D. Iverson and S. V. Garimella, "Recent advances in microscale pumping technologies: a review and evaluation," *Microfluidics and Nanofluidics,* vol. 5, pp. 145-174, Aug 2008.

[16]   W. Mamanee, A. Tuantranont, N. V. Afzulpurkar, N. Porntheerapat, S. Rahong, and A. Wisitsoraat, "PDMS Based Thermopnuematic Peristaltic Micropump for Microfluidic Systems," *Journal of Physics: Conference Series,* vol. 34, pp. 564-569, 2006.

[17]   W. L. Benard, H. Kahn, A. H. Heuer, and M. A. Huff, "Thin-film shape-memory alloy actuated micropumps," *Journal of Microelectromechanical Systems,* vol. 7, pp. 245-251, Jun 1998.

[18]   Y. C. Hsu, J. L. Hsu, and N. B. Le, "An experimental and numerical investigation into the effects of the PZT actuator shape in polymethylmethacrylate (PMMA) peristaltic micropumps," *Microsystem Technologies-Micro-and Nanosystems-Information Storage and Processing Systems,* vol. 15, pp. 565-571, Apr 2009.

[19]   T. R. Pan, S. J. McDonald, E. M. Kai, and B. Ziaie, "A magnetically driven PDMS micropump with ball check-valves," *Journal of Micromechanics and Microengineering,* vol. 15, pp. 1021-1026, May 2005.

[20]   T. B. Xu and J. Su, "Development, characterization, and theoretical evaluation of electroactive polymer-based micropump diaphragm," *Sensors and Actuators A-Physical,* vol. 121, pp. 267-274, May 31 2005.

[21]   A. Richter, S. Klatt, G. Paschew, and C. Klenke, "Micropumps operated by swelling and shrinking of temperature-sensitive hydrogels," *Lab on a Chip,* vol. 9, pp. 613-618, 2009.

[22]   G. H. Pollack, "Muscle contraction as a polymer-gel phase-transition," *Smart Structures and Materials 1999: Electroactive Polymer Actuators and Devices,* vol. 3669, pp. 45-50, 1999.

[23]   F. Carpi, R. Kornbluh, P. Sommer-Larsen, and G. Alici, "Electroactive polymer actuators as artificial muscles: are they ready for bioinspired applications?," *Bioinspiration & Biomimetics,* vol. 6, pp. 045006-10, Dec 2011.

[24]   G. Bohannan, H. Schmidt, D. Brandt, and M. Mooibroek, "Piezoelectric polymer actuators for active vibration isolation in space applications," *Ferroelectrics,* vol. 224, pp. 211-217, Mar 1 1999.

[25]   Z. Y. Cheng, V. Bharti, T. B. Xu, H. S. Xu, T. Mai, and Q. M. Zhang, "Electrostrictive poly(vinylidene fluoride-trifluoroethylene) copolymers," *Sensors and Actuators A-Physical,* vol. 90, pp. 138-147, May 1 2001.

[26]   S. Rosset, M. Niklaus, P. Dubois, M. Dadras, and H. R. Shea, "Mechanical properties of electroactive polymer microactuators with ion implanted electrodes," *Electroactive Polymer Actuators and Devices (EAPAD) 2007,* vol. 6524, 2007.

[27]   S. Akbari and H. R. Shea, "An array of 100 mu m x 100 mu m dielectric elastomer actuators with 80% strain for tissue engineering applications," *Sensors and Actuators a-Physical,* vol. 186, pp. 236-241, Oct 2012.

[28]   C. J. Yu, Z. Duan, P. X. Yuan, Y. H. Li, Y. W. Su, X. Zhang*, et al.*, "Electronically Programmable, Reversible Shape Change in Two- and Three-Dimensional Hydrogel Structures," *Advanced Materials,* vol. 25, pp. 1541-1546, Mar 20 2013.

[29]   M. J. Bassetti, A. N. Chatterjee, N. R. Aluru, and D. J. Beebe, "Development and modeling of electrically triggered hydrogels for microfluidic applications," *Journal of Microelectromechanical Systems,* vol. 14, pp. 1198-1207, Oct 2005.

[30]   K. Asaka and K. Oguro, "Bending of polyelectrolyte membrane platinum composites by electric stimuli Part II. Response kinetics," *Journal of Electroanalytical Chemistry,* vol. 480, pp. 186-198, Jan 25 2000.

[31]   S. Nemat-Nassera, S. Zamani, and Y. Tor, "Effect of solvents on the chemical and physical properties of ionic polymer-metal composites," *Journal of Applied Physics,* vol. 99, May 15 2006.

62

[32]   R. K. Nagarale, G. S. Gohil, and V. K. Shahi, "Recent developments on ion-exchange membranes and electro-membrane processes," *Advances in Colloid and Interface Science,* vol. 119, pp. 97-130, Feb 28 2006.

[33]   M. Banister, S. Vohnout, and D. Kenman, "Development of a PACS digital pump (TM) and implications for other industries - art. no. 65270N," *Industrial and Commercial Applications of Smart Structures Technologies 2007,* vol. 6527, pp. N5270-N5270, 2007.

[34]   G. Alici, P. Metz, and G. M. Spinks, "A methodology towards geometry optimization of high performance polypyrrole (PPy) actuators," *Smart Materials & Structures,* vol. 15, pp. 243-252, Apr 2006.

[35]   B. Gaihre, G. Alici, G. M. Spinks, and J. M. Cairney, "Effect of electrolyte storage layer on performance of PPy-PVDF-PPy microactuators," *Sensors and Actuators B-Chemical,* vol. 155, pp. 810-816, Jul 20 2011.

[36]   R. H. Baughman, C. X. Cui, A. A. Zakhidov, Z. Iqbal, J. N. Barisci, G. M. Spinks*, et al.*, "Carbon nanotube actuators," *Science,* vol. 284, pp. 1340-1344, May 21 1999.

[37]   J. Yip, F. Ding, K. L. Yick, C. W. M. Yuen, T. T. Lee, and W. H. Choy, "Tunable carbon nanotube ionic polymer actuators that are operable in dry conditions," *Sensors and Actuators B-Chemical,* vol. 162, pp. 76-81, Feb 20 2012.

[38]   S. B. Rossmurphy and H. Mcevoy, "Fundamentals of Hydrogels and Gelation," *British Polymer Journal,* vol. 18, pp. 2-7, Jan 1986.

[39]   S. Chaterji, I. K. Kwon, and K. Park, "Smart polymeric gels: Redefining the limits of biomedical devices," *Progress in Polymer Science,* vol. 32, pp. 1083-1122, Aug-Sep 2007.

[40]   A. Richter, G. Paschew, S. Klatt, J. Lienig, K. F. Arndt, and H. J. P. Adler, "Review on hydrogel-based pH sensors and microsensors," *Sensors,* vol. 8, pp. 561-581, Jan 2008.

[41]   P. Calvert, "Hydrogels for Soft Machines," *Advanced Materials,* vol. 21, pp. 743-756, Feb 16 2009.

[42]   K. Deligkaris, T. S. Tadele, W. Olthuis, and A. van den Berg, "Hydrogel-based devices for biomedical applications," *Sensors and Actuators B-Chemical,* vol. 147, pp. 765-774, Jun 3 2010.

[43]   H. Meng and J. L. Hu, "A Brief Review of Stimulus-active Polymers Responsive to Thermal, Light, Magnetic, Electric, and Water/Solvent Stimuli," *Journal of Intelligent Material Systems and Structures,* vol. 21, pp. 859-885, Jun 2010.

[44]   N. S. Satarkar, D. Biswal, and J. Z. Hilt, "Hydrogel nanocomposites: a review of applications as remote controlled biomaterials," *Soft Matter,* vol. 6, pp. 2364-2371, 2010.

[45]   T. Khaleque, S. Abu-Salih, J. R. Saunders, and W. Moussa, "Experimental Methods of Actuation, Characterization and Prototyping of Hydrogels for BioMEMS/NEMS Applications," *Journal of Nanoscience and Nanotechnology,* vol. 11, pp. 2470-2479, Mar 2011.

[46]   R. Messing and A. M. Schmidt, "Perspectives for the mechanical manipulation of hybrid hydrogels," *Polymer Chemistry,* vol. 2, pp. 18-32, 2011.

[47]   M. Lei, A. Baldi, E. Nuxoll, R. A. Siegel, and B. Ziaie, "A hydrogel-based implantable micromachined transponder for wireless glucose measurement," *Diabetes Technology & Therapeutics,* vol. 8, pp. 112-122, Feb 2006.

[48]   G. Lin, S. Chang, H. Hao, P. Tathireddy, M. Orthner, J. Magda, *et al.*, "Osmotic swelling pressure response of smart hydrogels suitable for chronically implantable glucose sensors," *Sensors and Actuators B-Chemical,* vol. 144, pp. 332-336, Jan 29 2010.

[49]   T. Miyata, N. Asami, and T. Uragami, "A reversibly antigen-responsive hydrogel," *Nature,* vol. 399, pp. 766-769, Jun 24 1999.

[50]   T. Miyata, N. Asami, and T. Uragami, "Structural Design of Stimuli-Responsive Bioconjugated Hydrogels That Respond to a Target Antigen," *Journal of Polymer Science Part B-Polymer Physics,* vol. 47, pp. 2144-2157, Nov 1 2009.

[51]   J. D. Ehrick, S. K. Deo, T. W. Browning, L. G. Bachas, M. J. Madou, and S. Daunert, "Genetically engineered protein in hydrogels tailors stimuli-responsive characteristics," *Nature Materials,* vol. 4, pp. 298-302, Apr 2005.

[52]   P. D. Thornton, R. J. Mart, and R. V. Ulijn, "Enzyme-responsive polymer hydrogel particles for controlled release," *Advanced Materials,* vol. 19, pp. 1252-1256, May 7 2007.

[53]   W. Kuhn, B. Hargitay, A. Katchalsky, and H. Eisenberg, "Reversible Dilation and Contraction by Changing the State of Ionization of High-Polymer Acid Networks," *Nature,* vol. 165, pp. 514-516, 1950.

[54]   S. K. De, N. R. Aluru, B. Johnson, W. C. Crone, D. J. Beebe, and J. Moore, "Equilibrium swelling and kinetics of pH-responsive hydrogels: Models, experiments, and simulations," *Journal of Microelectromechanical Systems,* vol. 11, pp. 544-555, Oct 2002.

[55]   D. Szabo, G. Szeghy, and M. Zrinyi, "Shape transition of magnetic field sensitive polymer gels," *Macromolecules,* vol. 31, pp. 6541-6548, Sep 22 1998.

[56]   N. S. Satarkar, W. L. Zhang, R. E. Eitel, and J. Z. Hilt, "Magnetic hydrogel nanocomposites as remote controlled microfluidic valves," *Lab on a Chip,* vol. 9, pp. 1773-1779, 2009.

[57]   A. Suzuki and T. Tanaka, "Phase-Transition in Polymer Gels Induced by Visible-Light," *Nature,* vol. 346, pp. 345-347, Jul 26 1990.

[58]   S. R. Sershen, G. A. Mensing, M. Ng, N. J. Halas, D. J. Beebe, and J. L. West, "Independent optical control of microfluidic valves formed from optomechanically responsive nanocomposite hydrogels," *Advanced Materials,* vol. 17, pp. 1366-+, Jun 6 2005.

[59]   K. Sumaru, K. Ohi, T. Takagi, T. Kanamori, and T. Shinbo, "Photoresponsive properties of poly(N-isopropylacrylamide) hydrogel partly modified with spirobenzopyran," *Langmuir,* vol. 22, pp. 4353-4356, Apr 25 2006.

[60]   S. Sugiura, A. Szilagyi, K. Sumaru, K. Hattori, T. Takagi, G. Filipcsei, *et al.*, "On-demand microfluidic control by micropatterned light irradiation of a photoresponsive hydrogel sheet," *Lab on a Chip,* vol. 9, pp. 196-198, 2009.

[61]   K. M. Al-Aribe, G. K. Knopf, and A. S. Bassi, "Photo-electric biotransducer for activating ionic hydrogel microactuators," *Sensors and Actuators B: Chemical,* vol. 176, pp. 1056-1064, Jan 2013.

[62]   J. Hoffmann, M. Plotner, D. Kuckling, and W. J. Fischer, "Photopatterning of thermally sensitive hydrogels useful for microactuators," *Sensors and Actuators A-Physical,* vol. 77, pp. 139-144, Oct 12 1999.

64

[63]   M. E. Harmon, M. Tang, and C. W. Frank, "A microfluidic actuator based on thermoresponsive hydrogels," *Polymer,* vol. 44, pp. 4547-4556, Jul 2003.

[64]   A. Richter, D. Kuckling, S. Howitz, T. Gehring, and K. F. Arndt, "Electronically controllable microvalves based on smart hydrogels: Magnitudes and potential applications," *Journal of Microelectromechanical Systems,* vol. 12, pp. 748-753, Oct 2003.

[65]   J. Wang, Z. Y. Chen, M. Mauk, K. S. Hong, M. Y. Li, S. Yang*, et al.*, "Self-actuated, thermo-responsive hydrogel valves for lab on a chip," *Biomedical Microdevices,* vol. 7, pp. 313-322, Dec 2005.

[66]   A. K. Agarwal, S. S. Sridharamurthy, D. J. Beebe, and H. R. Jiang, "Programmable autonomous micromixers and micropumps," *Journal of Microelectromechanical Systems,* vol. 14, pp. 1409-1421, Dec 2005.

[67]   K. K. Westbrook and H. J. Qi, "Actuator designs using environmentally responsive hydrogels," *Journal of Intelligent Material Systems and Structures,* vol. 19, pp. 597-607, May 2008.

[68]   G. Paschew and A. Richter, "High-resolution tactile display operated by an integrated "Smart Hydrogel" actuator array," *Electroactive Polymer Actuators and Devices (EAPAD) 2010,* vol. 7642, 2010.

[69]   T. Guan, F. Godts, F. Ceyssens, E. Vanderleyden, K. Adesanya, P. Dubruel*, et al.*, "Development and fabrication of a novel photopatternable electric responsive Pluronic hydrogel for MEMS applications," *Sensors and Actuators A-Physical,* vol. 186, pp. 184-190, Oct 2012.

[70]   G. H. Kwon, G. S. Jeong, J. Y. Park, J. H. Moon, and S. H. Lee, "A low-energy-consumption electroactive valveless hydrogel micropump for long-term biomedical applications," *Lab on a Chip,* vol. 11, pp. 2910-2915, 2011.

[71]   G. H. Kwon, Y. Y. Choi, J. Y. Park, D. H. Woo, K. B. Lee, J. H. Kim*, et al.*, "Electrically-driven hydrogel actuators in microfluidic channels: fabrication, characterization, and biological application," *Lab on a Chip,* vol. 10, pp. 1604-1610, 2010.

[72]   E. Birgersson, H. Lib, and S. Wua, "Transient analysis of temperature-sensitive neutral hydrogels," *Journal of the Mechanics and Physics of Solids,* vol. 56, pp. 444-466, Feb 2008.

[73]   T. Caykara, S. Kiper, and G. Demirel, "Thermosensitive poly(N-isopropylacrylamide-co-acrylamide) hydrogels: Synthesis, swelling and interaction with ionic surfactants," *European Polymer Journal,* vol. 42, pp. 348-355, Feb 2006.

[74]   X. G. Wang, "Modeling the nonlinear large deformation kinetics of volume phase transition for the neutral thermosensitive hydrogels," *Journal of Chemical Physics,* vol. 127, Nov 7 2007.

[75]   H. Katono, A. Maruyama, K. Sanui, N. Ogata, T. Okano, and Y. Sakurai, "Thermo-responsive swelling and drug release switching of interpenetrating polymer networks composed of poly(acrylamide-co-butyl methacrylate) and poly (acrylic acid)," *Journal of Controlled Release,* vol. 16, pp. 215-227, Jun 1991.

[76]   J. Wu, Z. G. Su, and G. H. Ma, "A thermo- and pH-sensitive hydrogel composed of quaternized chitosan/glycerophosphate," *International Journal of Pharmaceutics,* vol. 315, pp. 1-11, Jun 6 2006.

[77]   Y. Qiu and K. Park, "Environment-sensitive hydrogels for drug delivery," *Advanced Drug Delivery Reviews,* vol. 53, pp. 321-339, Dec 31 2001.

[78]   L. Dong, A. K. Agarwal, D. J. Beebe, and H. R. Jiang, "Adaptive liquid microlenses activated by stimuli-responsive hydrogels," *Nature,* vol. 442, pp. 551-554, Aug 3 2006.

[79]   N. Nath and A. Chilkoti, "Creating "Smart" surfaces using stimuli responsive polymers," *Advanced Materials,* vol. 14, pp. 1243-+, Sep 3 2002.

[80]   D. Brock, W. J. Lee, D. Segalman, and M. Witkowski, "A Dynamic-Model of a Linear-Actuator Based on Polymer Hydrogel," *Journal of Intelligent Material Systems and Structures,* vol. 5, pp. 764-771, Nov 1994.

[81]   Y. Chu, P. P. Varanasi, M. J. Mcglade, and S. Varanasi, "Ph-Induced Swelling Kinetics of Polyelectrolyte Hydrogels," *Journal of Applied Polymer Science,* vol. 58, pp. 2161-2176, Dec 19 1995.

[82]   D. T. Eddington, R. H. Liu, J. S. Moore, and D. J. Beebe, "An organic self-regulating microfluidic system," *Lab on a Chip,* vol. 1, pp. 96-99, 2001.

[83]   Q. Yu, J. M. Bauer, J. S. Moore, and D. J. Beebe, "Responsive biomimetic hydrogel valve for microfluidics," *Applied Physics Letters,* vol. 78, pp. 2589-2591, Apr 23 2001.

[84]   J. Y. Park, H. J. Oh, D. J. Kim, J. Y. Baek, and S. H. Lee, "A polymeric microfluidic valve employing a pH-responsive hydrogel microsphere as an actuating source," *Journal of Micromechanics and Microengineering,* vol. 16, pp. 656-663, Mar 2006.

[85]   S. H. Lee, D. T. Eddington, Y. M. Kim, W. S. Kim, and D. J. Beebe, "Control mechanism of an organic self-regulating microfluidic system," *Journal of Microelectromechanical Systems,* vol. 12, pp. 848-854, Dec 2003.

[86]   R. H. Liu, Q. Yu, and D. J. Beebe, "Fabrication and characterization of hydrogel-based microvalves," *Journal of Microelectromechanical Systems,* vol. 11, pp. 45-53, Feb 2002.

[87]   A. Baldi, Y. D. Gu, P. E. Loftness, R. A. Siegel, and B. Ziaie, "A hydrogel-actuated environmentally sensitive microvalve for active flow control," *Journal of Microelectromechanical Systems,* vol. 12, pp. 613-621, Oct 2003.

[88]   D. T. Eddington and D. J. Beebe, "A valved responsive hydrogel microdispensing device with integrated pressure source," *Journal of Microelectromechanical Systems,* vol. 13, pp. 586-593, Aug 2004.

[89]   J. B. Prettyman and D. T. Eddington, "Leveraging stimuli responsive hydrogels for on/off control of mixing," *Sensors and Actuators B-Chemical,* vol. 157, pp. 722-726, Oct 20 2011.

[90]   D. Kim and D. J. Beebe, "Hydrogel-based reconfigurable components for microfluidic devices," *Lab on a Chip,* vol. 7, pp. 193-198, 2007.

[91]   J. Kim, S. Nayak, and L. A. Lyon, "Bioresponsive hydrogel microlenses," *Journal of the American Chemical Society,* vol. 127, pp. 9588-9592, Jul 6 2005.

[92]   G. Gerlach, M. Guenther, J. Sorber, G. Suchaneck, K. F. Arndt, and A. Richter, "Chemical and pH sensors based on the swelling behavior of hydrogels," *Sensors and Actuators B-Chemical,* vol. 111, pp. 555-561, Nov 11 2005.

[93]   M. Guenther, G. Gerlach, and T. Wallmersperger, "Piezoresistive biochemical sensors based on hydrogels," *Microsystem Technologies-Micro-and Nanosystems-Information Storage and Processing Systems,* vol. 16, pp. 703-715, May 2010.

[94]   J. Z. Hilt, A. K. Gupta, R. Bashir, and N. A. Peppas, "Ultrasensitive biomems sensors based on microcantilevers patterned with environmentally responsive hydrogels," *Biomedical Microdevices,* vol. 5, pp. 177-184, Sep 2003.

[95]   X. Cao, S. Lai, and L. James Lee, "Design of a Self-Regulated Drug Delivery Device," *Biomedical Microdevices,* vol. 3, pp. 109-118, Jun 1 2001.

[96]   J. K. Oh, R. Drumright, D. J. Siegwart, and K. Matyjaszewski, "The development of microgels/nanogels for drug delivery applications," *Progress in Polymer Science,* vol. 33, pp. 448-477, Apr 2008.

[97]   Y. J. Lee and P. V. Braun, "Tunable inverse opal hydrogel pH sensors," *Advanced Materials,* vol. 15, pp. 563-566, Apr 17 2003.

[98]   R. A. Barry and P. Wiltzius, "Humidity-sensing inverse opal hydrogels," *Langmuir,* vol. 22, pp. 1369-1374, Jan 31 2006.

[99]   K. Lee and S. A. Asher, "Photonic crystal chemical sensors: pH and ionic strength," *Journal of the American Chemical Society,* vol. 122, pp. 9534-9537, Oct 4 2000.

[100]   P. J. Flory, *Principles of Polymer Chemistry*: Cornell University Press, 1953.

[101]   D. Ballhause and T. Wallmersperger, "Coupled chemo-electro-mechanical finite element simulation of hydrogels: I. Chemical stimulation," *Smart Materials & Structures,* vol. 17, pp. 045011-10, Aug 2008.

[102]   S. K. De and N. R. Aluru, "A chemo-electro-mechanical mathematical model for simulation of pH sensitive hydrogels," *Mechanics of Materials,* vol. 36, pp. 395-410, May 2004.

[103]   H. Li, Y. K. Yew, and T. Y. Ng, "Modeling for analysis of the effect of Young's modulus on soft active hydrogels subject to pH stimulus," *Smart Materials & Structures,* vol. 18, Apr 2009.

[104]   T. Wallmersperger, F. K. Wittel, M. D'Ottavio, and B. Kroplin, "Multiscale modeling of polymer gels - Chemo-electric model versus discrete element model," *Mechanics of Advanced Materials and Structures,* vol. 15, pp. 228-234, 2008.

[105]   R. P. Hamlen, C. E. Kent, and S. N. Shafer, "Electrolytically Activated Contractile Polymer," *Nature,* vol. 206, pp. 1149-1150, 1965.

[106]   A. J. Grodzinsky and N. A. Shoenfeld, "Tensile Forces Induced in Collagen by Means of Electromechanochemical Transductive Coupling," *Polymer,* vol. 18, pp. 435-443, 1977.

[107]   D. D. Rossi, P. Parrini, P. Chiarelli, and G. Buzzigoli, "Electrically Induced Contractile Phenomena in Charged Polymer Networks: Preliminary Study on the Feasibility of Muscle-Like Structures," *ASAIO Journal,* vol. 31, pp. 60-65, 1985.

[108]   T. Tanaka, I. Nishio, S. T. Sun, and S. Uenonishio, "Collapse of Gels in an Electric-Field," *Science,* vol. 218, pp. 467-469, 1982.

[109]   T. Shiga and T. Kurauchi, "Deformation of Polyelectrolyte Gels under the Influence of Electric-Field," *Journal of Applied Polymer Science,* vol. 39, pp. 2305-2320, Jun 5 1990.

[110]   P. E. Grimshaw, A. J. Grodzinsky, M. L. Yarmush, and D. M. Yarmush, "Selective Augmentation of Macromolecular Transport in Gels by Electrodiffusion and Electrokinetics," *Chemical Engineering Science,* vol. 45, pp. 2917-2929, 1990.

[111] P. E. Grimshaw, J. H. Nussbaum, A. J. Grodzinsky, and M. L. Yarmush, "Kinetics of Electrically and Chemically-Induced Swelling in Polyelectrolyte Gels," *Journal of Chemical Physics,* vol. 93, pp. 4462-4472, Sep 15 1990.

[112] Y. Osada, H. Okuzaki, and H. Hori, "A Polymer Gel with Electrically Driven Motility," *Nature,* vol. 355, pp. 242-244, Jan 16 1992.

[113] I. C. Kwon, Y. H. Bae, and S. W. Kim, "Characteristics of Charged Networks under an Electric Stimulus," *Journal of Polymer Science Part B-Polymer Physics,* vol. 32, pp. 1085-1092, Apr 30 1994.

[114] Y. R. Oh, W. S. Lee, O. O. Park, and Y. K. Han, "Quantitative-Analysis on Swelling Behavior of Hsma Pva Ipn Ionic Gels under Electric-Field," *Korean Journal of Chemical Engineering,* vol. 11, pp. 104-110, Apr 1994.

[115] H. Okuzaki and Y. Osada, "Electro-Driven Chemomechanical Polymer Gel as an Intelligent Soft Material," *Journal of Biomaterials Science-Polymer Edition,* vol. 5, pp. 485-496, 1994.

[116] S. Y. Kim, H. S. Shin, Y. M. Lee, and C. N. Jeong, "Properties of electroresponsive poly(vinyl alcohol)/poly(acrylic acid) IPN hydrogels under an electric stimulus," *Journal of Applied Polymer Science,* vol. 73, pp. 1675-1683, Aug 29 1999.

[117] H. B. Schreyer, N. Gebhart, K. J. Kim, and M. Shahinpoor, "Electrical activation of artificial muscles containing polyacrylonitrile gel fibers," *Biomacromolecules,* vol. 1, pp. 642-647, 2000.

[118] S. J. Kim, S. J. Park, M. S. Shin, and S. I. Kim, "Characteristics of electrical responsive chitosan/polyallylamine interpenetrating polymer network hydrogel," *Journal of Applied Polymer Science,* vol. 86, pp. 2290-2295, Nov 28 2002.

[119] S. J. Kim, S. G. Yoon, K. B. Lee, Y. D. Park, and S. I. Kim, "Electrical sensitive behavior of a polyelectrolyte complex composed of chitosan/hyaluronic acid," *Solid State Ionics,* vol. 164, pp. 199-204, Nov 2003.

[120] S. J. Kim, S. J. Park, S. M. Lee, Y. M. Lee, H. C. Kim, and S. I. Kim, "Electroactive characteristics of interpenetrating polymer network hydrogels composed of poly(vinyl alcohol) and poly(N-isopropylacrylamide)," *Journal of Applied Polymer Science,* vol. 89, pp. 890-894, Jul 25 2003.

[121] S. J. Kim, S. R. Shin, J. H. Lee, S. H. Lee, and S. I. Kim, "Electrical response characterization of chitosan/polyacrylonitrile hydrogel in NaCl solutions," *Journal of Applied Polymer Science,* vol. 90, pp. 91-96, Oct 3 2003.

[122] S. J. Kim, S. G. Yoon, S. M. Lee, J. H. Lee, and S. I. Kim, "Characteristics of electrical responsive alginate/poly(diallyldimethylammonium chloride) IPN hydrogel in HCl solutions," *Sensors and Actuators B-Chemical,* vol. 96, pp. 1-5, Nov 15 2003.

[123] S. J. Kim, K. J. Lee, S. I. Kim, Y. M. Lee, T. D. Chung, and S. H. Lee, "Electrochemical behavior of an interpenetrating polymer network hydrogel composed of poly(propylene glycol) and poly(acrylic acid)," *Journal of Applied Polymer Science,* vol. 89, pp. 2301-2305, Aug 29 2003.

[124] S. J. Kim, C. K. Lee, Y. M. Lee, I. Y. Kim, and S. I. Kim, "Electrical/pH-sensitive swelling behavior of polyelectrolyte hydrogels prepared with

hyaluronic acid-poly(vinyl alcohol) interpenetrating polymer networks," *Reactive & Functional Polymers,* vol. 55, pp. 291-298, 2003.

[125] S. J. Kim, S. G. Yoon, and S. I. Kim, "Effect of the water state on the electrical bending behavior of chitosan/poly(diallyidimethylammonium chloride) hydrogels in NaCl solutions," *Journal of Polymer Science Part B-Polymer Physics,* vol. 42, pp. 914-921, Mar 1 2004.

[126] E. A. Moschou, S. F. Peteu, L. G. Bachas, M. J. Madou, and S. Daunert, "Artificial muscle material with fast electroactuation under neutral pH conditions," *Chemistry of Materials,* vol. 16, pp. 2499-2502, Jun 15 2004.

[127] S. J. Kim, S. R. Shin, S. M. Lee, I. Y. Kim, and S. I. Kim, "Electromechanical properties of hydrogels based on chitosan and poly(hydroxyethyl methacrylate) in NaCl solution," *Smart Materials & Structures,* vol. 13, pp. 1036-1039, Oct 2004.

[128] S. J. Kim, H. I. I. Kim, S. J. Park, and S. I. Kim, "Shape change characteristics of polymer hydrogel based on polyacrylic acid/poly(vinyl sulfonic acid) in electric fields," *Sensors and Actuators a-Physical,* vol. 115, pp. 146-150, Sep 15 2004.

[129] S. J. Kim, S. G. Yoon, Y. H. Lee, and S. I. Kim, "Bending behavior of hydrogels composed of poly(methacrylic acid) and alginate by electrical stimulus," *Polymer International,* vol. 53, pp. 1456-1460, Oct 2004.

[130] S. J. Kim, C. K. Lee, and S. I. Kim, "Electrical/pH responsive properties of poly(2-acrylamido-2-methylpropane sulfonic acid)/hyaluronic acid hydrogels," *Journal of Applied Polymer Science,* vol. 92, pp. 1731-1736, May 5 2004.

[131] S. J. Kim, K. J. Lee, and S. I. Kim, "Electrostimulus responsive behavior of poly(acrylic acid)/polyacrylonitrile semi-interpenetrating polymer network hydrogels," *Journal of Applied Polymer Science,* vol. 92, pp. 1473-1477, May 5 2004.

[132] S. J. Kim, S. J. Park, and S. I. Kim, "Properties of smart hydrogels composed of polyacrylic acid/poly(vinyl sulfonic acid) responsive to external stimuli," *Smart Materials & Structures,* vol. 13, pp. 317-322, Apr 2004.

[133] S. J. Kim, S. G. Yooon, Y. M. Lee, H. C. Kim, and S. I. Kim, "Electrical behavior of polymer hydrogel composed of poly(vinyl alcohol)-hyaluronic acid in solution," *Biosensors & Bioelectronics,* vol. 19, pp. 531-536, Jan 15 2004.

[134] S. G. Yoon, I. Y. Kim, S. I. Kim, and S. J. Kim, "Swelling and electroresponsive characteristics of interpenetrating polymer network hydrogels," *Polymer International,* vol. 54, pp. 1169-1174, Aug 2005.

[135] G. Q. Liu and X. P. Zhao, "Electromechanochemical behavior of gelatin hydrogel under electric field," *Journal of Macromolecular Science-Pure and Applied Chemistry,* vol. A42, pp. 51-59, Jan 2005.

[136] S. J. Kim, H. I. Kim, S. J. Park, I. Y. Kim, S. H. Lee, T. S. Lee*, et al.,* "Behavior in electric fields of smart hydrogels with potential application as bio-inspired actuators," *Smart Materials & Structures,* vol. 14, pp. 511-514, Aug 2005.

[137] R. K. Shamsudeen, S. Nair, and V. G. Jayakumari, "Equilibrium swelling, conductivity and electroactive characteristics of polyacrylamide hydrogels," *Indian Journal of Engineering and Materials Sciences,* vol. 13, pp. 62-68, Feb 2006.

[138] G. Q. Liu and X. P. Zhao, "Electroresponsive behavior of gelatin/alginate semi-interpenetrating polymer network membranes under direct-current electric field," *Journal of Macromolecular Science-Pure and Applied Chemistry,* vol. A43, pp. 345-354, 2006.

[139] S. J. Kim, M. S. Kim, S. I. Kim, G. M. Spinks, B. C. Kim, and G. G. Wallace, "Self-oscillatory actuation at constant DC voltage with pH-sensitive chitosan/polyaniline hydrogel blend," *Chemistry of Materials,* vol. 18, pp. 5805-5809, Nov 28 2006.

[140] C. K. Lee, S. J. Kim, S. I. Kim, B. J. Yi, and S. Y. Han, "Preparation of chitosan microfibres using electro-wet-spinning and their electroactuation properties," *Smart Materials & Structures,* vol. 15, pp. 607-611, Apr 2006.

[141] E. A. Moschou, M. J. Madou, L. G. Bachas, and S. Daunert, "Voltage-switchable artificial muscles actuating at near neutral pH," *Sensors and Actuators B-Chemical,* vol. 115, pp. 379-383, May 23 2006.

[142] J. Shang, Z. Z. Shao, and X. Chen, "Electrical behavior of a natural polyelectrolyte hydrogel: Chitosan/carboxymethylcellulose hydrogel," *Biomacromolecules,* vol. 9, pp. 1208-1213, Apr 2008.

[143] S. W. Yang, G. Q. Liu, Y. Q. Cheng, and Y. H. Zheng, "Electroresponsive Behavior of Sodium Alginate-g-Poly (acrylic acid) Hydrogel Under DC Electric Field," *Journal of Macromolecular Science Part a-Pure and Applied Chemistry,* vol. 46, pp. 1078-1082, 2009.

[144] W. W. Cui, L. Z. Liu, and X. S. Zhu, "Bending Characteristics of Electrical Responsive Poly(vinyl alcohol)/Poly(acrylic acid) Semi-Interpenetrating Polymer Network Hydrogel under DC Electric Field," *Multi-Functional Materials and Structures Ii, Pts 1 and 2,* vol. 79-82, pp. 1595-1598, 2009.

[145] J. K. Shim, S. R. Oh, S. B. Lee, and K. M. Cho, "Preparation of hydrogels composed of poly(vinyl alcohol) and polyethyleneimine and their electrical response," *Journal of Applied Polymer Science,* vol. 107, pp. 2136-2141, Feb 15 2008.

[146] K. Tian, Z. Z. Shao, and X. Chen, "Natural Electroactive Hydrogel from Soy Protein Isolation," *Biomacromolecules,* vol. 11, pp. 3638-3643, Dec 2010.

[147] J. Y. Song, G. Q. Liu, and S. W. Yang, "Electroresponsive Behavior of 2-Hydroxypropyltrimethyl Ammonium Chloride Chitosan Hydrogel Under DC Electric Field," *Journal of Macromolecular Science Part a-Pure and Applied Chemistry,* vol. 48, pp. 164-168, 2011.

[148] G. Q. Liu and J. Y. Song, "Electroresponsive behavior of 2-hydroxypropyltrimethyl ammonium chloride chitosan/poly(vinyl alcohol) interpenetrating polymer network hydrogel," *Polymer International,* vol. 61, pp. 596-601, Apr 2012.

[149] T. Guan, F. Godts, F. Ceyssens, P. Dubruel, H. P. Neves, and R. Puers, "Micropatterning and dynamic swelling of photo-crosslinkable electroactive Pluronic hydrogel," *Eurosensors Xxv,* vol. 25, 2011.

[150] X. F. Shi, Z. Y. Yu, X. Guo, C. F. Wang, and S. Chen, "Electrochromic performances and photoluminescence characteristics of versatile N-vinylimidazole-based hybrid hydrogels," *Colloid and Polymer Science,* vol. 290, pp. 371-377, Feb 2012.

[151] S. J. Kim, I. Y. Kim, and S. I. Kim, "Electroactive polymer hydrogels for bio-inspired actuators," *Smart Structures and Materials 2005: Electroactive Polymer Actuators and Devices(EAPAD),* vol. 5759, pp. 144-152, 2005.

[152] S. J. Kim, S. J. Park, I. Y. Kim, M. S. Shin, and S. I. Kim, "Electric stimuli responses to poly(vinyl alcohol)/chitosan interpenetrating polymer network hydrogel in NaCl solutions," *Journal of Applied Polymer Science,* vol. 86, pp. 2285-2289, Nov 28 2002.

[153] S. J. Kim, S. G. Yoon, S. M. Lee, S. H. Lee, and S. I. Kim, "Electrical sensitivity behavior of a hydrogel composed of polymethacrylic acid/poly(vinyl alcohol)," *Journal of Applied Polymer Science,* vol. 91, pp. 3613-3617, Mar 15 2004.

[154] J. T. Ma, L. R. Liu, X. J. Yang, and K. Deyao, "Bending Behavior of Gelatin Poly(Hydroxyethyl Methacrylate) Ipn Hydrogel under Electric Stimulus," *Journal of Applied Polymer Science,* vol. 56, pp. 73-77, Apr 4 1995.

[155] S. X. Lu and K. S. Anseth, "Photopolymerization of multilaminated poly(HEMA) hydrogels for controlled release," *Journal of Controlled Release,* vol. 57, pp. 291-300, Feb 22 1999.

[156] B. Isik, "Swelling behavior of acrylamide-2-hydroxyethyl methacrylate hydrogels," *Turkish Journal of Chemistry,* vol. 24, pp. 147-156, 2000.

[157] L. Li and L. J. Lee, "Photopolymerization of HEMA/DEGDMA hydrogels in solution," *Polymer,* vol. 46, pp. 11540-11547, Nov 28 2005.

[158] J. D. Kaufman, G. J. Miller, E. F. Morgan, and C. M. Klapperich, "Time-dependent mechanical characterization of poly(2-hydroxyethyl methacrylate) hydrogels using nanoindentation and unconfined compression," *Journal of Materials Research,* vol. 23, pp. 1472-1481, May 2008.

[159] L. Bostan, F. Munteanu, M. I. Popa, and L. Verestiuc, "Preliminary Studies on Fatigue Analysis of Hydrogels Based on p(HEMA)," *Revista De Chimie,* vol. 61, pp. 1235-1238, Dec 2010.

[160] H. Omidian, K. Park, U. Kandalam, and J. G. Rocca, "Swelling and Mechanical Properties of Modified HEMA-based Superporous Hydrogels," *Journal of Bioactive and Compatible Polymers,* vol. 25, pp. 483-497, Sep 2010.

[161] T. Shiga, Y. Hirose, A. Okada, and T. Kurauchi, "Electrically Driven Polymer Gel Finger Working in the Air," *Journal of Intelligent Material Systems and Structures,* vol. 4, pp. 553-557, October 1 1993.

[162] S. M. Liang, J. Xu, L. H. Weng, L. N. Zhang, X. L. Guo, and X. L. Zhang, "Electrically induced linear locomotion of polymer gel in air," *Journal of Polymer Science Part B-Polymer Physics,* vol. 45, pp. 1187-1197, May 15 2007.

[163] S. Murdan, "Electro-responsive drug delivery from hydrogels," *Journal of Controlled Release,* vol. 92, pp. 1-17, Sep 19 2003.

[164] S. Ramanathan and L. H. Block, "The use of chitosan gels as matrices for electrically-modulated drug delivery," *Journal of Controlled Release,* vol. 70, pp. 109-123, Jan 29 2001.

[165] P. Bawa, V. Pillay, Y. E. Choonara, and L. C. du Toit, "Stimuli-responsive polymers and their applications in drug delivery," *Biomedical Materials,* vol. 4, pp. 022001-15, Apr 2009.

[166] I. C. Kwon, Y. H. Bae, and S. W. Kim, "Heparin Release from Polymer Complex," *Journal of Controlled Release,* vol. 30, pp. 155-159, May 1994.

[167] K. Ueno, J. Sakamoto, Y. Takeoka, and M. Watanabe, "Electrochromism based on structural colour changes in a polyelectrolyte gel," *Journal of Materials Chemistry,* vol. 19, pp. 4778-4783, 2009.

[168]   G. H. Kwon, J. Y. Park, J. Y. Kim, M. L. Frisk, D. J. Beebe, and S. H. Lee, "Biomimetic Soft Multifunctional Miniature Aquabots," *Small,* vol. 4, pp. 2148-2153, Dec 2008.

[169]   T. L. Sounart, T. A. Michalske, and K. R. Zavadil, "Frequency-dependent electrostatic actuation in microfluidic MEMS," *Journal of Microelectromechanical Systems,* vol. 14, pp. 125-133, Feb 2005.

[170]   V. Mukundan, P. Ponce, H. E. Butterfield, and B. L. Pruitt, "Modeling and characterization of electrostatic comb-drive actuators in conducting liquid media," *Journal of Micromechanics and Microengineering,* vol. 19, pp. 1-9, Jun 2009.

[171]   V. Mukundan and B. L. Pruitt, "MEMS Electrostatic Actuation in Conducting Biological Media," *Journal of Microelectromechanical Systems,* vol. 18, pp. 405-413, Apr 2009.

[172]   H. V. Panchawagh, T. L. Sounart, and R. L. Mahajan, "A Model for Electrostatic Actuation in Conducting Liquids," *Journal of Microelectromechanical Systems,* vol. 18, pp. 1105-1117, Oct 2009.

[173]   J. G. Boyd and D. Kim, "Nanoscale electrostatic actuators in liquid electrolytes," *Journal of Colloid and Interface Science,* vol. 301, pp. 542-548, Sep 15 2006.

[174]   T. B. Jones, M. Gunji, M. Washizu, and M. J. Feldman, "Dielectrophoretic liquid actuation and nanodroplet formation," *Journal of Applied Physics,* vol. 89, pp. 1441-1448, Jan 15 2001.

[175]   T. B. Jones, K. L. Wang, and D. J. Yao, "Frequency-dependent electromechanics of aqueous liquids: Electrowetting and dielectrophoresis," *Langmuir,* vol. 20, pp. 2813-2818, Mar 30 2004.

[176]   H. Moon, S. K. Cho, R. L. Garrell, and C. J. Kim, "Low voltage electrowetting-on-dielectric," *Journal of Applied Physics,* vol. 92, pp. 4080-4087, Oct 1 2002.

[177]   M. J. Schertzer, R. Ben-Mrad, and P. E. Sullivan, "Mechanical Filtration of Particles in Electrowetting on Dielectric Devices," *Journal of Microelectromechanical Systems,* vol. 20, pp. 1010-1015, Aug 2011.

[178]   J. Lee, H. Moon, J. Fowler, T. Schoellhammer, and C. J. Kim, "Electrowetting and electrowetting-on-dielectric for microscale liquid handling," *Sensors and Actuators a-Physical,* vol. 95, pp. 259-268, Jan 1 2002.

[179]   T. Shiga, Y. Hirose, A. Okada, and T. Kurauchi, "Bending of Ionic Polymer Gel Caused by Swelling under Sinusoidally Varying Electric-Fields," *Journal of Applied Polymer Science,* vol. 47, pp. 113-119, Jan 5 1993.

[180]   T. Shiga, Y. Hirose, A. Okada, and T. Kurauchi, "Deformation of Ionic Polymer Gel Films in Electric-Fields," *Journal of Materials Science,* vol. 29, pp. 5715-5718, Nov 1 1994.

[181]   J. H. Masliyah and S. B. Bhattacharjee, *Electrokinetic and Colloid Transport Phenomena*: John Wiley & Sons, Inc., 2006.

[182]   J. R. Saunders, S. Abu-Salih, T. Khaleque, S. Hanula, and W. A. Moussa, "Modeling Theories of Intelligent Hydrogel Polymers," *Journal of Computational and Theoretical Nanoscience,* vol. 5, pp. 1942-1960, 2008.

[183]   S. N. Wu, H. Li, J. P. Chen, and K. Y. Lam, "Modeling investigation of hydrogel volume transition," *Macromolecular Theory and Simulations,* vol. 13, pp. 13-29, Jan 12 2004.

[184] F. Ganji, S. Vasheghani-Farahani, and E. Vasheghani-Farahani, "Theoretical description of hydrogel swelling: a review," *Iranian Polymer Journal,* vol. 19, pp. 375-398, 2010.

[185] P. J. Flory, "Thermodynamics of High Polymer Solutions," *The Journal of Chemical Physics,* vol. 10, pp. 51-61, Jan 1942.

[186] P. J. Flory, "Fifteenth Spiers Memorial Lecture. Thermodynamics of polymer solutions," *Discussions of the Faraday Society,* vol. 49, pp. 7-29, 1970.

[187] B. Erman and P. J. Flory, "Critical Phenomena and Transitions in Swollen Polymer Networks and in Linear Macromolecules," *Macromolecules,* vol. 19, pp. 2342-2353, Sep 1986.

[188] O. Okay, S. Durmaz, and B. Erman, "Solution cross-linked poly(isobutylene) gels: Synthesis and swelling behavior," *Macromolecules,* vol. 33, pp. 4822-4827, Jun 27 2000.

[189] T. Hino and J. M. Prausnitz, "Molecular thermodynamics for volume-change transitions in temperature-sensitive polymer gels," *Polymer,* vol. 39, pp. 3279-3283, Jun 1998.

[190] O. Okay and S. B. Sariisik, "Swelling behavior of poly(acrylamide-co-sodium acrylate) hydrogels in aqueous salt solutions: theory versus experiments," *European Polymer Journal,* vol. 36, pp. 393-399, Feb 2000.

[191] W. M. Lai and V. C. Mow, "Drag-Induced Compression of Articular-Cartilage during a Permeation Experiment," *Biorheology,* vol. 17, pp. 111-123, 1980.

[192] W. M. Lai, V. C. Mow, and V. Roth, "Effects of Non-Linear Strain-Dependent Permeability and Rate of Compression on the Stress Behavior of Articular-Cartilage," *Journal of Biomechanical Engineering-Transactions of the Asme,* vol. 103, pp. 61-66, May 1981.

[193] Y. Lanir, "Biorheology and Fluid Flux in Swelling Tissues .1. Bicomponent Theory for Small Deformations, Including Concentration Effects," *Biorheology,* vol. 24, pp. 173-187, 1987.

[194] W. M. Lai, J. S. Hou, and V. C. Mow, "A Triphasic Theory for the Swelling and Deformation Behaviors of Articular-Cartilage," *Journal of Biomechanical Engineering-Transactions of the Asme,* vol. 113, pp. 245-258, Aug 1991.

[195] W. M. Lai, V. C. Mow, D. D. Sun, and G. A. Ateshian, "On the electric potentials inside a charged soft hydrated biological tissue: Streaming potential versus diffusion potential," *Journal of Biomechanical Engineering-Transactions of the Asme,* vol. 122, pp. 336-346, Aug 2000.

[196] W. Y. Gu, W. M. Lai, and V. C. Mow, "Transport of multi-electrolytes in charged hydrated biological soft tissues," *Transport in Porous Media,* vol. 34, pp. 143-157, Mar 1999.

[197] W. Y. Gu and H. Yao, "Effects of hydration and fixed charge density on fluid transport in charged hydrated soft tissues," *Annals of Biomedical Engineering,* vol. 31, pp. 1162-1170, Nov 2003.

[198] D. N. Sun, W. Y. Gu, X. E. Guo, W. M. Lai, and V. C. Mow, "A mixed finite element formulation of triphasic mechano-electrochemical theory for charged, hydrated biological soft tissues," *International Journal for Numerical Methods in Engineering,* vol. 45, pp. 1375-1402, Aug 10 1999.

[199] X. Zhou, Y. C. Hon, S. Sun, and A. F. T. Mak, "Numerical simulation of the steady-state deformation of a smart hydrogel under an external

electric field," *Smart Materials & Structures,* vol. 11, pp. 459-467, Jun 2002.

[200]   H. Li, J. Chen, and K. Y. Lam, "Multiphysical modeling and meshless simulation of electric-sensitive hydrogels," *Journal of Polymer Science Part B-Polymer Physics,* vol. 42, pp. 1514-1531, Apr 15 2004.

[201]   Y. Chen, X. Chen, and T. Hisada, "Non-linear finite element analysis of mechanical electrochemical phenomena in hydrated soft tissues based on triphasic theory," *International Journal for Numerical Methods in Engineering,* vol. 65, pp. 147-173, Jan 8 2006.

[202]   J. H. Nussbaum and A. J. Grodzinsky, "Proton Diffusion Reaction in a Protein Poly-Electrolyte Membrane and the Kinetics of Electro-Mechanical Forces," *Journal of Membrane Science,* vol. 8, pp. 193-219, 1981.

[203]   T. Wallmersperger, K. Keller, B. Kroplin, M. Gunther, and G. Gerlach, "Modeling and simulation of pH-sensitive hydrogels," *Colloid and Polymer Science,* vol. 289, pp. 535-544, Apr 2011.

[204]   T. Wallmersperger, B. Kroplin, J. Holdenried, and R. W. Gulch, "A coupled multi-field-formulation for ionic polymer gels in electric fields," *Smart Structures and Materials 2001: Electroactive Polymer Actuators and Devices,* vol. 4329, pp. 264-275, 2001.

[205]   T. Wallmersperger, B. Kroplin, and R. W. Gulch, "Coupled chemo-electro-mechanical formulation for ionic polymer gels - numerical and experimental investigations," *Mechanics of Materials,* vol. 36, pp. 411-420, May 2004.

[206]   T. Wallmersperger and D. Ballhause, "Coupled chemo-electro-mechanical finite element simulation of hydrogels: II. Electrical stimulation," *Smart Materials & Structures,* vol. 17, pp. 045012-10, Aug 2008.

[207]   R. W. Gulch, J. Holdenried, A. Weible, T. Wallmersperger, and B. Kroplin, "Polyelectrolyte gels in electric fields - A theoretical and experimental approach," *Smart Structures and Materials 2000: Electroactive Polymer Actuators and Devices (EAPAD),* vol. 3987, pp. 193-202, March 2000.

[208]   J. R. Saunders, S. Abu-Salih, and W. A. Moussa, "Parametric Chemo-Electro-Mechanical Modeling of Smart Hydrogels," *Journal of Computational and Theoretical Nanoscience,* vol. 5, pp. 1961-1975, Oct 2008.

[209]   H. Li, Y. Yew, K. Y. Lam, and T. Ng, "Numerical simulation of pH-stimuli responsive hydrogel in buffer solutions," *Colloids and Surfaces a-Physicochemical and Engineering Aspects,* vol. 249, pp. 149-154, Nov 30 2004.

[210]   H. Li, T. Y. Ng, Y. K. Yew, and K. Y. Lam, "Modeling and simulation of the swelling behavior of pH-stimulus-responsive hydrogels," *Biomacromolecules,* vol. 6, pp. 109-120, Jan-Feb 2005.

[211]   H. Li, Y. K. Yew, T. Y. Ng, and K. Y. Lam, "Meshless steady-state analysis of chemo-electro-mechanical coupling behavior of pH-sensitive hydrogel in buffered solution," *Journal of Electroanalytical Chemistry,* vol. 580, pp. 161-172, Jun 15 2005.

[212]   Q. X. Wang, H. Li, and K. Y. Lam, "Meshless simulation of equilibrium swelling/deswelling of PH-sensitive hydrogels," *Journal of Polymer Science Part B-Polymer Physics,* vol. 44, pp. 326-337, Jan 15 2006.

74

[213] T. Y. Ng, H. Li, Y. K. Yew, and K. Y. Lam, "Effects of initial-fixed charge density on pH-sensitive hydrogels subjected to coupled pH and electric field stimuli: A meshless analysis," *Journal of Biomechanical Engineering-Transactions of the Asme,* vol. 129, pp. 148-155, Apr 2007.

[214] Y. K. Yew, T. Y. Ng, H. Li, and K. Y. Lam, "Analysis of pH and electrically controlled swelling of hydrogel-based micro-sensors/actuators," *Biomedical Microdevices,* vol. 9, pp. 487-499, Aug 2007.

[215] H. Li and Y. K. Yew, "Simulation of soft smart hydrogels responsive to pH stimulus: Ionic strength effect and case studies," *Materials Science & Engineering C-Materials for Biological Applications,* vol. 29, pp. 2261-2269, Aug 31 2009.

[216] H. Li and Y. K. Yew, "Numerical Analysis of Soft pH-Sensitive Hydrogel: Effect of Multivalent Ionic Compositions," *Polymer Engineering and Science,* vol. 50, pp. 429-439, Mar 2010.

[217] T. Y. Ng, H. Li, and Y. K. Yew, "Computational analysis of smart soft hydrogels subjected to pH-electrical coupled stimuli: Effects of initial geometry," *International Journal of Solids and Structures,* vol. 47, pp. 614-623, Mar 1 2010.

[218] H. Li, T. Y. Ng, Y. K. Yew, and K. Y. Lam, "Meshless modeling of pH-sensitive hydrogels subjected to coupled pH and electric field stimuli: Young modulus effects and case studies," *Macromolecular Chemistry and Physics,* vol. 208, pp. 1137-1146, May 21 2007.

[219] S. Sun and A. F. T. Mak, "The dynamical response of a hydrogel fiber to electrochemical stimulation," *Journal of Polymer Science Part B-Polymer Physics,* vol. 39, pp. 236-246, Jan 15 2001.

[220] H. Li, Z. Yuan, K. Y. Lam, H. P. Lee, J. Chen, J. Hanes*, et al.*, "Model development and numerical simulation of electric-stimulus-responsive hydrogels subject to an externally applied electric field," *Biosensors & Bioelectronics,* vol. 19, pp. 1097-1107, Apr 15 2004.

[221] H. Li, "Kinetics of smart hydrogels responding to electric field: A transient deformation analysis," *International Journal of Solids and Structures,* vol. 46, pp. 1326-1333, Mar 15 2009.

[222] H. Li, J. Chen, and K. Y. Lam, "Transient simulation of kinetics of electric-sensitive hydrogels," *Biosensors & Bioelectronics,* vol. 22, pp. 1633-1641, Mar 15 2007.

[223] H. Li, R. Luo, E. Birgersson, and K. Y. Lam, "Modeling of multiphase smart hydrogels responding to pH and electric voltage coupled stimuli," *Journal of Applied Physics,* vol. 101, pp. 114905-7, Jun 1 2007.

[224] H. Li, R. M. Luo, and K. Y. Lam, "Modeling of ionic transport in electric-stimulus-responsive hydrogels," *Journal of Membrane Science,* vol. 289, pp. 284-296, Feb 15 2007.

[225] H. Li, R. M. Luo, and K. Y. Lam, "Multiphysics Modeling of Electrochemomechanically Smart Microgels Responsive to Coupled pH/Electric Stimuli," *Macromolecular Bioscience,* vol. 9, pp. 287-297, Mar 10 2009.

[226] R. Luo, H. Li, and K. Y. Lam, "Modeling and simulation of chemo-electro-mechanical behavior of pH-electric-sensitive hydrogel," *Analytical and Bioanalytical Chemistry,* vol. 389, pp. 863-873, Oct 2007.

[227] R. M. Luo and H. Li, "A modeling study of the effect of environmental ionic valence on the mechanical characteristics of pH-electrosensitive hydrogel," *Acta Biomaterialia,* vol. 5, pp. 2920-2928, Oct 2009.

[228] R. M. Luo, H. Li, and K. Y. Lam, "Modeling and analysis of pH-electric-stimuli-responsive hydrogels," *Journal of Biomaterials Science-Polymer Edition,* vol. 19, pp. 1597-1610, 2008.

[229] A. E. H. Ali, H. A. A. El-Rehim, E. S. A. Hegazy, and M. M. Ghobashy, "Synthesis and electrical response of acrylic acid/vinyl sulfonic acid hydrogels prepared by gamma-irradiation," *Radiation Physics and Chemistry,* vol. 75, pp. 1041-1046, Sep 2006.

[230] O. Okay and S. Durmaz, "Charge density dependence of elastic modulus of strong polyelectrolyte hydrogels," *Polymer,* vol. 43, pp. 1215-1221, Feb 2002.

[231] T. Shiga, "Deformation and viscoelastic behavior of polymer gels in electric fields," *Neutron Spin Echo Spectroscopy Viscoelasticity Rheology,* vol. 134, pp. 131-163, 1997.

[232] S. Nemat-Nasser and J. Y. Li, "Electromechanical response of ionic polymer-metal composites," *Journal of Applied Physics,* vol. 87, pp. 3321-3331, Apr 1 2000.

[233] J. H. Nussbaum, "Electric field control of mechanical and electrochemical properties of polyelectrolyte gel membranes," Doctor of Philosophy Department of Electrical Engineering and Computer Science, Massachusetts Institute of Technology, 1986.

[234] J. S. Mackie and P. Meares, "The Diffusion of Electrolytes in a Cation-Exchange Resin Membrane .1. Theoretical," *Proceedings of the Royal Society of London Series a-Mathematical and Physical Sciences,* vol. 232, pp. 498-509, 1955.

[235] A. Einstein, "The motion of elements suspended in static liquids as claimed in the molecular kinetic theory of heat," *Annalen Der Physik,* vol. 17, pp. 549-560, Jul 1905.

[236] S. Jafari and H. Modarress, "A study on swelling and complex formation of acrylic acid and methacrylic acid hydrogels with polyethylene glycol," *Iranian Polymer Journal,* vol. 14, pp. 863-873, Oct 2005.

[237] W. Hong, Z. S. Liu, and Z. G. Suo, "Inhomogeneous swelling of a gel in equilibrium with a solvent and mechanical load," *International Journal of Solids and Structures,* vol. 46, pp. 3282-3289, Aug 15 2009.

[238] X. H. Zhao, W. Hong, and Z. G. Suo, "Inhomogeneous and anisotropic equilibrium state of a swollen hydrogel containing a hard core," *Applied Physics Letters,* vol. 92, pp. 051904-3, Feb 4 2008.

[239] R. Marcombe, S. Q. Cai, W. Hong, X. H. Zhao, Y. Lapusta, and Z. G. Suo, "A theory of constrained swelling of a pH-sensitive hydrogel," *Soft Matter,* vol. 6, pp. 784-793, 2010.

[240] M. V. Gandhi, S. R. Kasiviswanathan, and M. Usman, "Finite Extension and Torsion of a Cylindrical Solid-Fluid Mixture Featuring a Rigid Core," *Acta Mechanica,* vol. 103, pp. 177-190, 1994.

[241] M. V. Gandhi and M. Usman, "On the Non-Homogeneous Finite Swelling of a Non-Linearly Elastic Cylinder with a Rigid Core," *International Journal of Non-Linear Mechanics,* vol. 24, pp. 251-261, 1989.

[242] T. He, M. Li, and J. X. Zhou, "Modeling deformation and contacts of pH sensitive hydrogels for microfluidic flow control," *Soft Matter,* vol. 8, pp. 3083-3089, 2012.

[243] J. W. Yoon, S. Q. Cai, Z. G. Suo, and R. C. Hayward, "Poroelastic swelling kinetics of thin hydrogel layers: comparison of theory and experiment," *Soft Matter,* vol. 6, pp. 6004-6012, 2010.

[244] S. Q. Cai, Y. H. Hu, X. H. Zhao, and Z. G. Suo, "Poroelasticity of a covalently crosslinked alginate hydrogel under compression," *Journal of Applied Physics,* vol. 108, pp. 113514-8, Dec 1 2010.

[245] M. Galli, E. Fornasiere, J. Cugnoni, and M. L. Oyen, "Poroviscoelastic characterization of particle-reinforced gelatin gels using indentation and homogenization," *Journal of the Mechanical Behavior of Biomedical Materials,* vol. 4, pp. 610-617, May 2011.

[246] Z. I. Kalcioglu, R. Mahmoodian, Y. H. Hu, Z. G. Suo, and K. J. Van Vliet, "From macro- to microscale poroelastic characterization of polymeric hydrogels via indentation," *Soft Matter,* vol. 8, pp. 3393-3398, 2012.

[247] M. Ahearne, Y. Yang, A. J. El Haj, K. Y. Then, and K. K. Liu, "Characterizing the viscoelastic properties of thin hydrogel-based constructs for tissue engineering applications," *Journal of the Royal Society Interface,* vol. 2, pp. 455-463, Dec 22 2005.

[248] U. Chippada, N. Langrana, and B. Yurke, "Complete mechanical characterization of soft media using nonspherical rods," *Journal of Applied Physics,* vol. 106, pp. 063528-5, Sep 15 2009.

[249] Y. Li, Z. B. Hu, and C. F. Li, "New Method for Measuring Poisson Ratio in Polymer Gels," *Journal of Applied Polymer Science,* vol. 50, pp. 1107-1111, Nov 10 1993.

[250] T. Takigawa, Y. Morino, K. Urayama, and T. Masuda, "Poisson's ratio of polyacrylamide (PAAm) gels," *Polymer Gels and Networks,* vol. 4, pp. 1-5, 1996.

[251] C. F. Li, Z. B. Hu, and Y. Li, "Poisson Ratio in Polymer Gels near the Phase-Transition Point," *Physical Review E,* vol. 48, pp. 603-606, Jul 1993.

[252] M. F. Beatty, "Topics in Finite Elasticity: Hyperelasticity of Rubber, Elastomers, and Biological Tissues - with Examples," *Applied Mechanics Review* vol. 40, pp. 1699-1734, December 1987.

[253] R. W. Ogden, "Elements of the Theory of Finite Elasticity," in *Nonlinear Elasticity: Theory and Applications*, Y. B. Fu and R. W. Ogden, Eds., ed: Cambridge University Press, 2001, pp. 1-58.

[254] L. Bostan, A. M. Trunfio-Sfarghiu, L. Verestiuc, M. I. Popa, F. Munteanu, J. P. Rieu*, et al.*, "Mechanical and tribological properties of poly(hydroxyethyl methacrylate) hydrogels as articular cartilage substitutes," *Tribology International,* vol. 46, pp. 215-224, Feb 2012.

[255] F. A. Aouada, M. R. Guilherme, G. M. Campese, E. M. Girotto, A. F. Rubira, and E. C. Muniz, "Electrochemical and mechanical properties of hydrogels based on conductive poly (3,4-ethylene dioxythiophene)/poly (styrenesulfonate) and PAAm," *Polymer Testing,* vol. 25, pp. 158-165, Apr 2006.

[256] F. Horkay, M. H. Han, I. S. Han, I. S. Bang, and J. J. Magda, "Separation of the effects of pH and polymer concentration on the swelling pressure and elastic modulus of a pH-responsive hydrogel," *Polymer,* vol. 47, pp. 7335-7338, Oct 4 2006.

[257] J. A. Stammen, S. Williams, D. N. Ku, and R. E. Guldberg, "Mechanical properties of a novel PVA hydrogel in shear and unconfined compression," *Biomaterials,* vol. 22, pp. 799-806, Apr 2001.

[258] S. Lin-Gibson, S. Bencherif, J. M. Antonucci, R. L. Jones, and F. Horkay, "Synthesis and Characterization of Poly(ethylene glycol) Dimethacrylate Hydrogels," *Macromolecular Symposia,* vol. 227, pp. 243-254, July 2005.

[259] E. C. Muniz and G. Geuskens, "Compressive elastic modulus of polyacrylamide hydrogels and semi-IPNs with poly(N-isopropylacrylamide)," *Macromolecules,* vol. 34, pp. 4480-4484, Jun 19 2001.

[260] T. P. Davis and M. B. Huglin, "Some Mechanical-Properties of Poly(2-Hydroxyethyl Methacrylate) Gels Swollen in Water 1,4-Dioxane Mixtures," *Makromolekulare Chemie-Rapid Communications,* vol. 9, pp. 39-43, Jan 1988.

[261] S. M. Malmonge and A. C. Arruda, "Artificial articular cartilage: Mechanoelectrical transduction under dynamic compressive loading," *Artificial Organs,* vol. 24, pp. 174-178, Mar 2000.

[262] B. D. Johnson, D. J. Beebe, and W. Crone, "Effects of swelling on the mechanical properties of a pH-sensitive hydrogel for use in microfluidic devices," *Materials Science & Engineering C-Biomimetic and Supramolecular Systems,* vol. 24, pp. 575-581, Jun 1 2004.

[263] S. P. Marra, K. T. Ramesh, and A. S. Douglas, "Mechanical characterization of active poly(vinyl alcohol)-poly(acrylic acid) gel," *Materials Science & Engineering C-Biomimetic and Supramolecular Systems,* vol. 14, pp. 25-34, Aug 15 2001.

[264] S. Popovic, H. Tamagawa, and M. Taya, "Mechanical testing of hydrogels and PAN gel fibers," in *Smart Materials and Structures 2000: Electroactive Polymer Actuators and Devices (EAPAD),* Newport Beach, CA, 2000, pp. 177-186.

[265] M. Solari, "Evaluation of the Mechanical-Properties of a Hydrogel Fiber in the Development of a Polymeric Actuator," *Journal of Intelligent Material Systems and Structures,* vol. 5, pp. 295-304, May 1994.

[266] W. K. Wan, G. Campbell, Z. F. Zhang, A. J. Hui, and D. R. Boughner, "Optimizing the tensile properties of polyvinyl alcohol hydrogel for the construction of a bioprosthetic heart valve stent," *Journal of Biomedical Materials Research,* vol. 63, pp. 854-861, Dec 5 2002.

[267] A. Ikehata and H. Ushiki, "Effect of salt on the elastic modulus of poly(N-isopropylacrylamide) gels," *Polymer,* vol. 43, pp. 2089-2094, Mar 2002.

[268] B. Johnson, J. M. Bauer, D. J. Niedermaier, W. C. Crone, and D. J. Beebe, "Experimental techniques for mechanical characterization of hydrogels at the microscale," *Experimental Mechanics,* vol. 44, pp. 21-28, Feb 2004.

[269] X. Tong, J. Zheng, Y. Lu, Z. Zhang, and H. Cheng, "Swelling and mechanical behaviors of carbon nanotube/poly(vinyl alcohol) hybrid hydrogels," *Materials Letters,* vol. 61, pp. 1704-1706, April 2007.

[270] J. A. Hinkley, L. D. Morgret, and S. H. Gehrke, "Tensile properties of two responsive hydrogels," *Polymer,* vol. 45, pp. 8837-8843, Dec 2004.

[271] C. Migliaresi, L. Nicodemo, L. Nicolais, and P. Passerini, "Physical Characterization of Microporous Poly(2-Hydroxyethyl Methacrylate) Gels," *Journal of Biomedical Materials Research,* vol. 15, pp. 307-317, May 1981.

[272] Y.-C. Lai and T. Quinn Edmond, "The Effects of Initiator and Diluent on the Photopolymerization of 2-Hydroxyethyl Methacrylate and on Properties of Hydrogels Obtained," in *Photopolymerization.* vol. 673, ed: American Chemical Society, 1997, pp. 35-50.

[273] X. Lou and C. van Coppenhagen, "Mechanical characteristics of poly(2-hydroxyethyl methacrylate) hydrogels crosslinked with various

difunctional compounds," *Polymer International,* vol. 50, pp. 319-325, Mar 2001.

[274] B. Johnson, D. J. Niedermaier, W. C. Crone, J. Moorthy, and D. J. Beebe, "Mechanical properties of a pH sensitive Hydrogel," in *SEM Annual Conference Proceedings*, Milwaukee, WI, 2002, pp. 1-4.

[275] J. F. Mano, R. L. Reis, and A. M. Cunha, "Dynamic mechanical analysis in polymers for medical applications," *Polymer Based Systems on Tissue Engineering, Replacement and Regeneration,* vol. 86, pp. 139-164, 2002.

[276] J. S. Park, J. W. Park, and E. Ruckenstein, "Thermal and dynamic mechanical analysis of PVA/MC blend hydrogels," *Polymer,* vol. 42, pp. 4271-4280, Apr 2001.

[277] C. S. Drapaca, S. Sivaloganathan, and G. Tenti, "Nonlinear constitutive laws in viscoelasticity," *Mathematics and Mechanics of Solids,* vol. 12, pp. 475-501, Oct 2007.

[278] A. Martínez-Ruvalcaba, E. Chornet, and D. Rodrigue, "Viscoelastic properties of dispersed chitosan/xanthan hydrogels," *Carbohydrate Polymers,* vol. 67, pp. 586-595, Feb 19 2007.

[279] S. Piskounova, R. Rojas, K. Bergman, and J. Hilborn, "The Effect of Mixing on the Mechanical Properties of Hyaluronan-Based Injectable Hydrogels," *Macromolecular Materials and Engineering,* vol. 296, pp. 944-951, Oct 12 2011.

[280] F. Lionetto, A. Sannino, G. Mensitieri, and A. Maffezzoli, "Evaluation of the degree of cross-linking of cellulose-based superabsorbent hydrogels: A comparison between different techniques," *Macromolecular Symposia,* vol. 200, pp. 199-207, Sep 2003.

[281] T. K. L. Meyvis, B. G. Stubbe, M. J. Van Steenbergen, W. E. Hennink, S. C. De Smedt, and J. Demeester, "A comparison between the use of dynamic mechanical analysis and oscillatory shear rheometry for the characterisation of hydrogels," *International Journal of Pharmaceutics,* vol. 244, pp. 163-168, Sep 5 2002.

[282] J. V. Cauich-Rodriguez, S. Deb, and R. Smith, "Effect of cross-linking agents on the dynamic mechanical properties of hydrogel blends of poly(acrylic acid)-poly(vinyl alcohol-vinyl acetate)," *Biomaterials,* vol. 17, pp. 2259-2264, 1996.

[283] M. G. Cascone, "Dynamic-mechanical properties of bioartificial polymeric materials," *Polymer International,* vol. 43, pp. 55-69, May 1997.

[284] K. Nakamura and T. Nakagawa, "Dynamic Mechanical-Properties of Poly(2-Hydroxyethyl Methacrylate) Hydrogels," *Journal of Polymer Science Part B-Polymer Physics,* vol. 13, pp. 2299-2311, 1975.

[285] G. D. Marco, M. Lanza, and M. Pieruccini, "Dynamic Mechanical Measurements in Dry PHEMA and its Hydrogels," *Il Nuovo Cimento,* vol. 16, pp. 849-854, July, 1994 1994.

Chapter 3

Parametric Chemo-Electro-Mechanical Modeling of Smart Hydrogels[1]

3.1   Introduction

Hydrogels are a special type of polymer, with three-dimensional cross-linked networks immersed in solvent that respond to external stimulus by swelling or deswelling their volume. Hydrogels can be stimulated by exposure to pH [1-3], electrical fields [4], magnetic fields [5-7], light [8], temperature [9-12], enzymes [13], and antigens [14].   The large volume transition that accompanies this stimulation promotes the use of hydrogels for a variety of applications, such as synthetic muscles [15, 16], actuators for microfluidic components [17-19], and drug delivery [20-22]. In addition to experimental research on hydrogels, several numerical models have been formulated to simulate the volume transition of hydrogels. These include thermodynamic models [23, 24], multiphasic mixture theory [25, 26], transport models [2, 3], and molecular dynamics [27, 28]. These numerical models allow researchers to bypass some of the high fabrication costs of prototyping and design optimization.

The pH and electrical stimulation of a hydrogel caused the osmotic pressure based swelling and deswelling phenomena to develop.

---

[1] A version of this chapter has been published. Saunders, Abu-Salih, Moussa 2008. Journal of Computational and Theoretical Nanoscience. 5(11): 1961-1975. Contributions from S. Abu-Salih towards that publication have been removed from this thesis chapter.

Chemically and electrically stimulated hydrogels can be either anionic [29], cationic [22], or polyampholyte [30], whereby they have fixed negative ions, positive ions, or a distribution of both attached to their polymer backbone, respectively. When the hydrogel is chemically stimulated the fixed charges deprotonate or protonate, altering the pH distribution across both the hydrogel and buffer domains. This developed pH distribution causes two mechanisms to occur, the further diffusion of mobile ions into the hydrogel from a surrounding solution and, more importantly, the establishment of ionic gradients between the hydrogel and surrounding solution. When these ionic gradients are established an osmotic pressure is developed at the exterior surface of the hydrogel, causing swelling or deswelling. Electrical stimulation works very much the same; however, instead of diffusion in pH stimulation established ionic gradients, these ionic gradients are established through the electrically forced migration of mobile ions throughout the hydrogel and surrounding solution.

This work examines the fully nonlinear and coupled chemo-electro-mechanical multiphysics of pH (chemical) and electrical stimulation of hydrogels using the transport model that will be detailed in following sections. pH and electrical stimulation methods have a large range of applications, as well the electrical stimulation methods have been shown to produce the fastest swelling and deswelling response times. Compared to other numerical models, the transport models that are the greatest validity for the scale examined. This work will expand on the previous numerical results of Wallmersperger *et al.* [31], adding displacement of the hydrogel to the published numerical model; in addition, the use of, or lack thereof, Donnan theory is discussed. This chemo-electro-mechanical numerical model is then examined under a varied hydrogel relative permittivity, increased applied electrical potential, and reversed electrical field.

3.2 Theory

The swelling-deswelling phenomena exhibited by hydrogels was initially examined by Grimshaw *et al.* [32] to study the swelling of polymethacrylic acid (PMMA) membranes. Additional numerical models employing transport equations were implemented to study the chemical stimulation of hydrogels by Chu *et al.* [33], Li *et al.* [34-37], and De *et al.* [2, 3]. Numerical models used to study both chemical and electrical stimulation were employed by Bassetti *et al.* [4] and Wallmersperger *et al.* [31, 38].

To accurately model the swelling phenomena of hydrogels subjected to an external chemical and/or electrical stimulus, a coupled multi-field numerical model was employed. This multiphysics model was composed of coupled electrical and chemical field equations, which were subsequently coupled with structural field equations. This combination gave a fully coupled chemo-electro-mechanical numerical model describing the transient swelling and deswelling phenomena of hydrogels.

The applied electrical field was governed by Poisson's equation, accounting for contributions from mobile and fixed ions, given by

$$\nabla \cdot \left(\varepsilon_0 \varepsilon_e \nabla \overline{\psi} \right) = -F \left(\sum_{k=1}^{N} \overline{c}_k z_k + \overline{c}_f z_f \right) \qquad (3\text{-}1)$$

where ε_0 and ε_e are the dielectric constant of vacuum and the effective dielectric constant of the hydrogel, respectively. $\overline{\psi}$ is the intermembrane (interior of hydrogel) electrical potential, F is the Faraday constant, $\overline{c}_k$ is the intermembrane concentration of the *k*th ionic species, z_k is the valence of the *k*th ionic species, $\overline{c}_f$ is the intermembrane concentration of the fixed ions, and z_f is the valence of the fixed ions. The sign ($^-$) denotes a quantity within the hydrogel membrane. Note that Eq. 3-1 can also be implemented in regions exterior to the hydrogel; however, no fixed ions will be present and the variables represent the surrounding buffer domain.

The chemical field, which determined the concentration of mobile ionic species in the hydrogel and buffer regions, was governed by the Nernst-Planck equation

$$\frac{\partial\left(\overline{c}_k\right)}{\partial t} = -\nabla\cdot\left(-\overline{D}_k\nabla\cdot\overline{c}_k - z_k\overline{\mu}_k\overline{c}_k\nabla\cdot\overline{\psi}\right) \tag{3-2}$$

where t is time, $\overline{D}_k$ is the intermembrane diffusivity of the *k*th ionic species and $\overline{\mu}_k$ is the intermembrane ionic mobility of the *k*th ionic species. Note that Eq. 3-2 can be implemented in regions other than the hydrogel, but the equation's components would not have a (¯) denotation. From the ionic mobility in aqueous solution, the diffusivity can be calculated using the Einstein relationship:

$$D_k = \frac{\mu_k RT}{F} \tag{3-3}$$

where R is the universal gas constant and T is temperature.

To obtain the displacement of the hydrogel polymer network, the following structural field equations, or equations of motion were implemented

$$\rho\frac{\partial^2 u}{\partial t^2} + f\frac{\partial u}{\partial t} = \nabla\cdot\sigma + \rho b \tag{3-4}$$

where ρ is the density of the hydrogel, u is the calculated displacement of the polymer network, f is the viscous damping parameter between the polymer network and the solution, σ is the stress tensor, and b is the body forces acting on the hydrogel. For the cases considered within this work the body forces and frictional forces were neglected. In the chemo-electro-mechanical response of hydrogels the flux of mobile ions occurs much slower than the mechanical displacement response. Therefore, the hydrogel's inertial terms were neglected and the following quasi-static equilibrium mechanical equations are solved.

$$\nabla\cdot\sigma = 0 \tag{3-5}$$

Isolating the x-component of a two-dimensional system gives

$$\frac{\partial \sigma_{xx}}{\partial x} + \frac{\partial \tau_{xy}}{\partial y} = 0 \tag{3-6}$$

where σ_{xx} is the normal stress on the x-plane in the x-direction and τ_{xy} is the shear stress on the x-plane in the y-direction. The x-component of the normal stress for a plane strain condition can then be given by

$$\sigma_{xx} = \frac{E}{(1+v)(1-2v)}\left[(1-v)\frac{\partial u_x}{\partial x} + v\frac{\partial u_y}{\partial y}\right] - (P_{osmotic}) \tag{3-7}$$

where E is Young's Modulus of the hydrogel, ʋ is Poisson's ratio of the hydrogel, u_x and u_y are the x-component y-component of the polymer network displacement, respectively. $P_{osmotic}$ is the osmotic pressure. Isolating the shear stress term of Eq. 3-6, the x-component is given by

$$\tau_{xy} = G\left[\frac{\partial u_x}{\partial y} + \frac{\partial u_y}{\partial x}\right] \tag{3-8}$$

where G is the shear modulus of the hydrogel. The following x-component of the mechanical field equations is obtained from substituting Eqs. 3-7 and 3-8 into Eq. 3-6.

$$0 = \frac{E(1-v)}{(1+v)(1-2v)}\frac{\partial^2 u_x}{\partial x^2} + \frac{Ev}{(1+v)(1-2v)}\frac{\partial^2 u_y}{\partial x \partial y} + G\left[\frac{\partial^2 u_y}{\partial x^2} + \frac{\partial^2 u_x}{\partial x \partial y}\right] - \frac{\partial[P_{osmotic}]}{\partial x} \tag{3-9}$$

Eq. 3-9 is analogous in the y-direction. The calculation of the osmotic pressure requires that the concentrations outside of the hydrogel and inside the hydrogel be known, and can be determined from the following

$$P_{osmotic} = RT\sum_{k=1}^{n}\left(\overline{c}_k - c_k^0\right) \tag{3-10}$$

where *n* is the number of mobile ionic species contributing to the osmotic pressure, $\overline{c}_k$ is the intermembrane concentration of the *k*th mobile ionic species, c_k^0 is the extramembrane concentration of the *k*th mobile ionic species.

Overall, the full coupling of the electrical field equations (Eq. 3-1)), the chemical field equations (Eqs. 3-2 and 3-3), and the structural field

equations (Eqs. 3-9 and 3-10) yields the transient displacement for a chemically or electrically stimulated hydrogel.

3.3   Numerical Model

The theoretical model overviewed in Section 3.2 was implemented using COMSOL Multiphysics 3.3 to numerically model the chemical and electrical stimulation of a hydrogel. The geometry analyzed was exactly the same for both chemical and electrical stimulation, shown in Figure 3.1. The solution domain was composed of a 15 mm square buffer domain with an inset 5 mm square hydrogel domain, which was centered in the buffer domain. All the equations reviewed in Section 3.2 were implemented in the hydrogel domain; however, the structural equations were not implemented in the buffer domain. Something to note was the implementation of a 'virtual membrane'. COMSOL requires that all solution variables be continuous across all domains, which required geometrically inserting a hydrogel 'membrane' layer 100 μm in thickness between the buffer and bulk hydrogel material. This region acts exactly as the hydrogel does, but it was within this region that the sharp gradients for ionic concentrations occur. All solution variables were found to be independent of membrane thickness for membranes smaller than 100 μm. For discretization purposes a 100 μm 'virtual membrane' was implemented.

For chemical stimulation the model boundary conditions imposed were as follows; electrical insulation on the exterior buffer boundary and continuity of electrical flux on the hydrogel-buffer interface, and chemical 'insulation' on the exterior buffer boundary and continuity of chemical flux on the hydrogel-buffer interface. Structurally, the hydrogel was constrained by a 1 mm diameter cylinder at the center of the hydrogel, and the osmotic pressure was applied at the hydrogel-buffer interface. This constraining cylinder was only 'visible' to the structural model, as the electrical and chemical field equations treated it as part of the bulk

hydrogel material. For electrical stimulation the structural and chemical field boundary conditions were the same. However, for the electrical field the applied potential was applied (anode and cathode) at the left and right exterior buffer boundaries, the boundary at x = 0 (for all y) and x=15 mm (for all y), respectively. The upper and lower exterior boundaries of the buffer domain were considered electrically insulated.

The solution was discretized using COMSOL's mesh generator, with a typical mesh distribution seen in Figure 3.2, consisting of 25,228 elements. The mesh was refined around the hydrogel-buffer interface, as accuracy around these boundaries was paramount. In addition, COMSOL's Arbitrary Langrangian-Eulerian (ALE) module was employed to enhance the accuracy of the solutions.
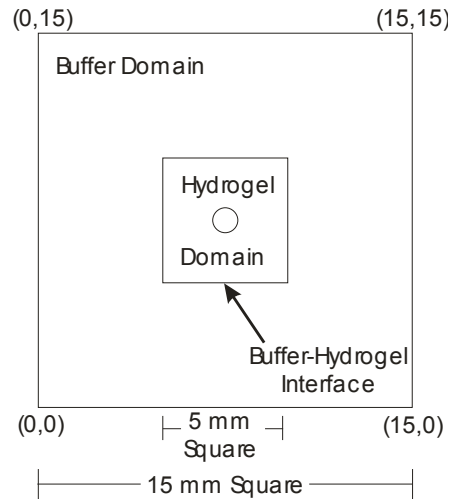
Figure 3.1: Geometry of hydrogel immersed in buffer solution for chemical and electrical stimulation.
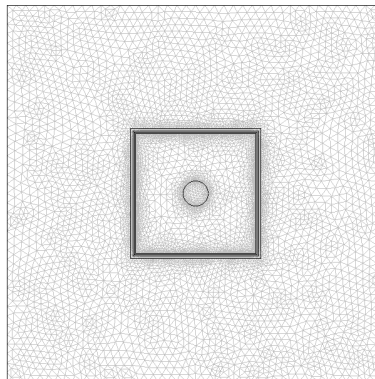
Figure 3.2: Discretized solution domains with a total 25,228 elements

Table 3.1: Numerical parameters used within the chemo-electro-mechanical simulation of a chemically and electrically stimulated hydrogel [31].

Fixed ion concentration [mMol]	2
Buffer solution concentration [mMol]	1
Temperature [K]	293
Diffusion coefficients [m^2/s]	1.00E-07
Hydrogel permittivity [unitless]	78
Buffer Domain [mm]	15 x 15
Hydrogel Domain [mm]	5 x 5

3.4   Results and Discussion

The theoretical and numerical model presented was employed to analyze the transient response of a hydrogel immersed in a buffer solution responding to chemical and electrical stimulation. Baseline investigations were performed for chemical and electrical stimulation of a hydrogel in Sections 3.4.1 and 3.4.2, respectively. Model results were validated in Section 3.4.3 against published literature. The final sections investigated hydrogel swelling by varying critical parameters under electrical stimulation, such as relative permittivity, Section 3.4.4, increased electrical potential, Section 3.4.5, and reversed electrical field, Section 3.4.6.

3.4.1   Chemical (pH) Stimulation

This section presents the chemical stimulation of a hydrogel causing swelling. The mobile ions, sodium and chloride, within the hydrogel domain had initial (t = 0) concentrations of 3.25 mol/m^3 and 1.25 mol/m^3, respectively. The fixed ion's initial concentration had a uniform distribution and constant for all time, concentration equal to 2 mol/m^3. To simulate chemical stimulation the hydrogel it was placed within a buffer solution with 1 mol/m^3 sodium and chloride concentrations. The equations of Section 3.2 were then applied to the hydrogel and buffer domains, and time was allowed to progress. The transient response (time = 0 to 800 s) of the electrical potential, mobile ion concentrations, and total displacement were solved for and are shown in Figure 3.3 for both the buffer and hydrogel domains (no displacement of buffer domain). Figure

3.3 displays a cross-section of the buffer and hydrogel domains across the x-position at a y-position of 7.5 mm. The stationary solution, i.e. equilibrium state, for all variables were obtained at a time of 800 s. The electrical potential, seen in Figure 3.3(b), within the hydrogel domain decreased with time from -15.2 mV to an equilibrium value of -22.3 mV. Little change in the electrical potential within the buffer domain was observed. The electrical potential within the hydrogel domain decreased due to the transient equilibrating of the mobile ions. The transient response of sodium and chloride can be observed in Figure 3.3(c)-(f) for the buffer and hydrogel domain. The arrows in the figure show the progression of that particular quantity with time. It can be seen in Figure 3.3(c) and (e) that, while the concentrations of sodium and chloride within the hydrogel are decreasing, the concentrations in the buffer are increasing due to diffusion of the mobile ions out of the hydrogel domain. As time progresses the mobile ion concentrations in the buffer domain reach a maximum, and then return to their equilibrium value of 1.0 mol/m^3, as seen in Figure 3.3(d) and (f). It is also shown in Figure 3.3(d) and (f) that the equilibrium values of sodium and chloride are 2.41 mol/m^3 and 0.41 mol/m^3, respectively, with a constant concentration profile across the hydrogel domain. Electroneutrality within the hydrogel and buffer domains was maintained, as the mobile and fixed ions were balanced appropriately. The hydrogel's displacement, shown in Figure 3.3(g), decreased from an initial maximum of 31.9 µm to an overall minimum of 9.0 µm at a time of 10 s. The displacement decreased because the mobile ion gradients, between the buffer and hydrogel, were decreasing. At 10 s the ion gradients reach a minimum, and after 10 s these gradients increase slightly to reach their equilibrium state. This response can be seen in Figure 3.3(h) as the displacement increases from 10 to 800 s reaching a final magnitude of 10.2 µm. The hydrogel's displacement behavior was governed by the applied osmotic pressure, which also displayed the same behavior of an initial global maximum, a global

minimum and an equilibrium local maximum, as displayed in Figure 3.4. The initial maximum osmotic pressure was 3.83 kPa progressing to a minimum pressure of 1.73 kPa, and an equilibrium pressure of 2.02 kPa. The osmotic pressure, a function of ionic gradients, displayed this behavior due to the transient diffusion of mobile ions between the hydrogel and buffer domains. The aforementioned osmotic pressure was studied at the positions y = 7.5 mm and x = 5 mm or 10 mm. Since the hydrogel domain was square the edges had slightly larger osmotic pressure and displacement. Had the hydrogel domain been a circle, displacements and osmotic pressures would have been constant around the circumference. The equilibrium state of chemical stimulation was used for the initial state of electrical stimulation.

3.4.2 Electrical Stimulation (Applied Potential = ± 0.05 V)

This section presents the numerical results for the electrical stimulation of a hydrogel causing swelling or deswelling. The initial conditions for electrical stimulation were assumed to be the equilibrium conditions of chemical stimulation. To electrically stimulate the hydrogel an electric potential of ±0.05 V was applied at the electrodes. The position x = 0 (for all y) was the cathode where a potential of -0.05 V was applied, and the position x = 15 mm (for all y) was the anode where a potential of +0.05 V was applied. The equations of Section 3.2 were then applied to the hydrogel and buffer domains, and time was allowed to progress. The transient responses (time = 0 to 800 s) of the electrical potential, mobile ion concentrations, and total displacement are shown in Figure 3.5, which displays a cross-section of the buffer and hydrogel domains across the x-position at a y-position of 7.5 mm. The equilibrium state was achieved 800 s after electrical stimulation was implemented. The electrical potential, shown in Figure 3.5(a) and (b), followed a linear profile between the cathode and anode. This linear profile had a potential well in the hydrogel domain caused by the chemical potential between ions in the buffer and hydrogel domains. The electrical potential was seen initially (t < 10 s)

89
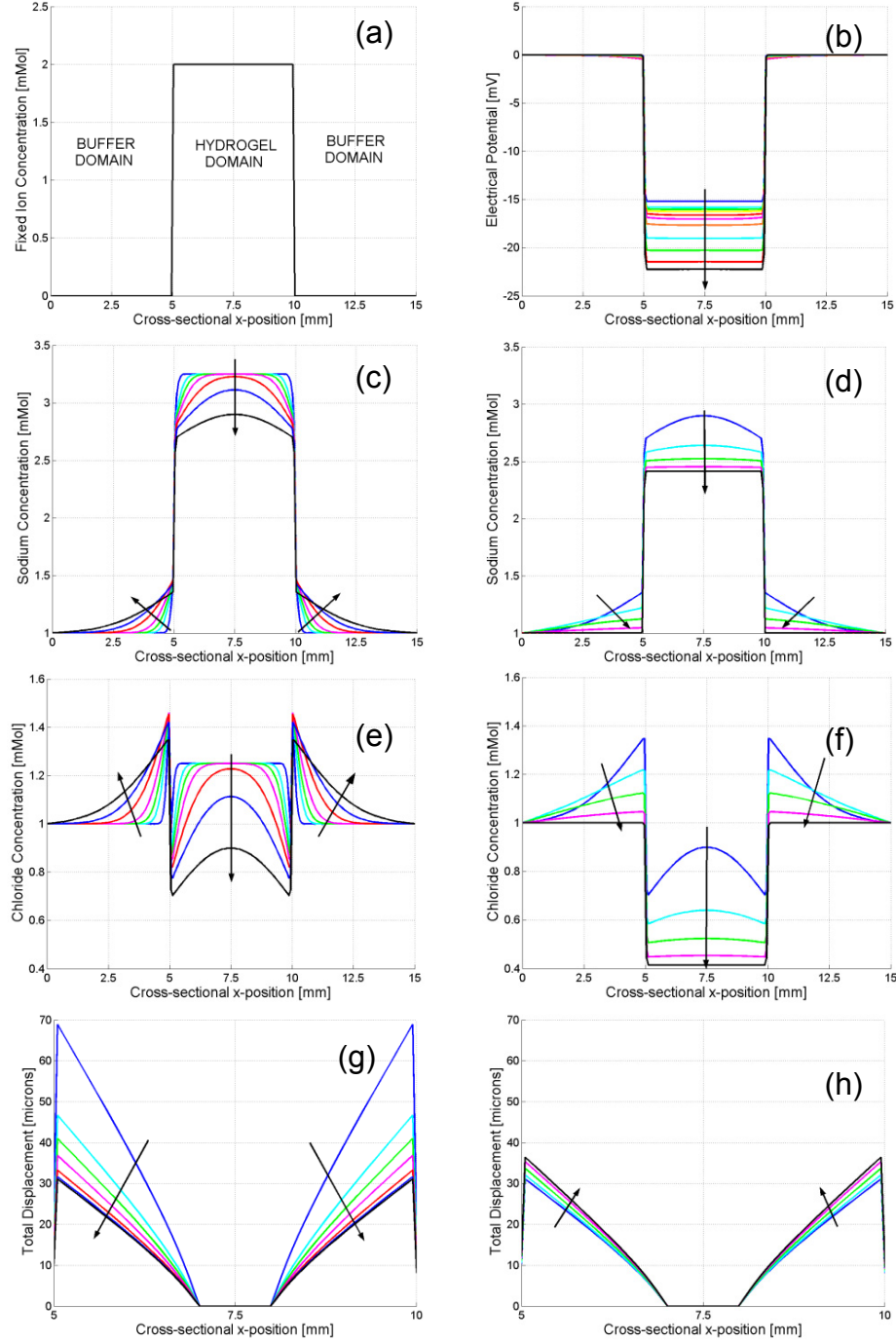
Figure 3.3: Chemical stimulation of a hydrogel results for electric potential, ionic concentration, and displacement versus x-position at the y-position = 0.0075 m. a) Numerical model domains; b) Electric potential at t = 0, 0.1, 0.5, 1, 2, 5, 10, 20, 50, 100, 200, 800 s; c) Sodium concentration at t = 0, 0.1, 0.5, 1, 2, 5, 10 s; d) Sodium concentration at t = 10, 20, 50, 100, 200, 800 s; e) Chloride concentration at t = 0, 0.1, 0.5, 1, 2, 5, 10 s; f) Chloride concentration at t = 10, 20, 50, 100, 200, 800 s; g) Total displacement at t = 0, 0.1, 0.5, 1, 2, 5, 10 s; h) Total displacement at t = 10, 20, 50, 100, 200, 800 s.

90
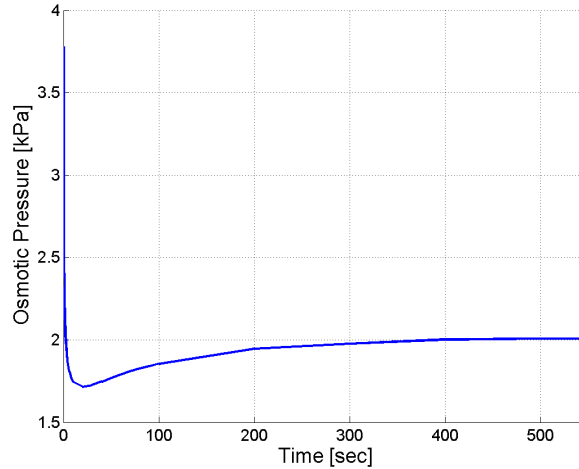
Figure 3.4: Transient response of the osmotic pressure generated due to chemical stimulation, corresponding to the positions y = 7.5 mm and x = 5 mm or 10 mm.

increasing near the cathode side of the hydrogel and decreasing near the anode side of the hydrogel, adjusting to the migration of mobile ions. After 10 s the electrical potential decreased throughout both domains. The transient ionic concentration profiles for sodium and chloride can be seen in Figure 3.5(c)-(f). In the hydrogel domain, sodium and chloride ion concentrations increased near the cathode side of the hydrogel, and decreased near the anode side of the hydrogel. Sodium and chloride ions in the buffer domain also increased near the cathode side of the hydrogel, and decreased near the anode side of the hydrogel. Electroneutrality was maintained as the ionic concentrations were balanced for all time. The electrically induced migration of mobile ions caused new ionic gradients to be established, and hence further displacement of the hydrogel was observed, as seen in Figure 3.5(g) and (h). The hydrogel's displacement near the cathode decreased with time to a minimum of 6.3 µm, or deswelling of the hydrogel near the cathode occurred. The hydrogel's displacement on the anode side increased to a maximum of 15.3 µm, or further swelling of the hydrogel occurred near the anode. The hydrogel's swelling and deswelling was caused by a varying osmotic pressure, depicted in Figure 3.6. The osmotic pressure at both the cathode and anode was initially 2.02 kPa, and upon application of electrical stimulus

91
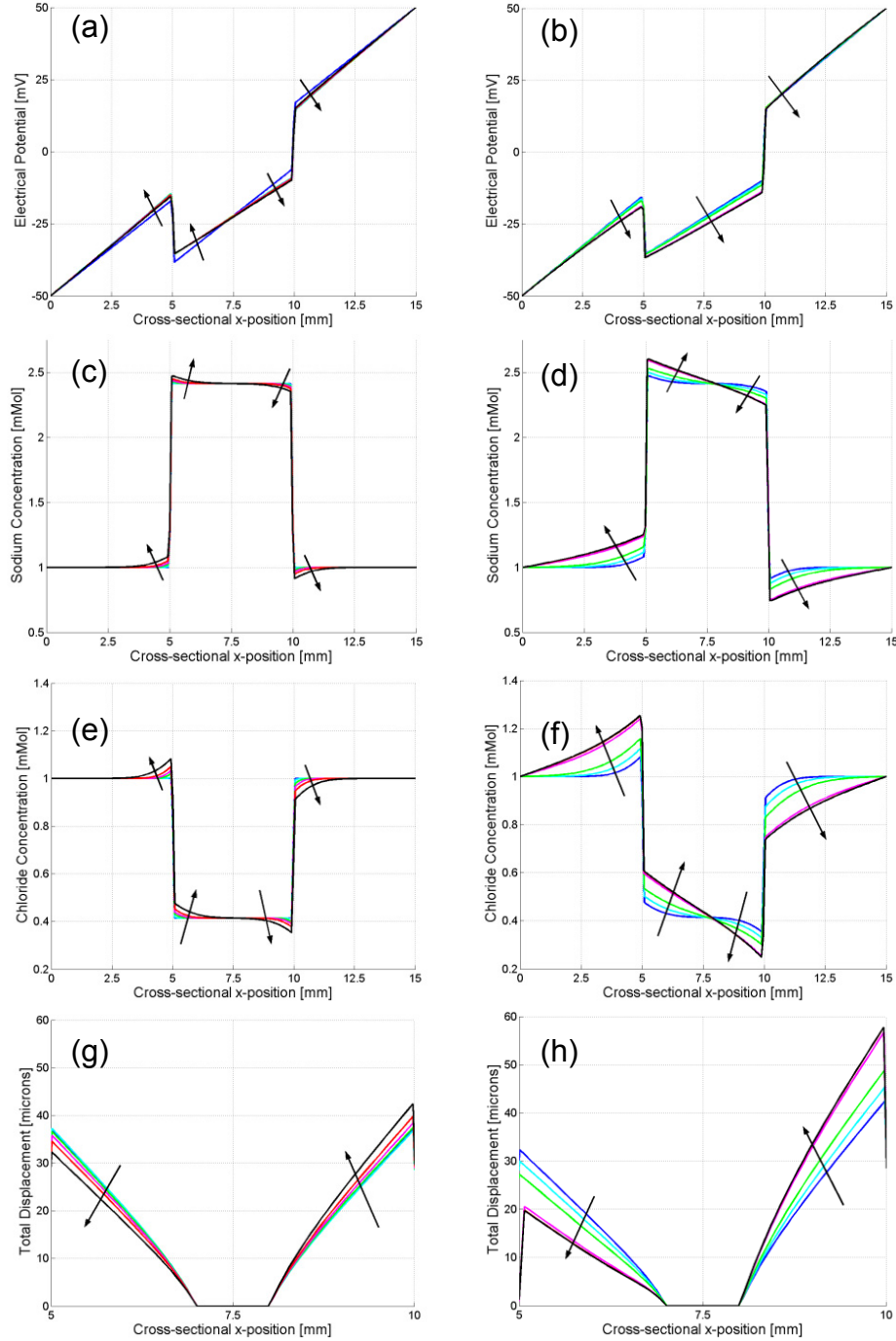
Figure 3.5: Electrical stimulation (± 0.05 V) of a hydrogel results for electric potential, ionic concentration, and displacement versus x-position at the y-position = 0.0075 m. The anode is located at x-position = 0.015 m, and the cathode is located at x-position = 0 m. a) Electric potential at t = 0, 0.1, 0.5, 1, 2, 5, 10 s; b) Electric potential at t = 10, 20, 50, 100, 200, 800 s; c) Sodium concentration at t = 0, 0.1, 0.5, 1, 2, 5, 10 s; d) Sodium concentration at t = 10, 20, 50, 100, 200, 800 s; e) Chloride concentration at t = 0, 0.1, 0.5, 1, 2, 5, 10 s; f) Chloride concentration at t = 10, 20, 50, 100, 200, 800 s; g) Total displacement at t = 0, 0.1, 0.5, 1, 2, 5, 10 s; h) Total displacement at t = 10, 20, 50, 100, 200, 800 s.

Figure 3.6: Osmotic pressure as a result of electrical stimulation (± 0.05 V) of a hydrogel, corresponding to the positions y = 7.5mm and x = 5mm (cathode side) and 10 mm (anode side).

the mobile ions established new ionic gradients between the hydrogel and buffer. As such, the ionic gradients were quantitatively smaller near the cathode, and deswelling occurred, and larger near the anode where swelling occurred. The equilibrium state osmotic pressures near the cathode and anode were 1.72 kPa and 2.45 kPa, respectively. The aforementioned osmotic pressure was studied at the positions y = 7.5 mm and x = 5 mm or 10 mm.

3.4.3 Verification of Chemical and Electrical Stimulation Numerical Models

The chemical and electrical stimulation studies of Sections 3.4.1 and 3.4.2, respectively, were expanded from the numerical simulations of Wallmersperger *et al.* [31]. Wallmersperger *et al.*'s work concentrated on the transient responses of the electrical potential and ionic concentrations, hence validation of this work will compare against those quantities. Comparing the results for chemical stimulation, as seen in Figure 3.7, shows excellent agreement for all time. Note that normalized osmotic pressure was compared, since this was a function of ionic concentrations. Comparing the results for electrical stimulation shows some minor

quantitative deviations between the two numerical models, illustrated in Figure 3.8(a). At a point (x = 6 mm, y = 7.5 mm) Wallmersperger *et al.*'s electrical potential had an equilibrium value of -31.2mV, compared against a value of -32.0 mV obtained in this work, a 2.56 % deviation. Also illustrated in Figure 3.8(b), the normalized osmotic pressure deviated from literature through a decrease and increase in pressure at the anode and cathode hydrogel-buffer interface, respectively. The compared equilibrium normalized osmotic pressure values deviated by 1.2 % and 1.8 % at the anode and cathode, respectively. The major cause of these aforementioned deviations stems from the implementation of Donnan theory, or lack thereof here. Within this work all solution variables were continuous across all domains, and hence did not require the implementation of discontinuous boundary conditions governing the electrical potential, such as Donnan theory used in Wallmersperger *et al.* A discussion comparing the differences between Donnan theory and the chemo-electro-mechanical model is performed in the published version of this chapter [39], and solidifies the validity of this model for all stimulation methods considered.
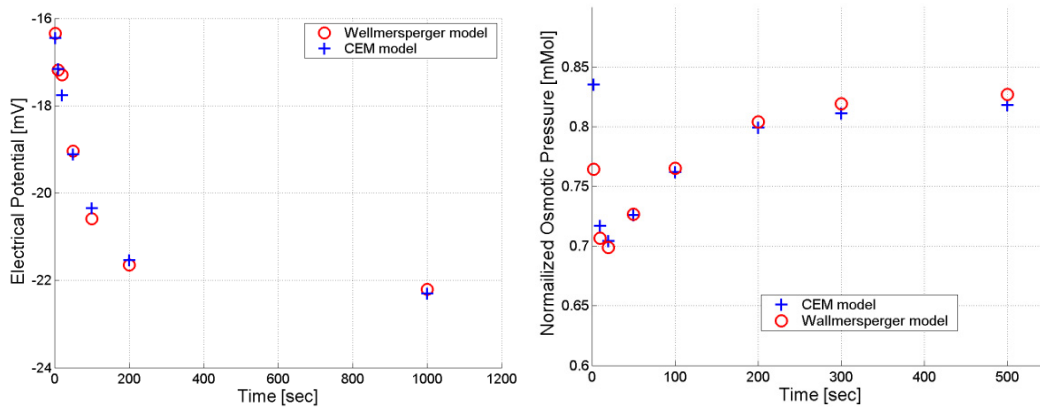
Figure 3.7: Comparison of chemo-electro-mechanical chemical stimulation with Wallmersperger *et al.* [31]. The electric potential was observed at the position x = 7.5 mm and y = 7.5 mm. The normalized osmotic pressure was observed at the position y = 7.5 mm and x = 5 mm or 10 mm.
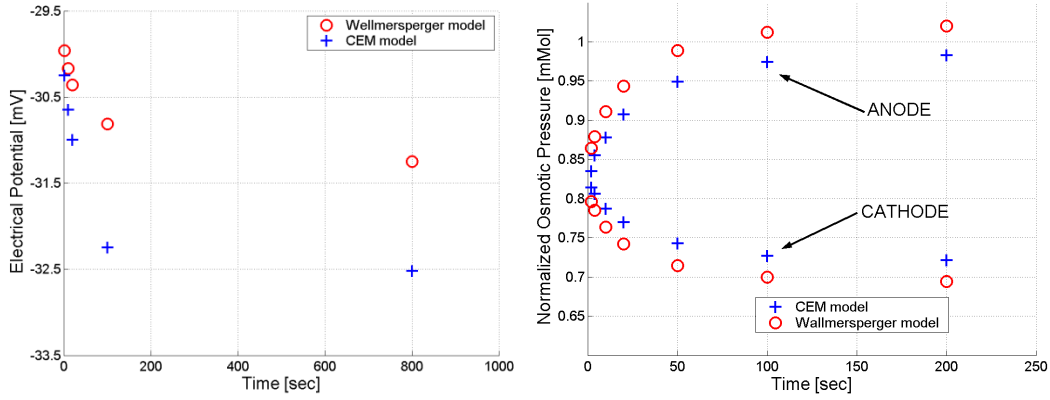
Figure 3.8: Comparison of chemo-electro-mechanical electrical stimulation with Wallmersperger *et al.* [31]. The electric potential was observed at the position y = 7.5 mm and x = 6 mm. The normalized osmotic pressure was observed at the hydrogel-buffer interface at the anode and cathode sides of the hydrogel.

3.4.4 Examining the Effect of Relative Permittivity

The Poisson equation depends on the dielectric permittivity of the hydrogel, and thus is interesting to examine the effect of this parameter on the electrical stimulation swelling process. The relative dielectric permittivity of the buffer solution (in our case sodium chloride (NaCl) solution) was taken to be to 78, equal to that of water. The dielectric permittivity of the hydrogel has been changed from 78 (as examined in Section 3.4.2) to 7.8. This gives a relative permittivity ratio between the hydrogel and buffer of 0.1. In this thesis only the ratios 1 (Section 3.4.2) and 0.1 are examined, as ratios in between these two ratios display the same qualitative characteristics.

Figure 3.5 and Figure 3.9 show the chloride and sodium concentration distributions, electrical potential and the total displacement for two different dielectric permittivity ratios (hydrogel to buffer) of 1 and 0.1, respectively. Figure 3.5(e,f) and Figure 3.9(a) show the chloride concentration distribution for dielectric permittivity ratio 1 and 0.1, respectively. As shown, in both cases the concentration distribution results are almost identical, except that the transition from the solution domain to the hydrogel domain was sharper for the dielectric permittivity ratio of 1. Figure 3.5(c,d) and Figure 3.9(b) show very similar results for the sodium

concentration distribution. The electrical potential in the solution and the hydrogel domains for dielectric permittivity ratios 1 and 0.1 are shown in Figure 3.5(a,b) and Figure 3.9(c), respectively. As shown the effect of the dielectric permittivity on the transient process of the swelling was very small and can be negligible. The total displacement in the hydrogel as a result of dielectric permittivity 0.1 was smaller than total displacement of the initial dielectric permittivity ratio, as shown in Figure 3.5(g,h) and Figure 3.9(d). This decrease could be attributed to the mathematical definition of the osmotic pressure that is developed at the hydrogel-buffer interface. This osmotic pressure directly depended on the transition of the concentration functions from the solution domain to the hydrogel domain.

3.4.5 Electrical Stimulation (Applied Potential = ±0.25 V)

This section examines the electrical stimulation of a hydrogel causing swelling or deswelling. The initial conditions for electrical stimulation were the equilibrium conditions of chemical stimulation, reviewed in Section 3.4.1. The electrical potential was applied in the same manner as in Section 3.4.2, but was increased from ±0.05 V to ±0.25 V. The transient responses (time = 0 to 800 s) of the electrical potential, mobile ion concentrations, and total displacement are shown in Figure 3.10, using the now familiar cross-sectional format. Equilibrium state was achieved 800 s after electrical stimulation was implemented. The electrical potential was seen to initially (t < 10) display a linear profile for all regions considered, displayed in Figure 3.10(a); however, for larger time (t > 10) non-linear profiles are seen to develop in the buffer region near the hydrogel-buffer interface, displayed in Figure 3.10(b). These non-linearities result from the much larger (versus Section 3.4.2) non-linear ionic concentrations within the buffer region near the hydrogel-buffer interface, illustrated in Figure 3.10(c)-(f). The linear electrical potential profile within the hydrogel was maintained, as the steady state ionic concentrations of both species within the hydrogel displays a linear

96
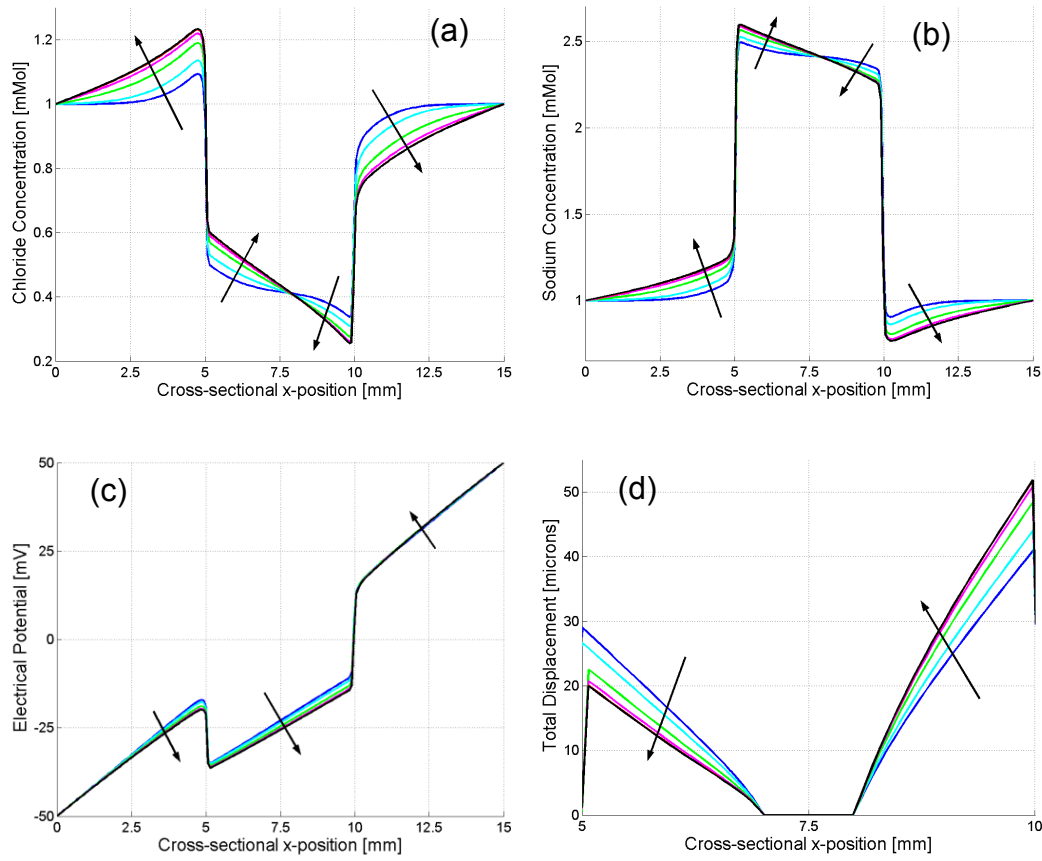
Figure 3.9: Electrical stimulation (± 0.05 V, relative permittivity ratio = 0.1) of a hydrogel results for ionic concentration, electrical potential and displacement versus x-position at the y-position = 0.0075 m. The anode is located at x-position = 0.015 m, and the cathode is located at x-position = 0 m. a) Chloride concentration at t = 10, 20, 50, 100, 200, 800; b) Sodium concentration at t = 10, 20, 50, 100, 200, 800; c) Electrical potential at t = 10, 20, 50, 100, 200, 800; d) Total displacement at t = 10, 20, 50, 100, 200, 800.

profile as well, shown in Figure 3.10(d) and (f). Figure 3.10(c)-(f) also presents the transient ionic concentration responses, which shows both the sodium and chloride concentrations, for both solution domains, increasing near the cathode side and decreasing near the anode side of the hydrogel-buffer interface. Increasing the applied electrical potential, versus Section 3.4.2, caused larger ionic gradients to be established. Overall, these larger concentration gradients cause much larger total displacement of the hydrogel to occur, with transient displacement results given in Figure 3.10(g) and Figure 3.10(h). Figure 3.10(g) shows the total displacement near the cathode decreasing to near zero, but with time (t >

97

10) this side's displacement increases to 4.1 μm, as seen in Figure 3.10(h). The anode side of the hydrogel transiently increased to reach a maximum displacement of 38.1 μm, as seen in Figure 3.10(h), which was a 374 % increase versus the displacement results of Section 3.4.2. The increased hydrogel displacement was a result of larger osmotic pressure being established at the hydrogel-buffer interface near the anode, compared to Section 3.4.2, with the osmotic pressure within the hydrogel shown in Figure 3.11. The ionic gradients established as a result of the applied electrical potential of ±0.25 V caused higher osmotic pressure at the anode, and lower osmotic pressure at the cathode versus an applied electrical potential of ±0.05 (osmotic pressure shown in Figure 3.6). The steady-state osmotic pressures at the anode and cathode sides of the hydrogel were 4.47 kPa and 1.25 kPa, respectively.

3.4.6 Effect of Reversing the Electric Field (Applied Potential = ± 0.25 V)

This section investigates the effect of reversing the electrical potential on the swelling and deswelling of the hydrogel. This section's initial conditions were the steady-state conditions achieved in Section 3.4.5, with the same numerical methods applied as in previous sections. In this study the hydrogel was stimulated with an applied electrical potential of ±0.25 V; however, differing from previous situations examined, was that the anode and cathode positions were at x = 0 mm (for all y) and x = 15 mm (for all y), respectively. The transient responses of the electrical potential, mobile ion concentrations and total displacement are shown in Figure 3.12, with steady state achieved 800 s after reversing the electrical potential. As seen in Figure 3.12(a) and (b), the electrical potential remained linear in the hydrogel for all time, and was initially linear (t < 20 s) in the buffer domain at the anode side near the hydrogel-buffer interface, but became non-linear as time progressed. The mobile ions within the buffer and hydrogel reacted to the reversed electrical field by migrating in a direction opposite to that seen in Sections 3.4.2 and 3.4.5,
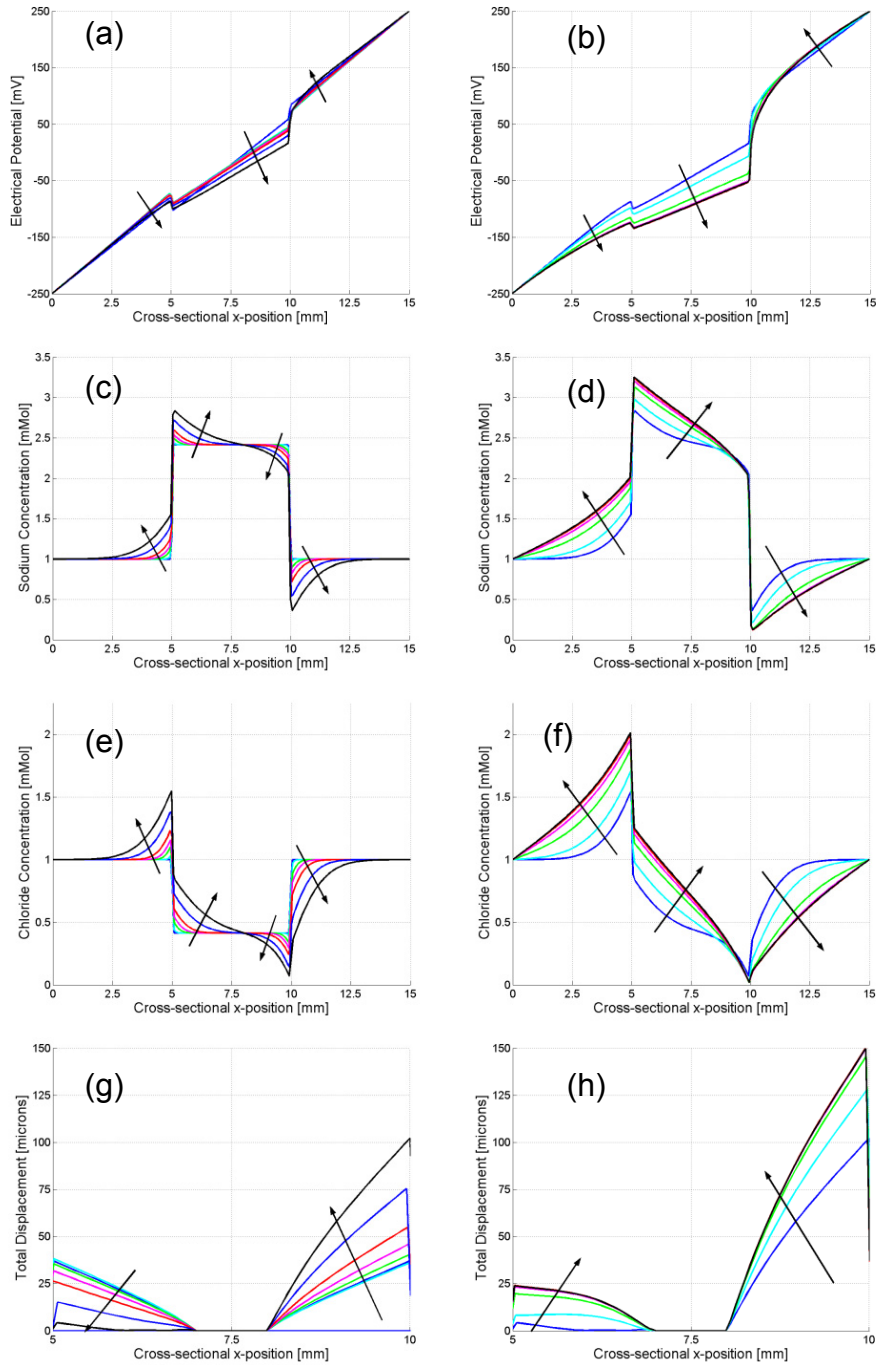
Figure 3.10: Electrical stimulation (± 0.25 V) of a hydrogel results for electric potential, ionic concentration, and displacement versus x-position at the y-position = 0.0075 m. The anode is located at x-position = 0.015 m, and the cathode is located at x-position = 0 m. a) Electric potential at t = 0.1, 0.5, 1, 2, 5, 10 s; b) Electric potential at t = 10, 20, 50, 100, 200, 800 s; c) Sodium concentration at t = 0.1, 0. 5, 1, 2, 5, 10 s; d) Sodium concentration at t = 10, 20, 50, 100, 200, 800 s; e) Chloride concentration at t = 0.1, 0.5, 1, 2, 5, 10 s; f) Chloride concentration at t = 10, 20, 50, 100, 200, 800 s; g) Total displacement at t = 0.1, 0.5, 1, 2, 5, 10 s; h) Total displacement at t = 10, 20, 50, 100, 200, 800 s.

99
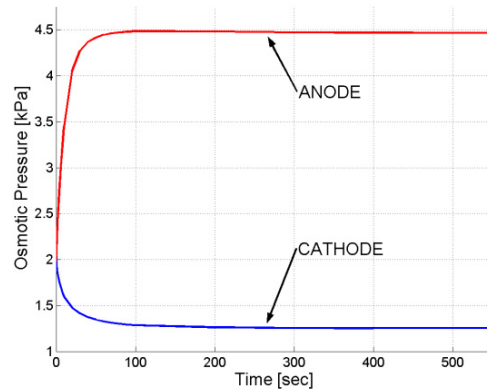
Figure 3.11: Osmotic pressure as a result of electrical stimulation (± 0.25 V) of a hydrogel, corresponding to the positions y = 7.5 mm and x = 5 mm (cathode side) and x = 10 mm (anode side).

depicted in Figure 3.12(c)-(f). Sodium and chloride concentrations decreased in both domains near the anode side of the hydrogel-buffer interface, and increased in both domains near cathode side of the hydrogel-buffer interface. During this transition period some highly non-linear profiles can be observed in Figure 3.12 for both mobile ions in both domains; however, steady-state profiles were linear for both mobile ions within the hydrogel, as seen previously in Sections 3.4.2 and 3.4.5. As these mobile ions migrate the ionic gradients they establish across the hydrogel-buffer interface dynamically change as well, influencing the displacement of the hydrogel accordingly. The total displacement of the hydrogel, depicted in Figure 3.12(g,h), followed this trend as the hydrogel near both the cathode and anode deswelled initially, then swelled according to the new ionic gradients established. The steady state displacements at the anode and cathode sides of the hydrogel were 38.1 μm and 4.1 μm, respectively. These displacements had the same magnitude as in Section 3.4.5; however, were found on opposite sides of the hydrogel, as a result of the reversed electrical field. The transient nature of the osmotic pressure causing these reversed displacements can be seen in Figure 3.13. The osmotic pressure for the anode and cathode side of the hydrogel was seen to decrease and increase, respectively,

100
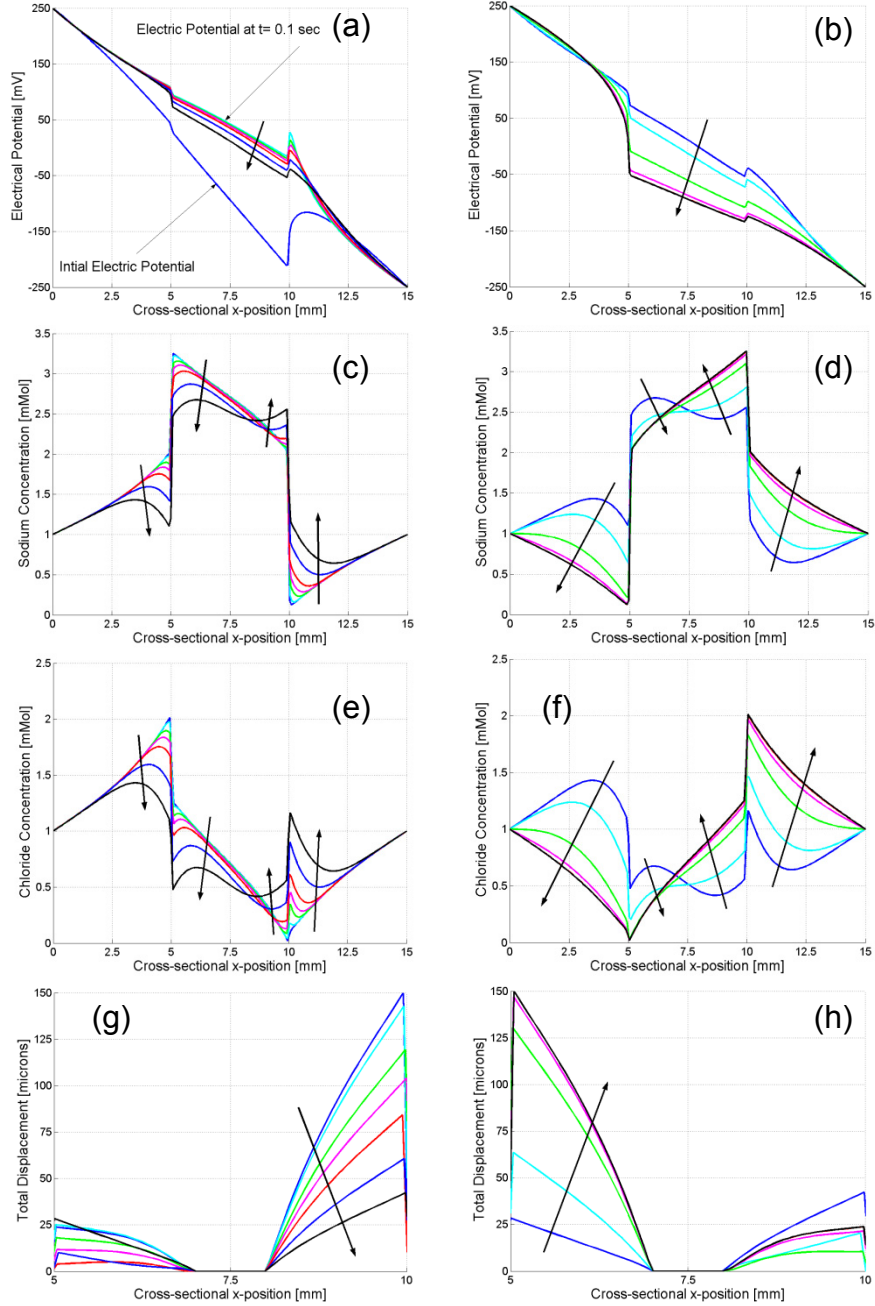
Figure 3.12: Reversed electrical field stimulation (± 0.25 V) of a hydrogel results for electric potential, ionic concentration, and displacement versus x-position at the y-position = 0.0075 m. The *cathode* is located at x-position = *0.015 m*, and the *anode* is located at x-position = *0 m*. a) Electric potential at t = 0, 0.1, 0.5, 1, 2, 5, 10 s; b) Electric potential at t = 10, 20, 50, 100, 200, 800 s; c) Sodium concentration at t = 0, 0.1, 0.5, 1, 2, 5, 10 s; d) Sodium concentration at t = 10, 20, 50, 100, 200, 800 s; e) Chloride concentration at t = 0, 0.1, 0.5, 1, 2, 5, 10 s; f) Chloride concentration at t = 10, 20, 50, 100, 200, 800 s; g) Total displacement at t = 0, 0.1, 0.5, 1, 2, 5, 10 s; h) Total displacement at t = 10, 20, 50, 100, 200, 800 s.

101
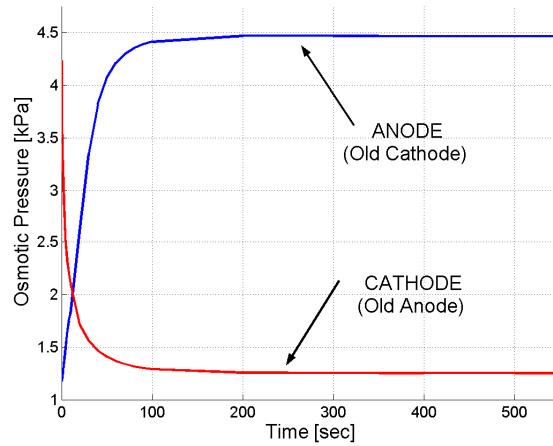
Figure 3.13: Osmotic pressure as a result of the electrical stimulation (± 0.25 V) with reversed electrical field from initial condition, corresponding to the positions y = 7.5 mm and x = 5 mm (cathode side) and x = 10 mm (anode side).

adjusting to the new ionic gradients being established at the hydrogel-buffer interface. At the anode side of the hydrogel the osmotic pressure increased from a minimum of 1.25 kPa to a steady-state maximum of 4.47 kPa. The cathode side of the hydrogel decreased from a maximum of 4.47 kPa to a steady-state minimum of 1.25 kPa. At 13 s the osmotic pressure at both sides of the hydrogel was equal, with a magnitude of 2.0 kPa. The examined electrical potential, mobile ion concentrations, total displacements, and osmotic pressure had the same steady state magnitude as that of Section 3.4.5; however, the locations of these magnitudes were on opposite sides of the hydrogel reacting to the reversed electrical field. This section highlights the reversible nature of the hydrogel swelling phenomena responding to electrical stimulus.

3.5 Conclusions

This work presents and examines a multiphysics coupled chemo-electro-mechanical numerical model for the simulation of a stimulated hydrogel's swelling and deswelling phenomena. The examined stimulation methods were chemical (pH) and electrical. Numerical results presented the transient response of the electrical and chemical fields for both the buffer and hydrogel domains. In addition, the displacement field of the

102

hydrogel was solved and presented, with the associated osmotic pressure. Numerical results were in good agreement with published literature. Furthermore, this work examined the effect of varied values of hydrogel relative permittivity, increased stimulating electrical potential, and of a reversed stimulating electrical field. Lowering the hydrogel's relative permittivity affected the applied electrical field, which induced small non-linearities in the electrical potential and ionic concentrations near the hydrogel-buffer interface. The effect of the increased stimulating potential was the generation of much larger ionic gradients between the hydrogel and buffer solution, which subsequently caused a much larger displacement of the hydrogel. Reversing the applied electrical field effectively reversed the mobile ions migration, which caused these ions to establish ionic gradients on opposite sides of the hydrogel. These reversed ionic gradients caused the hydrogel to deswell where once swollen, and swell where once shrunken. In addition, the magnitude of hydrogel displacement was the same as the previous equilibrium state, since the stimulating electrical field was of equal magnitude to the previous equilibrium state.

Hydrogels have excellent potential as actuators in various microfluidic components. Further work will be performed to simulate hydrogels at the microscale to accurately represent their integration with microfluidics. As simulations using transport models can give an accurate representation of swelling and deswelling, these will continue to be implemented for various geometric considerations and device optimization.

References

[1]   D. J. Beebe, J. S. Moore, J. M. Bauer, Q. Yu, R. H. Liu, C. Devadoss, *et al.*, "Functional hydrogel structures for autonomous flow control inside microfluidic channels," *Nature,* vol. 404, pp. 588-590, Apr 6 2000.

[2]   S. K. De, N. R. Aluru, B. Johnson, W. C. Crone, D. J. Beebe, and J. Moore, "Equilibrium swelling and kinetics of pH-responsive hydrogels: Models, experiments, and simulations," *Journal of Microelectromechanical Systems,* vol. 11, pp. 544-555, Oct 2002.

[3]   S. K. De and N. R. Aluru, "A chemo-electro-mechanical mathematical model for simulation of pH sensitive hydrogels," *Mechanics of Materials,* vol. 36, pp. 395-410, May 2004.

[4]   M. J. Bassetti, A. N. Chatterjee, N. R. Aluru, and D. J. Beebe, "Development and modeling of electrically triggered hydrogels for microfluidic applications," *Journal of Microelectromechanical Systems,* vol. 14, pp. 1198-1207, Oct 2005.

[5]   G. Filipcsei, I. Csetneki, A. Szilagyi, and M. Zrinyi, "Magnetic field-responsive smart polymer composites," *Oligomers Polymer Composties Molecular Imprinting,* vol. 206, pp. 137-189, 2007.

[6]   S. G. Starodoubtsev, E. V. Saenko, A. R. Khokhlov, V. V. Volkov, K. A. Dembo, V. V. Klechkovskaya, *et al.*, "Poly(acrylamide) gels with embedded magnetite nanoparticles," *Microelectronic Engineering,* vol. 69, pp. 324-329, SEP 2003.

[7]   N. J. Francois, S. Allo, S. E. Jacobo, and M. E. Daraio, "Composites of polymeric gels and magnetic nanoparticles: Preparation and drug release behavior," *Journal of Applied Polymer Science,* vol. 105, pp. 647-655, JUL 15 2007.

[8]   K. Al-Aribe, G. K. Knopf, and S. B. Amarjeet, "Photo-responsive hydrogel for controlling flow on a microfluidic chip," in *Photonics North*, 2006.

[9]   W. Xue, I. W. Hamley, and M. B. Huglin, "Rapid swelling and deswelling of thermoreversible hydrophobically modified poly(N-isopropylacrylamide) hydrogels prepared by freezing polymerisation," *Polymer,* vol. 43, pp. 5181-5186, SEP 2002.

[10]   K. Takahashi, T. Takigawa, and T. Masuda, "Swelling and deswelling kinetics of poly(N-isopropylacrylamide) gels," *Journal of Chemical Physics,* vol. 120, pp. 2972-2979, FEB 8 2004.

[11]   V. Ozturk and O. Okay, "Temperature sensitive poly(N-t-butylacrylamide-co-acrylamide) hydrogels: synthesis and swelling behavior," *Polymer,* vol. 43, pp. 5017-5026, AUG 2002.

[12]   T. Caykara, S. Kiper, and G. Demirel, "Thermosensitive poly(N-isopropylacrylamide-co-acrylamide) hydrogels: Synthesis, swelling and interaction with ionic surfactants," *European Polymer Journal,* vol. 42, pp. 348-355, Feb 2006.

[13]   M. Zourob, K. G. Ong, K. F. Zeng, F. Mouffouk, and C. A. Grimes, "A wireless magnetoelastic biosensor for the direct detection of organophosphorus pesticides," *Analyst,* vol. 132, pp. 338-343, 2007.

[14]   T. Miyata, N. Asami, and T. Uragami, "A reversibly antigen-responsive hydrogel," *Nature,* vol. 399, pp. 766-769, Jun 24 1999.

[15]   T. F. Otero and J. M. Sansinena, "Soft and wet conducting polymers for artificial muscles," *Advanced Materials,* vol. 10, pp. 491-+, APR 16 1998.

[16]   T. F. Otero, S. Villanueva, M. T. Cortes, S. A. Cheng, A. Vazquez, I. Boyano*, et al.*, "Electrochemistry and conducting polymers: soft, wet, multifunctional and biomimetic materials.," *Synthetic Metals,* vol. 119, pp. 419-420, MAR 15 2001.

[17]   Q. Yu, J. M. Bauer, J. S. Moore, and D. J. Beebe, "Responsive biomimetic hydrogel valve for microfluidics," *Applied Physics Letters,* vol. 78, pp. 2589-2591, Apr 23 2001.

[18]   A. K. Agarwal, S. S. Sridharamurthy, D. J. Beebe, and H. R. Jiang, "Programmable autonomous micromixers and micropumps," *Journal of Microelectromechanical Systems,* vol. 14, pp. 1409-1421, Dec 2005.

[19]   J. Wang, Z. Y. Chen, M. Mauk, K. S. Hong, M. Y. Li, S. Yang*, et al.*, "Self-actuated, thermo-responsive hydrogel valves for lab on a chip," *Biomedical Microdevices,* vol. 7, pp. 313-322, Dec 2005.

[20]   Y. Dai, P. Li, and A. Q. Wang, "Intelligent drug delivery system of intelligent high polymer materials," *Progress in Chemistry,* vol. 19, pp. 362-369, MAR 2007.

[21]   C. Alexander and K. M. Shakesheff, "Responsive polymers at the biology/materials science interface," *Advanced Materials,* vol. 18, pp. 3321-3328, DEC 18 2006.

[22]   Y. H. Huang, H. Q. Yu, and C. B. Xiao, "pH-sensitive cationic guar gum/poly (acrylic acid) polyelectrolyte hydrogels: Swelling and in vitro drug release," *Carbohydrate Polymers,* vol. 69, pp. 774-783, JUL 2 2007.

[23]   P. J. Flory, *Principles of polymer chemistry*. Ithaca, N.Y.: Cornell University Press, 1953.

[24]   B. Erman and P. J. Flory, "Critical Phenomena and Transitions in Swollen Polymer Networks and in Linear Macromolecules," *Macromolecules,* vol. 19, pp. 2342-2353, Sep 1986.

[25]   H. Li, J. Chen, and K. Y. Lam, "Multiphysical modeling and meshless simulation of electric-sensitive hydrogels," *Journal of Polymer Science Part B-Polymer Physics,* vol. 42, pp. 1514-1531, Apr 15 2004.

[26]   H. Li, Z. Yuan, K. Y. Lam, H. P. Lee, J. Chen, J. Hanes*, et al.*, "Model development and numerical simulation of electric-stimulus-responsive hydrogels subject to an externally applied electric field," *Biosensors & Bioelectronics,* vol. 19, pp. 1097-1107, Apr 15 2004.

[27]   D. W. Yin, Q. L. Yan, and J. J. de Pablo, "Molecular dynamics simulation of discontinuous volume phase transitions in highly-charged crosslinked polyelectrolyte networks with explicit counterions in good solvent," *Journal of Chemical Physics,* vol. 123, pp. -, NOV 1 2005.

[28]   S. S. Jang, W. A. Goddard, and M. Y. S. Kalani, "Mechanical and transport properties of the poly(ethylene oxide)-poly(acrylic acid) double network hydrogel from molecular dynamic simulations," *Journal of Physical Chemistry B,* vol. 111, pp. 1729-1737, FEB 22 2007.

[29]   B. Kim, K. La Flamme, and N. A. Peppas, "Dynamic swelling Behavior of pH-sensitive anionic hydrogels used for protein delivery," *Journal of Applied Polymer Science,* vol. 89, pp. 1606-1613, AUG 8 2003.

[30]   J. Feng, H. Liu, and Y. Hu, "Molecular dynamics simulations of polyampholyte solutions: osmotic coefficient," *Molecular Simulation,* vol. 32, pp. 51-57, JAN 2006.

[31]   T. Wallmersperger, B. Kroplin, J. Holdenried, and R. W. Gulch, "A Coupled Multi-Field-Formulation for Ionic Polymer Gels in Electric Fields,"

in *Smart Structures and Materials 2001: Electroactive Polymer Actuators and Devices*, 2001, pp. 264-275.

[32]   P. E. Grimshaw, J. H. Nussbaum, A. J. Grodzinsky, and M. L. Yarmush, "Kinetics of Electrically and Chemically-Induced Swelling in Polyelectrolyte Gels," *Journal of Chemical Physics,* vol. 93, pp. 4462-4472, Sep 15 1990.

[33]   Y. Chu, P. P. Varanasi, M. J. Mcglade, and S. Varanasi, "Ph-Induced Swelling Kinetics of Polyelectrolyte Hydrogels," *Journal of Applied Polymer Science,* vol. 58, pp. 2161-2176, Dec 19 1995.

[34]   H. Li, Y. Yew, K. Y. Lam, and T. Ng, "Numerical Simulation of Hydrogel-Based pH-responsive Biosensors in BioMEMS," in *Design, Test, Integration & Packaging of MEMS/MOEMS*, Cannes-Mandelieu, 2003, pp. 218-222.

[35]   H. Li, Y. Yew, K. Y. Lam, and T. Ng, "Numerical simulation of pH-stimuli responsive hydrogel in buffer solutions," *Colloids and Surfaces a-Physicochemical and Engineering Aspects,* vol. 249, pp. 149-154, Nov 30 2004.

[36]   H. Li, T. Y. Ng, Y. K. Yew, and K. Y. Lam, "Modeling and simulation of the swelling behavior of pH-stimulus-responsive hydrogels," *Biomacromolecules,* vol. 6, pp. 109-120, JAN-FEB 2005.

[37]   H. Li, Y. K. Yew, T. Y. Ng, and K. Y. Lam, "Meshless steady-state analysis of chemo-electro-mechanical coupling behavior of pH-sensitive hydrogel in buffered solution," *Journal of Electroanalytical Chemistry,* vol. 580, pp. 161-172, Jun 15 2005.

[38]   T. Wallmersperger, B. Kroplin, and R. W. Gulch, "Coupled chemo-electro-mechanical formulation for ionic polymer gels - numerical and experimental investigations," *Mechanics of Materials,* vol. 36, pp. 411-420, May 2004.

[39]   J. R. Saunders, S. Abu-Salih, and W. A. Moussa, "Parametric Chemo-Electro-Mechanical Modeling of Smart Hydrogels," *Journal of Computational and Theoretical Nanoscience,* vol. 5, pp. 1961-1975, Oct 2008.

Chapter 4

Microfabrication and Experimental Methods

4.1   Introduction

Detailed methodologies for the microfabrication of electrically stimulated hydrogel microactuator systems are described. The experimental methods implemented to test the hydrogel's mechanical, the system's electrical properties, and to characterize the hydrogel actuator's response kinetics are also included within. A mature microfabrication process flow to prototype hydrogel microactuators is provided, with details relevant to each particular stage of development. Challenges encountered relevant to microfabrication processes critical to device operation are presented, and the solutions developed to overcome these challenges are briefly overviewed. Such challenges include in-situ photolithography and vapor deposition of Parylene. Techniques employed for electrical stimulation of hydrogel actuators and the subsequent characterization of transient in-plane deformation are presented.

4.2   Microfabrication of Prototype Devices and Hydrogels

Microfabrication was necessary to develop techniques enabling the testing, characterization, and integration of hydrogels within prototype microactuator devices. Techniques were employed to fabricate hydrogels for direct integration into devices. A mature microfabrication process flow was developed to ensure that hydrogels could be fabricated with the desired range of material properties and geometries useful to their application as microactuators.

An overview of the microfabrication process is presented first, which highlights the milestone stages through the fabrication process. Following an overview of these processes, each particular stage with specific details is discussed. To verify that the implemented techniques had been performed successfully, characterization of processes was performed where appropriate and available. The verification techniques employed were optical inspection, surface profilometry, and spectral reflectance measurements. Through continuous improvement of each particular process stage, the addition of certain stages, and complete removal of other process stages; a mature repeatable process flow was developed. Components of this mature process flow were also adapted to fabricate hydrogels for testing of their dynamic mechanical properties and subsequent examination of their morphology using electron microscopy. Furthermore, several manufacturing runs were performed during microactuator prototyping to create systems with different characteristics by modifying Parylene-N thicknesses, hydrogel diameters, and electrode materials.

The main microfabrication process flow can be seen in Figure 4.1, which depicts two separate fabrication process flows combined together to create a third and final microfabrication process flow to complete the prototype. Process flow A begins with a 4" square 0211 glass wafer, which was Piranha cleaned and had positive photoresist spun upon it, shown in step A1. In step A2 UV photolithography was performed using a photomask to define the features for electrodes. Lithography was followed in step A3 by developing the positive photoresist, and sputtering metal electrodes over the entire surface of the wafer. Step A4 depicts a milestone stage after performing lift-off to define electrodes, wafer segmentation, polydimethylsiloxane (PDMS) window fabrication, and physical vapor deposition of Parylene-N. In parallel, process flow B starts with the computer aided design (CAD) and fabrication of a rapid prototype
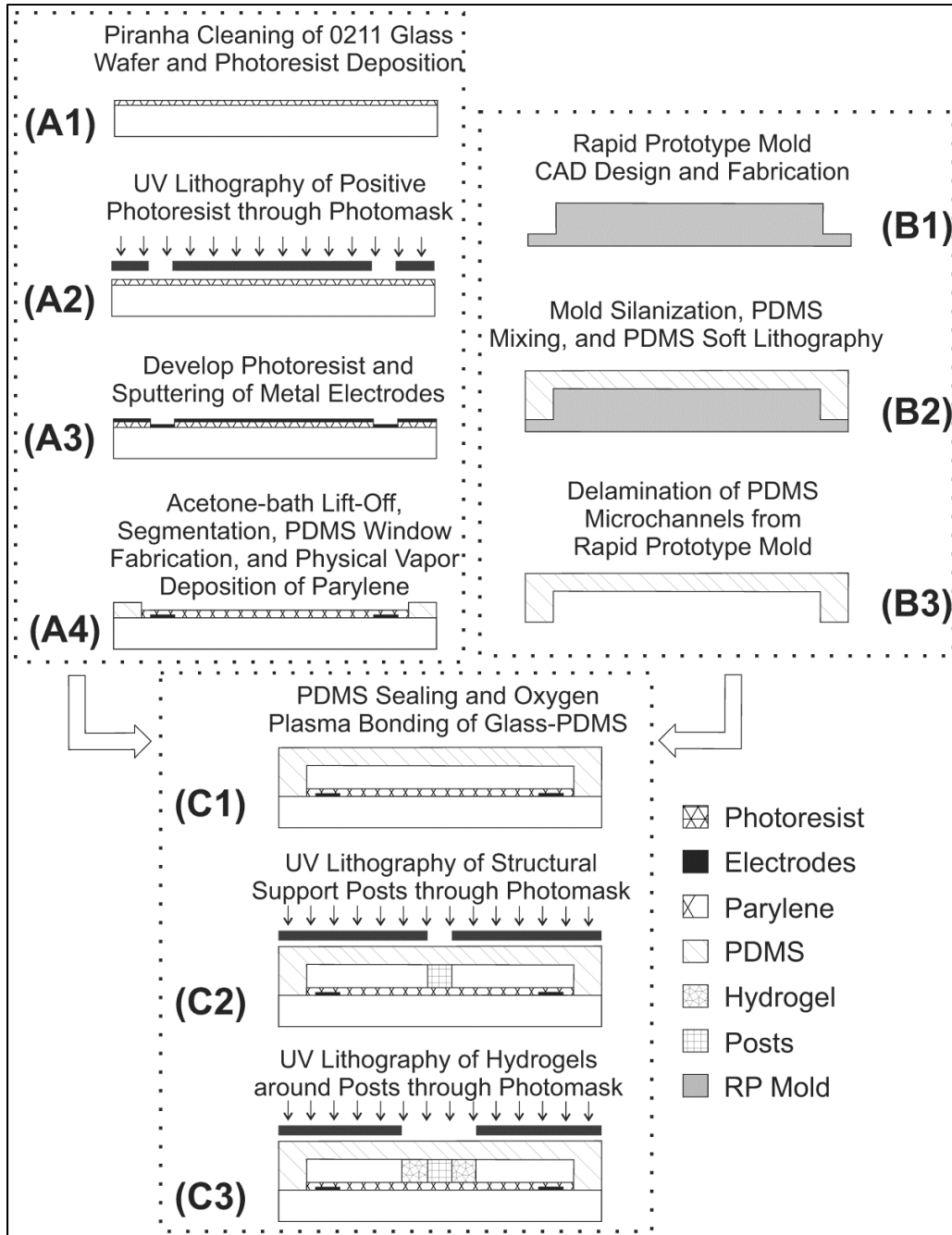
Figure 4.1: Overview of the manufacturing process flow for prototyping of hydrogel microactuators, depicting milestone stages of microfabrication. Detailed descriptions of the steps are found in Sections 4.2.1 to 4.2.7.

(RP) mold, shown in B1. Step B2 shows the salinization of the RP mold and soft lithography using thermoset PDMS. After curing, the microchannels were defined and delamination was performed, shown in milestone step B3. When finished the two milestone steps A4 and B3 were

combined together by PDMS sealing around the Parylene-N and oxygen plasma induced irreversible bonding of the PDMS to the glass substrate, shown in C1. This stage fully defines the microchannels that would house the hydrogel microactuator and the electrical stimulation system. Following bonding, step C2 UV photolithography was performed with a photomask to define a post for structural support of the active hydrogel structures, as seen in C2. The final microfabrication stage, step C3, employs UV photolithography together with another photomask to photopolymerize a hydrogel around the structural post. After completion of the prototype microactuator system the fabricated microchips were stored in deionized water until needed for testing, upon which time equalization of the hydrogel in electrolyte was performed.

Two photomasks were used throughout the process to define the electrode, structural support, and hydrogel geometries. Any changes to the electrode geometries and configurations required a new set of photomasks to be developed; however, the photomask used for support posts and hydrogels was designed to include several geometries and configurations. During manufacturing, processes were varied to create different systems, which included metal electrode sputtering, physical vapor deposition of Parylene-N, and UV photolithography of hydrogels. For sputtering different metals were deposited to create electrode systems that could either withstand electrochemical corrosion or that were optimum for dielectric deposition. The Parylene-N thickness was minimized to reduce the electric field loss through its thickness and to lower the system's characteristic actuation frequency. However, layers of Parylene-N that were too thin were prone to dielectric breakdown upon testing. Altering the hydrogel's fabrication parameters, such as exposure time or intensity, would change the hydrogel's mechanical properties. Changes in mechanical properties would directly affect the hydrogel's total actuation deformation and transient response.

The chemicals and materials used for microfabrication processes and experiments can be found in Appendix A-2, for those items purchased by the laboratory. All other materials were used within the University of Alberta NanoFab. All chemicals and materials should be used with the appropriate personal protective gear, and fume hoods be used when appropriate. Additionally all items should be stored and disposed of according to supplier and university protocols.

4.2.1 Photomask Design and Generation

Two photomask were outlined in the manufacturing process flow for prototyping of devices. These photomasks were 1:1 scale masks and were designed in accordance with the desired electrode and hydrogel geometries. Multiple hydrogel geometries were built into one photomask, but when new electrode geometries or configurations were implemented new photomasks were generated. Photomasks were designed using the CAD software L-Edit, and after completion the GDSII file was transferred to the University of Alberta NanoFab where mask fabrication occurred. Photomasks were patterned by the NanoFab on 5" square soda lime glass which was coated with ~70 nm chromium. The minimum resolution of these masks was ~2 μm, which was below the required minimum feature size of 100 μm. Masks were fabricated using a high-resolution laser mask writer to exposure deposited photoresist, and subsequently the photoresist layer was developed allowing for chrome etching to define features.

4.2.2 Surface Preparation & Photolithography

Several substrates were available as base layers, glass, silicon, or silicon on insulator. A 4" square 0211 glass substrate was selected due to its optical transparency, making it suitable for optical inspection methods. Furthermore the durability of glass wafers was higher than silicon.

To prepare the substrate for processing each glass wafer was immersed the cleaning agent piranha. This cleaning agent was a mixture of one part 30% hydrogen peroxide (H_2O_2), to three parts of 96% sulphuric

acid (H_2SO_4). Combining the two chemicals created an exothermic reaction that may reach over 120°C, and removed any organic material on the substrates. In addition, piranha may also react with some plastics or metals, thus Teflon containers should also be used and substrates were preprocessed to remove any organic deposits. In the case of reprocessing wafers after use with PDMS, the substrates must have almost all residual material removed before immersion within piranha or the mixture will turn a dark brown and start to react aggressively. For less aggressive substrate cleaning, or general cleaning of materials, solvents such as acetone, isopropanol, or methanol could be used. These solvents were especially helpful when performing preprocessing, but the wafers should be rinsed with deionized water to remove any residues.

After cleaning the substrates were ready for photolithography, which was the primary microfabrication method for substrate patterning. This process employs UV light to selectively expose a layer of positive photoresist to generate a two dimensional pattern. This photoresist material was sensitive to UV light and was spin-coated upon the wafer before exposure. When immersed in a developing solution the exposed areas of the positive photoresist dissolve, opening areas for further processing. Photoresist is commonly applied through spin-coating which achieves a uniform photoresist thickness, but the final thickness was dependent on the viscosity of the photoresist, spin speeds and spin times. This thickness must be tailored to the specific application, as finer photolithographic features require the deposition of thin layers of photoresist but further deep etching processes necessitate thicker photoresist layers. The outlined manufacturing process flow requires neither fine features nor deep etching, thus standard spin coating procedures were implemented to coat the wafer with ~1 µm thick positive photoresist. After photoresist deposition the wafer was then soft-baked within a convection oven to harden and remove solvent from the photoresist. After soft-baking the photoresist was rehydrated for 10-15

minutes within ambient humidity to ensure proper development, as the soft-baking processes also drives out moisture from the photoresist.

Contact photolithography was then performed with the aid of a mask aligner to expose the photoresist to UV light for a specific duration of time. The exposure energy required and subsequent development time were also dependent on the type and thickness of photoresist employed. Exposure energy, or the amount of light energy the photoresist was subjected to, depends on the duration of the exposure time and the intensity of the UV light. Surplus exposure energy will degrade the exposed features, while too little exposure energy will not allow for adequate removal of photoresist upon development leaving behind photoresist. For the implemented manufacturing process the photoresist was exposed for between 5-6 seconds using the first photomask to define the electrode geometries. Photoresist development then ensued to remove the exposed areas of the photoresist, through immersion in an agitated developer solution for 30-35 seconds. Development time was a function of the solvent concentration and the number of times the solution was reused for additional wafers. An increased solvent concentration or very long development times would also cause feature degradation, however low concentrations or short development times would not develop the desired features. After developing, areas of the glass substrate were exposed for metal electrode deposition; however, first the wafer must be hard-baked for sputtering. The hard-bake was used to drive out solvent to enable low vacuum pressures and harden the photoresist.

4.2.3 Defining Metal Electrodes & Segmentation

Metal electrode deposition was achieved through the technique of planar magnetron sputtering, which deposits uniform thin layers of metals onto a substrate. Sputtering was performed in a low-pressure chamber to reduce the amount of free atoms present that would collide with sputtered particles altering their energy and degrading film quality. To sputter, a 3" metal source was placed into a conductive holder, and the surface was

113

bombarded by high energy ions which were confined to the target surface by a system of magnets. The ions used here were argon, and were created by electron impact ionizations in the plasma discharge. The deposited flux was ejected from the target due to the momentum transferred to it by the bombarding electrons. These metallic flux ions then impact the substrate surface settling in place. As the substrate was coated with photoresist, significant deposition occurs on the vertical surfaces of the photoresist, especially because the open windows on the substrate have a very low aspect ratio. But, these sidewalls were removed during lift-off. For the sputtering system employed four substrates were loaded into the system, and before sputtering occurred the substrate-holder was set to rotate to ensure uniform film deposition across all wafers.

Within this work five different metallic materials were sputtered; Cr, Au, Ti, Pt, and Al. The Cr/Au comprised the combination primarily implemented within the electrical stimulation experiments, where the Cr was used as an adhesion layer for the Au. Cr readily reduces the glass surface to produce a strong bond, whereas Au is a relatively inert noble metal and thus requires an adhesion layer. The Ti/Pt combination was employed for electrical stimulation of non-dielectric coated systems, as the metals could withstand electrochemical corrosion, and the Ti served as an adhesion layer for the Pt. Aluminum electrodes were attempted to take advantage of their self-healing oxidation process [1]; however, it was found that the etching of Al by the strong or weak KOH electrolyte overpowered the thin aluminum oxide layer degrading electrodes. Each one of the aforementioned metals had different deposition rates, and the total sputtering time needed was calculated based off these empirical rates to obtain the overall final desired thickness.

After sputtering, the substrate must have the excess unexposed photoresist removed to define the electrode's geometry, a process called lift-off. The wafers were placed in an acetone bath, which was used to dissolve any unexposed photoresist. The bath was subjected to sonication

114

to agitate the acetone solution, expediting the lift-off process and ensuring diffusion into tight areas. Sonication also ensured that the electrodes were defined with straight edges, as the agitation provided additional force to cleanly break any metals at the edges of the photoresist. The bulk resistance of the electrodes from contact pad to electrode tip was measured at 130.6±5.1 Ω, whereas electrodes with defects or discontinuities would measure resistances orders of magnitude larger.

To conclude this phase of processing the substrate, now with defined electrodes, was diced to segment individual patterns from the overall wafer. A successful batch of wafers after metallization and segmentation can be seen in Figure 4.2, where inset A shows the photomask used and inset B the dicing saw employed. A successful batch produces a total of 24 chips for further processing, and at this point any segmented chips with defects can be removed from the manufacturing flow. To verify the electrodes have been adequately fabricated, surface profilometry was performed to determine the final electrode thickness, shown in Figure 4.3.
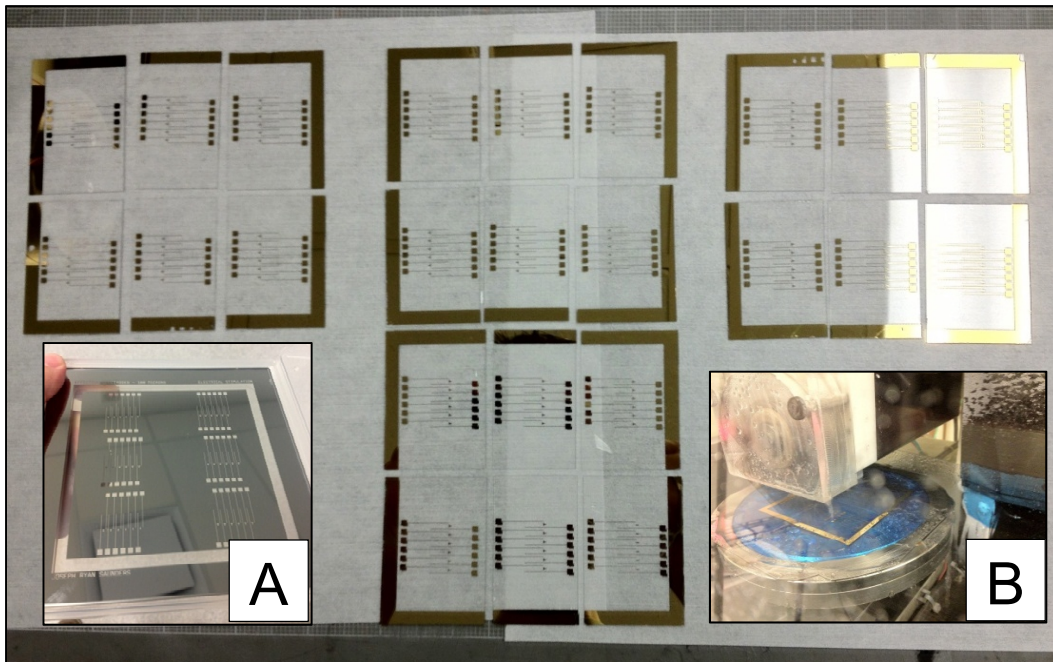
Figure 4.2: Metal electrode sputtering of Cr/Au, and segmentation of the wafer into six microchips. Inset (A) shows the photomask used in Section 4.2.2 for photolithography. Inset (B) depicts the diamond touch dicing saw.
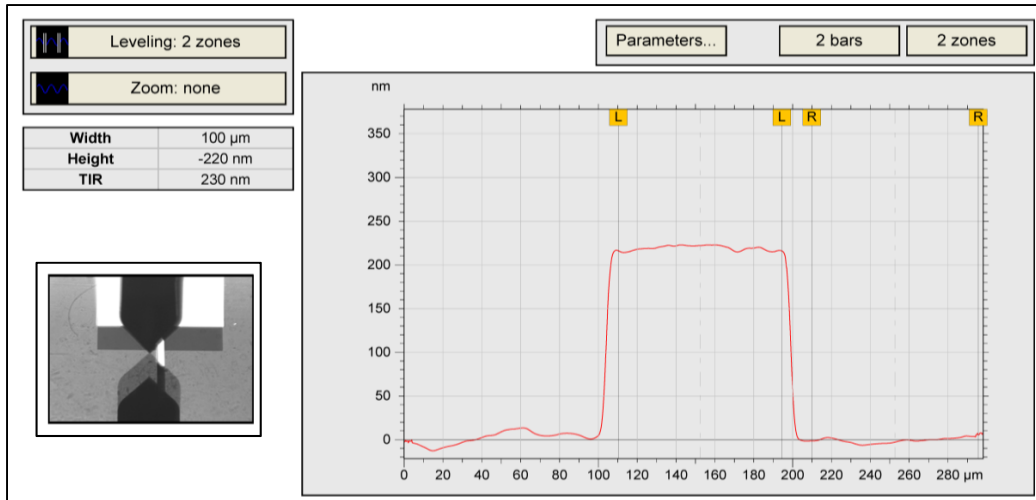
Figure 4.3: Surface profilometry of Cr/Au electrodes sputtered on 0211 glass with an electrode height of ~220 nm and a width of ~95 µm.

4.2.4 Selective Deposition of Parylene-N Dielectric

Deposition of a dielectric layer to coat the electrode was necessary to achieve electrolysis- and electrochemical reaction-free electrical stimulation of hydrogel microactuators. Various potential dielectric materials exist and some have been previously evaluated for electrowetting on dielectric systems [2], which require similar dielectric properties. These evaluated dielectrics include; PDMS, polyimide, Teflons, and Parylene compositions. Polyimide has been shown to be an effective dielectric layer for dielectrophoretic nanodroplet formation [3], and as with PDMS, can be spin-coated on a substrate's surface. However, both polyimide and PDMS are generally deposited with thicknesses between 1-40 µm, which was larger than desired for this application. Some Teflon compositions can be spin-coated or dipped within the desired thickness range below 1 µm. However, all aforementioned dielectrics have an order of magnitude lower dielectric strength than vapor deposited Parylene compositions [2], which made Parylene the primary candidate as a dielectric material in this system. In addition, the vapor deposition of Parylene could be controlled to selectively deposit in particular areas and deposited coatings were highly conformal around electrodes. Parylene

116

was also optically transparent lending itself well to optical measurement methods.

At least six compositions of Parylene exist, each with different end-use applications and properties. The most commonly implemented Parylene compositions as dielectric materials are Parylene-C and Parylene-N. Previously Parylene-C has been shown to perform satisfactory as a dielectric barrier in electrostatic comb-drive actuators in conducting media [4]; however, some electrolysis still occurred at the edges of electrodes apparently due to adhesion failure. Initially Parylene-C was fabricated within this work's primary electrical stimulation system; however, it was found that the deposited films were not of high quality and experienced breakdown at voltages less than 10 V_{ave}. This shifted fabrication towards Parylene-N for selection as the primary dielectric material. Parylene-C had a higher dielectric constant of ~3.1 compared with Parylene-N's 2.65, but Parylene-N's dielectric constant remains constant up to 1 MHz whereas Parylene-C's constant decreases with frequency [5]. Furthermore the dielectric strength of Parylene-N was slightly higher at 276 kV/mm compared with Parylene-C's dielectric strength of 220 kV/mm, for films measured at a thickness of 25.4 µm [5]. For thinner films any surface defects or non-uniform film areas promote breakdown below these magnitudes, as evidenced by breakdown of Parylene-C experienced under 10 V for 1 micron thick films. For the same Parylene-C deposition pressure Parylene-N deposits, or polymerizes, slower on the substrate surface thus producing films of higher quality promoting resistance to dielectric breakdown. Furthermore, the manufacturing recipe implemented was enhanced by lowering the deposition pressure from 75 mTorr to 35 mTorr, which increased deposition times but also produced films of higher quality that could withstand breakdown for the range of voltages applied. Lower pressure was used, as this decreased the quantity of in-chamber Parylene-N, thus a slower deposition rate would produce a higher quality film.

117

To prepare substrates for Parylene-N deposition, each substrate had PDMS elastomer poured on top. The elastomer had been previously mixed in a base:curing agent ratio of 10:1 and degassed under a vacuum. After curing of the elastomer, a scalpel was used to cut out a window in the PDMS, which exposed an area where selective deposition occurred. To promote adhesion of Parylene-N to the surface the substrate was immersed in a silane based adhesion promotion solution. The solution was composed of equal parts of IPA and DI water with a 0.5 % volume A-174 silane. Substrates were immersed in the solution for 30 minutes then allowed to air dry for 30 minutes, and afterwards were rinsed with IPA and DI water. Adhesion was important to ensure the Parylene-N did not delaminate during operation, and deposited uniformly over all surfaces. Various methods exist to promote adhesion, including a surface oxygen plasma treatment, a silane A-174 treatment, annealing the Parylene after deposition or a combination of these treatments [6]. Hassler *et al.* found that silane A-174 treatment alone provides the highest adhesion forces at chamber pressures between 20 and 80 mTorr.

The prepared substrates were then loaded into the chamber, in a configuration seen in Figure 4.4(A). Raw granular dimer was weighed and loaded into the system. The weight of initial dimer, the number of wafers loaded into the system, and the deposition pressure dictated the final thickness of the Parylene film. However, from run to run variations in Parylene-N thicknesses were still observed for similar manufacturing parameters. Parylene deposition began with the loaded dimer being heated until it sublimated in the vaporizer chamber. The vapor then moved into the pyrolysis chamber which further heated the gas and cleaved the Parylene into monomer form. The gaseous monomer then entered the deposition chamber where it simultaneously adsorbed and polymerized on the substrate's surface. Because a gaseous phase entered the deposition chamber, the deposition itself was highly conformal on all surfaces present. The deposition process itself occurred at pressures of 75 mTorr
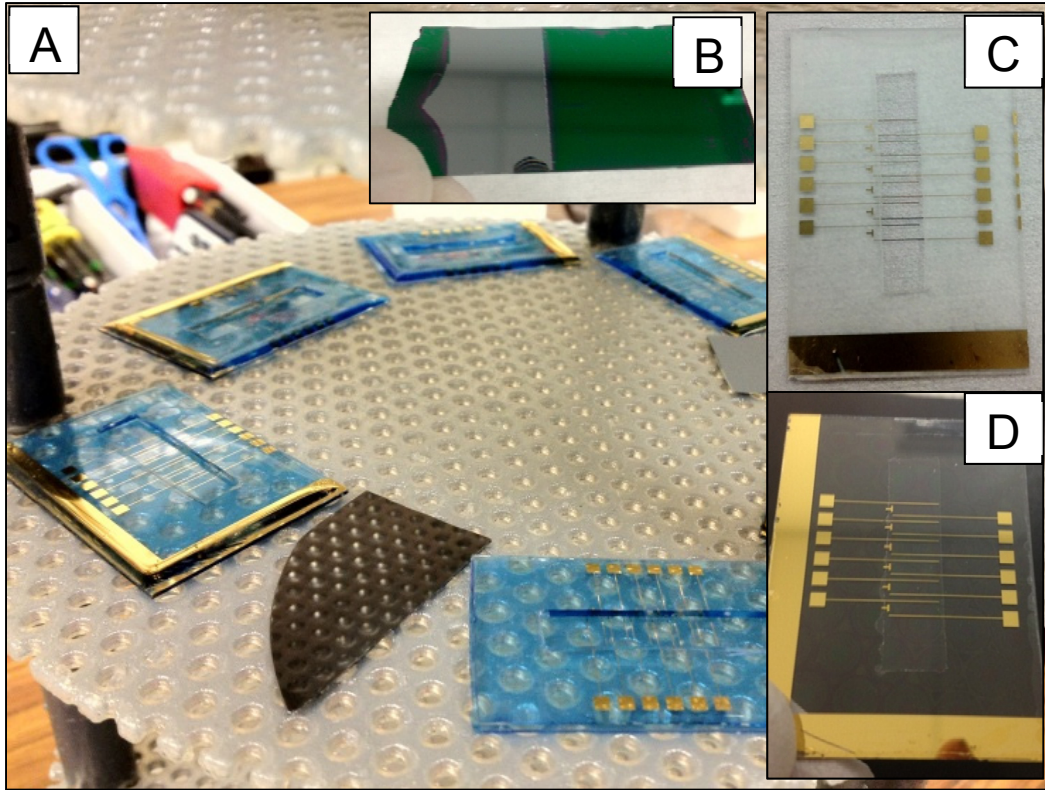
Figure 4.4: Selective deposition of Parylene-N (A) In-chamber chip arrangement (B) Silicon wafer used for spectral reflectance measurements of thickness (C) PDMS deposited on microchips for selective deposition of Parylene (D) As-deposited Parylene over the stimulating electrodes.

to 35 mTorr and at room temperature. Further details of the polymerization process can be found elsewhere [5, 7].

To determine the final deposited thickness of Parylene-N a clean silicon wafer was also placed in the deposition chamber. This wafer had Parylene-N deposited on it as well, as seen in Figure 4.4(B), and underwent spectral reflectance measurements to determine the Parylene-N thickness, as seen in Figure 4.5. Five measurements were taken using spectral reflectance and these measurements were averaged to provide the as-reported thickness. Additionally, thickness was also directly measured on the substrate surface itself using surface profilometry techniques to verify the range of spectral reflectance measurements, with a typical result shown in Figure 4.6. The roughness observed at the edge of the Parylene was indicative of the removal of the PDMS mask from the

wafer, with slight peeling. This was initially observed on the test electrode substrates, but was overcome by using a scalpel to gently cut the Parylene-N away from the PDMS mask. The thickness of the Parylene could have been measured in-chamber during deposition using a quartz crystal microbalance [8]; however, this equipment was not readily available.

A substrate directly out of the deposition chamber can be seen in Figure 4.4(C), noting the window cut out of the PDMS masking layer. Furthermore, note the cloudy discoloration of the Parylene coated PDMS. This cloudy discoloration prevents the vapor deposition of Parylene inside an already bonded microchip, which is a technique currently used to prevent biological analyte absorption into PDMS [9, 10]. This cloudy discoloration would prevent consistent *in-situ* photolithography of hydrogel components and optical hydrogel deformation measurements. The final substrate with Parylene-N coated electrodes can be seen in Figure 4.4(D), with an as-deposited Parylene-N area larger than the intended microchannel to bond with to ensure no contact between the electrolyte and electrodes.

The Parylene-N film was assessed to ensure the film was indeed closed and did not contain any major defects. To do so, a droplet of conductive electrolyte was place over each electrode and incubated for 15 min to allow electrolyte diffusion into any cavities, a technique developed by Rapp *et al.* [11]. The conductivity between the electrolyte droplet and the contact pad of that particular electrode was measured, with extremely high resistance (>10 MOhms) being characteristic of a closed film. Electrodes that registered low resistance were marked and left unused, or the entire microchip was discarded.
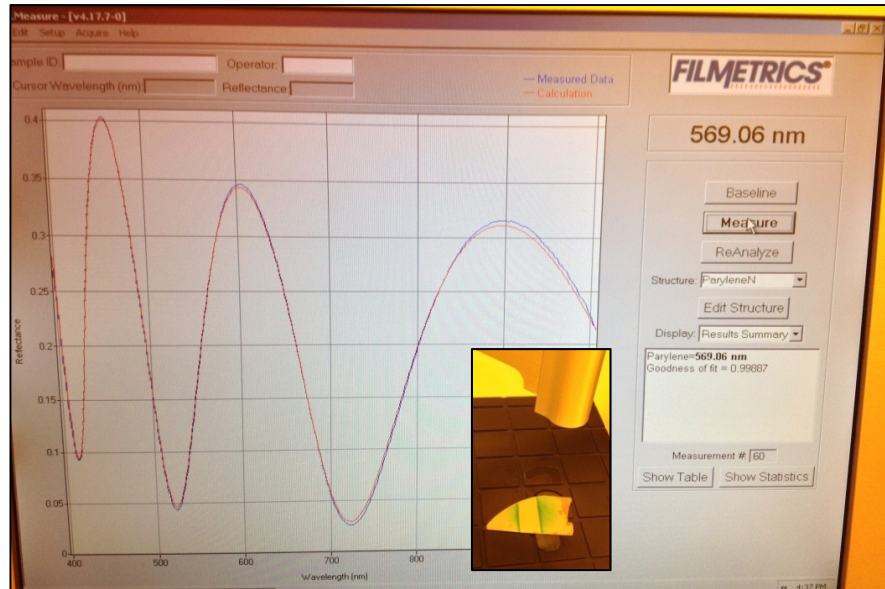
Figure 4.5: Typical spectral reflectance measurement to determine the Parylene-N thickness, showing a thickness of 569 nm. Five measurements per test wafer were taken and averaged to determine the thickness over the surface. The inset shows the wafer being measured.
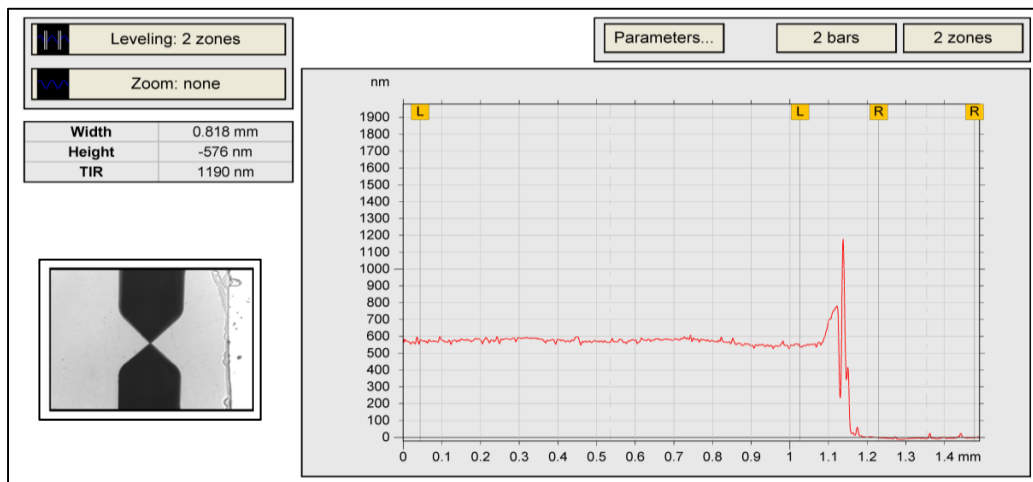
Figure 4.6: Surface profilometry of a Parylene surface to verify thickness, showing a thickness of 576 nm. Some surface roughness can be observed in the Parylene-N.

4.2.5 Soft Lithography of Microchannels

Soft lithography represents a series of stages to repeatedly produce elastomeric molds, out of which microchannels can be formed in combination with suitable substrates. This process included the fabrication of a molding master, preprocessing of the master, mixing and pouring of

121

the elastomer over the master, and curing and releasing the elastomer [12].

The molding master can be fabricated through various methods, most commonly available being negative photoresist processing [13], silicon wafer dry etching [14], or RP mold manufacturing. Both the negative photoresist mold, usually SU-8, and the silicon wafer require lithographic masks and processing. These two methods also require further developing or dry etching to fully define their features. Early in this work SU-8 molds were attempted, but the fabrication process was both immature and troubleshooting was very time consuming; thus, this molding technique was abandoned for alternative methods. RP mold manufacturing was employed, due to its ability to create the desired geometry in elastomer, robustness for repeated use, and both time- and cost-effectiveness. RP master molds were designed with the CAD software Pro/Engineer® and manufactured by the Mechanical Engineering Machine Shop. The master molds were manufactured with a glossy finish to reduce the feature's surface roughness, as significant roughness hindered repeatable bonding to substrates causing fluid leakage. After manufacturing master molds were prepared for elastomer curing by cleaning the mold and depositing a self-assembled monolayer. The molds were cleaned by immersion into a 2% solution of sodium hydroxide for 1-2 hours, and afterwards were thoroughly rinsed. This immersion process removed any acrylate residues left on the surface and also slightly improved surface finish. Four common master molds used within this work can be seen in Figure 4.7. The critical geometries of the master molds were verified through surface profilometry, with a typical cross section of the primary master mold shown in Figure 4.8. A self-assembled monolayer was deposited on the surface of the master molds through a process commonly known as silanization in a vacuum desiccator. This monolayer of silane helped to prevent curing between the elastomer and the master mold [15], making delamination easier and repeatable. This monolayer

122

also separated PDMS from the acrylic-based molds, as acrylates can inhibit the polymerization process. The compound used within this work was trichloro(1H,1H,2H,2H-perfluorooctyl)silane, but any similar compound that achieves the same goal would be acceptable.

The elastomer selected for use in soft lithography was PDMS. Potential alternatives to this elastomer exist, such as PMMA [16], polycarbonate [16], cyclic olefin copolymer (COC) [17]. However, PDMS provides various advantages that outweighed its drawbacks, including; easy fabrication and patterning through soft lithography, being optically transparent down to 240 nm [18], amenable to parallel fabrication, economical, and has a broad range of literature examining its properties and integration in microdevices. General drawbacks to employing PDMS would be adsorption of molecules from solution [10] and its inherent hydrophobicity [15]. However, these drawbacks do not affect the operation of hydrogel microactuators in their current configuration.
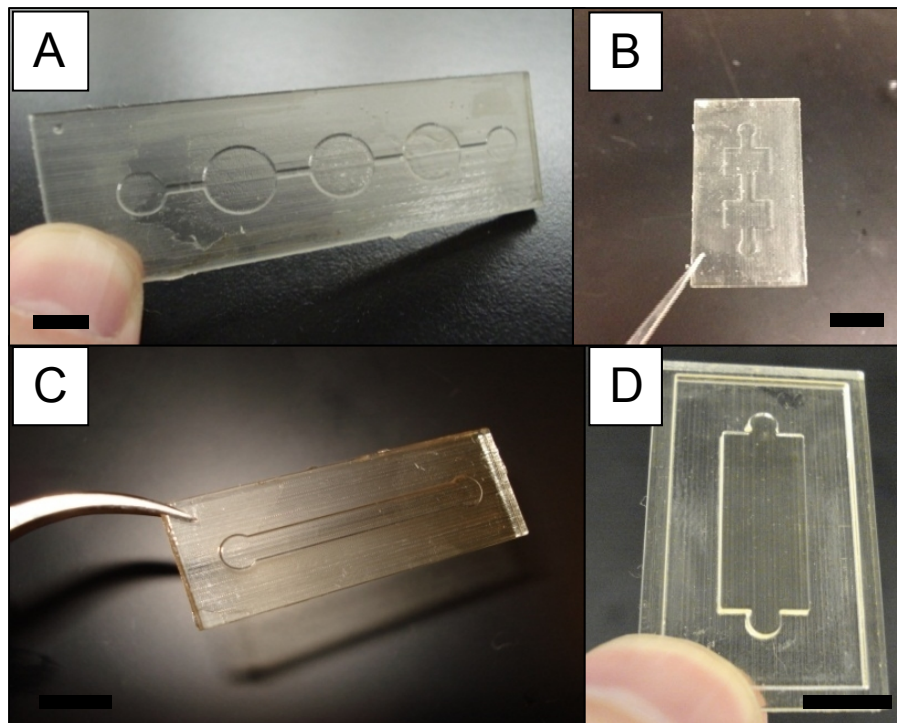
Figure 4.7: Rapid prototyped molds for soft lithography of PDMS for applications of (A) preliminary hydrogel photopolymerization (B) preliminary electrical stimulation (C) primary electrical stimulation (D) dynamic mechanical analysis. Scale bars represent 8mm.

To prepare PDMS for soft lithography a quantity of base agent was weighed and mixed with curing agent at a 10:1 weight ratio, respectively. This mixture was then degassed and poured over the master molds, ensuring uniform distribution of the elastomer over the molds. This was a common preparation procedure [12]. It's also important not to reintroduce bubbles into the PDMS during pouring, as any bubbles would alter the pathways of light through the PDMS making *in-situ* photolithography inconsistent and hampering optical measurement methods. Curing of the PDMS was performed at 80°C for 2 hours in a vacuum oven. Without proper cleaning of the acrylic-based master mold the curing process would be impeded, due to an acrylates' tendency to interrupt the cross-linking process. After curing, the elastomer was removed from the master mold, with four typical patterned elastomers shown in Figure 4.9. The mold primarily using within this work can be seen in Figure 4.9(C), which had a typical thickness above the microchannel of 1.29±0.23mm. This thickness varied due to the process of pouring PDMS over the mold, and its variation would slightly influence the exposure energy experienced by the precursor solution during photopolymerization. To retain a clean surface for further bonding processes, the elastomers were stored on a clean glass wafer.

4.2.6 Oxygen Plasma Irreversible Bonding

After manufacturing a patterned elastomer and performing Parylene-N coating of the electrode substrate, it was necessary to irreversibly bond the two materials together to create complete microchannels. Irreversible bonding of PDMS to glass has been shown to be repeatable through a short duration oxygen plasma exposure [19]. The oxygen plasma introduced polar silanol groups (Si-OH) on the PDMS surface replacing methyl groups (Si-CH3) [19]. When these polar groups were brought into contact with a glass surface the reaction produced strong covalent Si-O-Si bonds. These covalent bonds created an irreversible bond which resulted in failure of the PDMS when attempting to break the seal.

124
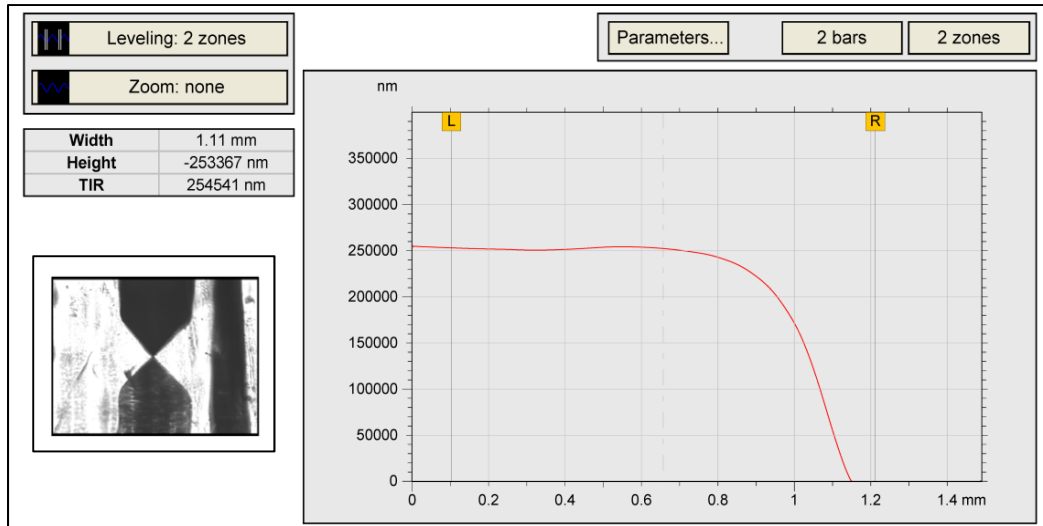
Figure 4.8: Surface profilometry of a rapid prototyped master mold to verify its features showing a height of 253 microns. This particular profile relates to Figure 4.7(C), which was used for the primary microchannels implemented for electrical actuation testing.
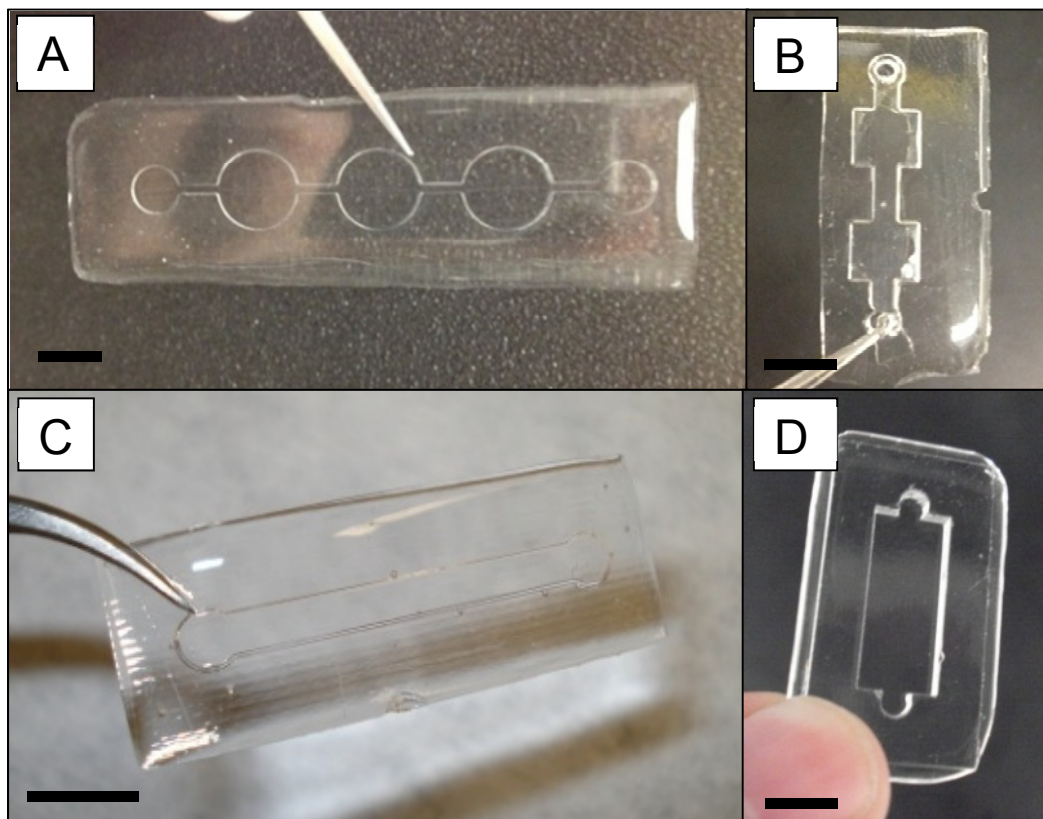
Figure 4.9: PDMS microchannel fabricated through soft lithography for (A) preliminary hydrogel photopolymerization (B) preliminary electrical stimulation (C) primary electrical stimulation (D) dynamic mechanical analysis. Scale bars represent 8 mm.

Oxygen plasma has also been shown to be an effective technique for dry etching of both Parylene-C [20] and Parylene-N [21]. This technique could be employed to decrease the thickness of Parylene after vapor deposition to enhance actuator performance, as a thinner layer reduces the electric field loss and lowers the system's critical AC actuation frequency. However, dielectric breakdown occurs first in the Parylene-N film's thinnest regions, and it has been shown that exposure to oxygen plasma can increase surface roughness causing uneven film thickness [22]. This technique was attempted to evaluate its applicability, but a higher surface roughness and dielectric breakdown at lower voltages was observed. To overcome this challenge, the PDMS that was cut out of the window for selective Parylene deposition was then placed over the Parylene to mask any exposure to oxygen plasma. Furthermore, irreversible bonding between Parylene and PDMS did not occur when using oxygen plasma, thus bonding between PDMS and glass did not occur until the edge of the Parylene is reached. It has been shown that Parylene can be bonded to PDMS using a combination of oxygen, nitrogen and sulfur hexafluoride gases [23]; however, the reported optimal recipe was attempted without successful results. Bonding at the PDMS-Parylene-Electrode interface was important because under electrical stimulation electrolysis and electrochemical reactions occurred at this interface. These electrochemical reactions created protons that diffused towards the hydrogel and caused drastic deswelling. Therefore, the interface of PDMS-Parylene-Electrodes was sealed with a thin layer of PDMS to inhibit these effects. The bulk PDMS microchannel would bond irreversibly to the thin layer of PDMS laid down over this interface, ensuring no electrolysis or electrochemical reactions occurred.

Systematic parametric studies have been previously performed to determine operational parameters for irreversible bonding in plasma enhanced chemical vapor deposition or inductively couple plasma reactive ion etcher [24]. These parameters provided an operational window to

126

apply to the accessible reactive ion etcher. A qualitative study of bond strength was performed and the final parameters employed were 27 W RF power, 250 mTorr chamber pressure, 80 sccm oxygen flow, with a 25 s exposure time. Higher RF power and prolonged exposure to oxygen plasma was observed to decrease bond strength causing leakage, which has been explained due to the formation of a brittle silica layer on the surface [24]. Patterned elastomer pieces and glass substrates placed within the reactive ion etcher can be seen in Figure 4.10.

Combining the substrates with the patterned elastomer pieces created complete microchannels of various configurations, as seen in Figure 4.11. The PDMS and glass surfaces should be brought into contact immediately or the surface radicals combine with ambient oxygen and the surface deactivates within hours. This surface activation can be prolonged by covering the surface with a polar solvent such as deionized water or isopropanol alcohol for quick alignment purposes, but IPA also swells PDMS thus it should be used sparingly. The microchannels shown in Figure 4.11 were used for (A) preliminary hydrogel fabrication to test fabrication conditions (B) preliminary electrical stimulation of hydrogels (C) primary electrical stimulation of hydrogel actuators with dielectric coated electrodes (D) secondary electrical stimulation of hydrogel actuators with bare Pt electrodes and under microchannel flow. These microchips were designed to process multiple samples within a single chip, and chip design evolved to ensure minimal microbubble trapping within microchannels during experimentation.

Figure 4.10: The reactive ion etching equipment exposed the surface of the glass substrates and patterned elastomers to oxygen plasma (plasma not shown). This induced silanol groups on the surfaces to form irreversible bonds when contacted together.
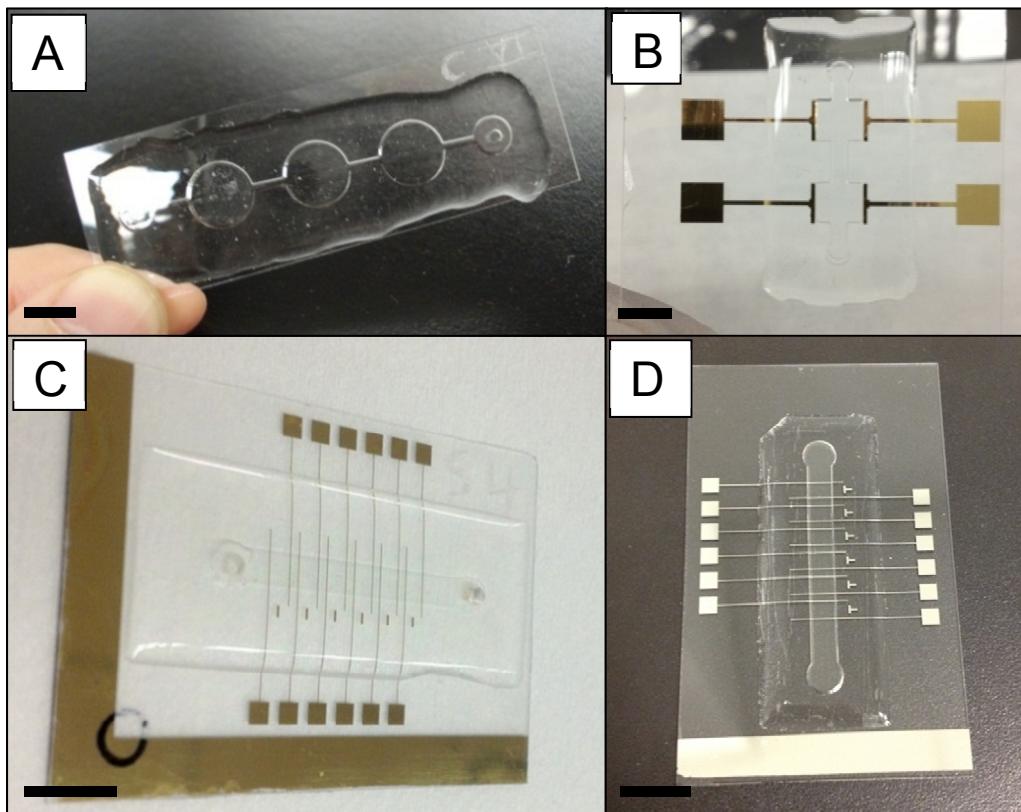
Figure 4.11: Final prototyped microfluidic chips for (A) preliminary hydrogel fabrication (B) preliminary electrical stimulation (C) final electrical stimulation with dielectric coated electrodes (D) secondary electrical stimulation without dielectric coated electrodes and microchannel flow. Scale bars represent 8 mm.

4.2.7 *In-situ* photolithography

Fabrication of both hydrogel microstructures and support posts was performed *in-situ* or in-place, positioned between electrodes, by employing photolithographic methods. The use of photolithographic methods to fabricate this specific composition of hydrogel was first demonstrated by Beebe *et al.* in 2000, for the development of chemically sensitive hydrogel microactuators [25].

Photolithography *in-situ* has several advantages, including: the potential for sequential fabrication of multiple structures, no handling of hydrogels post-fabrication was required, optical alignment of hydrogels between electrode components, altering lithography parameters to influence hydrogel material properties, and structures can be fabricated with varying geometries. This technique does have disadvantages though, which include; requirement for low aspect ratio features to ensure mechanical stability post-fabrication, slightly tapered cylindrical shapes are fabricated with positive side-walls observed, and for hydrogels the photopolymerization process must be performed in an oxygen free environment. To ensure mechanical stability, features were always fabricated with an aspect ratio less than 1 and hydrogels were fabricated as a jacket around support posts. To avoid oxygen inhibition during photopolymerization, the microchannel was entirely flushed with precursor. Because the length scale in small patterns is short, oxygen continually diffuses through the reaction zones and scavenges all formed radicals inhibiting polymerization processes [26]. This was effectively avoided in all samples by designing the inlet and outlet ports at least 2 mm from the polymerization locations.

Photomasks were employed to fabricate support posts and hydrogels with specific two dimensional geometries, with a photomask shown in Figure 4.12. The photomask was brought into contact with the surface of the microchannel, with only the thickness of the PDMS above the microchannel separating the hydrogel and the mask. Shown in Figure

4.12 (A) is an overview of the various geometries that could be employed for fabrication, (B) shows specific hydrogel geometries of varying diameter employed to fabricate cylindrical hydrogels (C) displays the constant-diameter support posts and (D) a test variation to encircle the hydrogel instead of employing a center post. It's important to note that the photomask must cover the length of the microchannel, and only the intended feature should be exposed to UV light. Exposing other areas would polymerize unwanted hydrogel features in the microchannels, and would degrade the Parylene-N covering the electrodes as Parylene-N experiences photodegregation under UV light exposure [27].

To stabilize the hydrogel structures, support posts were first photopolymerized *in-situ*. The posts were fabricated by mixing together isobornyl acrylate (IBA) monomer with tetraethylene glycol dimethacrylate (TEGDMA) crosslinker in a 9:1 weight ratio, together with 3 % weight Irgacure 651 photoinitiator. Alignment of these support posts between the electrodes was crucial, as these posts later served as alignment guides for hydrogel fabrication. Photopolymerization occurred when exposed to 365 nm UV light using the described photomask for 60 s at an intensity of 2.42 mW/cm^2. Cylindrical posts were always employed to ensure a uniform hydrogel jacket. These support posts also had an operational impact by reducing the volume of hydrogel material available for deformation and decreasing the maximum diffusion length scale required for steady state actuation.

Hydrogels employed within this work are HEMA copolymerized with AA, mixed in a 4:1 molar ratio. The photopolymerization process was initiated by Irgacure 651 photoinitiator and the crosslinking was performed by a 2% weight ethylene glycol dimethacrylate (EGDMA). The initial chemical structure of the monomer components and crosslinker can be seen in Figure 4.13, which also displays the final polymer structure after photopolymerization. Final fabrication parameters were dependent on the desired hydrogel mechanical properties. Alignment of the hydrogel

130

between electrodes was performed with both alignment markers found on the glass substrates and by ensuring the support posts were in the center of the circular mask features. The side view of an as-fabricated hydrogel that was photopolymerized and removed from the microchannel can be seen in Figure 4.14.
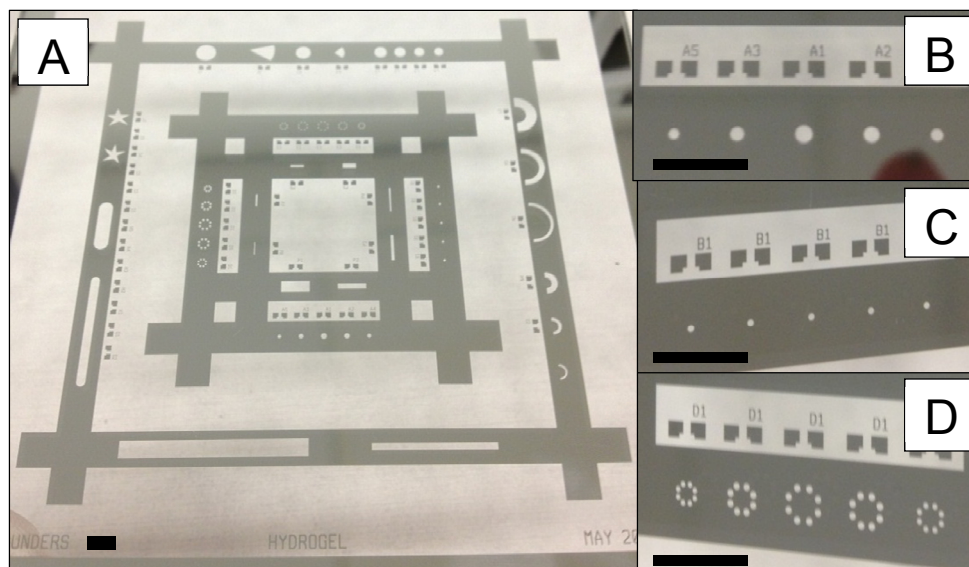
Figure 4.12: Photomask used for in-lab photolithography (A) overview of features available (B) various circular features for fabricating cylindrical hydrogels (C) multiple features for fabricating structural posts. (D) Alternative designs for structural posts. Scale bars represent 5 mm.
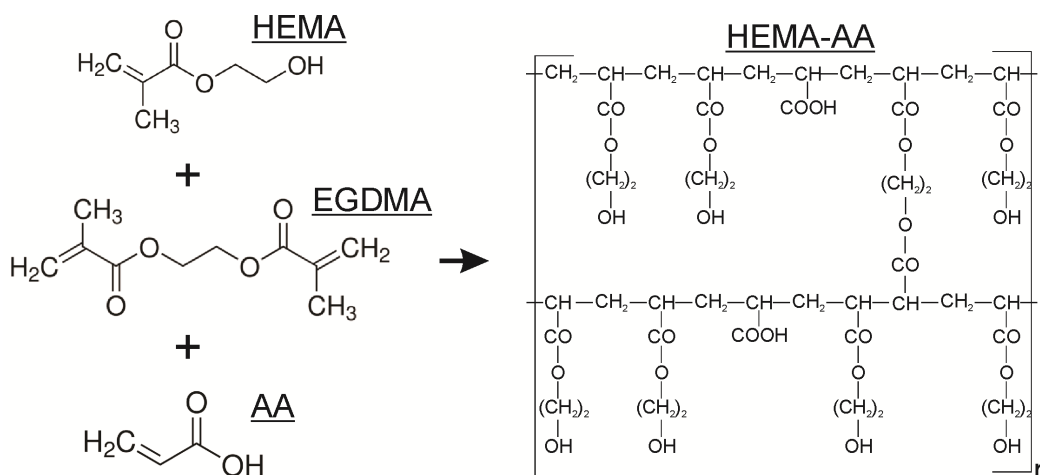
Figure 4.13: Chemical structure of monomer and crosslinker components, with the final hydrogel structure after photopolymerization. Precursor components include HEMA and AA monomers with EGDMA crosslinker, employing an Irgacure 651 photoinitiator.
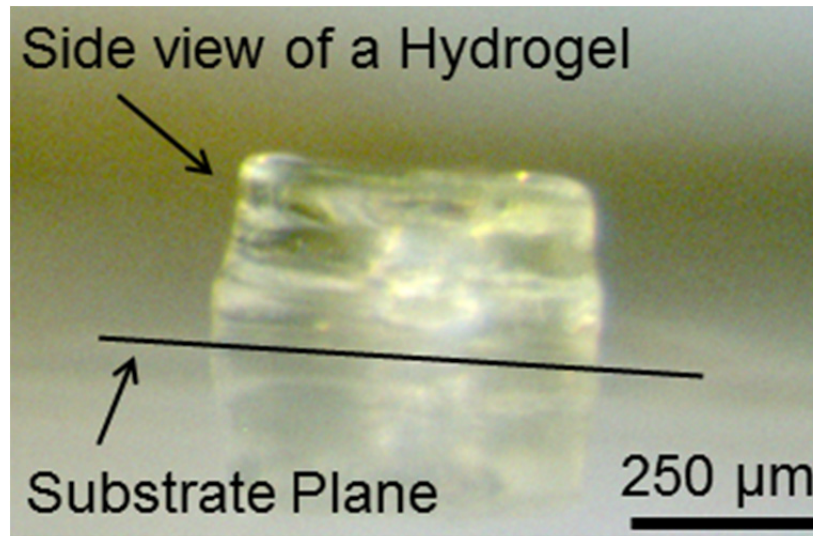
Figure 4.14: Side view of a slightly tapered hydrogel photopolymerized *in-situ* and exposed by removing the surrounding microchannel. The hydrogel shown was in its as-fabricated state, before any swelling due to electrolyte or electric fields.

4.2.8 Fabrication Defects affecting Performance

During the manufacturing process several microfabrication challenges were encountered that hindered the completion of a full manufacturing cycle, or necessitated alternative fabrication techniques. This section outlines these challenges, and the steps that were taken to mitigate their impact on electrical hydrogel microactuator performance.

Common microfabrication challenges experienced were: defects in the pattered electrodes, flaws in the deposited Parylene-N layer, inadequate sealing at the PDMS-Parylene-electrode interface, misalignment between the hydrogel and the structural support posts, and imperfections in the hydrogel jacket geometries. While other microfabrication challenges arose, the aforementioned challenges required continuous attention to enable a complete manufacturing cycle with hydrogels adequate for testing.

Defects in the patterned electrodes were one of the first challenges experienced. Typical examples discontinuous electrodes or degraded contact pads can be seen in Figure 4.15. These defects would not allow application of the electric field, and were not apparent until after lift-off of the sputtered electrodes was performed. This occurred due to inadequate

exposure of the positive photoresist, which resulted in the photoresist not being evenly removed from the wafer during development. To rectify this, slightly longer exposure and development times were employed to ensure complete exposure and development, respectively, of the positive photoresist.
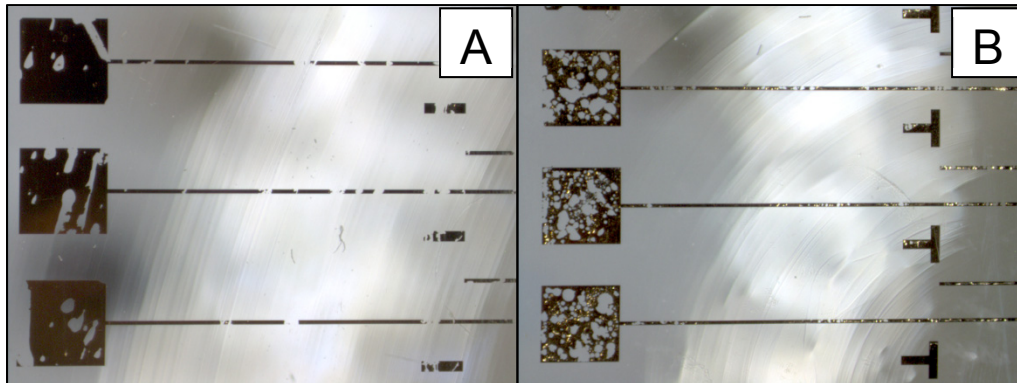
Figure 4.15: Defects in the pattered electrodes showing (A) non-continuous electrodes (B) degraded contact pads. The electrode widths are 100 μm.

Flaws in the vapor deposited Parylene-N dielectric film were also a major challenge that required considerable attention to rectify. Initially these flaws manifested through a non-uniformly deposited film, which can be seen in Figure 4.16(A), with different colors indicative of different film thicknesses. A uniform thickness dielectric layer over the electrodes was needed to both understand the operational principles of the system, and correlate thickness to system performance. This particular defect was a result of how the substrate was processed after immersion in the adhesion promotion solution. After soaking in adhesion promotion solution the substrate was immersed in isopropanol (IPA) and dried with a nitrogen gun, but sometimes a film of residues from the IPA remained on the surface which hindered the Parylene's surface polymerization process. To remedy this, after IPA the wafer was immersed in deionized water for 10 seconds and dried with a nitrogen gun. This was a deviation from the manufacturer's process recommendations and published literature, but resulted in uniform film deposition. However, even with a uniform film, location specific defects in the film occurred which resulted in dielectric

breakdown at voltages lower than desired for optimum operational performance. Four examples of these defects can be seen in Figure 4.16(B1-B4), which shows scratching of the electrodes (B1) and spots on the electrode surface (B2-B4). Scratching came from substrate processing after immersion in the adhesion promotion solution, where cleanroom wipes were placed between substrates for transportation. While a relatively gentle scratch, as it didn't scratch the electrodes themselves, it was still enough to alter the monolayer on the electrode's surface and thus disturb Parylene deposition. It was determined that the spot-defects on the electrode's surface were a result of two effects: fine particles being left on the surface after lift-off processing and outgassing of oils in the tape initially used for selective deposition of Parylene. The fine metal particles left after lift-off were removed by further sonication in a deionized water bath. The outgassing of oils was addressed by completely changing the masking material for selective deposition to PDMS (discussed earlier). PDMS does not outgas under vacuum, and could be removed without disturbing the deposited Parylene layer. An electrode that was free from surface defects can be seen in Figure 4.16(B5).

Once electrical testing of hydrogels started to occur, it was observed that an additional flaw in the manufacturing process existed. This flaw focused on the PDMS-Parylene-electrode interface. Since PDMS does not irreversibly bond to Parylene, electrolyte could diffuse towards this interface in between the PDMS and Parylene-N. When the electrolyte contacted an electrode that was under an applied electric field two responses occurred at the electrodes, electrochemical reactions and electrolyte electrolysis. The effect of electrochemical reactions can be seen in Figure 4.17(A1-A2), where a hydrogel experiencing electrical actuation towards the anode (A1) was chemically deswollen due to protons generated at the anode diffusing towards the hydrogel (A2). The protons combine with carboxyl groups on the hydrogel's backbone
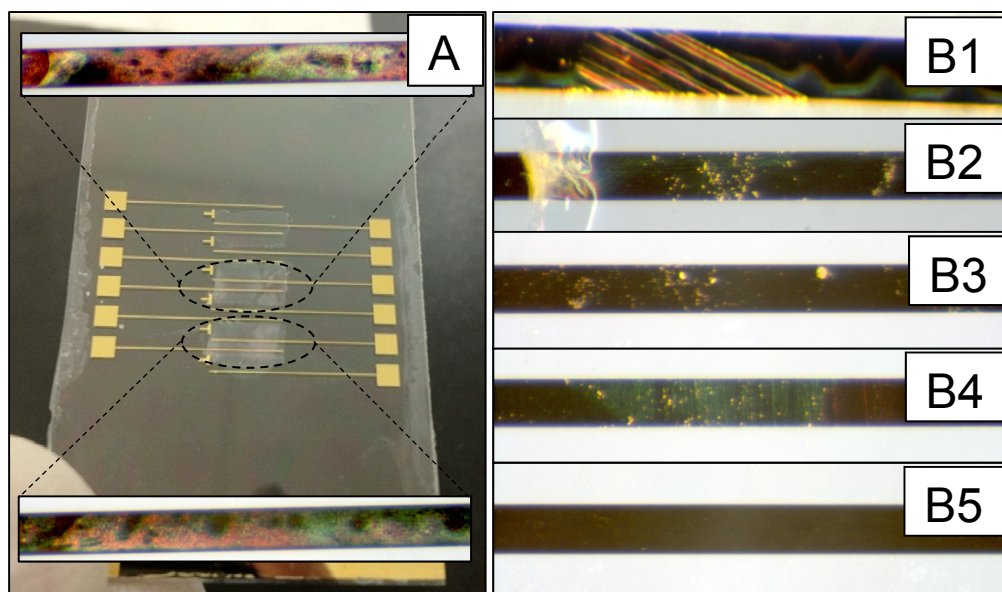
Figure 4.16: Flaws in the vapor deposited Parylene-N film showing (A) cloudy Parylene (B1) scratches in the Parylene film (B2-B4) surface defects in the film over electrodes (B5) flawless Parylene film. Electrode widths are 100 µm.

causing the hydrogel to become electrostatically neutral, thus mobile ions were expelled and the hydrogel was unable to response to electrical fields. Electrolysis was detrimental through two processes, shown in Figure 4.17(B), direct bubble generation (B1) displacing electrolyte and blocking the applied electric field, and by gas diffusing under the Parylene layer over the electrodes (B2) causing an air gap which has a lower dielectric permittivity than the Parylene layer, and thus caused increased electric field loss. To solve these problems the PDMS-Parylene-electrode interface had to be sealed. Sealing was performed by applying a thin layer of uncured PDMS with a Q-tip around the edge of the Parylene layer, before irreversible bonding between the substrate and elastomer had occurred. The thin layer was cured in an oven at a temperature of 80°C, much lower than the Parylene-N melting temperature of 410°C thus it remained unaffected. Irreversible bonding was then performed with the original recipe; however, the new interface created was only between PDMS and Parylene, thus electrolyte could not contact electrodes.
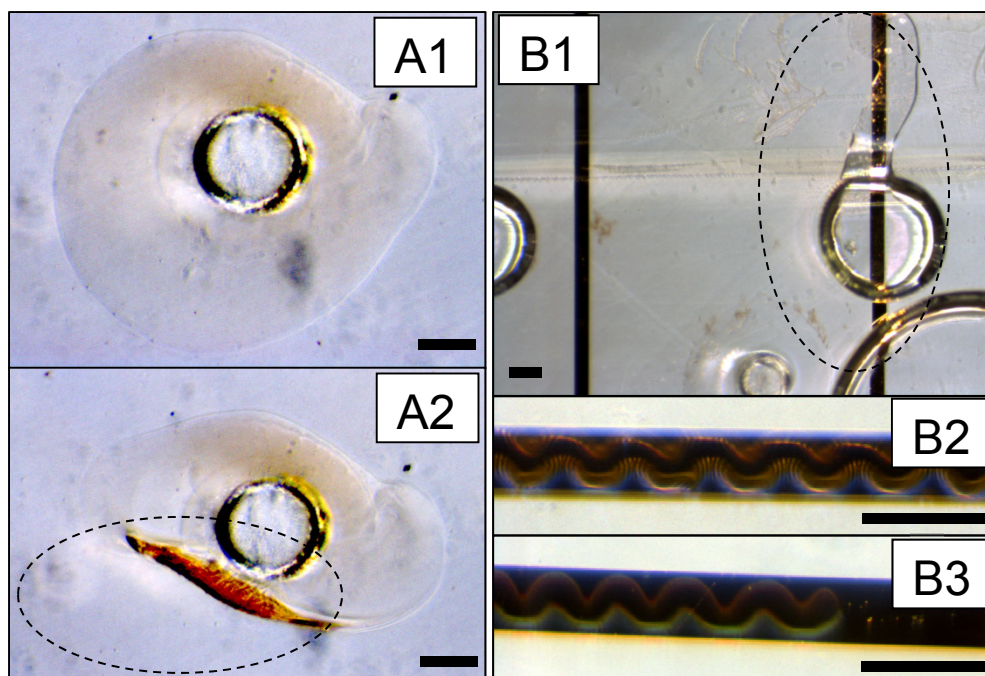
Figure 4.17: Inadequate sealing of the Parylene-Electrode-PDMS causing (A1/A2) hydrogen generation and diffusion towards hydrogel inducing deswelling (B1) electrolysis triggering bubble generation through to the microchannel (B2/B3) diffusion of gaseous species under Parylene, degrading actuator performance. Scale bars represent 200 μm.

Photolithographic patterning of hydrogels required alignment of the hydrogel around structural support posts. Periodically drastic misalignments would occur between the hydrogel and support posts, as seen in Figure 4.18. The misaligned hydrogels could be electrically stimulated to test manufacturing quality, but none of the samples could be rigorously investigated. Thus it was important to ensure adequate alignment, preferentially with posts in the center of the hydrogel or along the symmetry plane perpendicular to the electrodes. Alignment markers existed on the substrate deposited during electrode deposition; however, these markers were used as a guide to support post patterning and if the support post was initially misaligned the hydrogel would not benefit from these markers. Additionally, no alignment markers existed to align the microchannels with the substrate, thus hydrogels could be fabricated too close microchannel walls. To overcome these design limitations significant experience was obtained with photolithography system aligning hydrogels

with posts. Preliminary methods used just visual alignment, but more advanced alignment methods were introduced that employed an optical microscope to ensure the post was aligned in the center of the hydrogel mask feature prior to photolithography. This produced adequate alignment for testing, but could be further improved. The most significant alignment improvements would come from proper alignment between the substrate and microchannels during bonding. This would allow alignment markers to be employed for both x-y positioning of the posts, which would then transfer over to the hydrogels as well. Alignment would become more important as hydrogel size is deceased, and alignment tolerances become smaller.

Perhaps the most important component of the system was the hydrogel itself, thus even with a fully functioning manufacturing process the hydrogel must be defect-free to be tested reliably. However, occasionally hydrogels were fabricated with defects in their structures, as seen in Figure 4.19(A). This could generally be controlled by ensuring the photolithography mask and surface of the PDMS was properly cleaned prior to lithography, and confirming no microbubbles were present in the microchannel of PDMS during polymerization. In addition, the fabricated hydrogel must be able to withstand the pressures that will be applied to it during chemical equilibrium and electrical actuation. Hydrogels with mechanical properties too low will rupture under the applied pressure, as seen in Figure 4.19(B). Thus it was important to have a reliable measure of how the fabrication parameters affected the hydrogel's mechanical properties. The primary hydrogel composition employed within the electrical actuation characterization portion of this work was determined after assessing its ability to withstand the applied osmotic pressures. This was an important preliminary assessment, as hydrogels with mechanical stiffness too high would not deform significantly but with strength too low would rupture under the applied load.
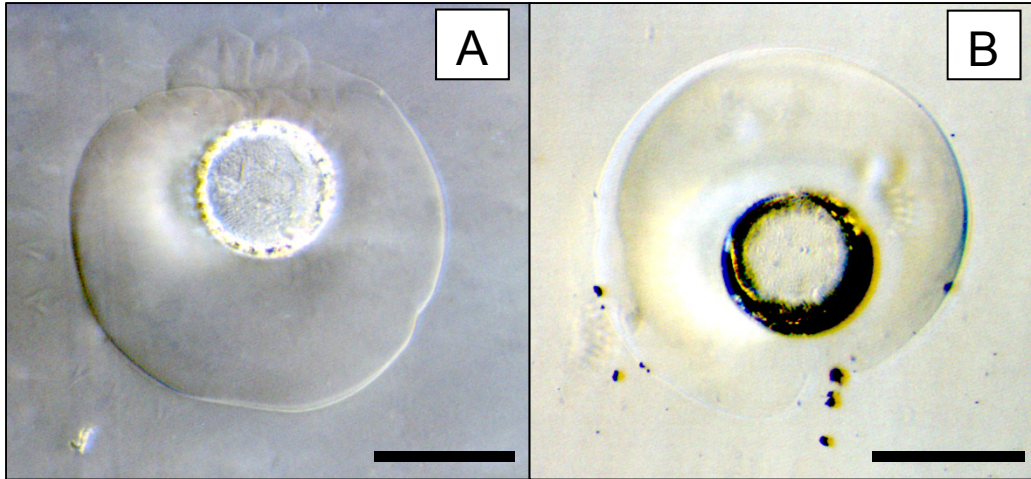
Figure 4.18: Photolithographic misalignment between structural support posts and the hydrogels jackets around those posts. (A) significant misalignment (B) slightly misaligned hydrogel. Scale bars represent 400 μm.
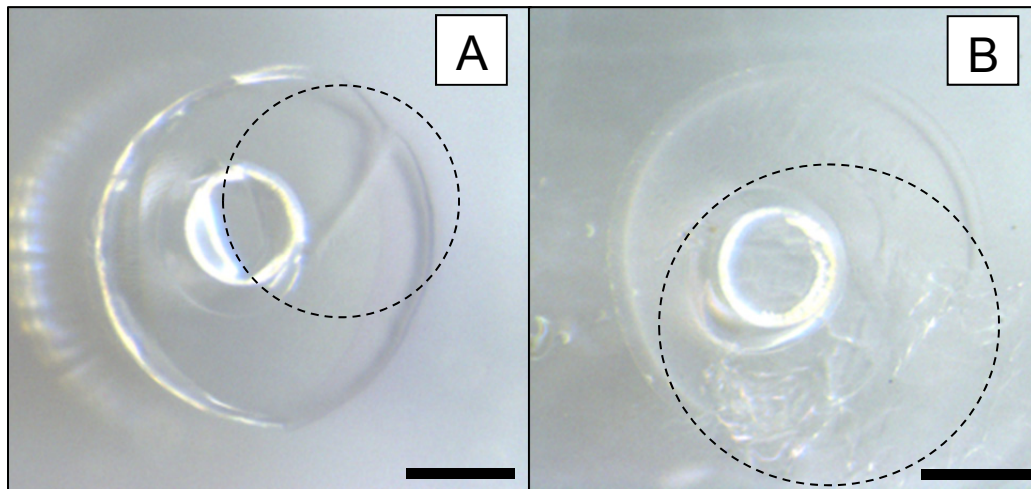
Figure 4.19: Hydrogel microfabrication defects showing (A) flaws in the structures (B) rupture due to inadequate mechanical stiffness. Scale bars represent 400 μm.

4.2.9 Post-testing Hydrogel Storage

Long-term storage of the hydrogel samples was undertaken to preserve their integrity after fabrication or for further testing. Hydrogels are a hydrated polymer, and thus leaving them exposed to air for any significant duration of time would allow solvent evaporation and dehydration. After hydrogel fabrication the microchannels were flushed with deionized water, and the microfluidic chip was placed in a mask holder full of deionized water, as seen in Figure 4.20. The container was

continually restocked with deionized water every couple of weeks to ensure water was always covering the microfluidic chips. Hydrogels have been tested up to a month after fabrication, with no apparent degradation in their performance. Before testing stored hydrogel samples, the microfluidic chips were flushed with the desired electrolyte to start the chemical equilibration process.

Figure 4.20: Multiple containers used for long-term storage of microchips containing hydrogels within deionized water. Inset (A) shows six microchips in deionized water.

4.2.10 Hydrogel's for DMA & SEM Microscopy

Macroscale hydrogels were fabricated for dynamic mechanical analysis (DMA) and subsequent structural morphology characterization under scanning electron microscopy (SEM). The fabrication procedure followed had aspects similar to that outlined in Section 4.2, such as using soft lithography for mold generation and photolithography to polymerize the hydrogel. The manufacturing was simplified by only needing these two major fabrication processes, which afforded a high throughput of samples.

Rapid prototyped molds, seen in Figure 4.7(D), were fabricated for soft lithography which produced the PDMS mold see in Figure 4.9(D). These PDMS molds were reversibly bonded to a substrate, and provided a chamber for hydrogel photopolymerization. The substrate was a glass

slide that had PDMS spin-coated and cured on top. It was found that the PDMS reversibly bonded to the PDMS better than glass, thus no precursor leakage occurred. The fabricated hydrogels would also delaminate easier from the PDMS than the glass. Using a glass substrate required forced delamination, which introduced cracks into the hydrogel and thus samples were not acceptable for testing. Hydrogel photopolymerization occurred with the same process as outlined in Section 4.2.7, through variations in the exposure time, light intensity, and hydrogel composition.

After polymerization, the hydrogels were immersed in methanol for 1 hour which removed any unpolymerized precursor mixture. The hydrogels were then immersed in 0.5 M KOH, and given a minimum 72 hours to reach equilibrium. After DMA testing at the first electrolyte concentration the hydrogels were then immersed in 0.05 M KOH, and given another 72 hours minimum to reach equilibrium. The equilibrium sample container had a volume of 25 mL and the maximum hydrogel volume, based off measured samples, was 1.56 mL; thus ensuring a consistent concentration was present during equalization.

The as-fabricated hydrogels have dimensions of 1 mm in height, a width of 8 mm, and a length of 20 mm. After equilibration the hydrogels would swell to some degree, depending on the electrolyte concentration and fabrication conditions. An example of a swollen hydrogel can be seen in Figure 4.21(A). The swollen hydrogels were too large for the DMA system, and had their width and length cut to an appropriate size. The width of the as-tested samples was between 7-8 mm, in order to ensure no grip effects were introduced into the measurement. An example of a hydrogel in the DMA can be seen in Figure 4.21(B). After dynamic mechanical measurements were performed, the samples were weighted to determine their weight degree of swelling.

To examine the hydrogel's morphology samples were observed using scanning electron microscopy. To prepare samples for the vacuum

140

system they were flash frozen in liquid nitrogen and then vacuum freeze-dried to sublimate any moisture, in a process similar to that in reference [28]. Dry samples were measured for weight degree of swelling measurements before mounting them on SEM sample stages. Samples mounted on stages can be seen in Figure 4.22, which show the hydrogel cross-sections for observation sputtered with gold to ensure conductivity.
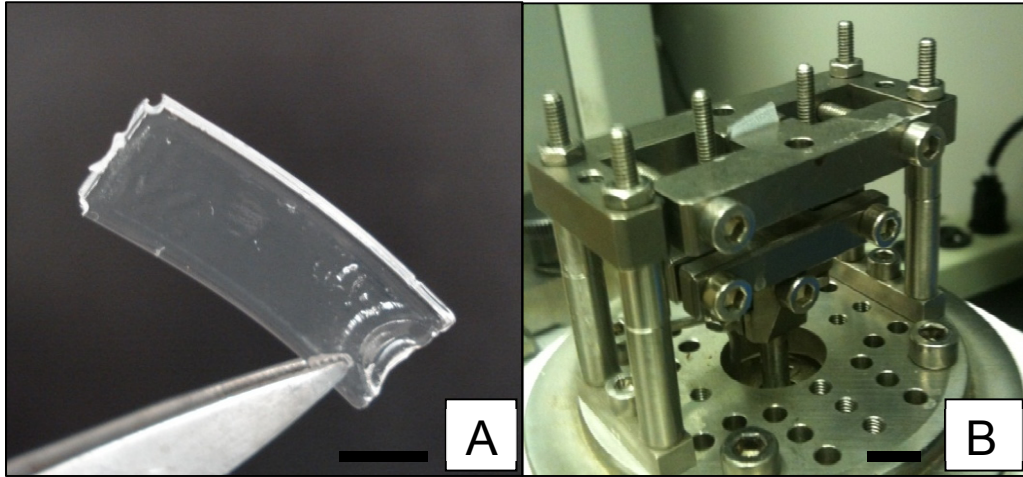
Figure 4.21: (A) Hydrogels swollen in electrolyte solution for dynamic mechanical analysis, sample shown after equalization and before cutting to testing size. (B) Hydrogel placed within the dynamic mechanical analyzer, showing the grips holding the hydrogel and the movable shaft applying cyclical deformation. Scale bars represent 8 mm.

Figure 4.22: Flash-frozen and freeze-dried hydrogel samples that were fractured to exposure their porous cross-sections. An ~10 nm thick layer of gold was sputtered on top to ensure conductivity.

4.3 UV Lithography System Development

A lithography system was developed to perform photopolymerization of polymers upon exposure to ultraviolet light. This system was developed as an alternative to systems at the University of Alberta NanoFab. Its implementation had two distinct advantages; variable intensity of the light source and continued accessibility. The variable intensity light source was important, because modifying the intensity of light also modified the mechanical properties of the hydrogels. It was necessary to characterize these properties to determine an intensity that was appropriate for the desired actuation application of the hydrogels. Furthermore, the ability to have constant access to a photolithography station allowed the research to progress continuously, without having other users book the station or generating large user fees at the NanoFab. To create a robust system several components had to be procured or manufactured. In addition, the intensity of the light had to be calibrated to ensure consistent photolithography, and this had to be measured at the location of the sample.

4.3.1 UV Lithography System Set-up

The developed photolithography system was a combination of purchased and manufactured components. For generation of the UV light an EXFO Acticure 4000 was procured that had the ability to generate up to 2.5 W/cm^2 of light with exposure times from 0.2 to 999 seconds. Light was transferred from the source to the sample through a fiber-optic light-guide that had its position fixed above a sample. To hold the photomask and perform microalignments of the photomask with the sample, a photomask aligner was manufactured with help from the Mechanical Engineering Machine Shop. This aligner incorporated three micropositioners to provide three axis movements for alignment and leveling of the aligner itself.

Alignment of the photomask with the sample underneath was performed through the aid of the optical microscope attached to the probing station. The optical microscope could swing on a boom-arm over the targeted feature, aiding in alignment together with the positioning of the stage. After alignment was achieved the probing station's stage could be lowered to bring the photomask in contact with the surface of the sample. Then the optical microscope was swung away, and the light-guide was placed over the desired feature, as seen in Figure 4.23.
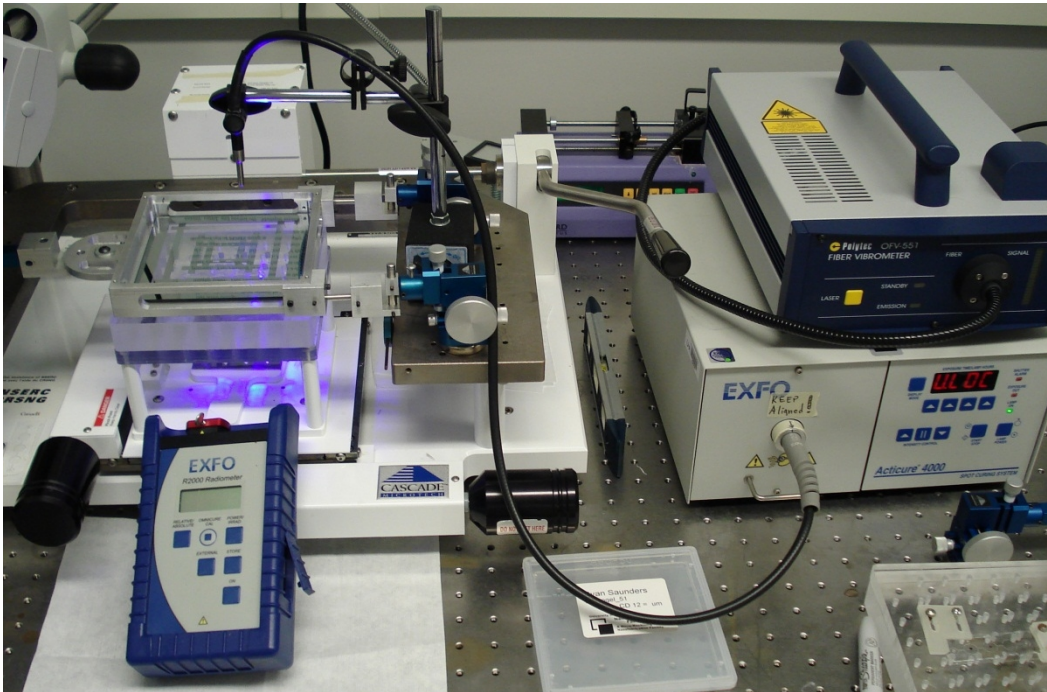
Figure 4.23: UV Photolithography system including photomask aligner, light-guide, UV light source, radiometer, and x-y positioning stage.

4.3.2 UV Intensity Calibration

Calibration of the photolithography system was performed to provide consistent intensity of UV light, as measured at the sample. It was necessary to recalibrate the system for each light-bulb used within the system, as they burnt out due to use or defects.

To begin calibration, the photolithography system was set-up to mimic the polymerization of hydrogel samples. Using a handheld radiometer the intensity of UV light at the tip of the light-guide was measured and recorded. This measurement would be used when

performing day-to-day photolithography. The ABM digital intensity meter was set to record the intensity at 365 nm wavelength, the wavelength that the hydrogel's photoinitiator activates at. The meter was then placed in the center of the positioning stage, as seen in Figure 4.24(A). The light-guide was fixed above the meter, and it's height above the meter was measured with a caliper, as seen in Figure 4.24(B). Since the light intensity at the sample would vary depending on the height of the light-guide above, for day-to-day photolithography this distance was held constant at the calibrated distance. The UV light source was then turned on, and the location of minimum intensity was found by moving the meter fixed to the stage below, seen in Figure 4.24(C). This minimum intensity location was the center of the intensity profile, and set as the origin. The meter was then systematically moved to increase the intensity, and the resulting displacement of the stage was measured with a caliper, as seen in Figure 4.24(D).

The intensity profiles can be seen in Figure 4.25, for three difference calibrations performed. The first calibration series was used for preliminary hydrogel fabrications to test capabilities, and to fabricate hydrogel samples for dynamic mechanical analysis. The second calibration series was performed after the initial bulb burnt out, and was primarily used for preliminary electrical stimulation experiments; however, this bulb had a defect and was only used for ~40 hours. The third and final calibration series was used for the primary electrical actuation testing. It can be seen that the profiles show a distinct minimum plateau at a certain distance, then the intensity increases dramatically. Hydrogel's fabricated for dynamic mechanical analysis were slightly larger than the plateau region when fabricated, introducing an anisotropy over the sample. However, their lengths and widths were cut before placing them within the DMA system effectively eliminating this anisotropy before any measurements were taken. Hydrogels fabricated for electrical actuation or characterization were a maximum 1 mm in diameter, and thus were

144

always in the plateaued intensity region. The second and third calibrations were performed to ensure at-sample intensities were consistent with the first calibration, thus the tip intensity had to be modified to achieve this. While in this work only one hydrogel sample was photopolymerized at a time, the plateau region was wide enough to facilitate fabrication of an array of hydrogels closely spaced together.
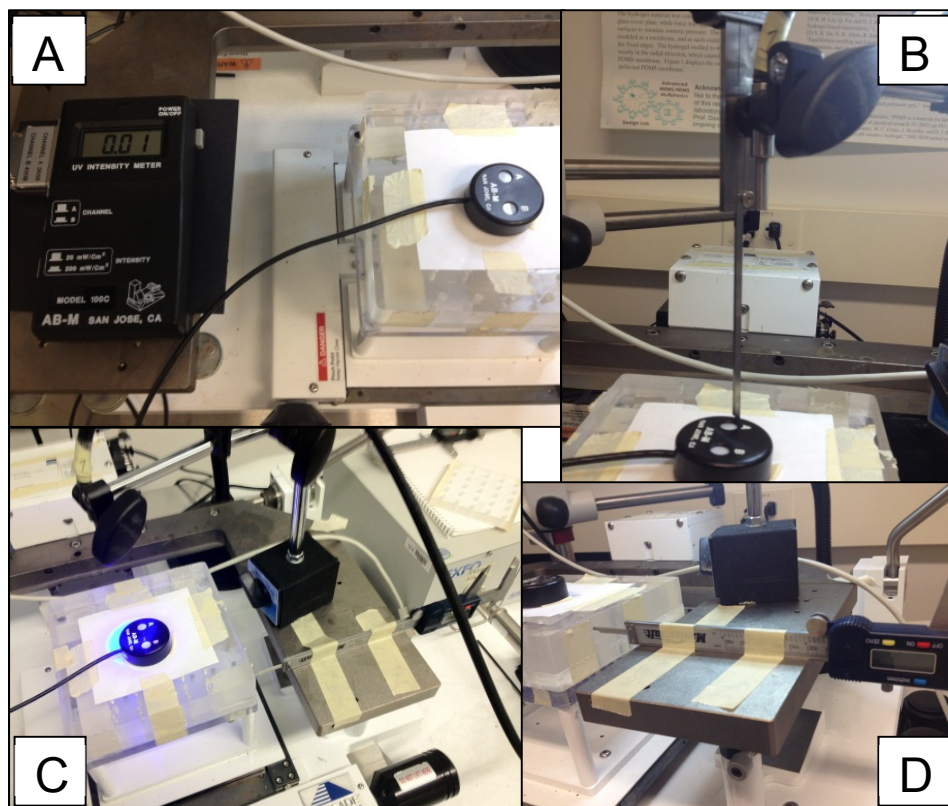
Figure 4.24: Intensity calibration of the UV photolithography system (A) obtaining a baseline of intensity (B) measuring the tip to sample distance (C) determining the origin of the intensity profile (D) distance measurements from the origin.
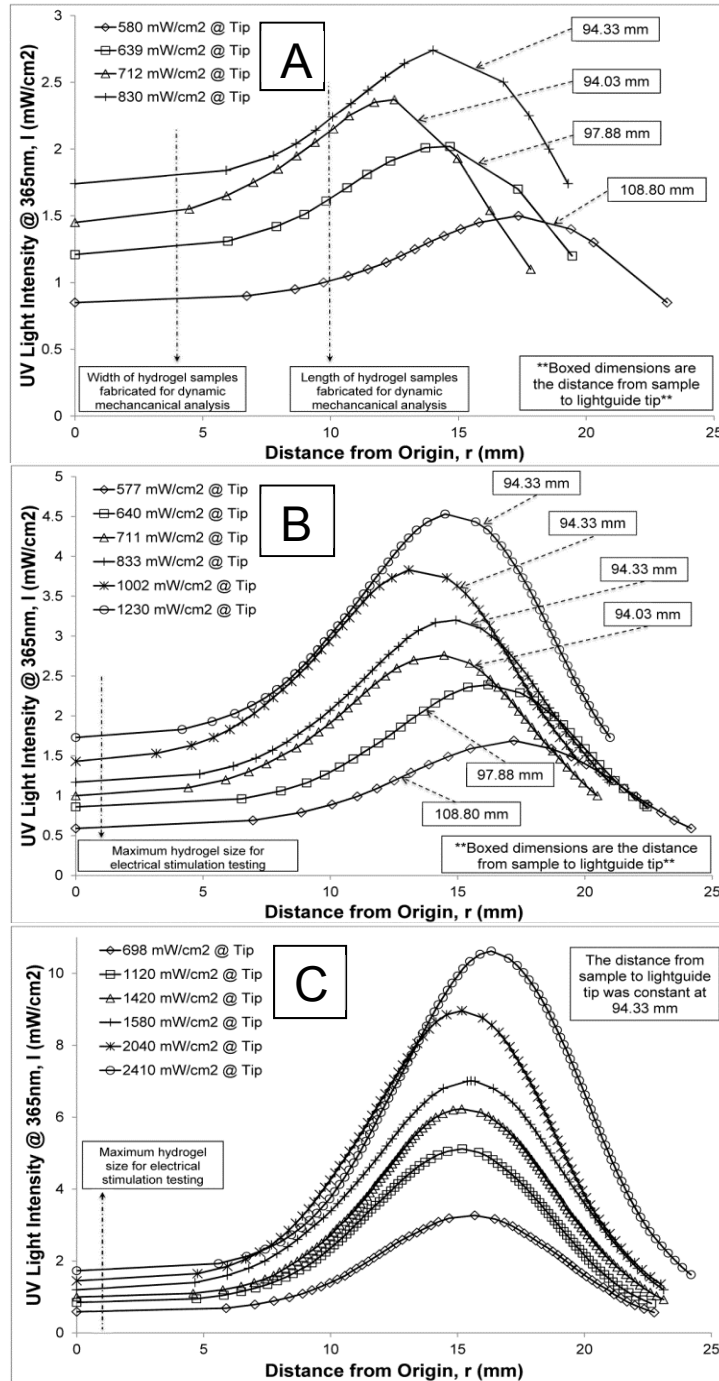
Figure 4.25: Intensity profiles of UV light generated by light-guide for (A) Round 1 used for dynamic mechanical measurements (B) Round 2 for preliminary electrical actuation testing (C) Round 3 for primary electrical actuation testing.

146

4.4　Hydrogel Electrical Testing

4.4.1　Electrical Equipment and Methods

Stimulation of electrical hydrogel microactuators required the procurement of a system of electrical equipment. The entire system can be seen in Figure 4.26(A), which included: a DC power supply, AC frequency generator, amplifier, oscilloscope, probes, syringe pump, and an optical microscope for measurements. The DC power supply, AC power supply and amplifier were set-up such that an alternating square wave with a DC offset could be applied across a microchip's electrodes, with an electrical circuit as outlined in Figure 4.27 incorporating an oscilloscope to monitor the electrical signal.

The DC power supply had a range up to 60 V_{DC}, while the AC frequency generator had a maximum 10 V_{pk-pk} with frequencies up to 10 MHz. The amplifier had a 5x gain, with a maximum 100 kHz and output voltage of 42 V. Combining these elements together allowed a square wave to be applied with a specific duty cycle. The largest magnitude electrical signal implemented for testing was a 40 V_{pk-pk} square wave with a 20 V_{DC} offset operating at 100 kHz and 80 % duty cycle. This was applied over electrodes spaced 2 mm for a peak electric field of 20 kV/m. Modification of the duty cycle allowed application of a varying electrical signal to the hydrogel, thus controlling the swelling-deswelling system. Examples of square waves implemented for electrical actuation at 20 % and 80 % duty cycle can be seen in Figure 4.26(B) and Figure 4.26(C), respectively. The square wave was not perfectly square at 100 kHz, displaying saw-tooth characteristics, but as frequency was decreased this effect was minimized. At 80 % duty cycle, this saw-tooth characteristic would decrease the signal residence time at 0V, necessary to completely overcome electrostatic shielding. This could slightly decrease the applied electric field; however, this effect would be minimized when the experimental system's characteristic frequency was well below 100 kHz.
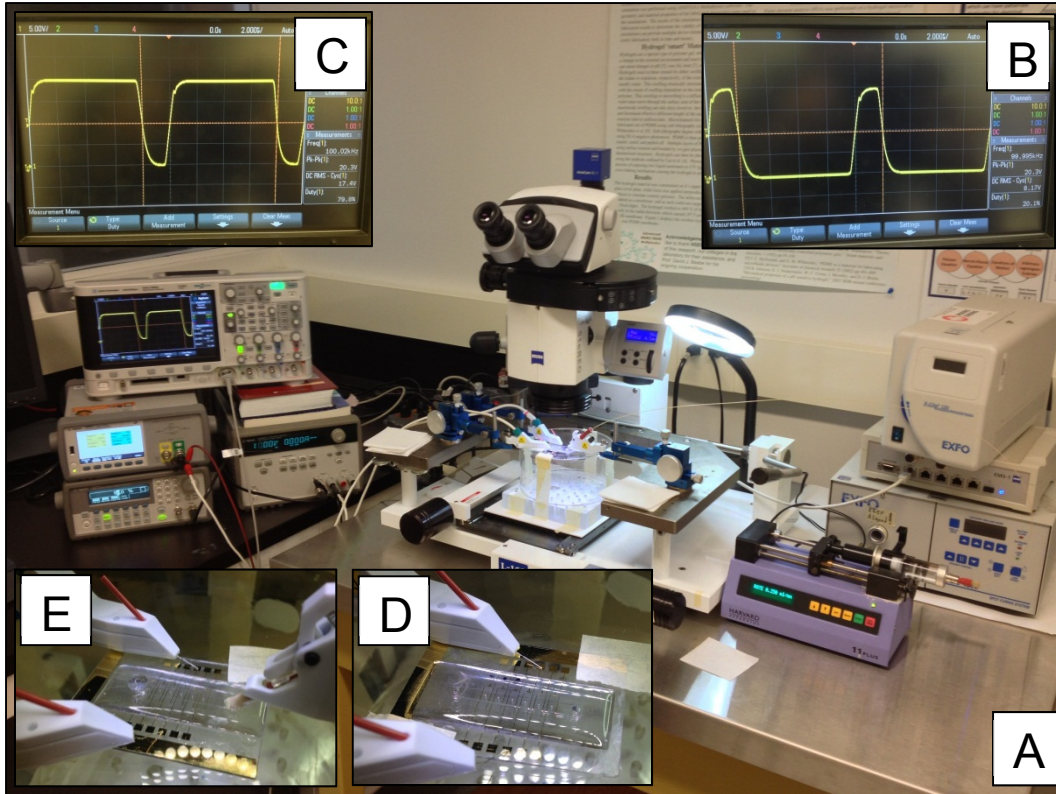
Figure 4.26: Electrical testing equipment for hydrogel actuation (A) Overview of the system (B) square wave with 20% duty cycle after amplification (C) square wave with 80 % duty cycle after amplification (D) primary electrical testing configuration (E) electrical testing of hydrogel with porting for microchannel flow.

Once an appropriate electrical signal was generated it was applied to the microchip's electrodes using Pt probes, as seen in Figure 4.26(D). These probes would make contact with the contact pads, and could be moved using micropositioners to systematically test samples. For a select set of samples, flow was introduced through the microchannel. This flow was achieved using a syringe pump with a programmable flowrate, depending on the size of the syringe. This syringe pump was attached using interconnecting tubing to a microport which was placed over a port in the microchip, as seen in Figure 4.26(E). Micropositioners were used to apply pressure between the microport and the microchannel port to ensure a leak-free seal during testing. For prolonged testing the flowing electrolyte exited through the backend of the microchip and was subsequently removed with a cleanroom wipe.

148

DC Power Supply

1-20 Volts DC

0.1-10 V$_{pk-pk}$
50 Ohms

AC Function Generator

Z_L C_L

Oscilloscope
1 MOhm

5x Gain
50 Ohms
100 kHz Max
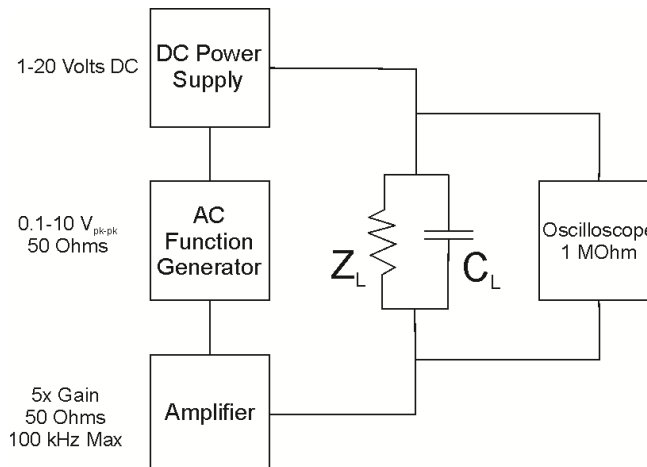
Amplifier

Figure 4.27: Circuit diagram for the electrical testing equipment including the DC power supply, AC function generator, amplifier, microchip load, and oscilloscope for monitoring.

4.4.2 Hydrogel Deformation Measurements

Measurement of the hydrogel's deformation at chemical equilibriums and under transient electrical stimulation was performed to characterize microactuator deformation and response times. The hydrogels had to be measured *in-situ*, in-place within the microchannel between two coplanar electrodes. To achieve the appropriate resolution necessary for accurate measurements the optical microscope imaging the hydrogel had to be paired with a CCD camera and the image capture software Axiovision. Hydrogels could be imaged because of the refractive index difference between the hydrogel and the surrounding electrolyte solution. This method of measuring a microscale cylindrical hydrogel's deformation under stimulus had been previously employed, most notably by Beebe *et al.* [25], De *et al.* [28], and Bassetti *et al.* [29].

Prior to its use for hydrogel measurement, the Axiovision software had to be calibrated for the correct scale at each particular optical magnification. To achieve this calibration a photomask was placed below the microscope, the same as that used for hydrogel fabrication as seen in Figure 4.12(B). The photomask fabrication process in the NanoFab has a resolution of ±300 nm and the minimum feature size used for scaling calibration was 100 microns. To begin scaling calibration, the minimum

149

magnification at 8x was calibrated by measuring the mask feature and then entering the known measurement. Subsequently each magnification in increments of 2x was calibrated to the maximum optical magnification of 100x. The distance between the microscope and the photomask was also measured to ensure an accurate working distance for measurements performed after calibration. While a large amount of magnifications could be used during measurements, typically a 54x magnification was implemented as this provided a large field of view but did not capture the electrodes on the side. Taking images with the electrodes on either side of the hydrogels was avoided when possible, because the black or gold electrode color caused the image to auto-adjust its white balance. This would reduce the contrast between the hydrogel and surrounding electrolyte making imaging difficult. For 54x magnification the distance from the microscope to the sample was 7.4 cm, as seen in Figure 4.28, which allowed for coarse image focusing. Fine image focusing was achieved by focusing on an electrode on either side of the hydrogel. Once the electrode was in focus, a process similar to focusing on the photomask used for calibration, then the hydrogel was positioned in the field of view using the probing station stage. This procedure allowed for consistent measurement of the hydrogel dimensions prior to and during electrical actuation.

Hydrogel measurements were taken using the CCD camera, which transferred images to the Axiovision software. Once calibrated using the aforementioned process, the software had multiple methods for measuring features in a micrograph. For characterization of hydrogels undergoing electrical actuation sequential measurements of the hydrogel's deformation were necessary. First the as-fabricated hydrogel, as seen in Figure 4.29(A), had its as-fabricated diameter and the diameter of the support post measured, as seen in Figure 4.29(B). This provided baseline information about the initial state of the hydrogel as-fabricated.

150
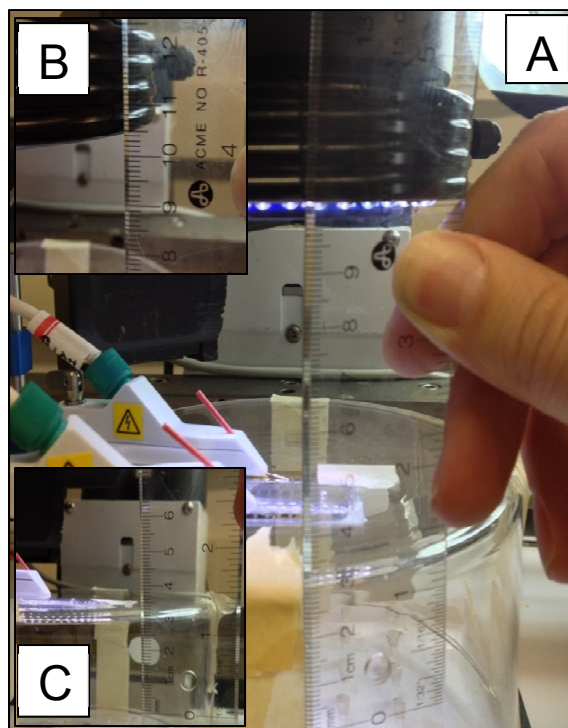
Figure 4.28: Coarse focusing on hydrogels for deformation measurements by roughly measuring the distance from stage to microscope. Fine focusing for deformation measurements was achieved by first focusing on the patterned electrodes found at the bottom of the microchannels.

The hydrogel would then be equilibrated in an electrolyte solution prior to electrical stimulation, and the diameter of the hydrogel was measured again. In addition, the digital caliper tool was used to measure the hydrogel jacket thickness, as seen in Figure 4.29(C), which was the distance from the support post to the hydrogel-electrolyte interface. These measurements provided a baseline jacket thickness prior to electrical stimulation, and the diameter measurement was combined with the as-fabricated measurements to determine the hydration state of the hydrogel. If necessary, the image could be zoomed in on the hydrogel-electrolyte interface to more accurately distinguish the interface position, shown in Figure 4.29(D). When electrically actuating the hydrogel an image was captured every 1 s, which, for some experiments, provided over 300 images for data analysis. Sequential measurements of the hydrogel jacket thickness from support post to hydrogel-electrolyte interface were taken as

151

the hydrogel was electrically actuated to swell and deswell. Data collection of this form was time consuming, but was necessary as no software could be found to perform the same function automatically.

The measurements performed in Figure 4.29 were typical of all actuation deformation measurements. The placements of the diameter measurements, as seen in Figure 4.29(B), were chosen around the sharpest boundary of the hydrogel and post. Imperfect placement could have occurred, and this would cause a measurement error in the hydrogel's initial hydration and thickness measurements. Further measurements of the change in jacket thickness were always referenced to the diameter measurements, thus measurement error for jacket thickness from a stimulated hydrogel would come from imperfect measurements of the hydrogel-electrolyte interface. Within this work measurement error was quantified as the hydrogel-electrolyte interface's visible thickness, thus at 1 mM, 5 mM, and 50 mM concentration the error was conservatively ±10 μm, and at 500 mM or as-fabricated the measurement error was ±5 μm. This was not the error from data point to data point, but rather the error across an entire set of data.

Alternative methods to measure hydrogel deformation have been proposed, such as incorporating beads in the backbone of the polymer matrix [30]. Then images are taken and the bead motion could be tracked with software, which would calculate deformation kinetics. However, these beads themselves could alter the hydrogel's mechanical properties and hence actuation properties. In addition, any mechanical characterization performed would have to be done with the beads incorporated in the structure as well. This work did not introduce any beads or particles into the system in attempts to avoid any effects which might alter the results.

4.4.3 System Capacitance and Impedance Measurements

The hydrogel system that was to be electrically actuated also had its capacitance and impedance properties measured, with both quantities being measured simultaneously.

152

Samples for capacitance and impedance measurements were fabricated with the same fabrication process as outlined in Section 4.2. The samples were fabricated with critical dimensions (e.g. Parylene thickness, hydrogel diameters) the same as those systems fabricated for electrical actuation. Samples for testing were equilibrated in the appropriate electrolyte concentration, thus they were swollen in a state
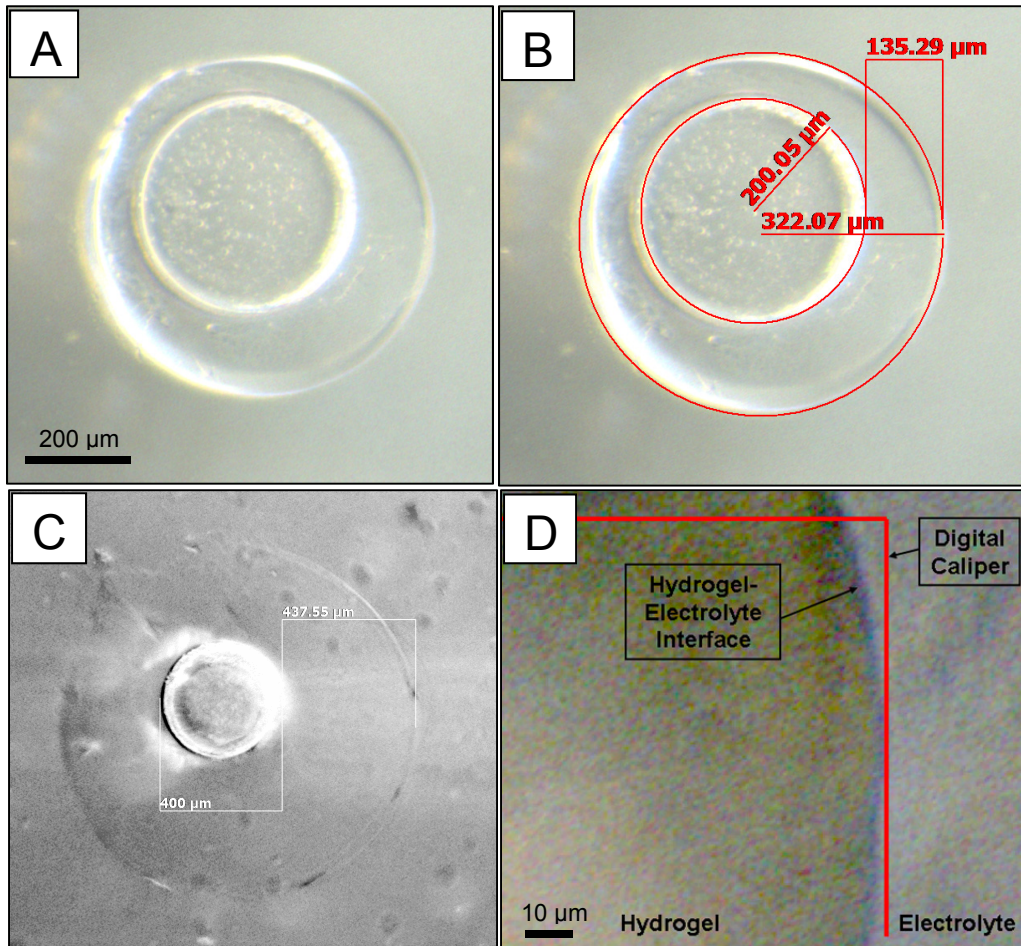
Figure 4.29: Hydrogel deformation measurements using the calibrated Axiovision software showing (A) an as-fabricated hydrogel before measurements are taken (B) a measured as-fabricated hydrogel using the digital diameter and caliper tools. (C) a measured swollen hydrogel using the digital caliper tool to determine hydrogel jacket thickness. (D) a zoomed section of the swollen hydrogel at the hydrogel-electrolyte interface for increased measurement accuracy.

Figure 4.30: Probing station used for capacitance and impedance measurements of the hydrogel microactuator system

that would be the initial conditions for electrical actuation. Samples had their capacitance and impedance measured by subjecting the system to 30 mV AC over electrodes 2 mm wide. The frequency was swept from 1 kHz to 10 MHz, and the resulting data was measured. The capacitance and impedance response was also measured with larger magnitude peak-to-peak voltages and by adding a DC offset; however, none of these testing modifications affected the measured capacitance and impedance.

4.5   Conclusion

A mature microfabrication process flow for the prototyping of electrically stimulated hydrogel microactuators was presented. In combination these processes fully define the procedures needed for experimentation, and overcome several impediments to prototype development. Furthermore, the equipment employed for testing and characterization of hydrogel microactuators was overviewed, focusing on the electrical stimulation equipment and deformation characterization system. Together these microfabrication processes and testing equipment encompass a full set of systems needed to develop the electrically stimulated hydrogel microactuator.

References

[1] M. Dhindsa, J. Heikenfeld, W. Weekamp, and S. Kuiper, "Electrowetting without Electrolysis on Self-Healing Dielectrics," *Langmuir,* vol. 27, pp. 5665-5670, May 3 2011.

[2] H. Liu, S. Dharmatilleke, D. K. Maurya, and A. A. O. Tay, "Dielectric materials for electrowetting-on-dielectric actuation," *Microsystem Technologies-Micro-and Nanosystems-Information Storage and Processing Systems,* vol. 16, pp. 449-460, Mar 2010.

[3] T. B. Jones, M. Gunji, M. Washizu, and M. J. Feldman, "Dielectrophoretic liquid actuation and nanodroplet formation," *Journal of Applied Physics,* vol. 89, pp. 1441-1448, Jan 15 2001.

[4] V. Mukundan, P. Ponce, H. E. Butterfield, and B. L. Pruitt, "Modeling and characterization of electrostatic comb-drive actuators in conducting liquid media," *Journal of Micromechanics and Microengineering,* vol. 19, 2009.

[5] S. C. System, "Parylene Electrical Properties," ed. Indianapolis, IN.

[6] C. Hassler, R. P. von Metzen, P. Ruther, and T. Stieglitz, "Characterization of parylene C as an encapsulation material for implanted neural prostheses," *Journal of Biomedical Materials Research Part B-Applied Biomaterials,* vol. 93B, pp. 266-274, Apr 2010.

[7] H. Sharifi, R. R. Lahiji, H. C. Lin, P. D. Ye, L. P. B. Katehi, and S. Mohammadi, "Characterization of Parylene-N as Flexible Substrate and Passivation Layer for Microwave and Millimeter-Wave Integrated Circuits," *Ieee Transactions on Advanced Packaging,* vol. 32, pp. 84-92, Feb 2009.

[8] G. Y. Lee, H. Ko, H. W. Jung, S. J. Ye, M. H. Kim, and J. C. Pyun, "On-line monitoring of parylene film deposition with quartz crystal microbalance (QCM)," *Eurosensors Xxv,* vol. 25, 2011.

[9] J. Flueckiger, V. Bazargan, B. Stoeber, and K. C. Cheung, "Characterization of postfabricated parylene C coatings inside PDMS microdevices," *Sensors and Actuators B-Chemical,* vol. 160, pp. 864-874, Dec 15 2011.

[10] H. Sasaki, H. Onoe, T. Osaki, R. Kawano, and S. Takeuchi, "Parylene-coating in PDMS microfluidic channels prevents the absorption of fluorescent dyes," *Sensors and Actuators B-Chemical,* vol. 150, pp. 478-482, Sep 21 2010.

[11] B. E. Rapp, A. Voigt, M. Dirschka, and K. Lange, "Deposition of ultrathin parylene C films in the range of 18 nm to 142 nm: Controlling the layer thickness and assessing the closeness of the deposited films," *Thin Solid Films,* vol. 520, pp. 4884-4888, May 31 2012.

[12] Y. N. Xia and G. M. Whitesides, "Soft lithography," *Annual Review of Materials Science,* vol. 28, pp. 153-184, 1998.

[13] H. Lorenz, M. Despont, N. Fahrni, N. LaBianca, P. Renaud, and P. Vettiger, "SU-8: a low-cost negative resist for MEMS," *Journal of Micromechanics and Microengineering,* vol. 7, pp. 121-124, Sep 1997.

[14] O. Larsson, O. Ohman, A. Billman, L. Lundbladh, C. Lindell, and G. Palmskog, "Silicon based replication technology of 3D-microstructures by conventional CD-injection molding techniques," presented at the International Conference on Solid-State Sensors and Actuators, Cicago, 1997.

[15]   J. M. K. Ng, I. Gitlin, A. D. Stroock, and G. M. Whitesides, "Components for integrated poly(dimethylsiloxane) microfluidic systems," *Electrophoresis,* vol. 23, pp. 3461-3473, Oct 2002.

[16]   S. Song and K. Y. Lee, "Polymers for microfluidic chips," *Macromolecular Research,* vol. 14, pp. 121-128, Apr 2006.

[17]   P. S. Nunes, P. D. Ohlsson, O. Ordeig, and J. P. Kutter, "Cyclic olefin polymers: emerging materials for lab-on-a-chip applications," *Microfluidics and Nanofluidics,* vol. 9, pp. 145-161, Aug 2010.

[18]   J. C. McDonald and G. M. Whitesides, "Poly(dimethylsiloxane) as a material for fabricating microfluidic devices," *Accounts of Chemical Research,* vol. 35, pp. 491-499, Jul 2002.

[19]   J. C. McDonald, D. C. Duffy, J. R. Anderson, D. T. Chiu, H. K. Wu, O. J. A. Schueller*, et al.*, "Fabrication of microfluidic systems in poly(dimethylsiloxane)," *Electrophoresis,* vol. 21, pp. 27-40, Jan 2000.

[20]   E. Meng, P. Y. Li, and Y. C. Tai, "Plasma removal of parylene c," *Journal of Micromechanics and Microengineering,* vol. 18, Apr 2008.

[21]   R. D. Tacito and C. Steinbruchel, "Fine-line patterning of parylene-n by reactive ion etching for application as an interlayer dielectric," *Journal of the Electrochemical Society,* vol. 143, pp. 1974-1977, Jun 1996.

[22]   K. S. Gadre and T. L. Alford, "Contact angle measurements for adhesion energy evaluation of silver and copper films on parylene-n and SiO2 substrates," *Journal of Applied Physics,* vol. 93, pp. 919-923, Jan 15 2003.

[23]   P. Rezai, P. R. Selvaganapathy, and G. Rwohl, "Plasma enhanced bonding of polydimethylsiloxane with parylene and its optimization," *Journal of Micromechanics and Microengineering,* vol. 21, Jun 2011.

[24]   S. Bhattacharya, A. Datta, J. M. Berg, and S. Gangopadhyay, "Studies on surface wettability of poly(dimethyl) siloxane (PDMS) and glass under oxygen-plasma treatment and correlation with bond strength," *Journal of Microelectromechanical Systems,* vol. 14, pp. 590-597, Jun 2005.

[25]   D. J. Beebe, J. S. Moore, J. M. Bauer, Q. Yu, R. H. Liu, C. Devadoss*, et al.*, "Functional hydrogel structures for autonomous flow control inside microfluidic channels," *Nature,* vol. 404, pp. 588-590, Apr 6 2000.

[26]   D. Biswal and J. Z. Hilt, "Analysis of Oxygen Inhibition in Photopolymerizations of Hydrogel Micropatterns Using FTIR Imaging," *Macromolecules,* vol. 42, pp. 973-979, Feb 24 2009.

[27]   M. Bera, A. Rivaton, C. Gandon, and J. L. Gardette, "Comparison of the photodegradation of parylene C and parylene N," *European Polymer Journal,* vol. 36, pp. 1765-1777, Sep 2000.

[28]   S. K. De, N. R. Aluru, B. Johnson, W. C. Crone, D. J. Beebe, and J. Moore, "Equilibrium swelling and kinetics of pH-responsive hydrogels: Models, experiments, and simulations," *Journal of Microelectromechanical Systems,* vol. 11, pp. 544-555, Oct 2002.

[29]   M. J. Bassetti, A. N. Chatterjee, N. R. Aluru, and D. J. Beebe, "Development and modeling of electrically triggered hydrogels for microfluidic applications," *Journal of Microelectromechanical Systems,* vol. 14, pp. 1198-1207, Oct 2005.

[30]   B. Johnson, J. M. Bauer, D. J. Niedermaier, W. C. Crone, and D. J. Beebe, "Experimental techniques for mechanical characterization of hydrogels at the microscale," *Experimental Mechanics,* vol. 44, pp. 21-28, Feb 2004.

Chapter 5

Dynamic Mechanical Properties and Swelling of UV-Photopolymerized Anionic Hydrogels[1]

5.1   Introduction

Hydrogels are crosslinked polymer chain networks with an interstitial fluid. They have been given research attention as active components in microfluidic systems, acting as actuators [1], valves [2], pumps [3], mixers [4], and lenses [5]. Their properties have also been investigated in other research areas, such as sensors design [6], drug delivery [7], and cell scaffolding [8]. Their structure in many ways is similar to some biological tissues, such as muscles [9], and articular cartilage or the eye's corneal stroma [10, 11].

Stimuli responsive hydrogels undergo a swelling or deswelling volume transformation, and can be fabricated to respond to temperature [12], pH [2], or electric fields [13]. Different compositions of hydrogels cause different physical kinetics to occur within that particular type of stimuli responsive hydrogel. The degree of volume transformation and response timescales depend significantly on the mechanical properties of that particular hydrogel composition and the electrolyte within which the hydrogel is immersed.

Previously, hydrogels of various compositions have had their mechanical properties tested using tensile tests [14-16], compression tests [17-19], surface acoustic waves [20], membrane deflection [21, 22], and dynamic mechanical analysis [23-25]. The two most relevant tests for hydrogels being used as active components in microfluidic systems are tensile testing and dynamic mechanical analysis. Tensile testing provides a material's fundamental tensile properties, but doesn't explicitly take into account the viscous effects of deformation, and usually only one deformation rate and electrolyte concentration is investigated. Dynamic mechanical analysis provides the fundamental dynamic mechanical properties and can be performed at different cyclical deformation rates under various environmental conditions.

This work examines an anionic gel composed of HEMA monomer and AA co-monomer. This composition is responsive to pH or electric field stimulation and is UV photopolymerized. Previously researchers have examined this composition using static tensile tests for mechanical properties [14, 15], and as an active material in microactuators [13, 26]; however, its tensile dynamic mechanical properties have never been reported over a range of fabrication parameters and environmental conditions.

The HEMA-co-AA polymer backbone has been functionalized with carboxyl groups, which can reversibly protonate or deprotonate based on the pH conditions of the interstitial electrolyte. At high pH the polymer network becomes negatively charged. This charged polymer network causes a flux of positively charged mobile ions into the hydrogel network and an osmotic pressure develops, producing a reversible volume transformation [27, 28].

Two factors determine an ionic hydrogel's osmotic pressure, the pH and concentration of the interstitial and surrounding electrolyte. Modifying an electrolyte's pH can cause protonation or deprotonation of the fixed anionic charged groups, electrically neutralizing or charging the polymer

158

structure, respectively. The presence of these fixed charges causes an influx of mobile ions and a concentration gradient to develop at the hydrogel-electrolyte interface causing a change in osmotic pressure [14]. The second mechanism to modify osmotic pressure relies on the concentration of the electrolyte, and therefore the magnitude of the concentration gradient established. Electric field stimulation takes advantage of the second, concentration based mechanism, to modify the pressure across the surfaces of a fiber or cylinder to produce actuation [29, 13].

Cyclic actuation and faster deformation timescales can be achieved through electric field stimulation. Thus it is necessary to investigate a hydrogel's tensile DMP under swollen states and under conditions mimicking the in-situ stimulation environment, similar to those being used for electric field stimulation [13]. Furthermore, the complex electro-chemical-mechanical dynamics of hydrogel volume transformation has been the focus of many numerical modeling studies for both pH and electric field responsive hydrogels [30, 31]. It is essential to have accurate dynamic mechanical properties for hydrogels as inputs to these numerical systems for them to produce an accurate representation of the physical system modeled, especially with shorter actuation timescales and cyclical actuation. These dynamic mechanical properties describe the viscoelastic nature of a hydrogel, namely the elastic response (storage modulus) and the viscous response (loss modulus), and the measure of internal friction-based damping (tan delta). Within a material's linear viscoelastic region this measurement will be reproducible.

In this work a hydrogel's dynamic mechanical properties are investigated under the influence of varying percent weight crosslinker, UV photopolymerization exposure time, and UV photopolymerization intensity (or intensity of UV irradiation). The fabricated hydrogels are subjected to loading frequencies of 0.1, 1, or 10 Hz under electrolyte concentrations of 0.5 M and 0.05 M potassium hydroxide (KOH). The resulting morphology

of the fabricated hydrogels was examined under a scanning electron microscope to show the morphologies influence on dynamic mechanical properties. The DMP were intended to give researchers more information fabricate, design, and model active hydrogel-based microfluidic components, with the potential for large-scale integration into microfluidic systems.

5.2 Experimental

5.2.1 Hydrogel Precursor and Electrolyte Composition

The hydrogels investigated here had a precursor mixture composed of monomer HEMA (Fisher Scientific), co-monomer AA (Fisher Scientific), crosslinker ethylene-glycol-dimethacrylate acid crosslinker (EGDMA, Fisher Scientific), and photoinitiator 2,2-dimethoxy-2-phenylacetophenone (DMPA, Irgacure 651 CIBA). The precursor components were determined by weight in an analytical balance (Mettler Toledo Classic-Plus) and were mixed for 30 minutes. The mixture was stored in the refrigerator using an amber bottle to block exposure to ambient UV light.

Experiments investigating the dynamic mechanical properties used varying photopolymerization fabrication conditions and precursor mixture compositions, which are outlined in Table 5.1. For all fabricated hydrogels the quantity of photoinitiator DMPA was held constant at 3 % weight. Throughout all fabricated hydrogels the quantity of AA was held constant at 12 % weight of the precursor composition, which translates into 1.8 M of fixed carboxyl groups attached to the polymer backbone of the hydrogel. It has been previously shown that the mechanical properties of a hydrogel depend on the concentration of fixed ionic groups [32]. It was shown that two opposing forces arise when examining the effects of fixed ion concentration; whereby, additional crosslinks are created by ion multiplet formation increasing the modulus, while the modulus is decreased due to the fixed ion electrostatic interaction effects modifying the elastic free

energy [32]. A constant fixed ion concentration neutralized these opposing effects within the current study.

Hydrogels were tested under two electrolyte solution compositions, 0.5 M (pH 13.7) and 0.05 M (pH 12.7) KOH. Throughout this study the focus was on the concentration of the electrolyte concentration, not specifically the pH. The two electrolyte concentrations of 0.5 M and 0.05 M KOH used are both larger than the dissociation constants of the fixed carboxyl groups of $10^{-5.1}$ [33], thus swelling differences among samples are dominated by electrolyte concentration considerations and not pH-based swelling. Therefore, when presenting the experimental results the data is referenced to the electrolyte concentration.

5.2.2 Hydrogel Sample Fabrication

Hydrogels undergo UV photopolymerization within an oxygen free polymer mold. The final mold for hydrogel polymerization was composed of polydimethylsiloxane (PDMS) molded in the hydrogel's as-fabricated dimensions, which was reversibly bonded to a PDMS coated glass slide. Reversible bonding of PDMS to PDMS requires clean surfaces, and can withstand pressures up to 5 psi [16]. A rapid prototyped (RP)

Table 5.1: Fabrication parameters for hydrogels tested using DMA

Experimental Set	Photopolymerization Exposure Time (seconds)	Photopolymerization Intensity (mW cm^{-2})	Weight Percent Crosslinker (% weight)
1	100, 130, 160, 190	1.21	4
2	100	0.86, 1.21, 1.45, 1.74	4
3	100	1.21	2, 4, 8

mold was used to fabricate the PDMS mold. The RP mold was designed using the computer aided design commercial tool Pro/Engineer[©] and fabricated using a rapid prototyping machine (Objet's Eden 350V). PDMS precursor (Dow Corning's Slygard 184) was mixed in a 10:1 ratio by weight, degassed, poured over the RP mold, which had been silanized for 2 hrs, and then was cured for 2 hrs at 80°C. The PDMS on the glass slide

was mixed in the same ratio and spin-coated for 2 min at 1500 rpm, and afterwards was cured for 2 hrs at 80°C.

The UV photopolymerization process exposes the hydrogel precursor solution to 365 nm wavelength UV light at intensities on the order of 1 mW cm^{-2} (measured at the sample) with exposure times on the order of 10s-100s of seconds. An EXFO Acticure 4000 was used to generate the UV light, while a light-guide with a circular UV-profile was used to position the UV light. The system was calibrated to determine the UV intensity measured at the sample for various exposure intensities. An ABM 2-Channel Digital Intensity Meter (ABM) was used to determine the UV intensity at the height of the sample for 365 nm wavelength light.

To perform photopolymerization the hydrogel precursor was injected into the rectangular PDMS mold and exposed to UV light. After photopolymerization, the PDMS mold was peeled back and the exposed sample was immersed in methanol for washing and then placed in 0.5 M KOH first. The samples were given a minimum 72 hours to reach equilibrium. After testing occurred at the stronger concentration, the samples were placed in 0.05 M KOH and given another minimum 72 hours to reach equilibrium. This was performed so each sample was tested at two different concentrations. To ensure the consistent concentration during equalization, the samples after reaching equilibrium had a maximum volume, based off measured dimensions, of 1.56 ml while container within which the sample was equilibrated had a volume of 25 ml. In addition, the electrolyte was exchanged with fresh solution after 48 hours and given another minimum 24 hours to equilibrate.

The PDMS mold had a channel height of 1 mm, width of 8 mm, and a length of 20 mm. This mold size produced 'as-fabricated' hydrogels of the same size. The as-fabricated samples were swollen in electrolyte solution of 0.5 M and 0.05 M KOH; with each concentration and fabrication condition producing different equilibrated dimensions. Each swollen sample had its width and length cut with a scalpel to reduce their

162

dimensions to fit within the dynamic mechanical analyzer. The 'as-tested' samples varied between 7-8 mm in width and 1-1.7 mm thickness, with the difference in final dimensions being dependent on the fabrication conditions and the equilibrated electrolyte concentration. The distance between the grips (the as-tested length) was constant at 6.1 mm throughout the testing.

A material anisotropy was avoided by encapsulating the hydrogel precursor in a PDMS mold during photopolymerization, as the presence of oxygen during the photopolymerization process inhibits the reaction rate [34]. Oxygen in the presence of UV light produces oxygen radicals due to the formation of ozone. These oxygen radicals can decrease the modulus of fabricated samples by breaking bonds during the photopolymerization process.

5.2.3 Weight Degree of Swelling & SEM Microscopy

The weight degree of swelling was calculated using the following relationships

$$Q_m = \frac{w_s - w_d}{w_d}$$

(5-1)

here w_s is the weight of the swollen gel and w_d is the weight of the dry gel. Test samples had dynamic mechanical measurements performed, and then the sample was dabbed dry with a cleanroom wipe and weighed on an analytical scale. This was performed after both tests in 0.5 M and 0.05 M electrolyte concentrations. The samples were then flash-frozen in liquid nitrogen and freeze-dried (Savant SuperModulyo) for 6 hours at -50°C and 7×10^{-2} Torr to remove any moisture in the sample. The dry samples were then measured with an analytical balance (Mettler Toledo Classic-Plus). Since these samples were flash-frozen, they retained their porous structure. Dry samples were cut with a scalpel through their cross-section and mounted on aluminum stubs. The samples then had gold sputtered on their surface (Denton Desk II) and were imaged in the SEM (LEO 1430).

5.2.4 Dynamic Mechanical Analyzer Methods

The equilibrated swollen hydrogel samples were prepared for measurement by cutting their width to testing dimensions, and measuring the length, width, and thickness with a vernier caliper. To improve accuracy two measurements were taken across the hydrogels dimensions and the averaged values were entered into the control software. The samples were then loaded into a dynamic mechanical analyzer (PerkenElmer DMA 8000), which applied a sinusoidally oscillating tensile strain, measured the resulting force waveform, and using the input geometrical parameters determined the resulting stress waveform. Samples were tested below 1 % tensile strain in the linear viscoelastic region, at frequencies of 0.1, 1, and 10 Hz under electrolyte concentrations of 0.5 M and 0.05 M KOH. These samples were tested for 15 minutes under isothermal conditions of $23\pm1^{o}C$.

5.3 Results

For each experimental parameter of interest five samples were tested. Each data point represents the average of these five values and the error bars represent the set's standard deviation. To avoid grip effects the samples were cut from their swollen dimensions to fit in the dynamic mechanical analyzer (DMA), and when placing samples within the grips it was ensured that no sample wedging or pinching occurred. Throughout all of the experimental studies examining the DMP, samples were tested at KOH electrolyte concentrations of 0.5 M and 0.05 M and applied frequencies of 0.1, 1, and 10 Hz.

5.3.1 Weight Degree of Swelling

A study was performed to investigate the influence of percent weight crosslinker, photopolymerization time, and photopolymerization intensity on the weight degree swelling of a hydrogel swollen in KOH electrolyte concentrations of 0.5 M and 0.05 M.

Increasing the precursor solution's percent weight crosslinker in fabricated samples showed a power-law decrease in the weight degree of swelling, as shown in Figure 5.1a. Decreasing the solution concentration also caused an increased weight degree of swelling, with both concentrations displaying a power-law decline. At 0.05 M the maximum weight degree of swelling was 14.27 at 1 % crosslinker, with a minimum of 2.68 at 8 % crosslinker. At 0.5 M concentration the maximum and minimum weight degrees of swelling was 8.32 and 1.95 at 1 % and 8 % crosslinker, respectively.

Increasing the fabrication photopolymerization exposure time caused a decrease in the weight degree of swelling, especially at and above 130 s exposure times. Between 130 s and 190 s of exposure a slight decline in weight degree of swelling was observed, but samples exhibited relatively the same weight degree of swelling. Decreasing the solution concentration caused samples to have a higher weight degree of swelling, as seen in Figure 5.1b. At 0.05 M the maximum weight degree of swelling was 5.55 at 100 s exposure time, with a minimum of 2.72 at 190 s exposure time. At 0.5 M the maximum and minimum weight degree of swelling was 3.65 and 2.06 at 100 and 190 s exposure time, respectively.

Increasing the fabrication photopolymerization intensity caused a linear decline in the weight degree of swelling, as shown in Figure 5.1c. The linear decline was steeper for samples swollen at lower concentration. Decreasing the solution concentration caused an increase in the weight degree of swelling. At 0.05 M the maximum weight degree of swelling was 7.11 at 0.86 mW cm^{-2}, with a minimum of 3.85 at 1.73 mW cm^{-2}. At 0.5 M the maximum and minimum weight degree of swelling was 4.63 and 2.69 at 0.86 mW cm^{-2} and 1.73 mW cm^{-2}, respectively.
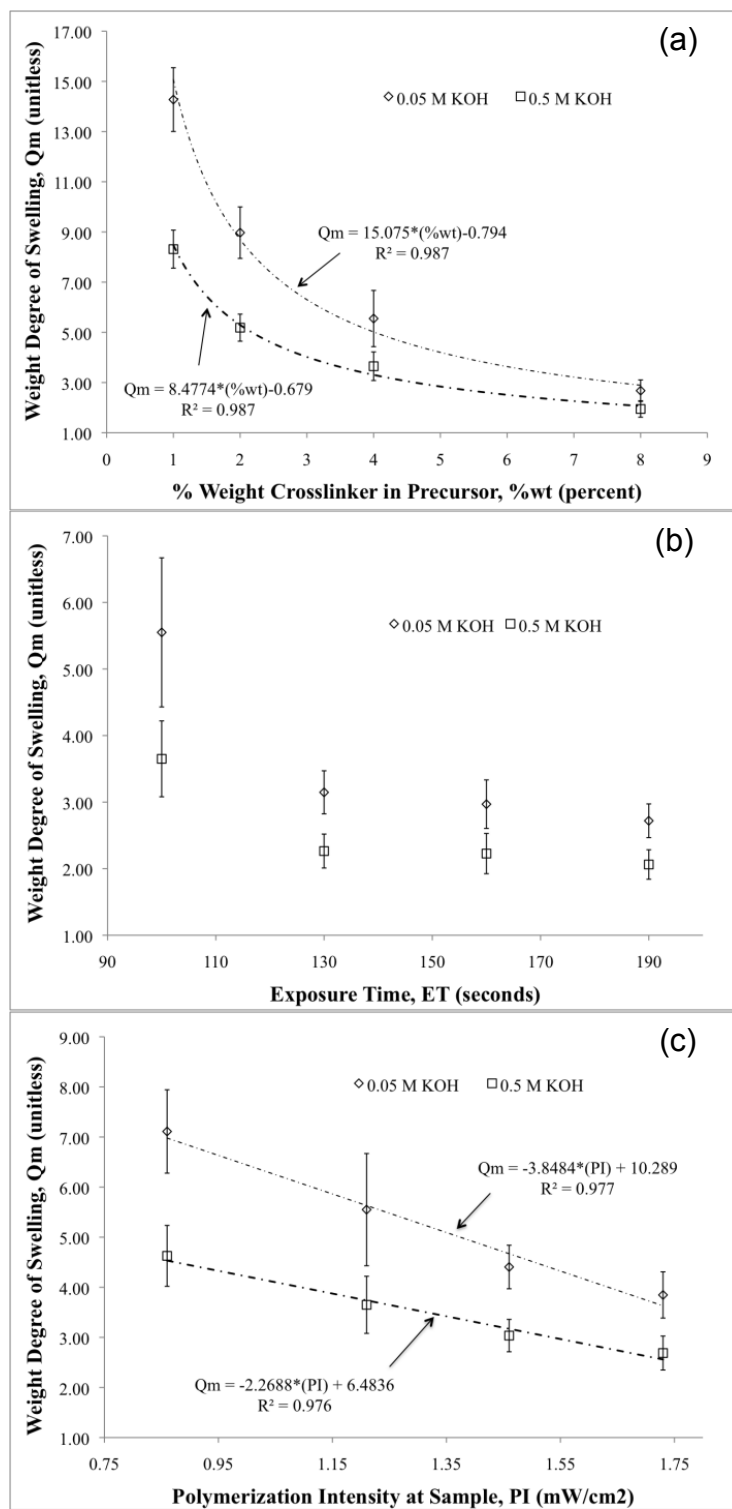
Figure 5.1: Hydrogel weight degree of swelling as effected by electrolyte concentration and (a) weight percent crosslinker (b) UV-photopolymerization exposure time, and (c) UV-photopolymerization intensity.

166

5.3.2 DMP Dependence on Percent Weight Crosslinker

Increasing the precursor solution's percent weight crosslinker caused fabricated hydrogels to have an increased storage modulus and loss modulus, as shown in Figure 5.2a-b with corresponding error values in Table 5.2. Increasing the testing frequency, to a lesser extent, also caused an increase in the storage and loss modulus. An increased frequency had the largest effect on the storage modulus of samples fabricated with 8 % crosslinker. Samples equilibrated at 0.5 M were shown to have their dynamic mechanical properties largely dominated by elastic effects. Samples equilibrated at 0.05 M showed an increase in loss modulus and a decline in the storage modulus of samples, versus the samples equilibrated at 0.5 M.

For samples tested at 1 Hz the maximum storage modulus was 1.67 MPa at 8 % crosslinker and 0.5 M, with a minimum storage modulus of 182 kPa at 0.5 M and 2 % crosslinker. These samples at 0.5 M had a maximum and minimum loss modulus of 214 kPa and 12 kPa at 8 % and 2 % crosslinker, respectively. For samples tested at 1 Hz and 0.05 M concentration the maximum and minimum storage modulus was 1.0 MPa and 129 kPa at 8 % and 2 % crosslinker, respectively, while the maximum and minimum loss modulus was 279 kPa and 42 kPa at 8 % and 2 % crosslinker, respectively.

Increasing the precursor solution's percent weight crosslinker caused a decline in the tan delta of samples equilibrated in 0.05 M concentrations while samples equilibrated in 0.5 M solution showed an increase in damping, as shown in Figure 5.2c. Error in Figure 5.2c is shown for samples tested at 1 Hz, with other error values calculable using the presented data. For samples equilibrated at 0.5 M increasing the testing frequency caused a slight increase in the damping of samples. It was unclear how frequency affected samples equilibrated at a concentration of 0.05 M. For samples tested at 1 Hz and 0.05 M, the maximum and minimum tan delta was 0.34 and 0.29 at 2 % and 8 % crosslinker,
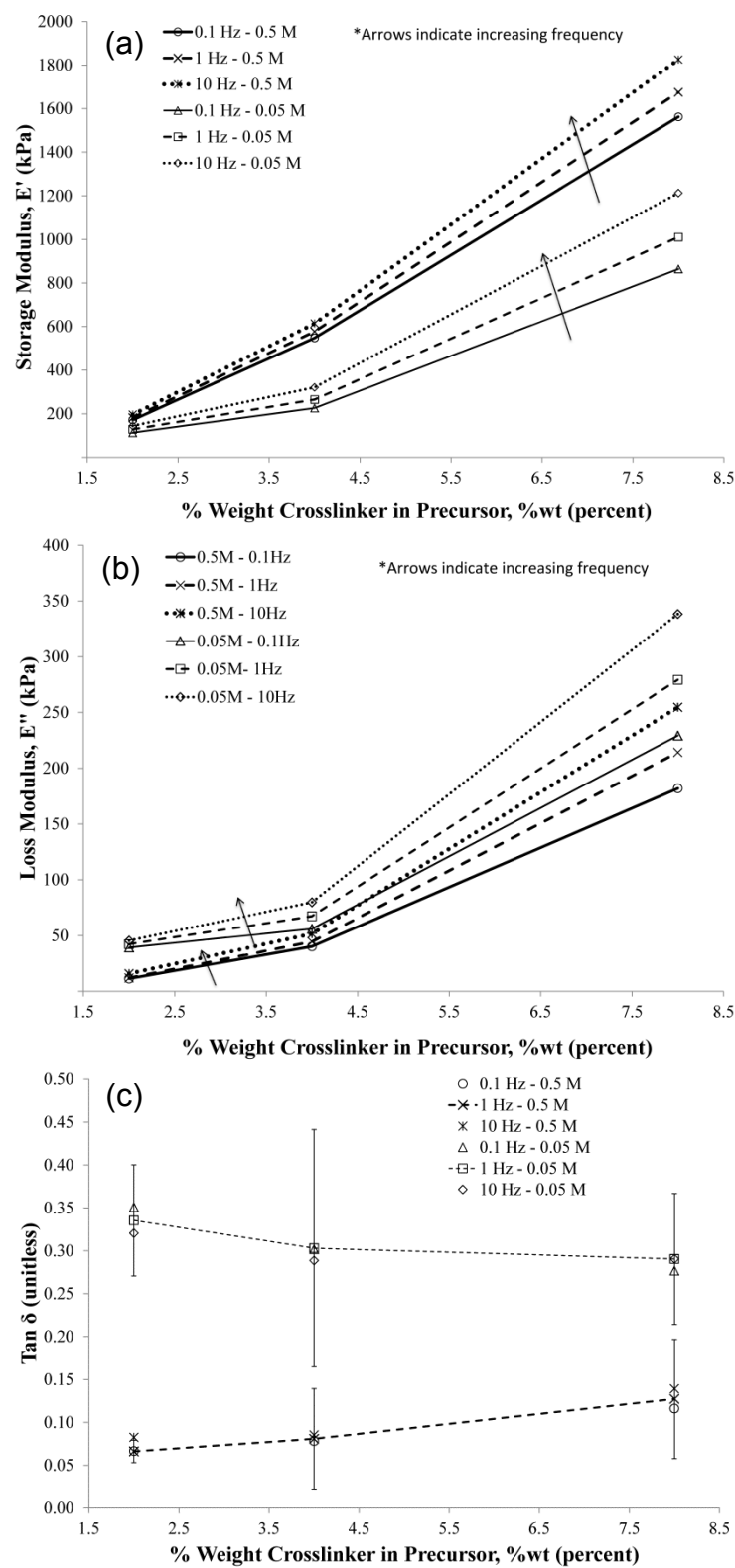
Figure 5.2: The effect of weight percent crosslinker, electrolyte concentration, and cyclic strain frequency on (a) storage modulus, (b) loss modulus, and (c) tan δ.

168

Table 5.2: Error in storage and loss modulus for percent weight crosslinker experimental set

% Weight Crosslinker in Precursor (% weight)	Analysis Frequency (Hertz)	Error in Storage Modulus		Error in Loss Modulus	
		0.5 M KOH ($Pa*10^4$)	0.05 M KOH ($Pa*10^4$)	0.5 M KOH ($Pa*10^4$)	0.05 M KOH ($Pa*10^4$)
2	0.1	± 3.08	± 1.47	± 0.21	± 0.57
	1	± 3.21	± 2.07	± 0.22	± 0.51
	10	± 3.36	± 2.27	± 0.38	± 0.52
4	0.1	± 19.22	± 16.25	± 2.54	± 2.66
	1	± 12.90	± 16.58	± 2.56	± 2.59
	10	± 20.27	± 19.78	± 3.07	± 3.37
8	0.1	± 15.67	± 26.41	± 13.42	± 4.47
	1	± 16.95	± 28.02	± 12.69	± 3.82
	10	± 17.91	± 28.82	± 11.49	± 4.91

respectively. For samples tested at 1 Hz and 0.5 M, the maximum and minimum tan delta was 0.13 and 0.07 at 8 % and 2 % crosslinker.

5.3.3 DMP Dependence on Photopolymerization Exposure Time

Increasing the photopolymerization exposure time increased both the storage modulus and loss modulus of tested samples, as seen in Figure 5.3a-b with corresponding error values in Table 5.3. Increasing the testing frequency also increased the storage modulus and loss modulus of samples, for all exposure times considered. The increase in frequency had a pronounced effect on the storage modulus of samples equilibrated in 0.05 M KOH. Samples equilibrated at 0.5 M showed that elastic effects dominate the sample's mechanical properties, as the storage modulus was always one order of magnitude larger than the loss modulus. Decreasing the solution concentration to 0.05 M causes a decrease in the storage modulus and an increase in the loss modulus of samples.

For samples tested at 1 Hz the maximum storage modulus was 1.67 MPa at 190 s and 0.5 M, with a minimum storage modulus of 577 kPa at 100 s and 0.5 M. These samples at 0.5 M and 1 Hz had a maximum and

minimum loss modulus of 93 kPa and 45 kPa at 160 s and 100 s, respectively. For samples tested at 0.05 M and 1 Hz, the maximum and minimum storage modulus was 884 kPa and 265 kPa at 160 s and 100 s exposure times, respectively. These samples had a maximum and minimum loss modulus of 375 kPa and 67 kPa at 190 s and 100 s exposure time, respectively.

Increasing the photopolymerization exposure time for tested at 0.5 M KOH had little effect on the tan delta, as shown in Figure 5.3c. Error in Figure 5.3c is shown for samples tested at 1 Hz, with the remaining error values calculable using the presented data. For samples equilibrated at 0.05 M a slight increase in as exposure time was increased; however, the error in these samples better helps to define a domain for tan delta. Decreasing the electrolyte concentration also caused an increase in the tan delta of samples, which shows the effects of decreased storage modulus and increased loss modulus at 0.05 M. At 0.05M it was observed that increasing the testing frequency caused a marked decline tan delta, while samples at 0.5 M showed a slight increase of tan delta with increased testing frequency. For samples tested at 1 Hz and 0.05 M, the maximum and minimum tan delta was 0.43 and 0.30 at 190 s and 100 s exposure times, respectively. Samples tested at 0.5 M did not have a clear maximum and minimum.

5.3.4 DMP Dependence on Photopolymerization Intensity

Increasing the photopolymerization intensity increased the storage modulus and loss modulus of samples for all tested electrolyte concentrations, as shown in Figure 5.4a-b with corresponding error values in Table 5.4. Increasing the testing frequency also increased the storage modulus and loss modulus of samples, with frequency having a pronounced effect on the storage modulus of samples equilibrated in 0.05 M solution concentrations. Samples tested at 0.5 M concentrations displayed largely elastic behavior, with increased photopolymerization intensity largely affecting the storage modulus of samples. Decreasing the
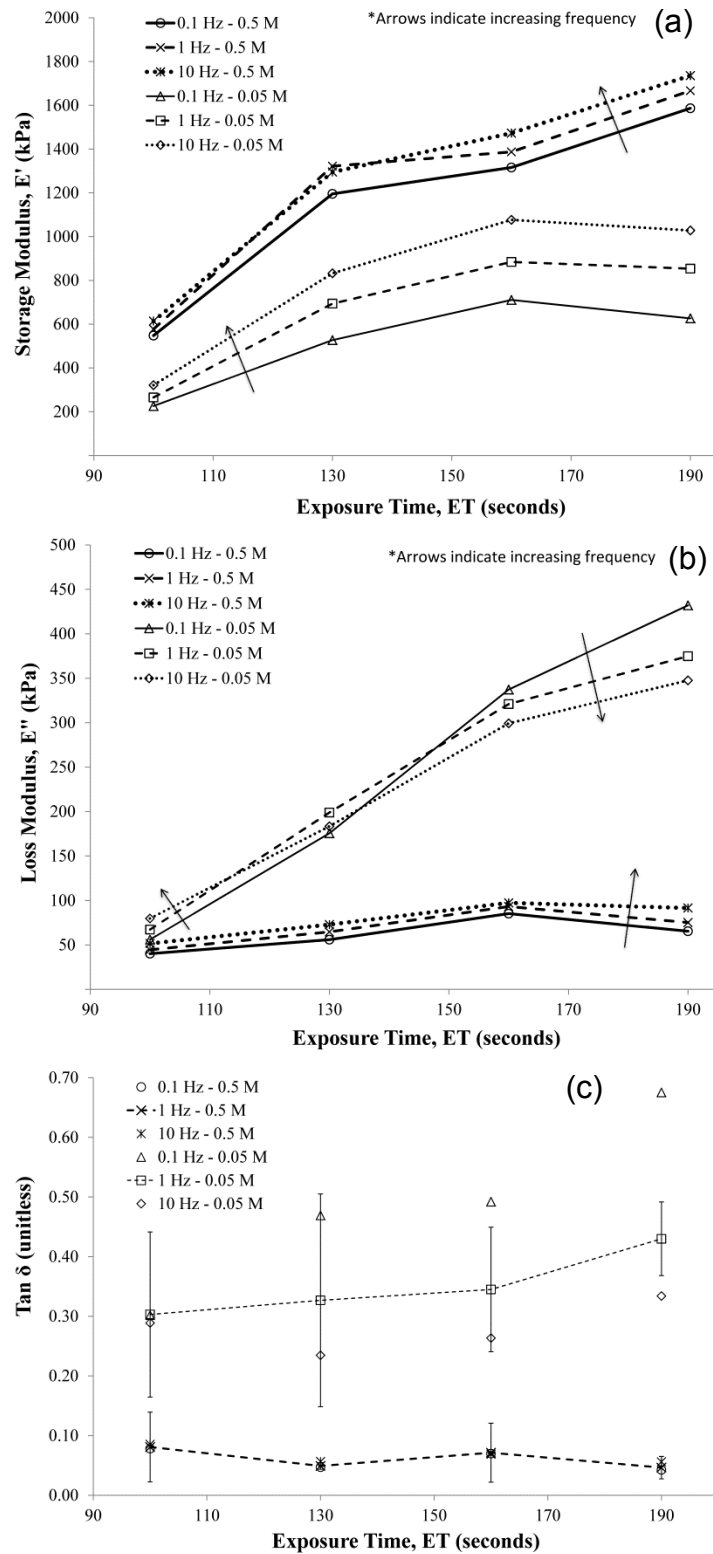
Figure 5.3: The effect of UV-photopolymerization exposure time, electrolyte concentration, and cyclic strain frequency on (a) storage modulus, (b) loss modulus, and (c) tan δ.

171

Table 5.3: Error in storage and loss modulus for UV-photopolymerization exposure time exp erimental set

Exposure Time (seconds)	Analysis Frequency (Hertz)	Error in Storage Modulus		Error in Loss Modulus	
		0.5 M KOH ($Pa*10^4$)	0.05 M KOH ($Pa*10^4$)	0.5 M KOH ($Pa*10^4$)	0.05 M KOH ($Pa*10^4$)
100	0.1	± 19.22	± 16.25	± 2.54	± 2.66
	1	± 12.90	± 16.57	± 2.56	± 2.59
	10	± 20.27	± 19.78	± 3.07	± 3.37
130	0.1	± 11.58	± 31.37	± 0.74	± 6.59
	1	± 16.22	± 24.91	± 0.86	± 8.20
	10	± 11.68	± 23.11	± 0.84	± 5.99
160	0.1	± 17.77	± 18.86	± 4.66	± 17.23
	1	± 17.17	± 21.52	± 4.96	± 9.93
	10	± 14.45	± 22.97	± 4.68	± 4.76
190	0.1	± 17.17	± 79.56	± 2.31	± 6.32
	1	± 15.82	± 11.05	± 2.52	± 4.20
	10	± 13.67	± 11.19	± 2.01	± 6.56

solution concentration to 0.05 M decreased the storage modulus of samples and increased the loss modulus. The increase in loss modulus becomes more pronounced at intensities of 1.45 mW cm^{-2} and above.

For samples tested at 1 Hz frequency the maximum storage modulus was 846 kPa at 1.74 mW cm^{-2} and 0.5 M, with a minimum storage modulus at 0.5 M of 139 kPa at 0.86 mW cm^{-2}. These samples at 0.5 M concentration and 1Hz frequency had a maximum and minimum loss modulus of 61 kPa and 7 kPa at 1.74 mW cm^{-2} and 0.86 mW cm^{-2}, respectively. For samples tested at 0.05 M and 1 Hz frequency, the maximum and minimum storage modulus was 588 kPa and 84 kPa at 1.74 mW cm^{-2} and 0.86 mW cm^{-2}, respectively. For these samples, the maximum and minimum loss modulus was 21 kPa and 3 kPa at 1.74 mW cm^{-2} and 0.86 mW cm^{-2}, respectively.

Increasing the photopolymerization intensity had inconsistent effects on the tan delta of samples, especially at 0.05 M concentrations, as seen

in Figure 5.4c. Error in Figure 5.4c is shown for samples tested at 1 Hz, with other error values calculable using presented data. It is clear that decreasing the electrolyte concentration to 0.05 M causes an increase in tan delta, but these tan delta results reflect the error in the measured storage modulus and loss modulus. At 0.5 M concentration increasing the testing frequency slightly increased the tan delta of samples. At 0.05 M the result of increased frequency are inconsistent; however, at 1.21 mW cm^{-2} and 1.45 mW cm^{-2} intensities samples are seen to have a decreased tan delta with an increased testing frequency. Tan delta results for both 0.5 M and 0.05 M concentrations have no discernible maximum or minimum.

5.4 Discussion

5.4.1 Effect of Electrolyte Concentration

As the concentration of electrolyte solution was decreased the weight degree of swelling increased, for all hydrogels fabricated. When the electrolyte concentration is decreased, the quantity of positively charged interstitial mobile ions increases relative to the surrounding mobile ions. Therefore, the gradient of interstitial to surrounding mobile ions is higher and a larger osmotic pressure is developed, and the hydrogel swells to a greater extent. This increased swelling will occur under the assumption that the fixed carboxyl groups are fully dissociated, as partial or fully associated fixed groups would negate the hydrogel's electrical charge, decrease the osmotic pressure, and deswell the hydrogel structure [14]. At some critical counterion concentration threshold the swelling of the hydrogel will not increase but start to decrease towards a deswollen gel, as seen by Marcombe *et al.* when examining free swelling of low salt concentration gels over a range of pHs [35]. Extending this notion and based off the results seen here, this critical counterion concentration threshold would represent the minimum storage modulus of the gel and decreasing the concentration further would cause an increase in storage modulus.

173
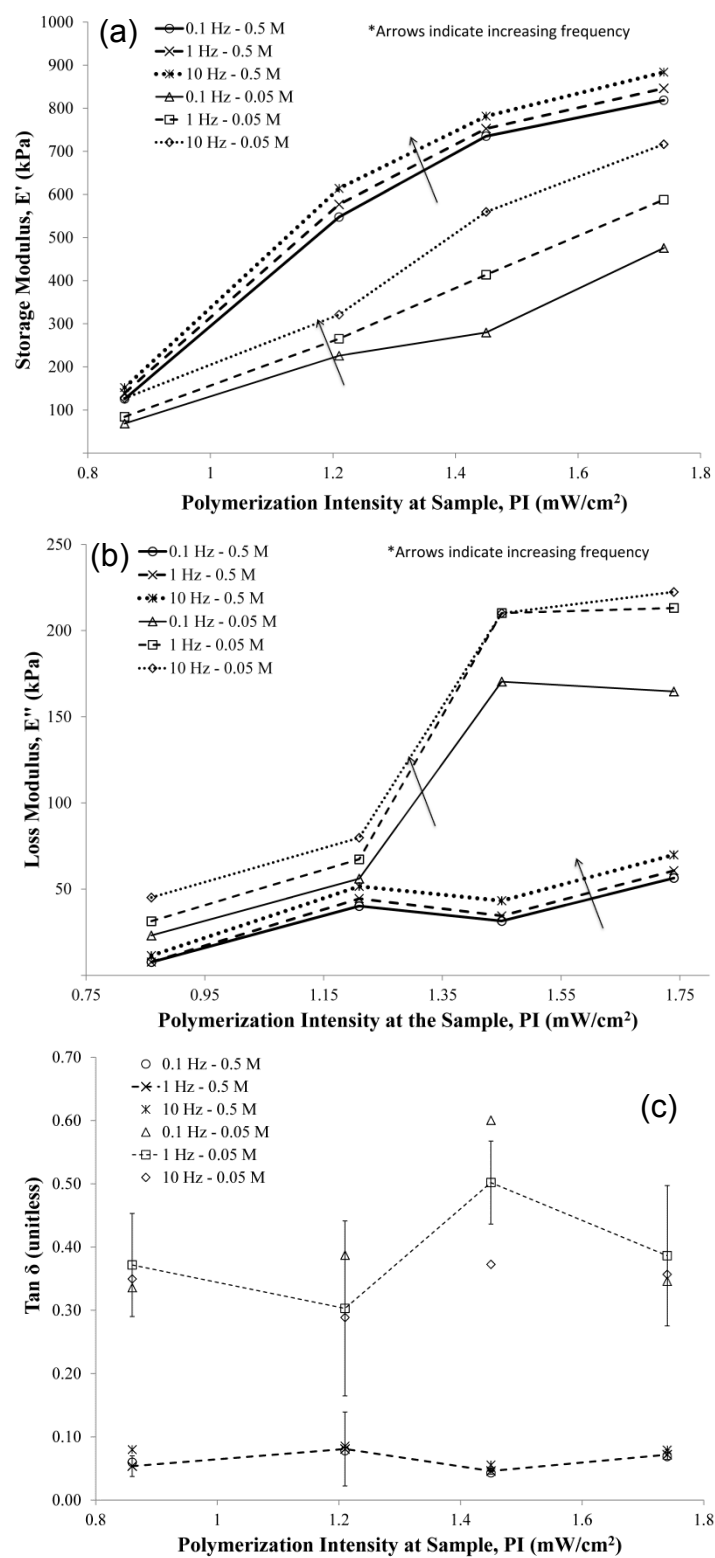
Figure 5.4: The effect of UV-photopolymerization intensity, electrolyte concentration, and cyclic strain frequency on (a) storage modulus, (b) loss modulus, and (c) tan δ

Table 5.4: Error in storage and loss modulus for UV-photopolymerization intensity experimental set

Polymerization Intensity (mW cm^{-2})	Analysis Frequency (Hertz)	Error in Storage Modulus		Error in Loss Modulus	
		0.5 M KOH (Pa*10^4)	0.05 M KOH (Pa*10^4)	0.5 M KOH (Pa*10^4)	0.05 M KOH (Pa*10^4)
	0.1	± 3.64	± 0.72	± 0.32	± 0.59
0.86	1	± 3.83	± 1.09	± 0.34	± 0.87
	10	± 3.92	± 1.72	± 0.47	± 1.45
	0.1	± 19.22	± 16.25	± 2.54	± 2.66
1.21	1	± 12.90	± 16.57	± 2.56	± 2.59
	10	± 20.27	± 19.78	± 3.07	± 3.37
	0.1	± 3.99	± 4.94	± 0.36	± 5.47
1.45	1	± 4.04	± 6.06	± 0.27	± 5.31
	10	± 4.15	± 7.43	± 0.47	± 6.08
	0.1	± 6.40	± 12.59	± 0.81	± 4.97
1.74	1	± 6.41	± 17.22	± 0.69	± 3.83
	10	± 5.67	± 24.92	± 0.46	± 4.46

The difference in weight degree of swelling between the two electrolyte concentrations examined was always higher at the low end of the fabrication parameter range. Swelling is dependent on the mechanical properties of the hydrogels [14], and for all hydrogels examined the low end of the fabrication parameter range had lower storage moduli. Increased swelling due to decreased electrolyte concentrations also caused a decrease in storage and loss modulus, having a larger effect on the storage modulus. As the hydrogel swells the polymer network disentangles due to an influx of water molecules, reducing the stiffness of individual polymer chains and hence the storage modulus. As the fabrication variables were increased the polymer network density increased, thereby decreasing swelling but also decreasing the network's porosity to mobile ions and water. This decreased porosity inhibits the motion of interstitial fluid inducing larger poroelastic effects, and thus a higher loss modulus was observed. Poroelasticity characteristics were not specifically examined in this study; however, poroelastic studies could supplement this work by examining explicitly how interstitial fluid can flow

through the hydrogel's porous solid polymer network for both the range of concentrations and fabrication parameters [36]. Poroelasticity has been characterized previously using compression tests [37], indentation with an atomic force microscope [36], or through free swelling and constrained swelling experiments [38]. At lower concentrations more swelling is observed, thus more interstitial fluid is moved in hydrogel's porous network during deformation explaining the increase in loss modulus at lower concentrations.

The observed changes in weight degree of swelling, storage modulus, and loss modulus due to electrolyte concentration can be seen in Figure 5.5a and 5.5b, which show scanning electron micrographs of the porous hydrogel at 0.5 M and 0.05 M KOH, respectively. At higher concentration the pores are smaller and more tightly packed together, while at low concentration the pores become enlarged due to the influx of electrolyte, which correlates with the observed increase in weight degree of swelling and loss modulus. Figure 5.5 also shows that the per unit volume crosslinked polymer available to resist deformation decreases, hence the storage modulus decreases.

5.4.2 Effect of Cyclical Testing Frequency

For all experimental sets, increasing the testing frequency increased the storage modulus of samples, as more internal friction of the polymer network restricted deformation. For almost all experimental sets, increasing the testing frequency increased the loss modulus of samples, as poroelastic effects become more pronounced and the fluidic portion of the hydrogel resists tensile stress based deformation [36]. Frequency had a greater effect on the storage and loss modulus of samples tested at lower concentrations, as the difference between results at 0.1 Hz and 10 Hz becomes greater. This effect became pronounced at the high range of fabrication parameters when the network density became larger, and it took more energy to cyclically deform the network. While increasing the frequency in this work in general increased the loss modulus, there exists
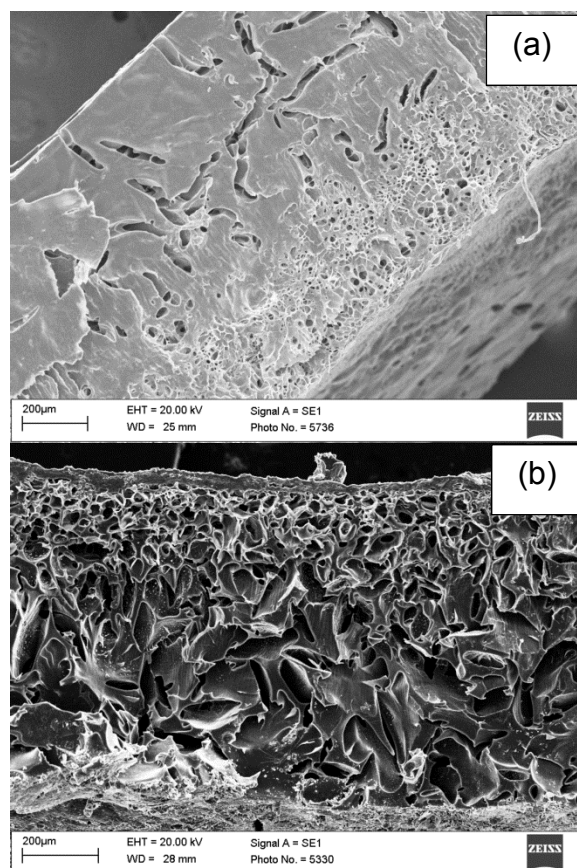
Figure 5.5: Scanning electron micrographs of hydrogel cross sections for samples photopolymerized at 1.74 mW/cm^2 for 100 s with 4% weight crosslinker and immersed in (a) 0.5 M KOH and (b) 0.05 M KOH.

a higher frequency at which glass transition occurs. At this critical frequency a peak in loss modulus would be observed, and further increasing the frequency would result in a decreased loss modulus back towards a dominant elastic response [39]. This would explain the loss modulus trends seen in Figure 5.3b; where for samples in 0.05 M KOH above 160 seconds exposure time, increasing the frequency decreased the observed loss modulus. The sample moving to and through glass transition with increased frequency occurs in much the same as lowering the temperature of the sample [39].

For traditional tensile testing a crosshead displacement rate of 5 mm min^{-1} (0.083 mm second^{-1}) is generally used. Here, frequencies between 0.1 Hz and 10 Hz altered the crosshead displacement rate within the range of 0.005 mm second^{-1} and 0.5 mm second^{-1}, respectively.

177

Therefore, the traditional crosshead displacement was covered in this range, and the max/min frequencies examined allowed determination of mechanical properties outside traditional deformation zones. For researchers moving towards higher frequency actuation devices, these changes to storage and loss modulus must be considered in device design and numerical modeling.

5.4.3 Effect of Fabrication Parameters

Increasing the photopolymerization intensity and exposure time, increases both the storage modulus and loss modulus of a hydrogel. Previously, a neutral-charge HEMA composition was examined using Photo-DSC [40]. Their results showed that the photopolymerization reaction reaches saturation after a critical exposure time and conversion of monomer plateaus, with this critical time being dependent on the photopolymerization intensity. For the range of intensities tested here, monomer conversion becomes complete between 4-8 minutes, which is above the range of photopolymerization times tested here and thus no definitive plateau in dynamic mechanical properties was observed. Therefore, the testing range for exposure time could be increased further to examine the affect on dynamic mechanical properties. These Photo-DSC experiments also showed that increasing the photopolymerization intensity increases the reaction rate, which leads to an increased conversion of monomer to polymer [40]. Thus, the polymer would have a higher storage modulus, and due to the increased cross-linking, higher loss modulus as is seen in Figure 5.3. A plateau in dynamic mechanical properties as affected by photopolymerization intensity was also not observed; therefore, the photopolymerization intensity range could be increased to examine the affects of higher intensities.

Increasing the photopolymerization intensity also decreases the pores size of the hydrogel, as seen when comparing Figures 5.5a and 5.6, but had a lesser effect on pore size than changing the electrolyte concentration. This decreased pore size also directly correlates to an

178

increase in the number of crosslinks occurring within the hydrogel, and hence the storage modulus of the sample is increases as the photopolymerization intensity is increased.

Increasing the percent weight crosslinker increases the hydrogel's polymer network density thereby making the structure more resistant to deformation and inhibiting swelling [15, 41]. This is observed in Figure 5.2a-b as both the storage and loss modulus increased for samples swollen at both concentrations. Examining the scanning electron micrographs of the hydrogel's porous structure at 8% and 2% weight crosslinker, as seen in Figures 5.7a and 5.7b, respectively, shows the largest difference in porous structure among all samples. The sample with 8% shows a very dense porous structure with a few macropores formed, while the 2% sample shows a very large pore size throughout the entire cross-section. These morphology deviations account for the very large differences in the maximum and minimum storage modulus and loss modulus observed over the parameter range examined.
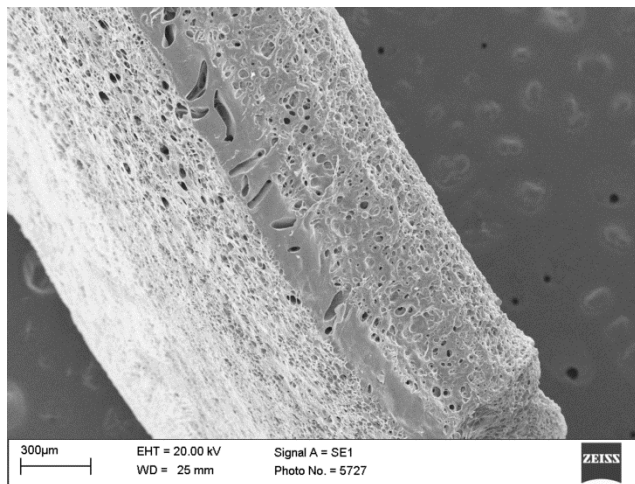
Figure 5.6: Scanning electron micrograph of hydrogel cross section for a sample photopolymerized at 0.86 mW/cm^2 for 100 s with 4% weight crosslinker and immersed in 0.5 M KOH.
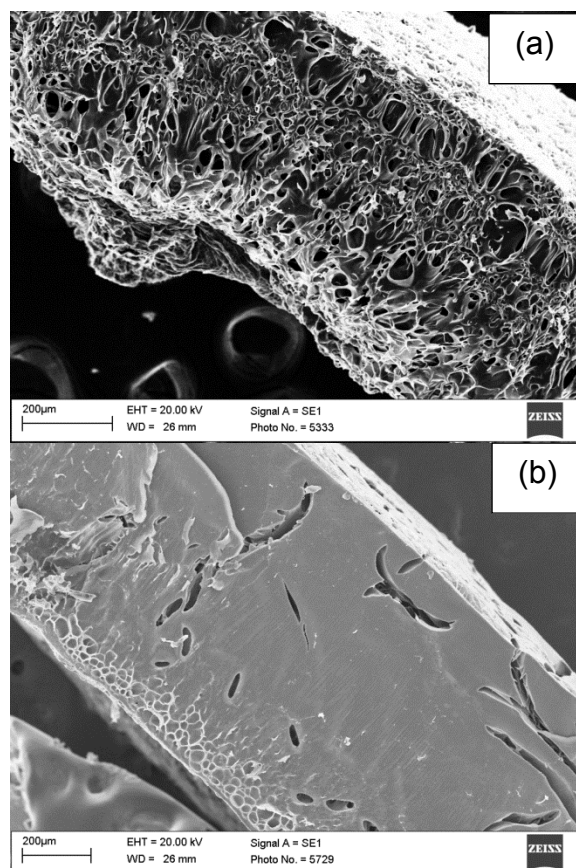
Figure 5.7: Scanning electron micrographs of hydrogel cross sections for samples photopolymerized at 1.21 mW/cm^2 for 100 s immersed in 0.5 M KOH with (a) 2% weight crosslinker and (b) 8% weight crosslinker.

5.5   Conclusions

The weight degree of swelling was influenced most significantly by a change in the percent weight crosslinker in precursor solution, and it was shown that increased electrolyte concentration also decreased weight degree of swelling for all fabrication parameters. The range of swelling observed was consistent with the photopolymerized hydroxyethyl starch-co-HEMA and thermally polymerized double-network poly(ethylene glycol) methyl ether methacrylates-co-poly(acrylic acid) [42, 43]. However, the swelling observed was orders of magnitudes higher than thermally polymerized poly(vinyl alcohol-vinyl acetate)-co-poly(acrylic acid) and photopolymerized poly(HEMA) [44, 45], and a magnitude lower than photopolymerized void containing double network poly(2-acrylamido-2-methylpropanesulfonic acid)-co-polyacrylamide [46].

The storage and loss modulus of hydrogels was also most significantly influenced by the percent weight crosslinker in precursor solution. An increased electrolyte concentration has opposite effects, decreasing the storage modulus and increasing the loss modulus of samples. For all cases increasing the cyclical testing frequency increased both the storage and loss modulus, with a greater effect on samples that had a high network density and that were at a lower concentration. The absolute maximum storage modulus was 1.83 ± 0.18 MPa at 10 Hz, 0.5 M, and 8 % weight crosslinker, while the absolute minimum storage modulus was 68.5 ± 7.2 kPa at 0.1 Hz, 0.05 M, and 0.86 mW cm^{-2}. This range of properties was lower than that typically used for stiffer (GPa range) biomedical materials [45, 47]. However, the reported range was within that previously reported desirable for active microfluidic components to deform under the osmotic pressure generated by pH and electric field stimulation [13, 30]. In addition, the ability to photopolymerize these anionic hydrogels within microchannels presents opportunities for large-scale integration in microfluidic devices [48].

This work presented an analysis of an anionic hydrogel's dynamic mechanical properties and weight degree of swelling, as a function of environmental conditions and fabrication parameters. It was of significant importance to researchers fabricating, designing, or modeling cyclically actuated hydrogel-based components. It also provided a platform for further mechanical property characterization, which could include; a reduced electrolyte concentration, higher cyclical testing frequencies, varied acrylic acid concentration, or increased strain to examine nonlinear viscoelastic behavior.

References

[1]   D. J. Beebe and D. Kim, "Hydrogel-based reconfigurable components for microfluidic devices," *Lab on a Chip,* vol. 7, pp. 193-198, 2007.

[2]   D. J. Beebe, J. S. Moore, J. M. Bauer, Q. Yu, R. H. Liu, C. Devadoss, *et al.*, "Functional hydrogel structures for autonomous flow control inside microfluidic channels," *Nature,* vol. 404, pp. 588-590, Apr 6 2000.

[3]   R. H. Davis, B. T. Good, and C. N. Bowman, "A water-activated pump for portable microfluidic applications," *Journal of Colloid and Interface Science,* vol. 305, pp. 239-249, Jan 15 2007.

[4]   A. K. Agarwal, S. S. Sridharamurthy, D. J. Beebe, and H. R. Jiang, "Programmable autonomous micromixers and micropumps," *Journal of Microelectromechanical Systems,* vol. 14, pp. 1409-1421, Dec 2005.

[5]   H. R. Jiang and L. Dong, "pH-adaptive microlenses using pinned liquid-liquid interfaces actuated by pH-responsive hydrogel," *Applied Physics Letters,* vol. 89, Nov 20 2006.

[6]   J. S. Moore, K. N. Plunkett, M. L. Kraft, and Q. Yu, "Swelling kinetics of disulfide cross-linked microgels," *Macromolecules,* vol. 36, pp. 3960-3966, Jun 3 2003.

[7]   X. Z. Zhang, D. Q. Wu, Y. X. Sun, X. D. Xu, S. X. Cheng, and R. X. Zhuo, "Biodegradable and pH-sensitive hydrogels for cell encapsulation and controlled drug release," *Biomacromolecules,* vol. 9, pp. 1155-1162, Apr 2008.

[8]   M. Gumusderelioglu, D. Cetin, and A. S. Kahraman, "Novel Scaffolds Based on Poly(2-hydroxyethyl methacrylate) Superporous Hydrogels for Bone Tissue Engineering," *Journal of Biomaterials Science-Polymer Edition,* vol. 22, pp. 1157-1178, 2011.

[9]   G. H. Pollack, "Muscle contraction as a polymer-gel phase-transition," *Smart Structures and Materials 1999: Electroactive Polymer Actuators and Devices,* vol. 3669, pp. 45-50, 1999.

[10]   B. Loret and F. M. F. Simoes, "Effects of the pH on the mechanical behavior of articular cartilage and corneal stroma," *International Journal of Solids and Structures,* vol. 47, pp. 2201-2214, Aug 15 2010.

[11]   S. R. Eisenberg and A. J. Grodzinsky, "The Kinetics of Chemically-Induced Nonequilibrium Swelling of Articular-Cartilage and Corneal Stroma," *Journal of Biomechanical Engineering-Transactions of the Asme,* vol. 109, pp. 79-89, Feb 1987.

[12]   M. E. Harmon, M. Tang, and C. W. Frank, "A microfluidic actuator based on thermoresponsive hydrogels," *Polymer,* vol. 44, pp. 4547-4556, Jul 2003.

[13]   M. J. Bassetti, A. N. Chatterjee, N. R. Aluru, and D. J. Beebe, "Development and modeling of electrically triggered hydrogels for microfluidic applications," *Journal of Microelectromechanical Systems,* vol. 14, pp. 1198-1207, Oct 2005.

[14]   S. K. De, N. R. Aluru, B. Johnson, W. C. Crone, D. J. Beebe, and J. Moore, "Equilibrium swelling and kinetics of pH-responsive hydrogels: Models, experiments, and simulations," *Journal of Microelectromechanical Systems,* vol. 11, pp. 544-555, Oct 2002.

[15]   B. D. Johnson, D. J. Beebe, and W. Crone, "Effects of swelling on the mechanical properties of a pH-sensitive hydrogel for use in microfluidic

devices," *Materials Science & Engineering C-Biomimetic and Supramolecular Systems,* vol. 24, pp. 575-581, JUN 1 2004.

[16]   S. P. Marra, K. T. Ramesh, and A. S. Douglas, "Mechanical characterization of active poly(vinyl alcohol)-poly(acrylic acid) gel," *Materials Science & Engineering C-Biomimetic and Supramolecular Systems,* vol. 14, pp. 25-34, Aug 15 2001.

[17]   F. Horkay, M. H. Han, I. S. Han, I. S. Bang, and J. J. Magda, "Separation of the effects of pH and polymer concentration on the swelling pressure and elastic modulus of a pH-responsive hydrogel," *Polymer,* vol. 47, pp. 7335-7338, Oct 4 2006.

[18]   F. A. Aouada, M. R. Guilherme, G. M. Campese, E. M. Girotto, A. F. Rubira, and E. C. Muniz, "Electrochemical and mechanical properties of hydrogels based on conductive poly (3,4-ethylene dioxythiophene)/poly (styrenesulfonate) and PAAm," *Polymer Testing,* vol. 25, pp. 158-165, Apr 2006.

[19]   E. C. Muniz and G. Geuskens, "Polyacrylamide hydrogels and semi-interpenetrating networks (IPNs) with poly(N-isopropylacrylamide): Mechanical properties by measure of compressive elastic modulus," *Journal of Materials Science-Materials in Medicine,* vol. 12, pp. 879-881, 2001.

[20]   E. A. Wilder, S. Guo, S. Lin-Gibson, M. J. Fasolka, and C. M. Stafford, "Measuring the modulus of soft polymer networks via a buckling-based metrology," *Macromolecules,* vol. 39, pp. 4138-4143, Jun 13 2006.

[21]   M. Ahearne, E. Siamantouras, Y. Yang, and K. K. Liu, "Mechanical characterization of biomimetic membranes by micro-shaft poking," *Journal of the Royal Society Interface,* vol. 6, pp. 471-478, May 6 2009.

[22]   M. Ahearne, Y. Yang, A. J. El Haj, K. Y. Then, and K. K. Liu, "Characterizing the viscoelastic properties of thin hydrogel-based constructs for tissue engineering applications," *Journal of the Royal Society Interface,* vol. 2, pp. 455-463, Dec 22 2005.

[23]   F. Lionetto, A. Sannino, G. Mensitieri, and A. Maffezzoli, "Evaluation of the degree of cross-linking of cellulose-based superabsorbent hydrogels: A comparison between different techniques," *Macromolecular Symposia,* vol. 200, pp. 199-207, Sep 2003.

[24]   J. S. Park, J. W. Park, and E. Ruckenstein, "Thermal and dynamic mechanical analysis of PVA/MC blend hydrogels," *Polymer,* vol. 42, pp. 4271-4280, Apr 2001.

[25]   J. V. Cauich-Rodriguez, S. Deb, and R. Smith, "Dynamic mechanical characterization of hydrogel blends of poly(vinyl alcohol-vinyl acetate) with poly(acrylic acid) or poly(vinyl pyrrolidone)," *Journal of Materials Science-Materials in Medicine,* vol. 7, pp. 349-353, Jun 1996.

[26]   R. H. Liu, Q. Yu, and D. J. Beebe, "Fabrication and characterization of hydrogel-based microvalves," *Journal of Microelectromechanical Systems,* vol. 11, pp. 45-53, FEB 2002.

[27]   S. J. Kim, I. Y. Kim, and S. I. Kim, "Electroactive polymer hydrogels for bio-inspired actuators," *Smart Structures and Materials 2005: Electroactive Polymer Actuators and Devices(EAPAD),* vol. 5759, pp. 144-152, 2005.

[28]   P. D. Topham, J. R. Howse, C. J. Crook, S. P. Armes, R. A. L. Jones, and A. J. Ryan, "Antagonistic triblock polymer gels powered by pH oscillations," *Macromolecules,* vol. 40, pp. 4393-4395, Jun 26 2007.

[29]   E. Jabbari, J. Tavakoli, and A. S. Sarvestani, "Swelling characteristics of acrylic acid polyelectrolyte hydrogel in a dc electric field," *Smart Materials & Structures,* vol. 16, pp. 1614-1620, Oct 2007.

[30]   S. K. De and N. R. Aluru, "A chemo-electro-mechanical mathematical model for simulation of pH sensitive hydrogels," *Mechanics of Materials,* vol. 36, pp. 395-410, May 2004.

[31]   J. R. Saunders, S. Abu-Salih, and W. A. Moussa, "Parametric Chemo-Electro-Mechanical Modeling of Smart Hydrogels," *Journal of Computational and Theoretical Nanoscience,* vol. 5, pp. 1961-1975, Oct 2008.

[32]   O. Okay and S. Durmaz, "Charge density dependence of elastic modulus of strong polyelectrolyte hydrogels," *Polymer,* vol. 43, pp. 1215-1221, Feb 2002.

[33]   W. V. G. Kortum, K. Andrussow, *Dissociation constants of organic acids in aqueous solutions*. London: Butterworths, 1961.

[34]   J. Z. Hilt and D. Biswal, "Analysis of Oxygen Inhibition in Photopolymerizations of Hydrogel Micropatterns Using FTIR Imaging," *Macromolecules,* vol. 42, pp. 973-979, Feb 24 2009.

[35]   R. Marcombe, S. Cai, W. Hong, X. Zhao, Y. Lapusta, and Z. Suo, "A theory of constrained swelling of a pH-sensitive hydrogel" *Soft Matter*, vol. 6, pp. 784-793, 2010.

[36]   M. Galli, E. Fornasiere, J. Cugnoni, and M. L. Oyen, "Poroviscoelastic characterization of particle-reinforced gelatin gels using indentation and homogenization" *Journal of the Mechanical Behavior of Biomedical Materials*, vol. 4, pp 610-617, 2011.

[37]   S. Cai, Y. Hu, X. Zhao, and Z. Suo, "Poroelasticity of a covalently crosslinked alginate hydrogel under compression" *Journal of Applied Physics*, vol. 108, 113514 (8 pgs), 2010.

[38]   J. Yoon, S. Cai, Z. Suo, and R. C. Hayward, "Poroelastic swelling kinetics of thin hydrogel layers: comparison of theory and experiment" *Soft Matter*, vol. 6, pp. 6004-6012, 2010.

[39]   Sperling, L. H. In Introduction to Physical Polymer Science; Wiley: New Jersey, 2006; 4th Edition, Chapter 8, pp 362-365.

[40]   L. Li and L. J. Lee, "Photopolymerization of HEMA/DEGDMA hydrogels in solution," *Polymer,* vol. 46, pp. 11540-11547, Nov 28 2005.

[41]   B. Isik, "Swelling behavior of acrylamide-2-hydroxyethyl methacrylate hydrogels" *Turkish Journal of Chemistry*, vol. 24, pp. 147-156, 2000.

[42]   E. A. Kamoun and H. Menzel, "HES-HEMA nanocomposite polymer hydrogels: swelling behavior and characterization," *Journal of Polymer Research* vol. 19, pp. 9851-9864, 2012.

[43]   S. Naficy, J. M. Razal, P. G. Whitten, G. G. Wallace, and G. M. Spinks, "A pH-sensitive, strong double-network hydrogel: poly(ethylene glycol) methyl ether methacrylates-poly(acrylic acid)," *Journal of Polymer Science Part B-Polymer Physics,* vol. 50, pp. 423-430, 2012.

[44]   W. C. Chang, S. J. Chang, and Y. J. Wang, "Preparation and properties of alpha-phenylcinnamylideneacetylated poly(2-hydroxyethyl methacrylate)," *Journal of Polymer Research,* vol. 11, pp. 317-322, 2004.

[45]   J. V. CauichRodriguez, S. Deb, and R. Smith, "Effect of cross-linking agents on the dynamic mechanical properties of hydrogel blends of poly(acrylic acid)-poly(vinyl alcohol vinyl acetate)," *Biomaterials,* vol. 17, pp. 2259-2264, Dec 1996.

[46]   T. Nakajima, H. Furukawa, Y. Tanaka, T. Kurokawa, and J. P. Gong, "Effect of void structure on the toughness of double network hydrogels," *Journal of Polymer Science Part B-Polymer Physics,* vol. 49, pp. 1246-1254, 2011.

[47]   M. G. Cascone, "Dynamic-mechanical properties of bioartificial polymeric materials," *Polymer International,* vol. 43, pp. 55-69, May 1997.

[48]   D. T. Eddington and D. J. Beebe, "A valved responsive hydrogel microdispensing device with integrated pressure source," *Journal of Microelectromechanical Systems,* vol. 13, pp. 586-593, Aug 2004.

Chapter 6

AC Frequency-based Electrical Stimulation of Hydrogel Microactuators Employing Parylene-N Coated Electrodes[1]

6.1　Introduction

Microscale fluidic regulation systems have presented an opportunity to industrialize processes previously confined to laboratory benches. However, fundamental technical issues remain hampering widespread proliferation of portable medical devices, which include issues such as the integration of pumps and valves that do not expose analytes to high electric charges or overheating [1]. Various microelectromechanical systems (MEMS) have been proposed for active valving [2] and pumping [3] solutions, but the challenge of complex peripherals required to activate devices and cost for disposable devices still remain [4].

One class of active material that has received attention as microfluidic regulation components are hydrogels, because of their ability to be photopatterned *in-situ*, having enhanced performance with reduced scale, and lack of complicated assembly [5]. Hydrogels are hydrated polymeric materials that have been widely employed in systems for drug

delivery [6], biomechanical implants [7], and sensor designs [8], among others. Specifically, stimuli responsive hydrogel polymers can be fabricated to respond to temperature [9], acidic and basic electrolytes [10], and electric fields [11]. Electric field sensitive hydrogels have been of particular interest because of their quick response times and relatively easily integration as actuation components without the need for complex peripherals. They have also been examined as electric field responsive artificial muscles, bending in response to an applied electric field from parallel plate electrodes [12, 13].

Application of an electric field across an anionic hydrogel and electrolyte system causes an electrochemical redistribution of mobile ions, which modifies the equilibrium osmotic pressure. This altered osmotic pressure causes hydrogel swelling towards the anode, and depending on the applied electric potential, deswelling near the cathode [11]. However, electric field responsive hydrogels require applied electric potentials >1.23 V, which cause electrolysis of electrolyte and electrochemical reactions at electrodes. The resulting bubbles, hydrogen, and hydroxide produced disrupt the applied electric field distribution, and modify the established osmotic pressure or change the chemical structure of the hydrogel.

Electrokinetic pumping systems have overcome bubble-related challenges through the application of a periodic, zero net charge current to generate a nonzero average potential between the electrodes [14]. Electrokinetic pumps have also employed selectively deposited dielectric layers to employ asymmetrically capacitance-modulated microelectrode arrays [15]. However, electrolysis aside hydrogel actuation still requires that absolutely no hydrogen or hydroxide is produced at the electrodes, as even small quantities can change the chemical structure of the hydrogel causing deswelling.

The operation of comb-drives in conducting media [16] and dielectrophoretic liquid actuation [17, 18] has however employed electrodes fully coated with dielectric material, in conjunction with

frequency-dependent electrostatic actuation, to overcome bubble, hydrogen, and hydroxide generation. DC electric potentials typical for hydrogel electrical actuation [11] cannot be applied, because electrostatic shielding of the electric field across the induced electric double layer (EDL) must be overcome by employing AC frequency-based electric potentials. The comb-drive systems used parallel electrode configurations with gap sizes of 2-5 μm and electric potentials of 5 V_{pk-pk}, thus requiring actuation frequencies from 5 kHz to 10 MHz depending on the electrolyte concentration [16]. Dielectrophoretic actuation employed coplanar electrodes with ~100 μm gap size and electric potentials of 700 V_{rms}, thus requiring actuation frequencies over 20 kHz [17].

In this work, we demonstrate for the first time that an AC electrical potential with a superimposed DC offset, combined with dielectric coated electrodes, can be used to prevent electrostatic shielding, bubble generation, and electrochemical reactions for the purpose of hydrogel electrical actuation. The dielectric layer halts any electrochemical reactions and electrolyte electrolysis; however, with pure DC electric potentials electrostatic shielding occurs thus AC signals must be applied. We present an analytical RC circuit model for predicting the characteristic actuation frequency where electrostatic shielding can be minimized, thereby allowing the applied electric field to actuate the hydrogel. This analytical model examined the main system parameters of dielectric thickness, electrolyte concentration, and electrode geometry. To evaluate the accuracy of the analytical model, capacitance measurements were undertaken to ascertain the effect of frequency and electrolyte concentration on the system. Moreover, the admittance of the system was measured to determine the impedance as a function of frequency and electrolyte concentration, and from the impedance the apparent power of the system was calculated for a typically applied electric potential. An experimental system was then fabricated based off an optimum operational range from the analytical system, and the hydrogel was

actuated employing the characteristic parameters chosen from the analytical model. The displacement of the hydrogel actuator was characterized, as a function of increasing AC frequency, decreasing Parylene-N dielectric thickness, and at two different electrolyte concentrations. It was shown that all current operational challenges associated with hydrogel electrical actuation could be overcome by applying the principles of frequency-dependent electrical signals employing dielectric coated electrodes.

6.2   Theory and Capacitance Modeling

The physics of electric field hydrogel electro-chemo-mechanical actuation can be described using a coupled combination of the Poisson's equation, Nernst-Planck equation, and the Equations of Motion. In addition, supplementary equations account for the number of fixed ions on the polymer backbone in acidic or basic electrolyte, the hydration of the hydrogel, diffusion through the hydrogel's porous structure, and the osmotic pressure generated. Saunders *et al.* performed a detailed review of this system, highlighting the ability of transport equations to accurately model Microscale hydrogel structures and capture the large-deformation effects of the hydrogel [19].

In a leaky dielectric electrolyte over which the electric field was applied, mobile ions accumulate in an EDL at the electrode-electrolyte interface, thus effectively eliminating any electric field applied to the hydrogel. Previously it was shown for comb-drives in electrolytes that even deionized water at actuation voltages of ~1V will effectively form an EDL to screen all applied electric field [20]. Thus, for DC actuated hydrogel systems with electrolyte concentrations ≥ 1 mM, electric field actuation employing dielectric coated electrodes was fundamentally not feasible. Electric double layer formation at the electrolyte-electrode interface can be prevented by utilizing an AC square wave at a frequency high enough, such that the mobile ions do not have time to accumulate on the dielectric-

coated electrodes. This characteristic frequency transitions the system from an EDL-screened electric field to a uniform field between two coplanar electrodes. Above this characteristic frequency the mobile ions do not have enough time to migrate to the interface, and thus does not form an electric double layer causing electrostatic shielding.

The required characteristic frequency (f_c) is a function of various system parameters, such as the electrolyte concentration, dielectric film thickness, effective electrode width, microchannel height, and electrode gap. To study f_c an analytical RC circuit model for the system's capacitance has been developed. The schematic representation of the analytical and experimental system for electric field hydrogel actuation can be seen in Figure 6.1 and Figure 6.2. A pair of coplanar electrodes on a glass substrate was coated with a dielectric layer. Upon this glass substrate a polymer microchannel was bonded to create a cavity for hydrogel actuation. The hydrogel was surrounded by a working electrolyte, which was influenced by the imposed electric field to modify the hydrogel's osmotic pressure causing actuation. A cross sectional view of the system is shown in Figure 6.2a-c, which shows the three cross-sectional capacitive pathways for the electric field generated and the individual components of these three pathways. Components where electric field lines are perpendicular to the surface can be solved using traditional capacitive equations, while the components where the electric field lines are bent through their capacitive element require the implementation of transformation techniques to solve them analytically. The analytical system was modeled after the experimental system, and thus had an electrode length of 3mm, electrode gap of 2mm, microchannel height of 254 μm, and hydrogel width of 1 mm (square). It is necessary to determine the portion of the electrodes that are active in the actuation of the hydrogel, and the portion that is inactive through the top of the microchannel. This allows the convenient determination of capacitances
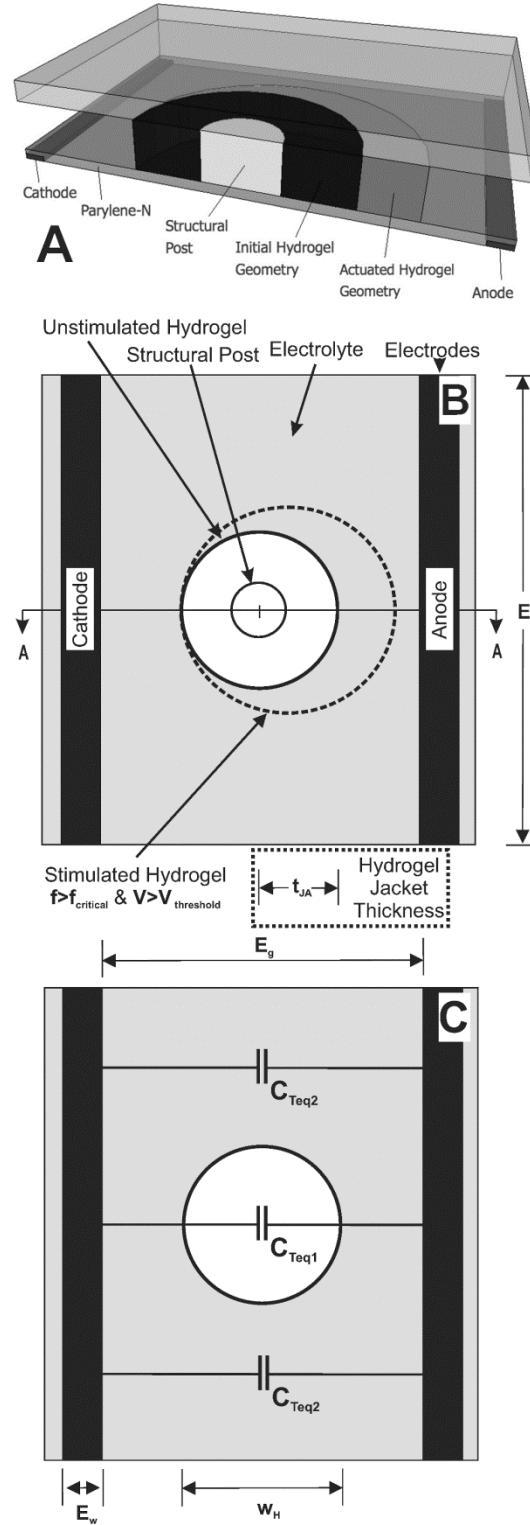
Figure 6.1: Schematic representation of the experimental and analytical system for electric field actuation and capacitance measurements (a) 3D cross section, (b) hydrogel jacket thickness, t_{JA}, due to asymmetrical swelling, and (c) two major capacitive pathways through the hydrogel and media.
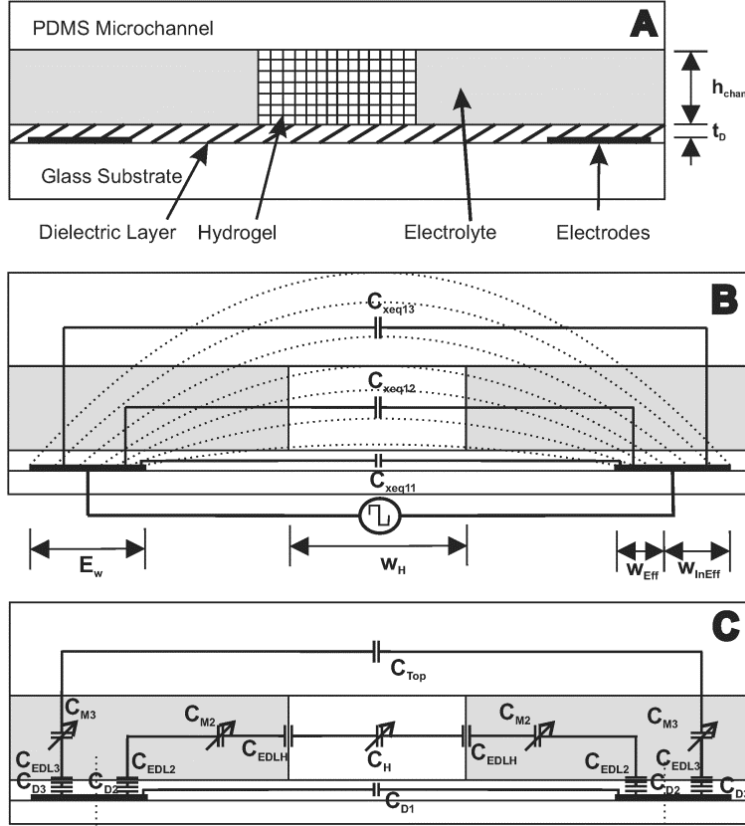
Figure 6.2: Electrical circuit representation of the system for Fig. 1's cross section A-A, displaying (a) major material components and critical dimensions, (b) equivalent circuit paths and effective electrode widths for the analytical model, (c) the individual capacitive and resistive elements through three major cross sectional pathways. *Note*: the top-view pathways through the media, C_{Teq1}, were similar but without the hydrogel components.

and resistances within the system. The extent of the electrode width, w_{eff}, can be determined from

$$w_{Eff} = \frac{E_G}{2}\left(\sqrt{1+\left(\frac{h_{chan}}{E_G/2}\right)^2} - 1\right)$$ (6-1)

where h_{chan} is the height of the microfluidic channel and E_G is the electrode gap from electrode edge-to-edge. The ineffective width, w_{InEff}, can be determined from subtracting the effective electrode width from the experimental electrode width. Hydrogel actuation requires room between the electrodes for a location to actuate into, thus the electrode gap must be large enough to accommodate the deformation. It is shown in Figure

192

6.3 that as the electrode gap was increased the effective electrode width decreased, thus the correct microchannel height must be chosen so that the hydrogel will be appropriately actuated. For the further modeling, the effective electrode width was determined from the experimental geometric system. The experimental electrode width was over 50 μm larger than needed, but was overdesigned to allow for future developments of the system.
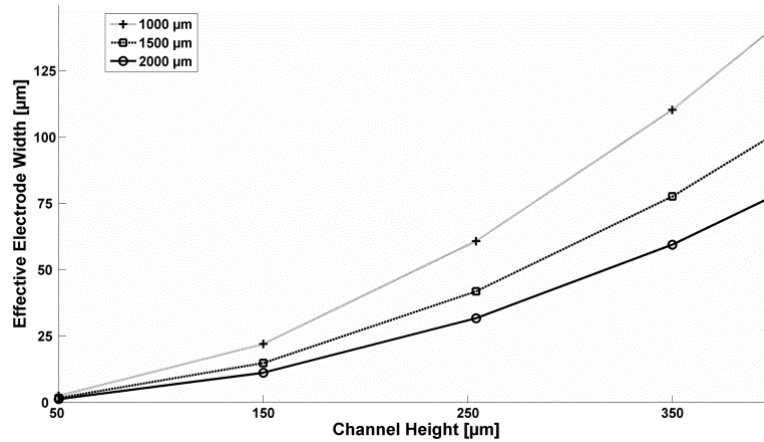
Figure 6.3: Effective electrode width of the coplanar electrodes used for electric field actuation of the hydrogel. The experimental system had a channel height of 254 μm and an electrode gap of 2 mm.

To determine the total capacitance of the system two major top-view capacitive pathways from electrode to electrode must be determined, shown in Figure 6.1b, the pathway running through the hydrogel, C_{Teq1}, and the pathway running through the electrolyte, C_{Teq2}. Both of these pathways can be broken down into components that run through the base dielectric layer on top of the electrodes, that run through the hydrogel, and that run through the top of the microchannel, as seen in Figure 6.2b. These components can be further broken into capacitive elements running through the dielectric layer, electric double layer (Stern and Debye layers), media, hydrogel, hydrogel electric double layer, and top of the microchannel, as see in Figure 6.2c. Excluding the hydrogel from the capacitance system would yield electrical circuits similar to electrowetting on dielectric systems [17, 21].

193

The elements where traditional capacitive equations can be applied are those elements where the electric field lines are approximately perpendicular to the dielectric layer. Taking a closer look at elements in C_{xeq12}; the dielectric layer, C_{D2}, Stern layer, C_{S2}, and Debye layer, C_{DL2}, capacitances at the electrode interface can be determined using

$$C_j = \frac{\varepsilon_j \varepsilon_o A_{Eff}}{t_j}$$
(6-2)

where j=D2, S2, or DL2. In Eq. 6, ε_j and t_j are the dielectric permittivity and thickness, respectively, of the dielectric layer, Stern layer, and Debye layer. The dielectric permittivity of the Parylene-N dielectric layer was assumed to be constant at 2.65. For other Parylene types, such as AF4, the permittivity displays frequency dependence [22]; however, Parylene-N has a frequency independent permittivity up to 60 GHz [23], hence it's choice as the dielectric layer in the system. The effective area, A_{Eff} is calculated by combining the effective electrode width with the square width of the hydrogel, w_H. The Debye layer thickness was primarily a function of the electrolyte concentration and the dielectric permittivity of the electrolyte. Eq. 6 can also be applied to calculate the dielectric layer, Stern layer, and Debye layer through C_{Teq2}. Because of the geometries of the system, these values are the same through C_{Teq1} and C_{Teq2}.

The capacitances of the dielectric layer, Stern layer, Debye layer, and media for the pathway through the microchannel top, C_{xeq13}, can be determined from Eq. 6 as well, where j=D3, S3, DL3, and M3. This calculation also requires that A_{Eff} be substituted with A_{InEff}, which can be determined from the ineffective electrode width, w_{InEff}, and the hydrogel width, w_H. The thicknesses of the dielectric layer, Stern layer, and Debye layer are the same for C_{xeq13} as with C_{xeq12}, while the height of the microchannel is the thickness of the media. For the Stern and Debye layer capacitances surrounding the hydrogel Eq. 6 can be used as well; however, substituting A_{Eff} with the effective area of the hydrogel or $w_H * h_{chan}$. For the purposes of this work it is assumed that the thicknesses

of the Stern and Debye layer surrounding the hydrogel and on top of the electrodes are of the same thickness.

To determine the media and hydrogel capacitances through C_{xeq12}, as seen in Figure 6.2b, and the media in C_{xeq22}, conformal mapping techniques were implemented [24], as the electric field lines are not perpendicular through the dielectric. This was an approximation of the capacitance, and for low ratios of electrode gap to electrode width Chen *et al.* showed that error can exceed 10% [24]. However, conformal mapping is a good replacement to determining the complete elliptical integral for the system, and has been successfully implemented for modeling the capacitive sensing of microdroplets[25]. The media capacitance in C_{xeq12} can be given by

$$C_{M2} = \frac{2\varepsilon_M \varepsilon_o w_H}{\pi} \ln\left[1 + \frac{w_{Eff}}{(E_G - w_H)/2} + \sqrt{\left(1 + \frac{w_{Eff}}{(E_G - w_H)/2}\right)^2 - 1}\right] \qquad (6\text{-}3)$$

Eq. 6-3 can also be used to determine the media capacitance through C_{xeq22}, which can be done by replacing $(E_G\text{-}w_H)/2$ with $E_G/2$. The hydrogel capacitance can be determined in a similar manner, given by

$$C_H = \frac{2\varepsilon_e \varepsilon_o w_H}{\pi} \ln\left[1 + \frac{w_{Eff}}{w_H/2} + \sqrt{\left(1 + \frac{w_{Eff}}{w_H/2}\right)^2 - 1}\right] \qquad (6\text{-}4)$$

since the hydrogel in this model is assumed to be square, the hydrogel width, w_H, is in the capacitance equations. In Eq. 6-4 the effective hydrogel permittivity, ε_e, is given by

$$\varepsilon_e = \varepsilon_p \left[\frac{\varepsilon_p + \varepsilon_m - \dfrac{H}{1+H}(\varepsilon_p - \varepsilon_m)}{\varepsilon_p + \varepsilon_m + \dfrac{H}{1+H}(\varepsilon_p - \varepsilon_m)}\right] \qquad (6\text{-}5)$$

where ε_p and H are the dielectric permittivity of the polymer chains and the hydration of the hydrogel, with constant values of 5.6 and 2, respectively. In this work it was assumed that hydration was constant at its initial

195

hydration state; however, for all hydrogel actuation the hydration would change with deformation. Thus, as the hydration increased with increased deformation the effective hydrogel permittivity would increase. This assumption would not affect the characteristic frequency but would affect the total capacitance.

Eq. 6-5 as well as almost all of the capacitance equations relies on the dielectric permittivity of the potassium hydroxide electrolyte media. In this work the permittivity was assumed to be constant for simplicity; however, in general electrolyte permittivity is frequency dependent following the Debye relaxation process [26]. Frequency dependency requires the determination of both real and imaginary electrolyte permittivities, which are a function of the angular frequency, admittance, electrolyte capacitance, and system capacitance in air. Increasing frequency effects reduce the real part of part of permittivity away from the real permittivity of water, and decrease the imaginary part of complex permittivity [26]. At microwave frequencies it was shown experimentally that increasing electrolyte concentration within this system of complex permittivity tends to increase the real part of complex impedance while decreasing the imaginary component [27], with similar trends assumed at lower frequencies. As this work deals with 1-10 mM solutions of KOH and frequencies below 10 MHz, the effects of the assumption of constant electrolyte permittivity would be minimized but should be included for future optimizations of the equation system.

The three capacitances in series above the electrode form the electrode interface capacitance, which was used to determine the characteristic frequency for hydrogel actuation. Bazant *et al.* proposed the electrode-electrolyte system is governed by the dominant time constant of the entire circuit model [28]. In this case the dominant time constant of the system was a function of the electrode interface capacitance. This capacitance can be determined by

$$C_{EINT} = \left(\frac{1}{C_{D2}} + \frac{1}{C_{S2}} + \frac{1}{C_{DL2}} \right)^{-1} = \left(\frac{1}{C_{D2}} + \frac{1}{C_{EDL2}} \right)^{-1} \qquad (6\text{-}6)$$

Combining all the capacitances in series affecting the hydrogel, C_{xeq12} can be determined by

$$C_{xeq12} = \left(\frac{2}{C_{D2}} + \frac{2}{C_{EDL2}} + \frac{2}{C_{M2}} + \frac{2}{C_{EDLH}} + \frac{1}{C_H} \right)^{-1} \qquad (6\text{-}7)$$

In the same way as C_{xeq12}, one can determine C_{xeq13}. In addition, C_{xeq22} can be calculated by combining the series capacitances of the dielectric layer, Stern layer, Debye layer, and media. The total capacitance of the system is determined by $C_{Total} = C_{Teq1} + 2C_{Teq2}$.

The capacitances of elements within the pathway C_{Teq1}, as calculated by the analytical model, can be seen in Figure 6.4a. The electrode interface capacitance, C_{EINT}, linearly decreased as the dielectric layer's thickness was increased from an initial thickness of 100 nm. The electrode interface capacitance was dominated by the dielectric layer's component; and thus as the thickness was increased, the influence of the Stern and Debye layer decreased causing a further decrease in the electrode interface capacitance. The media and hydrogel capacitances were not influenced by a change in the dielectric layer's thickness, and remained constant at 0.2 pF and 0.042 pF, respectively. The capacitance of C_{xeq12} was initially 0.027 pF, and decreased with increased dielectric thickness as the electrode interface capacitances become smaller and influenced the system to a larger degree. The capacitance of C_{xeq13} was not significantly influenced by dielectric thickness, and was always lower in magnitude than C_{xeq12} at a value of ~0.01 pF.

The total capacitance of the system, C_{Total}, and the major contributions to it are shown in Figure 6.4b. All of the capacitances examined decreased as the dielectric layer increased. Thus, the total capacitance started (at 100 nm) at a magnitude of 0.28 pF and decreased as the dielectric layer was increased, decreasing significantly with

thicknesses >2 µm. The total capacitance was a combination of C_{Teq1} and C_{Teq2}, with starting magnitudes of 0.037 pF and 0.12 pF, respectively. The hydrogel decreases the capacitance of C_{Teq1}, as its dielectric permittivity was lower than that of the surrounding electrolyte. Thus, for the system examined C_{Teq2} dominates the total capacitance of the system.
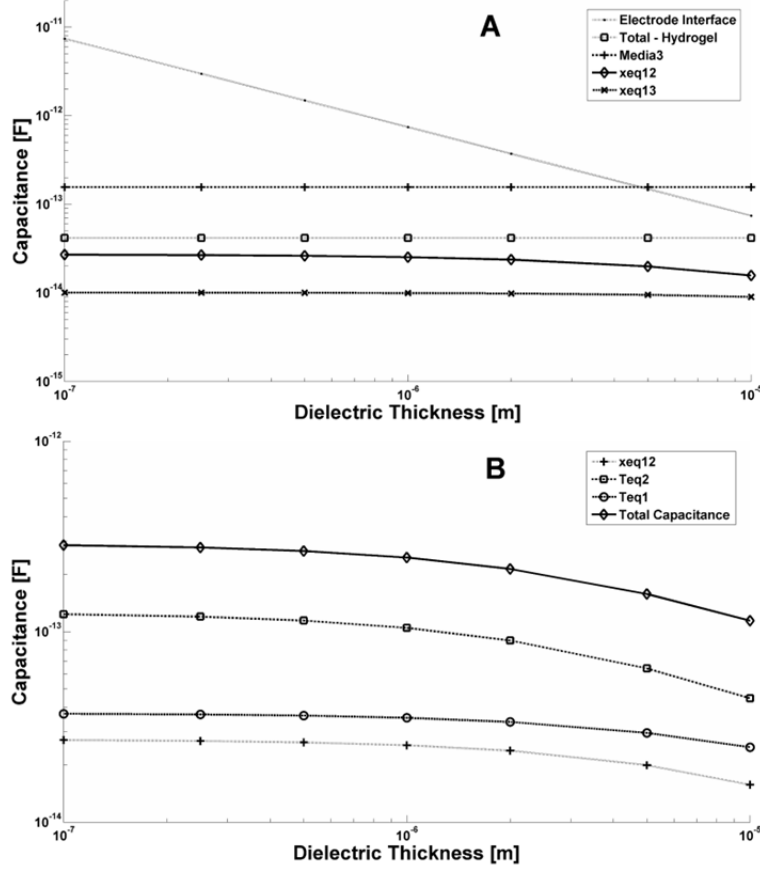
Figure 6.4: Main capacitance elements through (a) the hydrogel's cross section with the total capacitance through the hydrogel pathway (solid line), (b) the top view of the microchannel including paths through the hydrogel and media, and the total capacitance (solid line).

The characteristic actuation frequency of the hydrogel was a function of both the capacitance of the electrode interface and the resistance of the electrolyte. Conformal mapping techniques are employed to calculate the electrolyte resistance

$$R_{M2} = \frac{2\pi}{\sigma_M w_H} \ln\left[1 + \frac{w_{Eff}}{(E_G - w_H)/2} + \sqrt{\left(1 + \frac{w_{Eff}}{(E_G - w_H)/2}\right)^2 - 1} \right] \qquad (6\text{-}8)$$

where σ_M is the electrolyte conductivity. The hydrogel and electrolyte conductivity, σ_H and σ_H, respectively, are primarily a function of the electrolyte concentration but also the diffusivities of potassium and hydroxide, as the electrolyte solution is potassium hydroxide (KOH).

The time constants of the electrode interface can be calculated from $\tau_{EINT}=R_{M2}C_{EINT}$. Using the time constants of the electrode interface, the characteristic frequency can be determined from $f_c=2/(2\pi C_{EINT}R_{M2})$. Since C_{EINT} was determined by three capacitances in series the lowest of these three values dominates, in this case C_{D2}. The characteristic frequency for hydrogel electrical actuation can be seen in Figure's 6.5a and 6.5b, as a function of electrolyte concentration and dielectric thickness, respectively. Characteristic frequency increased as both the electrolyte concentration and the dielectric thickness was increased. For the electrode interface the electrolyte concentration affects the characteristic frequency through the media resistance. Concentration also affects the double layer thickness and hence the double layer capacitance; however, this capacitance was dominated by the dielectric layer capacitance in series at the electrode interface. The dielectric layer thickness directly impacts the determination of the dielectric layer capacitance.

For the thinnest dielectric layer considered (100 nm) and the lowest electrolyte concentration (1 mM KOH), the characteristic frequency was 10 kHz. Increasing the electrolyte concentration by an order of magnitude, while holding the dielectric thickness constant, caused the characteristic frequency to increase by an order of magnitude. Alternatively, holding the electrolyte concentration constant and increasing the dielectric thickness by an order of magnitude caused the characteristic frequency to increase by an order of magnitude. Above the characteristic actuation frequency all electrostatic shielding of the applied electric field can be minimized, and the full applied electric field induces actuation of the hydrogel.
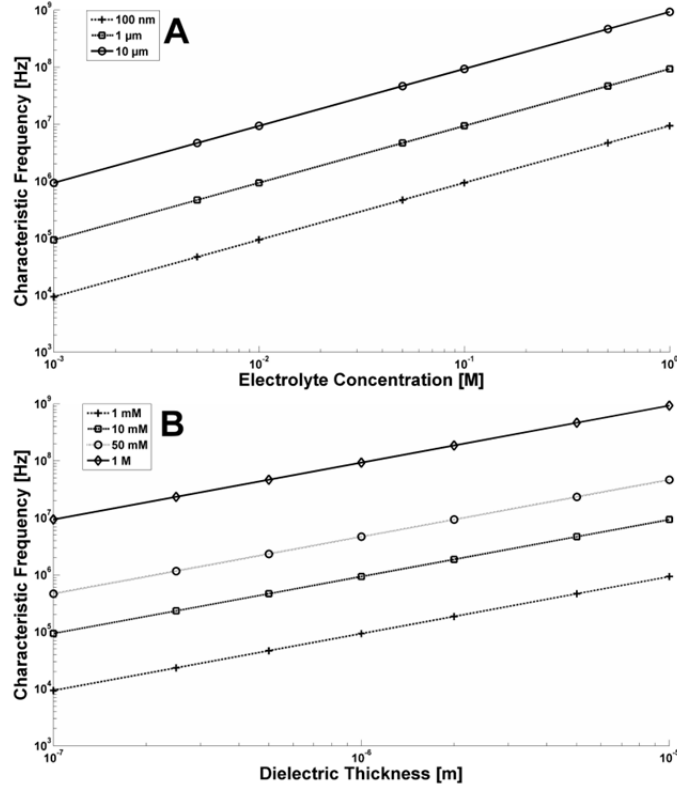
Figure 6.5: Analytical prediction of the characteristic frequency required for successful electrical actuation as affected by (a) an electrolyte concentration from 1 mM to 1 M KOH (b) a Parylene-N dielectric thickness from 100 nm to 10 μm. Subsequent characteristic frequencies span five orders of magnitude from 10 kHz to 1 GHz.

Within the analytical model developed steric effects of increasing electrolyte concentration were not included to determine the characteristic frequency or the total capacitance. For the characteristic frequency, the electrode-electrolyte interface would develop a nonlinear double layer at applied electric potentials higher than k_bT/e (25 mV at room temperature), as the number of ions attracted to this interface at higher voltages would lead to higher electrolyte concentrations; increasing electrostatic shielding. Kilic *et al.* developed a model to include the steric effect on the double layer capacitance [29]; but in this work the double layer was in series with the dielectric layer whose capacitance was at least an order of magnitude lower, dominating the interface's capacitance. Thus a linear double layer was assumed in this work. The steric effects caused by increased applied

electric potentials would increase the total capacitance observed, but only slightly as this capacitance was dominated by the electrolyte media.

Above the characteristic frequency some portion of the electric potential was applied across the electrolyte; however, a portion of the electric potential was also lost within the dielectric layer. Capacitive voltage division can be performed to determine the ratio of electric potential across the media to electric potential

$$\frac{V_M}{V_{app}} = \frac{C_{D2}/2}{C_{D2}/2 + C_{M2}}$$
(6-9)

where V_M is the electric potential across the electrolyte media and V_{app} is the electric potential applied at the electrodes. For a range of electric potentials between 10 V and 40 V the electric potential across the electrolyte media can be seen in Figure 6.6. As the dielectric thickness was increased, the voltage across the media decreased with significant reductions in voltage occurring for thicker films. The electrical system examined in Eq. 9 excluded the hydrogel. The voltage drop across the hydrogel varied with respect to the width, permittivity, and distribution of interior mobile ions. As these three quantities have been assumed constant within this work, it would provide little information to include the hydrogel in Eq. 9. More comprehensive finite element analyses have been previously performed to examine a hydrogel's electro-chemical-mechanical state under the influence of a DC electric field [30, 31]. Moreover, these numerical simulations rely on boundary conditions of applied electric potentials, which can be provided by the outcome of Eq. 6-9 shown in Figure 6.6. Also, not included in Eq. 6-9 are the Stern and Debye layer capacitances, because the system was above the f_c and it was assumed that their influence was negligible.

From an operational standpoint it was desirable to keep the dielectric thickness as small as possible to lower the characteristic frequency; however, fabrication challenges prevented exceptionally thin layers from being fabricated. For a dielectric thickness of ~1 μm, dielectric

breakdown will not occur at the range of electric potentials examined in this work. Parylene-N used in the fabrication of the dielectric barrier has a breakdown threshold of 276 MV/m. The dielectric breakdown was examined for the system under consideration; however, for Parylene-N thicknesses above the 100 nm thickness considered in the model breakdown would not theoretically occur. However, breakdown was experimentally observed for Parylene-N thicknesses greater than 300 nm, as will be discussed later.
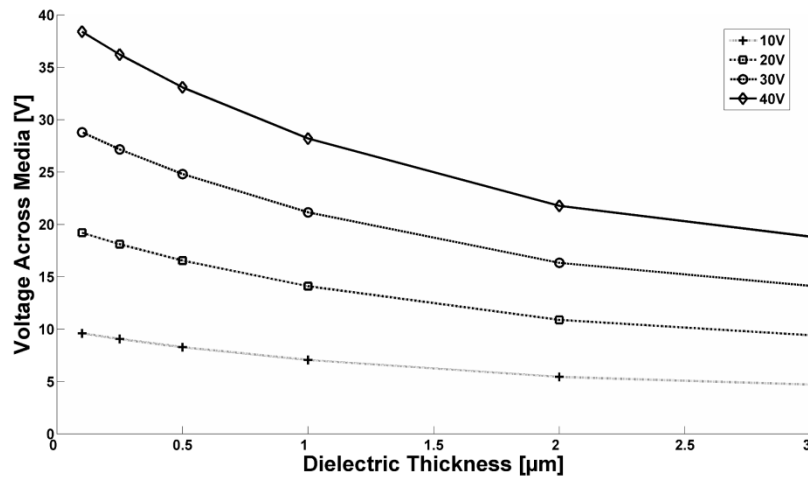
Figure 6.6: Applied potential loss through the Parylene-N dielectric layer, as affected by varying dielectric thickness for an electrode gap of 2 mm. The potentials applied in the experimental actuation section range from 15 V_{pk-pk} to 40 V_{pk-pk} with an 80% duty cycle.

6.3   Fabrication and Experimentation

Fabricating microfluidic chips with dielectric-coated electrodes involve standard cleanroom and non-cleanroom processes. The overview schematic of after each milestone fabrication process can be seen in Figure 6.7, showing cross sections of the substrate. To begin a standard 0211 wafer was Piranha cleaned, then spin-coated with positive photoresist, Figure 6.7-1, baked, exposed to UV-light under a photomask, Figure 6.7-2, and then the photoresist was developed. Afterwards, ~10 nm Cr and ~200 nm Au was deposited using a planar magnetron sputtering system. The electrodes were completed with lift-off in an acetone bath at 35°C under ultrasonic agitation. The 0211 wafers with patterned

202

electrodes were diced into six sections. After dicing poly(dimethylsiloxane) (PDMS) was mixed by adding base and curing agent in a 10:1 ratio, degassed, and then spread over each chip. The PDMS was cured in an oven at 80°C for 2 hours, and prior to Parylene-N deposition, windows were cut out of the PDMS with a scalpel to allow for selective Parylene-N deposition. The chips were then immersed in A-174 silane based adhesion promotion solution. Immediately afterwards, Parylene-N was deposited at room temperature in a vapor deposition polymerization system (SCS PDS 2012) at base pressure of 35 vacuum units, seen in Figure 6.7-4. Parylene-N thickness was measured using both a surface topography profiler (Alpha Step IQ) and an optical transparent film mapping system (Filmetrics F20 SS-1). The thinner the dielectric coating the lower the characteristic actuation frequency and electric field loss through the dielectric layer; however, fabrication challenges creating a uniform film over the electrodes were apparent when electrical actuation was undertaken.

A microchannel for in-situ hydrogel polymerization and subsequent actuation was fabricated using standard soft lithography techniques [32] and a rapid prototyped mold. To irreversibly bond the PDMS microchannel to Parylene-N coated electrodes, both were exposed to oxygen plasma at 250 mTorr, 30 W for 25 s in a reactive ion etcher (Oxford Plasmalab uEtch), seen in Figure 6.7-5. The Parylene-N was masked from the RIE using a piece of PDMS, because if Parylene-N is exposed to RIE it etches at ~100 nm/min [33] and also roughens the surface. Irreversible bonding occurs between the PDMS microchannel and the glass not covered with Parylene-N. Sealing at the edge of the Parylene-N layer's interface with the glass was performed by applying a small film of PDMS using a Q-tip.

After fabrication of the microchip structural support for the hydrogels was fabricated *in-situ* by flushing the microchannel with a precursor mixture of isobornyl acrylate (IBA) and tetraethylene glycol

203

(1) Cleaning +
Spin Coating Photoresist

(2) Photolithography

(3) Sputtering of
Metal Electrodes

(4) Electrode Lift Off +
Selective Parylene-N Deposition

(5) Irreversible Bonding
of PDMS Microchannels

(6) Photolithography of
IBA Support Posts

(7) Hydrogel
Photolithography

⊠ Photoresist ◻ PDMS
■ Electrodes ▨ Hydrogel
⬚ Parylene ▦ Posts
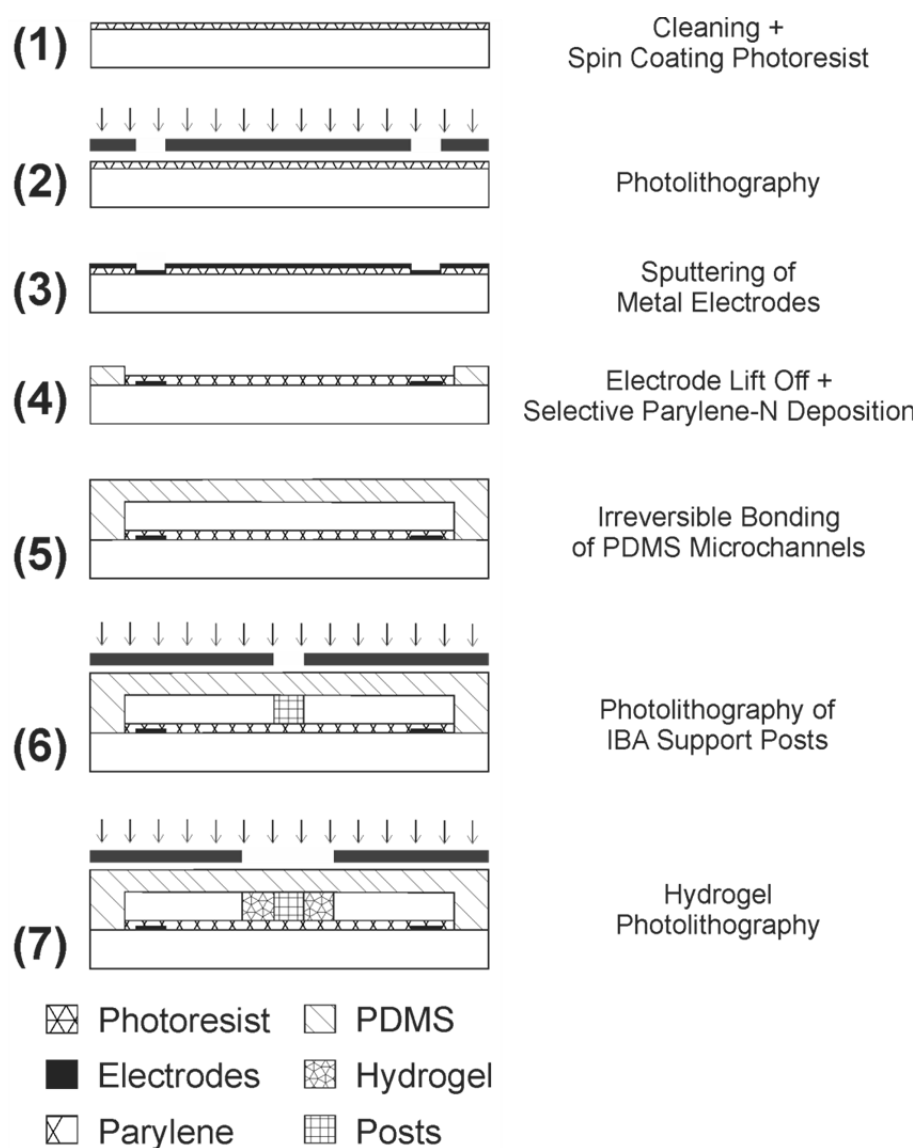
Figure 6.7: Fabrication process flow for the experimental microchips with *in-situ* hydrogels photopolymerized between electrodes. Cross-sections of the substrate were shown at each milestone stage.

dimethacrylate (TEGDMA) in a 9:1 weight ratio, and with 3% weight photoinitiator 2,2-dimethoxy-2-phenyl-acetophenone (DMPA). The precursor was exposed to 365 nm UV light (EXFO Acticure 4000) using a photomask for 60 seconds at 2.42 mW/cm^2 (measured at the sample). The UV intensity at the sample was measured with a ABM Mask Aligner cure-site radiometer. The channel was flushed with methanol to remove all

204

unpolymerized material, flushed with DI water and air, than heated at 30°C to drive out any remaining water vapor.

Active hydrogel structures are fabricated around the posts by flushing the channel with a precursor mixture composed of 2-hydroxyethyl methacrylate (HEMA) and Acrylic Acid (AA) in a 4:1 molar ratio, with 2% weight crosslinker ethylene glycol dimethacrylate (EGDMA) and 3% weight DMPA. To define the hydrogel structure the photomask was aligned to the posts and the precursor was exposed to 365 nm UV-light for 100 seconds at 1.21 mW/cm^2 (measured at the sample), as seen in Figure 6.7-7. The microchannel was flushed with methanol to remove any unpolymerized precursor material, than flushed with DI water to equilibrate the hydrogels and allow them to be stored until testing.

Two major testing sequences were undertaken; total capacitance and admittance measurements, and frequency-based electrical hydrogel actuation. Both testing sequences used microchips with *in-situ* that were fabricated with the same fabrication procedures, except with slightly different Parylene-N thicknesses. Electrical characterization of capacitance and admittance measurements was performed with a Keithley 4200 SCS system with a Signatone probe station. The samples were equilibrated in an appropriate potassium hydroxide (KOH) concentration, subjected to a 30 mV$_{pk-pk}$ AC signal with varying frequency, and the subsequent capacitance and admittance was measured. Each microchip had six reservoirs for testing, and thus measurements were taken on six samples at a particular combination of electrolyte and Parylene-N thickness. Microfabrication defects did not always allow all six reservoirs to be tested; however, a minimum of four measurements were always taken. Parylene-N thicknesses of 2145±55 nm, 648±11 nm, and 565±7 nm were measured, and at each Parylene-N thickness electrolyte concentration of 1 mM, 5 mM, and 10 mM KOH were used to equilibrate the samples.

Hydrogel frequency-based actuation and observations of deformation were performed with a system of equipment, as shown in Figure 6.8. Actuation was performed with a function generator (Agilent 33220A), a DC power source (Agilent E3647A), amplifier (Agilent 33502A), oscilloscope (Agilent DSO 2004A), and platinum tipped high voltage probes (Micralyne's Microfluidic Tool Kit) for contact with the chip's contact pads. Actuation was observed through a CCD camera (Ziess AxioCam ICc1) attached to an optical microscope (Ziess Discovery.V12), which outputted video to AxioVision's Labview where deformation measurements could be performed. Hydrogel's that underwent frequency-based actuation had Parylene-N thicknesses of 2166±77 nm, 648±11 nm, and 348±13 nm. These chips were equilibrated with KOH concentrations of 1 mM, 5 mM, and 10 mM prior to any actuation.
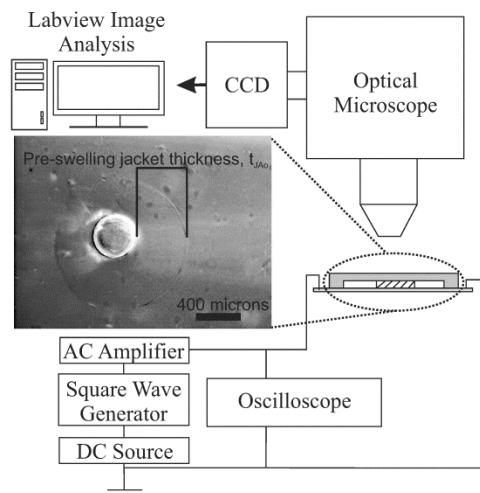
Figure 6.8: Experimental system for electric field actuation of hydrogels and subsequent characterization through video capture and image analysis software. The main electrical components include a function generator, DC power supply, amplifier, and oscilloscope.

6.4 System Capacitance Measurements

Measurements were performed to determine the total capacitance and admittance of hydrogel microchips on samples with varying Parylene-N thickness and electrolyte concentration. Experimental capacitance measurements were compared to the analytical total capacitance results.

206

The capacitance and admittance measurements taken were used to calculate the apparent power of the system under a typical electrical load.

The results of capacitive testing can be seen in Figures 6.9a, 6.9b, and 6.9c, which correspond with Parylene-N thicknesses of 2166±77 nm, 648±11 nm, and 565±7 nm, respectively. For samples with the thickest Parylene-N layer (2166±77 nm), seen in Figure 6.9a, after 10 kHz a higher electrolyte concentration within the chip caused a higher total capacitance. The larger amounts of mobile ions present in the system allow more charge to be accumulated within the system. The analytical model's prediction of the total system capacitance was 0.21 pF. For 1 mM concentration, the experimental system trends towards a frequency-independent capacitance of 0.22 pF at 3 MHz. Higher concentration of 5 mM and 10 mM trend towards higher capacitances of 0.23 pF and 0.3 pF at 4 MHz and 9 MHz, respectively.

For medium Parylene-N thickness samples (648±11 nm), as seen in Figure 6.9b, after ~10 kHz a higher electrolyte concentration within the chip caused a higher observed capacitance. The analytical model's prediction of total system capacitance was 0.26 pF. For 1 mM concentration, the system trended towards a frequency-independent capacitance of 0.25 pF at 800 kHz. For 5 mM and 10 mM concentrations, the total capacitance trended towards 0.3 pF and 0.35 pF at 4 MHz and 8 MHz, respectively.

After 10 kHz the thinnest Parylene-N samples (565±7 nm), seen in Figure 6.9c, displayed the same trend of higher electrolyte concentration causing a higher observed capacitance. Previous to 10 kHz the 5 mM samples were exhibiting a higher system capacitance and larger 1/f noise than previously observed for other samples tested. This could be due to fabrication imperfections within that particular chip causing a thinner Parylene-N layer than measured on the sample silicon wafer, as the higher total capacitance below 10 kHz is consistent with an even thinner Parylene-N layer. For 1 mM and 10 mM the frequency-independent
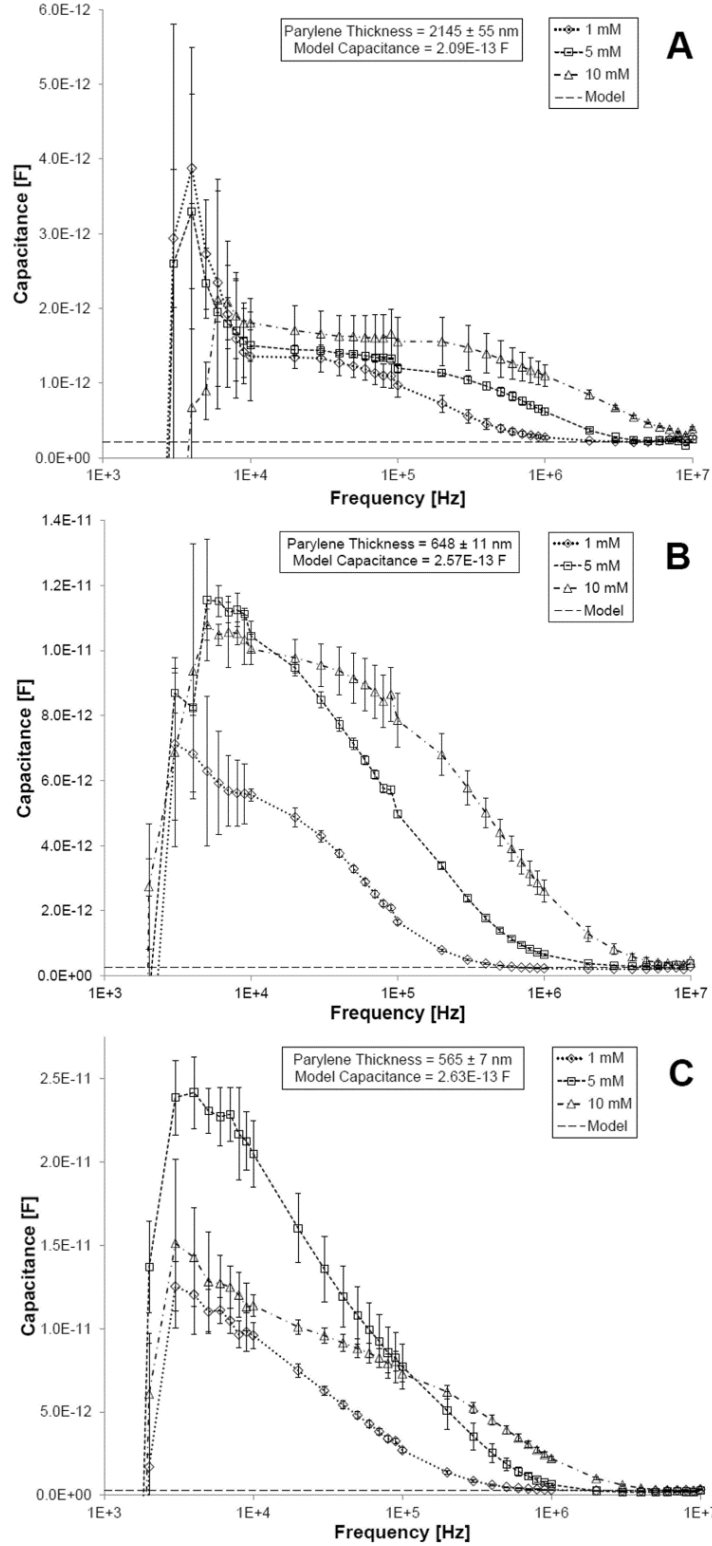
Figure 6.9: Experimental capacitance measurements as a function of applied frequency, electrolyte concentration and Parylene-N thicknesses of a) 2145±55 nm b) 648±11 nm c) 565±7 nm. Capacitance to be higher at lower frequencies and at higher frequencies plateau to magnitudes close to analytical model total capacitance predictions.

208

capacitance was 0.26 pF and 0.38 pF at 2 MHz and 4 MHz, respectively, compared to the analytical prediction of capacitance of 0.26 pF.

In general decreases in the Parylene-N thickness increased the peak total capacitance of the system, ranging from ~4 pF for the thickest samples to 24 pF for the thinnest samples. This trend displays the increased impact of electrolyte on the system as the effects of capacitance from the dielectric are diminished slightly. For all systems 1/f noise was observed in the lower frequency regimes, with higher electrolyte concentrations causing more noise throughout the frequency spectra.

The analytical model accurately predicted the frequency-independent capacitance of the systems when compared to experimental measurements. This model was more accurate for 1 mM samples, as with higher concentrations a higher capacitance was observed. At present the analytical model does not account for the impact of varying the electrolyte concentration, which would impact the dielectric properties of the media. In addition, the analytical model could be expanded to include the frequency-based effect of capacitance on the system. The most dominant portions of the model to the overall capacitance are the dielectric thickness and the electrolyte media, and including frequency-based effects in these two components could allow analytical prediction of frequency-based capacitance.

In parallel to capacitance measurements the admittance (G_p) of the system was measured, and from this and the capacitance (C) measurements the impedance of the system can be determined. In addition, this impedance can be used with typically applied electric potentials to calculate a sample of the apparent power for actuation purposes. The impedance (Z) of the system can be calculated from $Z=(sqrt(G_p^2+(jwC)^2))^{-1}$, and the apparent power from $P=(V_{rms}^2)/Z$. The impedance and the apparent power of the three systems tested can be seen in Figures 6.10a, 6.10b, and 10c. The power was calculated from a

V_{pk-pk}=40 V with a duty cycle of 80 %, because it was the highest electric potential applied in the forthcoming electrical actuation observations.

The thick Parylene-N samples, as seen in Figure 6.10a, had an initial impedance of 1.27 MΩ which increased to a peak of 13.2 MΩ at a frequency of 9 kHz, and decreased to 58.3 kΩ at 10 MHz. For both electrolyte concentrations 1 mM and 5 mM there was no discernible difference in impedance, except between ~200 kHz and ~2 MHz where 1 mM displayed higher impedance. Examining the apparent power of the system displays a mirror trend, where a minimum apparent power of 77.4 µVA occurred at 9 kHz and increased to 17.2 mVA at 10 MHz. Medium thickness Parylene-N samples, shown in Figure 6.10b, had observable impedance differences between 1 mM and 5 mM concentrations. The 1 mM concentration had an initial impedance of 1.57 MΩ which increased to a peak of 5.65 MΩ at 5 kHz and then decreased at higher frequencies to a final value of 56.4 kΩ at 10 MHz. For 5 mM the initial impedance was 1.71 MΩ which increased to a peak of 2.28 MΩ at 2 kHz and then decreased to a final value of 39.3 kΩ at 10 MHz. The apparent power displays a mirror trend, where at 1 mM the minimum apparent power of 181 µVA occurred at 5 kHz. The thinnest Parylene-N samples, shown in Figure 6.10c, also displayed distinct differences between 1 mM and 5 mM concentrations. However, not at initial, peak or final impedance values just throughout the frequency regime between the peak and final frequency. The initial impedance was 1.32 MΩ, the peak impedance was 4 MΩ at 2 kHz, and the final impedance was 45 kΩ at 10 MHz. The apparent power displays a mirror trend, where the minimum apparent power was 260 µVA at 2 kHz and the maximum was 27.2 mVA at 10 MHz.

Overall decreasing the Parylene-N thickness caused lower impedance within the system, as there was less dielectric present between the electrodes and the electrolyte. In addition, for the two lowest Parylene-N thicknesses examined it was apparent that a lower electrolyte
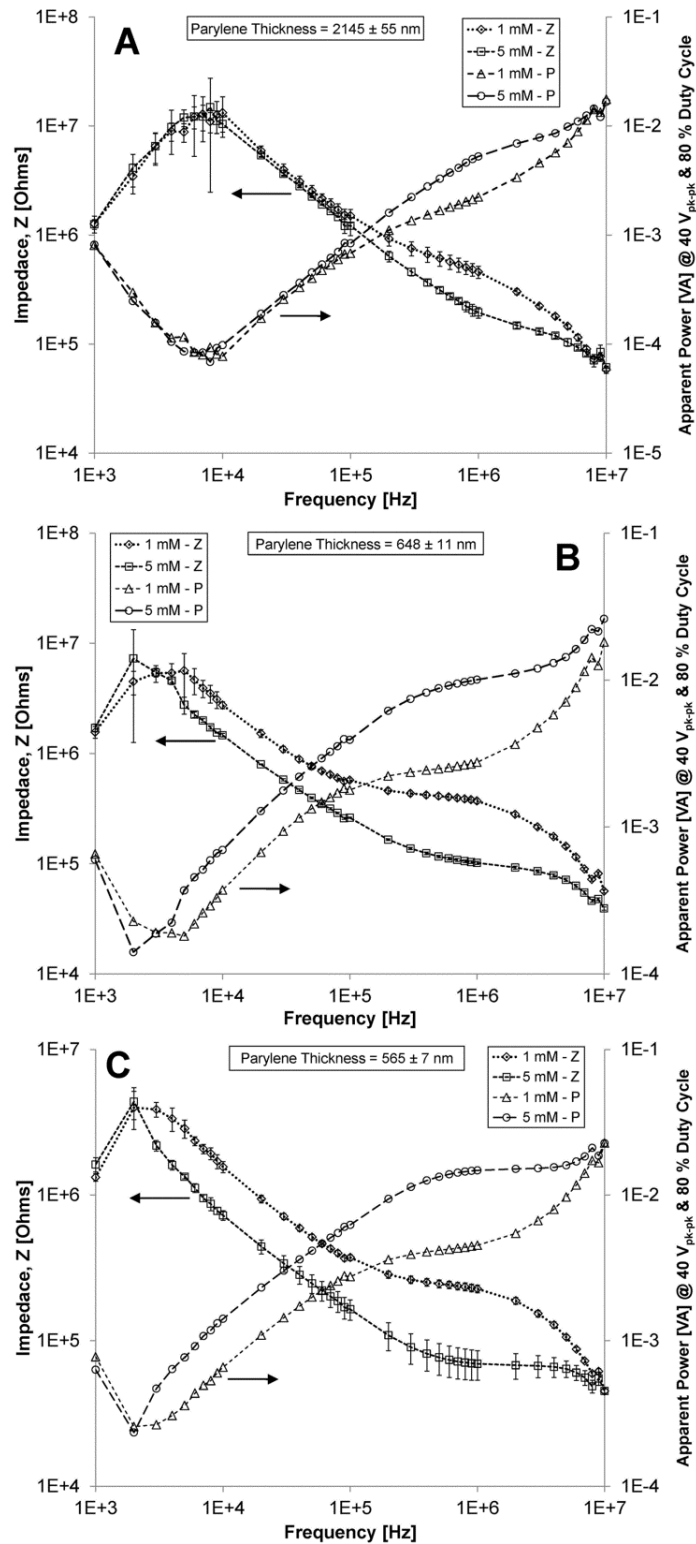
Figure 6.10: Impedance of the system as a function of applied frequency, electrolyte concentration and Parylene-N thicknesses of a) 2145±55 nm b) 648±11 nm c) 565±7 nm. The power was also determined for the system for an applied potential of 40 V_{pk-pk} with an 80 % duty cycle, which represents the maximum potential applied during actuation.

concentration caused more system impedance, as there are less mobile ions present to interact with the electric field. All three systems examined displayed impedance peaks, which were shifted to lower frequencies as the Parylene-N thickness was decreased. These impedance peaks correspond to an apparent power trough or perhaps a location of desired frequency-based operation, as the required apparent power for operation would be significantly decreased. Should the systems examined be operable (significant actuation occurs) at these power troughs it would be suggested to actuate at these frequencies. The impedance spectra observed here with varying Parylene-N thickness and electrolyte concentration was similar in magnitude and frequency response to devices employing dielectric coated electrodes for impedance spectroscopy to determine fluidic composition [34].

6.5 Frequency Dependent Deformation

Fundamental experiments were undertaken to measure hydrogel deformation under AC actuation, with specific focus on measuring the amount of strain induced and the actuation response time. The analytical model provided a prediction of the characteristic frequency where electrostatic shielding would be overcome. Two major systems were actuated with one above and one below the characteristic frequency, depending on the electrolyte concentration used. All systems were actuated with an AC square wave that had a DC offset equal to half the V_{pk-pk} magnitude and a duty cycle of 80 %. Three different Parylene-N thicknesses were used in conjunction with two electrolyte concentrations and varying electric potentials. Upon electrical actuation the hydrogel's transient deformation was measured until final equilibrium deformation was reached, with the last data point in figures being the final equilibrium deformation position. Response times given in figures were the ten-to-

ninety rise time or the speed of response between 10% and 90 % of the final equilibrium deformation.

The first system examined was actuated at frequencies below the predicted characteristic frequency, with 5 mM KOH and Parylene-N thicknesses of 648±11 nm and 348±13 nm corresponding to characteristic frequencies of 302.7 kHz and 162.9 kHz, respectively. Actuation below the characteristic frequency still provided deformation, as seen in Figure 6.11a, 6.11b, and 6.11c. The 648±11 nm sample was actuated at 40 V_{pk-pk}, seen in Figure 6.11a, producing a maximum deformation of 26.6 μm or 6.6 % true strain with a 14.9 second rise time at 100 kHz frequency. True strain was defined as $\delta\varepsilon=\delta t_{JA}/t_{JAo}$ or $\varepsilon=\ln(t_{JA}/t_{JAo})$, where t_{JAo} was the initial hydrogel jacket thickness before electrical actuation. A typical equilibrated hydrogel can be seen in Figure 6.12a prior to actuation, and upon actuation the hydrogel swells asymmetrically towards the anode shown in Figure 6.12b. The 348±13 nm samples were actuated at both 20 V_{pk-pk} and 30 V_{pk-pk} to examine the effects of increased electric potential. At 20 V_{pk-pk} the maximum deformation was 16.9 μm or 5.0 % true strain with a rise time of 37 seconds at 100 kHz, as seen in Figure 6.11b. Increasing the electric potential to 30 V_{pk-pk} increased the maximum deformation to 21.7 μm or 6.4 % true strain with a rise time of 30 seconds. A 50 % increase in the applied V_{pk-pk} only resulted in a 1.4 % increase in the observed true strain, representing a minimal increase in the electrically induced osmotic pressure. At both Parylene-N thicknesses deformation was observed at frequencies as low as 10 Hz, displaying that actuation can occur below the predicted characteristic frequency. For 348±13 nm Parylene-N layers electric potentials greater than 30 V_{pk-pk} were attempted; however, fabricated defects in the Parylene-N layer itself caused breakdown and consistent actuation was not achievable.

The second system examined electrolyte concentrations of 1 mM KOH which had characteristic frequencies below the maximum applied frequency (f_{app}). Since $f_{app}>f_c$ electrostatic shield was minimized.
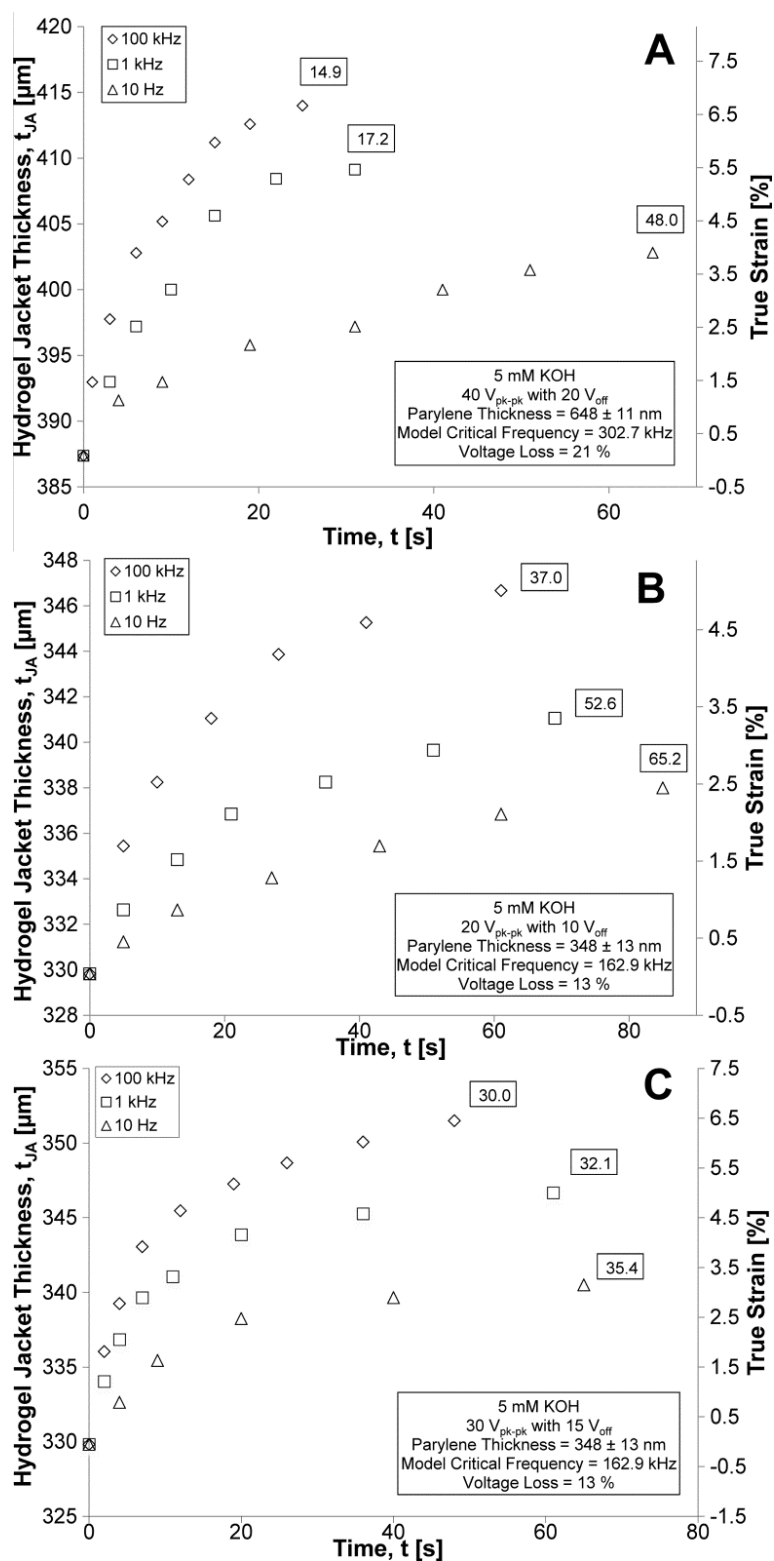
Figure 6.11: Hydrogel electrical actuation at 5 mM KOH as a function of applied frequencies between 10 Hz and 100 kHz with a A) Parylene-N thickness of 648±11 nm and 40 V_{pk-pk} applied potential B) Parylene-N thickness of 348±13 nm and 20 V_{pk-pk} applied potential C) Parylene-N thickness of 348±13 nm and 30 V_{pk-pk} applied electric potential.
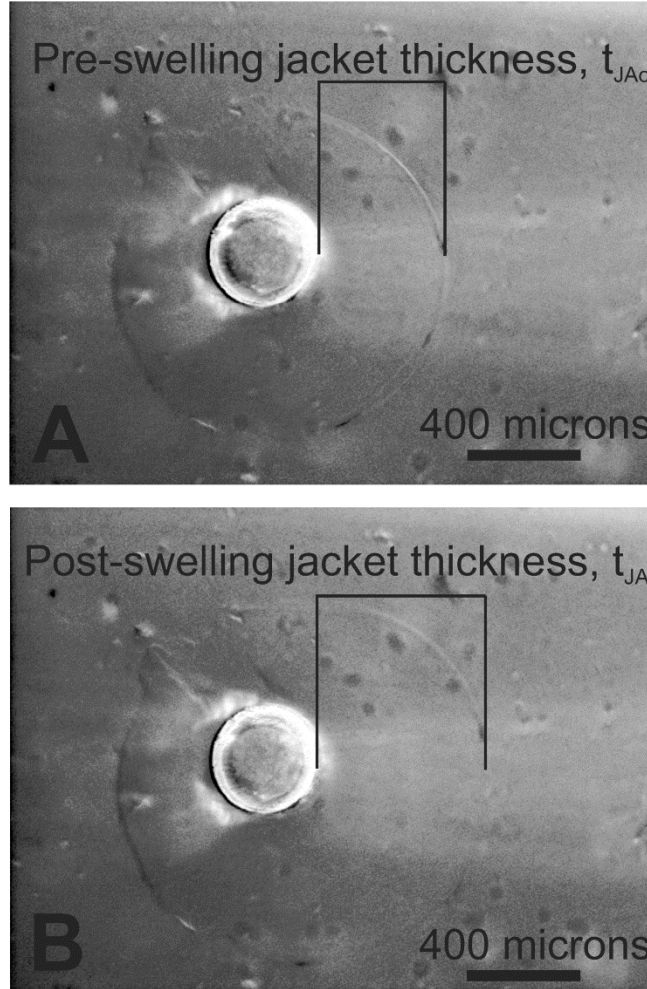
Figure 6.12: Micrograph of a hydrogel between two electrodes that was A) equilibrated in 1 mM KOH B) asymmetrically swollen towards the anode. This asymmetrical swelling comprises a change in the hydrogel jacket thickness, t_{JA}, and was two-dimensional in nature due to confinement by a PDMS microchannel.

This system was tested at Parylene-N thicknesses of 348±13 nm, 648±11 nm, and 907±28 nm, corresponding to predicted characteristic frequencies of 32.6 kHz, 60.7 kHz, and 85.1 kHz, respectively. The 348±13 nm Parylene-N thickness was actuated at 20 V_{pk-pk}, as seen in Figure 6.13a. This actuation resulted in a maximum deformation of 95.4 µm or 17.6 % true strain with a rise time of 15 seconds. Even at 10 Hz there was a deformation of 35.1 µm or 6.8 % true strain, but with a significantly longer rise time of 48 seconds. The 648±11 nm Parylene-N layer was actuated with 30 V_{pk-pk}, as seen in Figure 6.13b. At this electric potential the
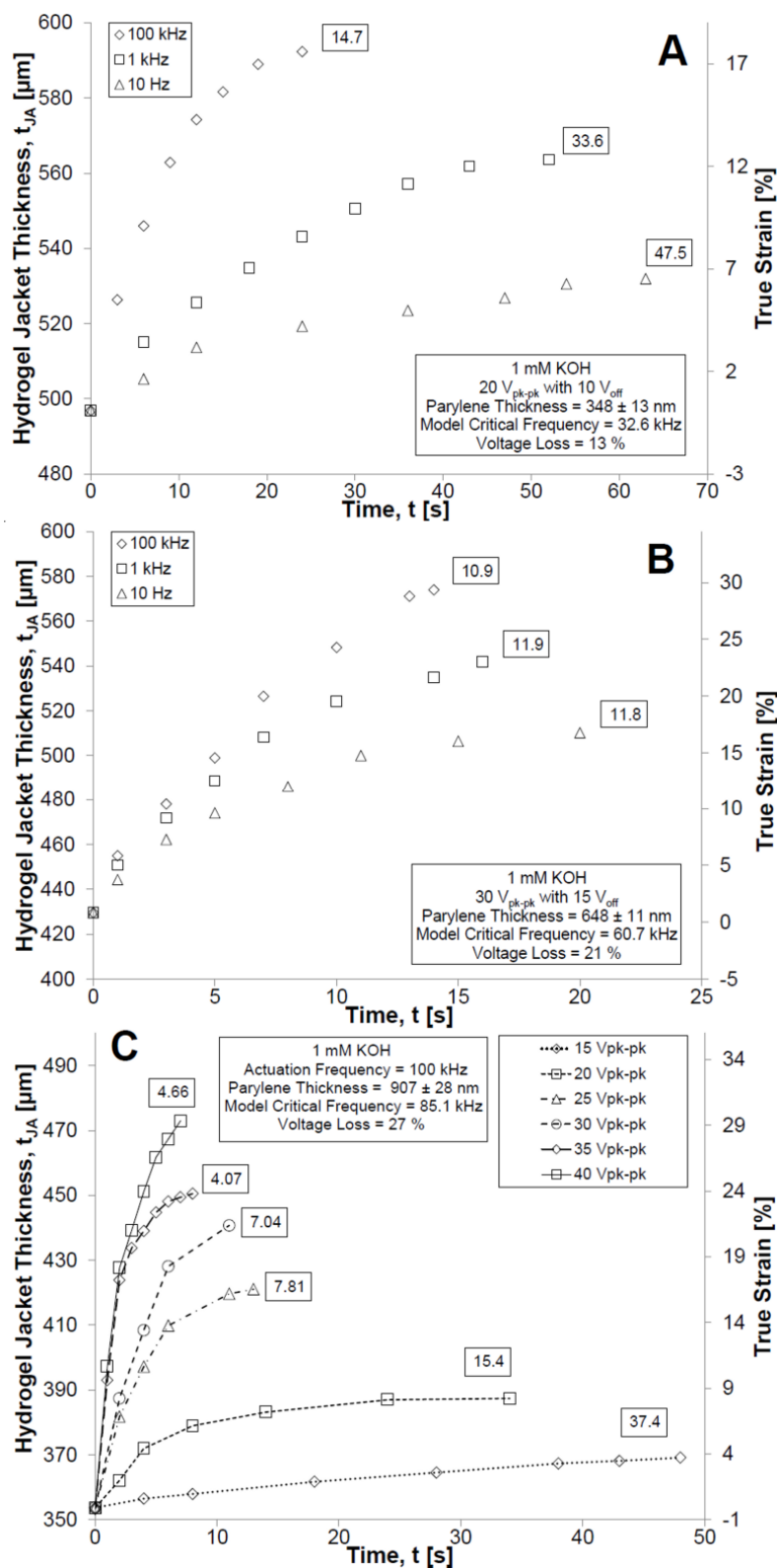
Figure 6.13: Hydrogel electrical actuation at 1 mM KOH as a function of applied frequencies between 10 Hz and 100 kHz with a A) Parylene-N thickness of 348±13 nm and 20 V_{pk} applied potential B) Parylene-N thickness of 648±11 nm and 30 V_{pk-pk} applied potential C) Parylene-N thickness of 907±28 nm and 15-40 V_{pk-pk} potential.

maximum deformation was 144.5 μm or 29 % true strain with a rise time of 11 seconds, and even at 10 Hz the deformation was 80.7 μm or 17 % true strain with a rise time of 12 seconds. The 907±28 nm Parylene-N layer was actuated from 15 to 40 V_{pk-pk}, as seen in Figure 6.13c, at a constant frequency of 100 kHz, above the f_c of 85.1 kHz. At a maximum 40 V_{pk-pk} the deformation observed was 119.3 μm or 30 % true strain with a rise time of 4.7 seconds, while at 37.5% of the maximum V_{pk-pk} the deformation was 15.4 μm or 4 % true strain with a rise time of 37 seconds. An increased electric potential can significantly affect deformation and rise times. Increasing the applied electric potential by 167 % caused a 675 % increase and 703 % decrease in deformation and rise times, respectively. Comparing the work here to Bassett *et al.*'s [11], which employed similar geometry, shows similar deformation and rise times. At 20 V DC Bassetti *et al.* observed 120 μm deformations with a ~1 sec response time, which was deformation comparable to the applied 40 V_{pk-pk} seen in Figure 6.13c. This work required higher applied electric potential because of the losses through the dielectric layer coating the electrodes and the use of a frequency-based duty cycle. Bassetti *et al.*'s faster response time was a result of a stronger buffer concentration and flushing this buffer continually through the microchannel.

In general, increasing the electric potential increased the magnitude of the osmotic pressure developed by increasing the concentration gradient between the hydrogel and electrolyte. This increased pressure directly results in both an increase in the maximum deformation and in most cases a decrease in the rise time responses. In addition, it was shown that increasing the frequency of actuation has a similar effect to increasing the electric potential, where deformation increased and rise times decreased. The effect of the actuation frequency was to disturb the EDL formed on the electrodes, allowing the electric potential to penetrate

217

through to the hydrogel. Thus, as the f_{app} was increased above f_c more of the electric potential was able to actuate the hydrogel.

The actuator system's response kinetics of swelling can be examined through a comparison between the hydrogel's observed response time and the calculated characteristic response time constants. These constants can be determined in response to purely chemical swelling with the diffusion-reaction time constant (DRT) [35], τ_{dr}, or combined chemo-electrical swelling with the electrodiffusion-reaction time constant (EDRT) [36, 37], τ_{edr}. These time constants for the mobile potassium ions were calculated using

$$\tau_{dr} = \frac{t_{JA}^{2}}{\pi^2 \left(\dfrac{H}{2+H}\right)^2 D_{K^+}}$$ (6-10)

$$\tau_{edr} = \frac{t_{JA}^{2}}{\pi^2 \left(\dfrac{H}{2+H}\right)^2 D_{K^+}} \left[1 + \left(\frac{t_{JA}EF}{2\pi RT}\right)^2\right]^{-1}$$ (6-11)

where H is hydrogel hydration before actuation, D_{K^+} is the diffusion coefficient of potassium (1.96×10^{-9} m^2/s), and E is the electric field experienced by mobile potassium ions. Examining a specific system, such as that in Figure 6.12B, shows an observed response time of 10.9 s for an applied electric field of 9.5 kV/m, with losses. The hydration of the system before actuation was 14.4. The calculated DRT was 12.4 s while the EDRT was 19 ms, a difference of three orders of magnitude. It's clear the observed system kinetics can be described more accurately with the DRT, even though an electric field was applied. This counterintuitive result occurred due to the electric field value used within Eq. 11. While 9.5 kV/m was applied between electrodes, the bulk of the hydrogel experiences a lower electric field due to electroneutrality between the mobile and fixed ions within the hydrogel. The hydrogel-electrolyte membrane interface experiences higher electric fields, as mobile ions flux through this interface

and the equilibrium osmotic pressure is modified. Outside the interface region the system's bulk kinetics are governed by diffusion of these mobile ions. Eq. 11 was derived assuming uniform electric fields throughout the hydrogel; however, that was not the case. The difference between the calculated DRT and observed response times could come as a result the inaccurate linearization assumption made during derivation of small changes in concentration and hydration, both experience large changes in this work. In addition, it's generally assumed that the mechanical response of the systems occurs instantaneously compared to the chemical or electrochemical kinetics for gels in high pH regimes [38]; however, Grimshaw *et al.* [37] did note cases where the mechanical deformation lagged behind the driving chemical processes. Further experimental measurements of the longitudinal modulus (M) and hydraulic permeability (k) would be needed to determine the mechanical diffusivity, and hence the quantitative characteristic mechanical response time constant of $\tau_{mech}=t_{JA}{}^2/(\pi^2 Mk)$ [36] in relation to the DRT and ERDT.

Non-uniform fabrication of the Parylene-N coating resulted in areas on the electrode being thinner than the bulk coating and prone to breakdown, or even no coating occurring at all. When an electric potential was applied sufficient to breakdown the dielectric barrier electrochemical reactions occurred generating protons and hydroxide ions at the anode and cathode, respectively. An example of dielectric breakdown at 20 V_{pk-pk} can be seen in Figure 6.14, with electrochemically generated protons diffusing towards the hydrogel causing drastic deswelling. The protons combine with the negatively charged carboxyl groups attached to the hydrogel's backbone, effectively neutralizing the local charge of the hydrogel. The neutral hydrogel then expels excess positive mobile ions previously maintaining electroneutrality, which effectively removes the osmotic pressure acting on the hydrogel. The example system was operated using 1 mM KOH, thus even small quantities of electrochemically generated protons can alter the system's pH. In addition, any electrolysis

that occurs as a result of dielectric breakdown will generate bubbles within the microchannel, also seen in Figure 6.14. These bubbles can significantly alter the electric field applied to the hydrogel system, and in some cases cause actuation failure by entirely blocking the applied electric field. Deposition of a uniform Parylene-N dielectric layer thick enough to withstand breakdown under the applied electric potentials can consistently overcome the negative effects of electrochemical reactions and electrolysis.
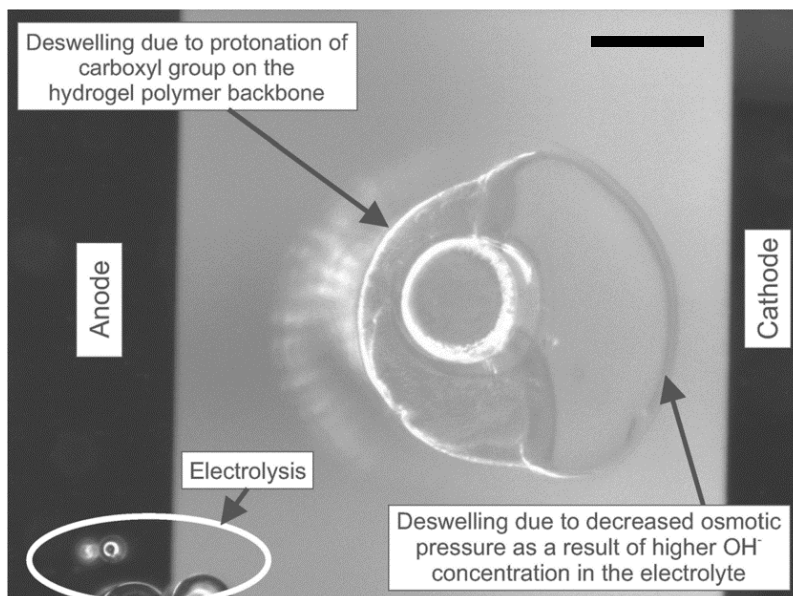
Figure 6.14: Chemical-based hydrogel deswelling due to dielectric breakdown of Parylene-N coating on planar electrodes. Hydrogen ions generated at the anode deswell the hydrogel by combining with the hydrogel's carboxyl groups; while the hydroxide produced at the cathode was of high enough concentration to decrease the osmotic pressure, with both effects causing deswelling. Scale bar represents 400 µm.

6.6   Conclusions

Previously electrical actuation of hydrogels required the application of electric potentials that caused electrolysis of electrolyte, and thus generation of microbubbles, protons, and hydroxide ions which induced deswelling in hydrogel actuators and caused device failure. This work employs Parylene-N dielectric coated electrodes to overcome these operational challenges, and applies AC-frequency based electric fields to overcome the effects of electrostatic shielding associated with the

220

application of DC fields. To determine the appropriate characteristic frequency at which electrostatic shielding effects would be minimized an RC circuit model of the hydrogel system was developed. This circuit model was used to determine the time constant of the electrode-dielectric-electrolyte interface, and thus the characteristic frequency of actuation which ranged from 10 kHz to 1 GHz for the range of electrolyte and dielectric thicknesses considered. The circuit model was verified by performing capacitance and impedance spectroscopy on the system, which showed agreement at high frequency. The total capacitance behavior of the system was both frequency and concentration dependent, effects which the current analytical model did not consider. The impedance of the system was also frequency dependent, dominated by the system's admittance, and show impedance peaks at the lower range of frequencies tested.

Using the characteristic frequency results, two major systems were fabricated for experimental electrical actuation. For a 1 mM KOH system, above its characteristic frequency, had true strains from 18 % to 30 % with response times from 14.7 seconds to 4.7 seconds, depending on the Parylene thickness and applied electric potential. The 1 mM system was also tested for its response to electric potential, demonstrating an increased actuation response as the electric potential was increased. The 5 mM system, actuated below its characteristic frequency, had a maximum true strain of ~7 % and response time of 14.9 seconds. All systems actuated displayed deformation at all frequencies tested; thus even a minimal frequency can disturb electrostatic shielding, but above the characteristic frequency deformation and response times were optimum. In addition, the impedance peaks observed would correspond to troughs of minimal apparent power required for actuation, and depending on the desired actuation response could provide operational zones for ultra-low power applications such as portable devices.

References

[1] P. Mitchell, "Microfluidics - downsizing large-scale biology", *Nature Biotechnology*, vol. 19, pp. 717-721, 2001.

[2] K.W. Oh, and C.H. Ahn, "A review of microvalves", *Journal of Micromechanics and Microengineering*, vol. 16, pp. R13-R39, 2006.

[3] B.D. Iverson, and S.V. Garimella, "Recent advances in microscale pumping technologies: A review and evaluation", *Microfluidics and Nanofluidics*, vol. 5, pp.145-174, 2008.

[4] L. Gervais, N. de Rooij, and E. Delamarche, "Microfluidic chips for point-of-care immunodiagnostics", *Advanced Materials*, vol. 23, pp. H151-H176, 2011.

[5] D.J. Beebe, J.S. Moore, J.M. Bauer, Q. Yu, R.H. Liu, C. Devadoss, et al., "Functional hydrogel structures for autonomous flow control inside microfluidic channels", *Nature*, vol. 404, pp. 588-590, 2000.

[6] N.A. Peppas, P. Bures, W. Leobandung, and H. Ichikawa, "Hydrogels in pharmaceutical formulations", *Eur J Pharm Biopharm*, vol. 50, pp. 27-46, 2000.

[7] S.M. Malmonge, C.A.C. Zavaglia, and W.D. Belangero, "Biomechanical and histological evaluation of hydrogel implants in articular cartilage", *Brazilian Journal of Medical and Biological Research*, vol. 33, pp. 307-312, 2000.

[8] S. Herber, W. Olthuis, P. Bergveld, and A. van den Berg, "Exploitation of a pH-sensitive hydrogel disk for CO_2 detection", *Sensor and Actuators B: Chemical*, vol. 103, pp. 284-289, 2004.

[9] A. Richter, D. Kuckling, S. Howitz, T. Gehring, and K.F. Arndt, "Electronically controllable microvalves based on smart hydrogels: Magnitudes and potential applications", *Journal Microelectromechanical Systems*, vol. 12, pp. 748-753, 2003.

[10] R.H. Liu, Q. Yu, and D.J. Beebe, "Fabrication and characterization of hydrogel-based microvalves", *Journal Microelectromechanical Systems*, vol. 11, pp. 45-53, 2002.

[11] M.J. Bassetti, A.N. Chatterjee, N.R. Aluru, and D.J. Beebe, "Development and modeling of electrically triggered hydrogels for microfluidic applications", *Journal Microelectromechanical Systems*, vol. 14, pp. 1198-1207, 2005.

[12] E. Jabbari, J. Tavakoli, and A.S. Sarvestani, "Swelling characteristics of acrylic acid polyelectrolyte hydrogel in a DC electric field", *Smart Materials & Structures*, vol. 16, pp. 1614-1620, 2007.

[13] G.H. Kwon, Y.Y. Choi, J.Y. Park, D.H. Woo, K.B. Lee, J.H. Kim, et al., "Electrically-driven hydrogel actuators in microfluidic channels: Fabrication, characterization, and biological application", *Lab on a Chip*, vol. 10, pp. 1604-1610, 2010.

[14]   P. Selvaganapathy, Y.S.L. Ki, P. Renaud, and C.H. Mastrangelo, "Bubble-free electrokinetic pumping", *Journal Microelectromechanical Systems*, vol. 11, pp. 448-453, 2002.

[15]   C.T. Kuo, and C.H. Liu, "A bubble-free AC electrokinetic micropump using the asymmetric capacitance-modulated microelectrode array for microfluidic flow control", *Journal Microelectromechanical Systems*, vol. 18, pp. 38-51, 2009.

[16]   V. Mukundan, P. Ponce, H.E. Butterfield, and B.L. Pruitt, "Modeling and characterization of electrostatic comb-drive actuators in conducting liquid media", *Journal Micromechanics Microengineering*, vol. 19, pp. 1-9, 2009.

[17]   T.B. Jones, M. Gunji, M. Washizu, and M.J. Feldman, "Dielectrophoretic liquid actuation and nanodroplet formation", *Journal of Applied Physics*, vol. 89, pp. 1441-1448, 2001.

[18]   M.R. King, O.A. Lomakin, R. Ahmed, and T.B. Jones, "Size-selective deposition of particles combining liquid and particulate dielectrophoresis", *Journal Applied Physics*, vol. 97, 054902 (9 pgs.), 2005.

[19]   J.R. Saunders, S. Abu-Salih, T. Khaleque, S. Hanula, and W.A. Moussa, "Modeling theories of intelligent hydrogel polymers", *Journal of Computational and Theoretical Nanoscience*, vol. 5, pp. 1942-1960, 2008.

[20]   T.L. Sounart, T.A. Michalske, and K.R. Zavadil, "Frequency-dependent electrostatic actuation in microfluidic MEMS", *Journal Microelectromechanical Systems*, vol. 14, pp. 125-133, 2005.

[21]   T.B. Jones, K.L. Wang, and D.J. Yao, "Frequency-dependent electromechanics of aqueous liquids: Electrowetting and dielectrophoresis", *Langmuir*, vol. 20, pp. 2813-2818, 2004.

[22]   A. Kahouli, A. Sylvestre, F. Jomni, E. Andre, J.L. Garden, B. Yangui, et al., "Dielectric properties of parylene AF_4 as low-k material for microelectronic applications", *Thin Solid Films*, vol. 520, pp. 2493-2497, 2012.

[23]   H. Sharifi, R.R. Lahiji, H.C. Lin, P.D. Ye, L.P.B. Katehi, and S. Mohammadi, "Characterization of parylene-n as flexible substrate and passivation layer for microwave and millimeter-wave integrated circuits", *IEEE Transactions on Advanced Packaging*, vol. 32, pp. 84-92, 2009.

[24]   J.Z. Chen, A.A. Darhuber, S.M. Troian, and S. Wagner, "Capacitive sensing of droplets for microfluidic devices based on thermocapillary actuation", *Lab on a Chip*, vol. 4, pp. 473-480, 2004.

[25]   C. Elbuken, T. Glawdel, D. Chan, and C.L. Ren, "Detection of microdroplet size and speed using capacitive sensors", *Sensors and Actuators A-Physical*, vol. 171, pp. 55-62, 2011.

[26]   J. Barthel, and R. Buchner, "High-frequency permittivity and its use in the investigation of solution properties", *Pure and Applied Chemistry*, vol. 63, pp. 1473-1482, 1991.

[27]   X.Q. Yang, and K. Huang, "The empirical formula for calculating the complex effective permittivity of an aqueous electrolyte solution at

microwave frequency", *IEEE Transactions on Geoscience and Remote Sensing*, vol. 43, pp. 315-320, 2005.

[28]   M.Z. Bazant, K. Thornton, and A. Ajdari, "Diffuse-charge dynamics in electrochemical systems", *Physical Review E*, vol. 70, 021506 (30 pgs.), 2004.

[29]   M.S. Kilic, M.Z. Bazant, and A. Ajdari, "Steric effects in the dynamics of electrolytes at large applied voltages. I. Double-layer charging", *Physical Review E*, vol. 75, 021502 (18 pgs.), 2007.

[30]   J.R. Saunders, S. Abu-Salih, and W.A. Moussa, "Parametric chemo-electro-mechanical modeling of smart hydrogels", *Journal of Computational and Theoretical Nanoscience*, vol. 5, pp. 1961-1975, 2008.

[31]   T. Wallmersperger, B. Kroplin, and R.W. Gulch, "Coupled chemo-electro-mechanical formulation for ionic polymer gels - numerical and experimental investigations", *Mechanics of Materials*, vol. 36, pp. 411-420, 2004.

[32]   Y.N. Xia, and G.M. Whitesides, "Soft lithography", *Annual Review of Materials Science*, vol. 28, pp. 153-184, 1998.

[33]   R.D. Tacito, and C. Steinbruchel, "Fine-line patterning of parylene-n by reactive ion etching for application as an interlayer dielectric", *Journal of the Electrochemical Society*, vol. 143, pp. 1974-1977, 1996.

[34]   T. Lederer, S. Clara, B. Jakoby, and W. Hilber, "Integration of impedance spectroscopy sensors in a digital microfluidic platform", Microsystem Technology, vol. 18, pp. 1163-1180, 2012.

[35]   T. Tanaka, and D.J. Fillmore, "Kinetics of swelling of gels", *Journal Chemical Physics*, vol. 70, pp. 1214-1218, 1979.

[36]   P.E. Grimshaw, A.J. Grodzinsky, M.L. Yarmush, and D.M. Yarmush, "Dynamic membranes for protein-transport - chemical and electrical control", *Chemical Engineering Science*, vol. 44, pp. 827-840, 1989.

[37]   P.E. Grimshaw, J.H. Nussbaum, A.J. Grodzinsky, and M.L. Yarmush, "Kinetics of electrically and chemically-induced swelling in polyelectrolyte gels", *Journal Chemical Physics*, vol. 93, pp. 4462-4472, 1990.

[38]   P. Chiarelli, and D. De Rossi, "Determination of mechanical parameters related to the kinetics of swelling in an electrically activated contractile gel", *Progress in Colloid & Polymer Science*, vol. 78, pp. 4-8, 1988.

Chapter 7

Cyclical Electrical Stimulation of Hydrogel Microactuators Employing Parylene-N Coated Electrodes[1]

7.1   Introduction

Microfluidics research has received enormous attention in the past two decades, expanding our fundamental scientific understanding and developing devices for commercial applications. The aim was to scale down conventional life science methods and protocols using MEMS for improved accuracy, efficiency, automation, throughput, and portability [1, 2]. Many actuating elements have been realized [3, 4]; however, they can have complex peripheral device requirements, high power, and high cost fabrication processes that hamper their widespread integration as microvalves and micropumps.   An alternative approach to microfluidic devices takes advantage of stimuli-responsive hydrogel (SRH) materials, which have been shown to actuate in response to pH changes [5-8], temperature gradients [9, 10], light [11], magnetics [12], and electric fields [13]. SRHs are also interesting because their response is controlled by diffusion (thermal or ionic) processes and thus scaling down hydrogels to the size necessary for MEMS integration improves their response times.

EFSH are of particular interest because of their ease-of-integration with the overall systems electrical components, relatively low power consumption, and fast response times on the order of seconds. Previous

to their microactuator applications macroscale EFSH's intrinsic expansion and contraction kinetics were investigated in relation to the applied electric field, hydrogel position with respect to the electrodes, and electrolyte composition [14-17]. EFSH were then investigated for their applicability as artificial muscles: examining a fiber's cyclical bending response when subjected to an external electric field, their deformation kinetics, and various material compositions [18-20]. This body of research significantly increased knowledge of EFSH, and displayed the ability of these hydrogels to respond cyclically and reversibly upon modification of the applied electric field.

EFSH as microactuators have previously been explored in a cylindrical configuration by Bassetti *et al.* [13], while Kwon *et al.* explored a fiber configuration for micropumping [21] and cell sorting [22]. However, EFSH's operational utility has been critically hampered by electrolysis of electrolyte generating bubbles at applied voltages >1.23V, since these bubbles attenuate the applied electric field and thus restrain hydrogel deformation. In addition, any protons or hydroxide generated at the electrodes modifies the chemical structure of the hydrogel or the chemical osmotic pressure, respectively [13]. Recently, our group overcame these effects by coating coplanar electrodes with a Parylene-N dielectric layer, which nullified the aforementioned challenges but necessitated the application of AC electric fields to overcome electrostatic shielding effects [23]. That study examined an EFSH's swelling response under increasing applied frequency and applied electric potential, displaying large deformation swelling and response times on the order of seconds with relatively low apparent power requirements. Dielectrophoretic liquid actuation [24] and electrostatic comb-drive actuators [25] systems have used similar methods of frequency-based actuation coupled with a dielectric barrier between the conductive media and electrodes.

In this work, we employ AC electric fields and pulse width modulation to cyclically actuate electrical hydrogels on dielectrics (EHOD) to complete

226

the swelling-deswelling actuation cycle. When an anionic hydrogel was immersed in alkaline KOH electrolyte, a chemically induced osmotic pressure between the hydrogel and electrolyte was established [26]. Applying an electric field over this system redistributed mobile ions within the hydrogel and electrolyte, modifying the initial osmotic pressure and causing further swelling [16]. This work examined a cylindrical hydrogel configuration with coplanar electrodes and a constant polarity electric field, which caused asymmetrical hydrogel swelling towards the anode. Here AC frequencies were employed to overcome electrostatic shielding that occurred when DC electric potentials were applied. The EHOD systems were actuated at 100 kHz, which was above the system's characteristic frequency (f_c) of 85.1 kHz [23]. Above this f_c electrostatic shielding would be minimized, and maximum electrically induced swelling would occur. A DC offset of half the peak-to-peak voltage was employed to ensure an electric field was established between electrodes. An offset larger than half V_{pk-pk} would not have allowed the V_{min} to reach 0 V necessary to minimize electrostatic shielding, while an offset smaller than half would have induced reverse-polarity swelling-deswelling effects. In addition, to cycle the hydrogel between two swollen states a pulse width modulation method was employed. This method cycled between 80 % and 20 % duty cycle, which would cycle up and down, respectively, the V_{rms} being applied to the electrodes. As the V_{rms} was cycled the electrically induced osmotic pressure would cycle too, effectively cycling the swollen state of the hydrogel.

This work examined the cycled deformation and actuation response times reacting to increased electric potential, for three cycles of actuation. For comparative purposes, cyclical actuation without dielectric coated electrodes was performed even though the aforementioned operating challenges existed. In addition, the hydration states of the hydrogels were measured to calculate the storage modulus and osmotic pressures of the hydrogels in each different system. Lastly, the conclusions section

227

examines how this work can be furthered; for three-dimensional cyclical actuation, by using new dielectric materials, or with alternative electrode configurations.

7.2   Materials and Experimental Methods

7.2.1 Microfluidic Chip & Hydrogel Fabrication

Standard cleanroom and non-cleanroom processes were implemented to fabricate the microfluidic chips, with subsequent *in-situ* hydrogel fabrication. Coplanar electrodes were patterned starting with the Piranha cleaning of standard 0211 glass bare wafers, which were spin-coated with positive photoresist, soft- and hard-baked, exposed to UV light under a photomask, after which the photoresist was developed. Metallization was performed using a planar magnetron sputtering system where ~10 nm Cr and ~200 nm Au was deposited. To complete the electrodes the wafers were placed in an acetone bath at 35°C with ultrasonic agitation. Six chips fit on each wafer, thus the patterned electrodes were diced into six sections after electrodes were developed.

The electrodes had Parylene-N selectively deposited on them to serve as a dielectric barrier. To perform selective deposition, PDMS was mixed in a 10:1 base:curing agent ratio, degassed, poured over each chip, and cured at 80°C for 2 hours. Afterwards, windows were cut out of the PDMS with a scalpel to expose the electrodes for selective deposition of Parylene-N. The PDMS was peeled off and the chips were then immersed in A-174 silane based adhesion promotion solution, and afterwards the PDMS was replaced on top. Parylene-N was deposited at room temperature with a base pressure of 35 vacuum units using a vapor deposition polymerization system (SCS PDS 2012). After deposition a surface topography profiler (Alpha Step IQ) and an optical transparent film mapping system (Filmetrics F20 SS-1) were used to measure Parylene-N thickness.

228

Microchannels for *in-situ* hydrogel polymerization and electrical actuation were fabricated using a rapid prototyped mold and PDMS-based soft lithography techniques [27]. The PDMS microchannels were irreversibly bonded to the glass microchips using a reactive ion etcher (Oxford Plasmalab µEtch) at 250 mTorr, 30 W, with 80 % O_2 for 25 s. Parylene-N etches at a rate of ~100 nm/min when exposed to oxygen plasma [28], thus Parylene-N coated electrodes were covered with a disposable piece of PDMS. Sealing at the PDMS/Glass/Parylene-N interface was achieved by applying a thin layer of PDMS around the edge of the Parylene-N with a Q-tip.

Structural support for hydrogel actuation was achieved by *in-situ* polymerization of posts. A precursor mixture was prepared, composed of IBA and TEGDMA in a 9:1 weight ratio, with a 3 % weight photoinitiator of DMPA. The precursor was flushed down the microchannel and using a photomask was exposed to 365 nm UV light (EXFO Acticure 4000) for 60 s with a wavelength specific intensity of 2.42 mW/cm^2. Calibration of the UV intensity was performed with an ABM Mask Aligner cure-site radiometer, specifically measuring the 365 nm wavelength intensity. To remove all unpolymerized precursor mixture the microchannel was flushed with methanol, then with DI water, then with air, and subsequently heated at 30°C to drive out any remaining water vapor.

Hydrogel precursor mixture was mixed with a composition of HEMA and AA in a 4:1 molar ratio, using EGDMA crosslinker at a 2 % weight, and 3 % weight DMPA. The microchannels were then flushed with precursor mixture, and using a photomask was exposed to 365 nm UV light at 1.21 mW/cm^2 for 100 s. Unpolymerized precursor mixture was flushed out of the channel with methanol, and then the hydrogels were equilibrated with DI water for storage before testing. Hydrogels must be fabricated in the absence of oxygen during polymerization, otherwise material anisotropies are introduced due to oxygen radicals inhibiting the polymerization process [29]. Copolymerization with acrylic acid creates

bound carboxyl groups on the polymer backbone, which in a basic solution cause the hydrogel to be negatively charged and thus responsive to an applied electric field.

The final microfluidic chip with an *in-situ* hydrogel can be seen in Figure 7.1. The width of the microchannel was 3 mm with a depth of 254 µm. The microchannel restricts all out of plane hydrogel deformation, and thus the hydrogel's volume was only a function of its in-plane dimensions. The cylindrical interior post and surrounding hydrogel jacket was fabricated with 400 µm and 600 µm mask feature sizes, respectively. The electrodes were 100 µm wide, and had a gap from electrode edge-to-edge of 2 mm.

7.2.2 Hydrogel Hydration Testing

The hydration state of hydrogel samples for four different potassium hydroxide electrolyte concentrations was tested. Hydrogels were fabricated within microfluidic chips, as outlined in the previous section. Twelve hydrogel samples were then equilibrated sequentially in 500 mM, 50 mM, 5 mM, and 1 mM concentrations. Hydrogel samples were given four hours at each concentration state to ensure equilibrium was achieved.

Hydrogel diameters were measured at their as-fabricated state, and each concentration specific state thereafter. Deformation was observed through an optical microscope (Ziess Discovery.V12) with an attached CCD camera (Ziess AxioCam ICc1), which used AxioVision's Labview software to perform measurements. The measurement scale was calibrated at the measurement magnification using predefined lithography mask features.

7.2.3 Cyclical Actuation Testing

Microfluidic chips and hydrogel samples were fabricated as outlined previously. They were equilibrated in 1 mM, 5 mM or 50 mM potassium hydroxide concentrations, specific to the test being performed. They were
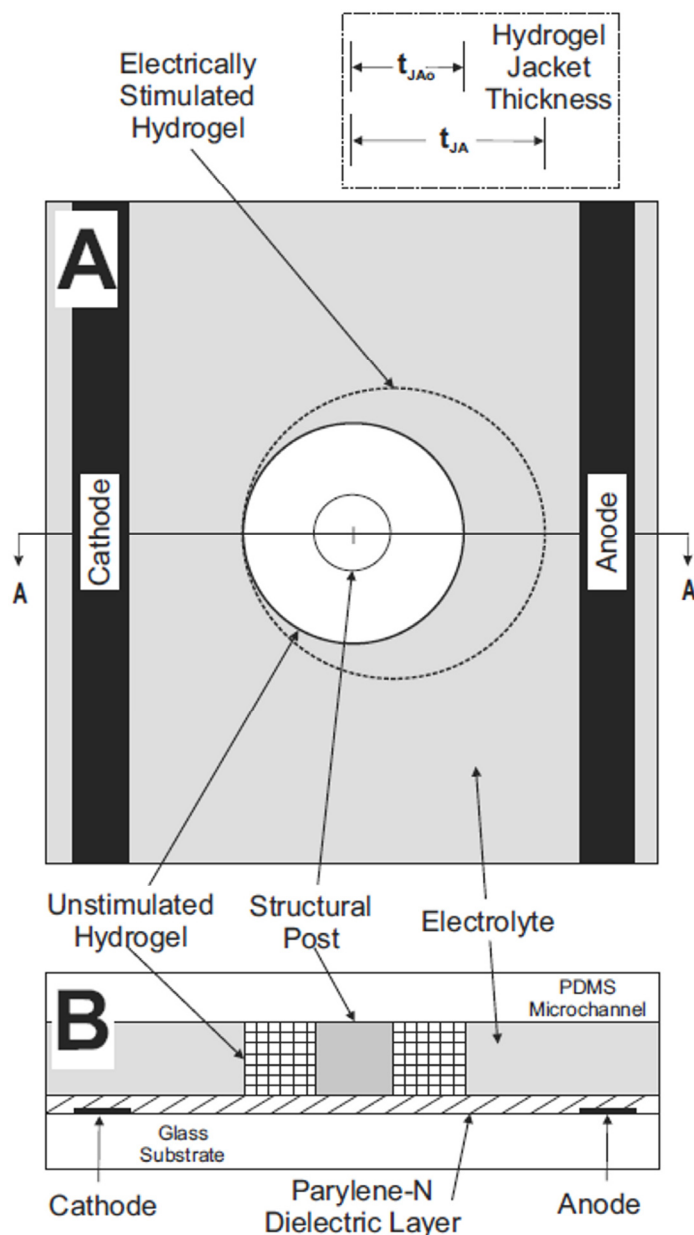
Figure 7.1: Schematic representation of the system for cyclical hydrogel electrical actuation (A) top view representation, highlighting the hydrogel jacket thickness observed during experiments (B) cross-section A-A side view, noting the Parylene-N dielectric layer enabling electrolysis-free actuation.

given at least four hours to equilibrate, and were injected with new electrolyte hourly.

Cyclical actuation of electrically stimulated hydrogels was performed with a system of electrical equipment, as seen in Figure 7.2. A square wave signal was generated with a function generator (Agilent 33220A)

supplied with a DC offset (Agilent E3647A) and amplified (Agilent 33502A). Contact with the microchips contact pads was made with platinum tipped high voltage probes (Micralyne's Microfluidic Tool Kit), and the signal was observed using an oscilloscope (Agilent DSO 2004A). Actuation was observed with the equipment discussed previously, which captured still photos at one second intervals. During cycling between 80% and 20% duty cycle the electric field was held constant for varied periods of time, which were long enough to establish that steady state actuation had been reached and that no change in deformation was experienced. The presented results contract the observed equilibrium region into one data point.

7.2.4 Scanning Electron Microscopy

To obtain micrographs of the dielectric Parylene-N layer, films were deposited using the techniques as previously outlined. The microchips with deposited Parylene-N (but not with microchannel, etc.) were flash frozen in liquid nitrogen and cryo-fractured to obtain a cross-section. Samples were then mounted on aluminum stubs using two-sided conductive tape, and an ~10 nm layer of gold was sputtered on their surface (Denton Desk II). Imaging of samples was then performed using a scanning electron microscope (LEO 1400).

7.3 Cyclical Hydrogel Actuation

Electric field based cyclical hydrogel actuation was performed for two major systems: one employing dielectric coated electrodes and the other without dielectric coated electrodes. Hydrogel jacket thickness deformation was measured optically. To ascertain an approximation of the induced osmotic pressure, the storage modulus at the appropriate electrolyte concentration was determined. The sections below outline the experimental and analytical process to determine osmotic pressure, and detail the two cyclically actuated systems.

232
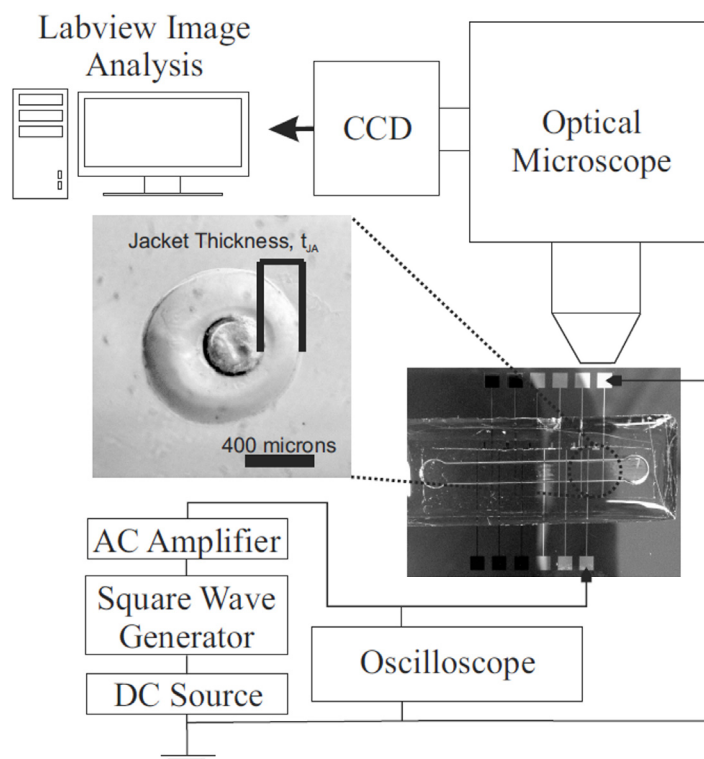
Figure 7.2: Testing system for cyclical hydrogel electrical actuation and subsequent characterization through image capture and analysis software. Main actuation components include: square wave generator, DC power supply, AC amplifier, and an oscilloscope.

7.3.1 Hydration, Storage Modulus and Osmotic Pressure

Cyclical electrical hydrogel actuation produced observable deformation; however, directly measuring the osmotic pressure generated by the microscale hydrogels posed significant challenges. But, combining the observed deformations with known hydrogel physics and dynamic mechanical properties from literature, an approximate calculation for osmotic pressure can be performed. Determining this pressure would be useful for comparative purposes between systems, and in designing future systems incorporating hydrogels for microfluidic regulation applications.

Hydrogels under electrical stimulus undergo chemo-electro-mechanical reaction kinetics. The electrolyte-hydrogel system's electric field distribution was governed by Poisson's Equation, which was coupled with the transient Nernst-Planck Equation governing mobile ion kinetics. These governing equations and supplementary equations are reviewed

elsewhere [30]. Here the mechanical response of the hydrogel and equations of motion are of interest.

To begin, the hydration state of the hydrogels at decreasing electrolyte concentrations were experimentally measured, as outlined in Section 7.2.2. The static interior post diameters were also measured, and combining these measurements the hydration can be calculated using

$$H = \frac{d^2 - d_o{}^2}{d_o{}^2 - d_p{}^2}$$

(7-1)

where H is the hydrogel hydration, d is the hydrogel's final diameter, d_o is the hydrogel's initial diameter, and d_p is the diameter of the interior post. The initial diameter represents the as-fabricated hydrogel diameter, and all hydration calculations were performed with respect to this diameter. With increasing electrolyte concentration, the hydrogel's hydration was shown to decrease, as seen in Figure 7.3. The minimum hydration at 500 mM was 0.26±0.04, while the maximum hydration at 1 mM was 6.04±0.18. The decreased hydration results from a lower osmotic pressure, as the difference between mobile ions within the hydrogel and outside the hydrogel was lower.

A higher hydrogel hydration also decreased the storage modulus of the hydrogel, as more fluidic electrolyte was present within the hydrogel. It was determined by Okay and Durmaz [31] that this hydration-modulus interaction can be analytically calculated using

$$E' = \frac{E_o'(1 + H_o)^{1/3}}{(1 + H)^{1/3}}$$

(7-2)

where E_o' is the storage modulus at an initial state, H_o is the hydration at an initial state, E' is the storage modulus at the final state, and H is the hydration at the final state. In this work, the initial state hydration and storage modulus were taken at 500 mM KOH reported from literature. All hydration values were taken directly from the observed measurements. Storage modulus values at 500 mM were taken from dynamic mechanical property measurements [32], performed at 0.1 Hz testing frequency as

234

that was most representative of the system being electrically actuated. It should be noted that all hydration measurements were made on a steady state system, thus the loss modulus of the hydrogel's viscoelastic properties was not taken into account. The storage modulus values, both from literature and calculated using Eq. 7-2, seen in Figure 7.3, decreased as hydration increased. At 50 mM the calculated and literature storage modulus values were compared, and were found to differ by 11.6 %. This was a moderate deviation, but both averages were within each range of standard deviations. The slightly larger calculated storage modulus will result in the average calculated osmotic pressures being slightly larger. The maximum calculated storage modulus was 126±24 kPa at 50 mM while the minimum calculated storage modulus was 97±18 kPa at 1 mM KOH. Storage modulus instead of Young's modulus was specifically targeted for Eq. 7-2 because of the cyclical nature of hydrogel electrical actuation in this work. While E'_o within Eq. 7-2 represents linear viscoelastic properties, the use of Eq. 7-2 allows determination of storage modulus with systems experiencing non-linear strains. Eq. 7-2 has been previously implemented for both chemical [8] and electrical [13] non-linear deformation simulations, providing good agreement between experimental results and numerical models for cylindrical microscale hydrogels.

Combining the analytically and experimentally determined storage modulus and hydration, respectively, an approximation for the hydrogel's osmotic pressure can be calculated. Hydrogel swelling here represents a plain strain system, as no swelling occurred out-of-plane. A glass substrate and a relatively thick layer of PDMS over the hydrogel ensured plain strain deformation. In this work we only measured one-dimensional deformation, t_{JA}, which was measured, as seen in Figure 7.1, at the cross-section A-A of the hydrogel and represents the largest deformation. Thus, the osmotic pressure calculated will only represent the pressure at this point. The mechanical field governing hydrogel deformation was quasi-static as the diffusion and migration of mobile ions were the rate limiting
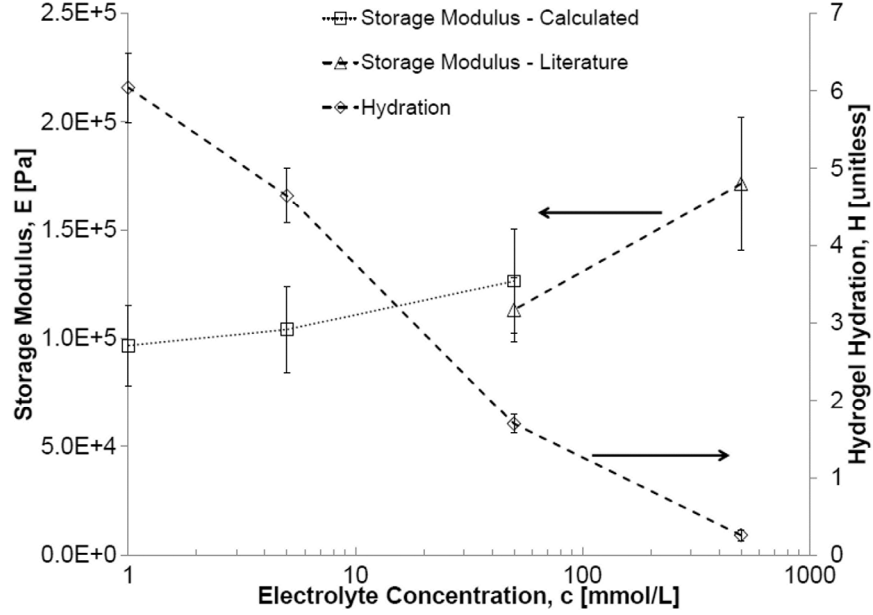
Figure 7.3: The measured hydration of samples at four different potassium hydroxide concentrations. These hydration values were then combined with published storage modulus values to calculate the storage moduli of hydrogels immersed in weaker electrolyte concentrations of 50 mM, 5 mM and 1 mM KOH.

physics of the electrolyte-hydrogel system. The friction factor between the hydrogel and substrate was neglected, and no body forces were present in this work. For one-dimensional quasi-static deformation the mechanical equilibrium, which describes the geometric non-linear deformation of the swollen hydrogels, can be shown as [33]

$$\frac{\partial \sigma}{\partial x} = \frac{\partial}{\partial x}\left[\left(\frac{E'}{(1+\nu)} + \frac{E'\nu}{(1+\nu)(1-2\nu)}\right)\left(\varepsilon_x + \frac{\varepsilon_x^2}{2}\right) - P_{osmotic}\right] = 0 \qquad (7\text{-}3)$$

where σ is the Cauchy stress, $P_{osmotic}$ is osmotic pressure, E' is storage modulus, υ is Poisson's ratio, ε_x is hydrogel strain. The electrostatic stresses and mixing pressures were neglected here, as the system under consideration was dominated by osmotic pressures [13]. The hydrogel's strain was represented by

$$\varepsilon_x = \ln\left(\frac{t_{JA}}{t_{JAo}}\right) \qquad (7\text{-}4)$$

where t_{JA} and t_{JAo} were the final and initial hydrogel jacket thickness after and before electrical actuation, respectively. True strain was implemented

in this work instead of engineering strain, as large deformations exist and this was a more accurate, and conservative, measure of deformation.

The osmotic pressure shown in Eq. 7-3 develops at the hydrogel-electrolyte interface. The osmotic pressure can be analytically or numerically determined by comparing the mobile ion concentrations within the hydrogel to the concentrations outside the hydrogel using [26]:

$$P_{osmotic} = RT \sum_{k=1}^{n} (c_k - c_k^0)$$ (7-5)

where R is the universal gas constant, T is temperature, c_k is the concentration of the kth ion inside the hydrogel and c_k^o is the concentration of the kth ion outside the hydrogel. Experimentally the ionic concentrations inside and outside the hydrogel cannot be easily determined with accuracy. Therefore, assuming the hydrogel undergoes no deformation at the post, and combining Eq. 7-3 and Eq. 7-4, the osmotic pressure at the hydrogel-electrolyte interface can be calculated using

$$P_{osmotic} = \frac{E'(1-\nu)}{(1+\nu)(1-2\nu)} \left(\ln(\frac{t_{JA}}{t_{JAo}}) + \frac{1}{2} \ln(\frac{t_{JA}}{t_{JAo}})^2 \right)$$ (7-6)

where the initial state of the hydrogel was considered to be the as-fabricated state, where no strains or osmotic pressure exist. At each state thereafter the hydrogel jacket thickness was measured.

To determine the osmotic pressure using Eq. 7-6 from electrical stimulation, the osmotic pressure induced by the chemical equilibrium state before actuation must first be determined. Using the measurements from the hydration observations, the chemical osmotic pressure for 500 mM, 50 mM, 5 mM, and 1 mM were 92.4±26.6 kPa, 361.4±78.5 kPa, 588.6±120.3 kPa, and 635.9±128.8 kPa, respectively. These chemical osmotic pressures were the initial osmotic pressure before electrical actuation. All osmotic pressures noted within figure descriptions (P_{peak}, P_{trough}) describe electrically induced osmotic pressures above and beyond these chemical baselines. The strain induced by these chemical osmotic

pressures caused non-linear deformation. Therefore, these strains must be incorporated as initial pre-strain to the electrically induced strain when calculating the electrically induced osmotic pressure. Within this work, the $P_{osmotic}$ from Eq. 7-6 will be calculated for each system being cyclically actuated, at its maximum and minimum values during electrical actuation.

7.3.2 Electric Hydrogel on Dielectrics

Cyclical electrical actuation of hydrogels employing Parylene-N coated electrodes was performed at five different applied electric potentials, examining three cycles of actuation at each potential. To inhibit the generation of hydrogen and hydroxide at the electrodes and electrolysis of the electrolyte, the electrodes were coated with a 907±28 nm thick Parylene-N dielectric layer. This dielectric layer necessitated the use of frequency-based actuation. The system's characteristic frequency was 85.1 kHz and the dielectric caused an electric potential loss of ~27 % of the applied electric potential [23].

Figure 7.4 displays actuation responses with applied electric potentials from 20 V_{pk-pk} to 40 V_{pk-pk}. As the electric field between electrodes was increased a larger osmotic pressure was established on the hydrogel-electrolyte interface, which caused a larger observed deformation and generally faster rise time constants. From 20 V_{pk-pk} to 40 V_{pk-pk} the maximum true strain observed increased from 9.2 % to 29.1 %. The $P_{osmotic,peak}$ at 20 V_{pk-pk} was 60.6±11.6 kPa compared with 201.1±38.3 kPa $P_{osmotic,peak}$ at 40 V_{pk-pk}. Thus doubling the applied electric potential had a significant impact on the osmotic pressure and deformation. Electric potentials larger than 40 V_{pk-pk} could not be implemented due to the electrical equipment available. However, enhanced responses above this potential would be expected, until osmotic pressures large enough to rupture the hydrogel were generated. Figure 7.5 displays the asymmetrically swelling towards the anode, as the cylindrical hydrogel was electrically actuated. This asymmetrical swelling toward the anode caused the hydrogel to become slightly elliptical, because swelling was

238
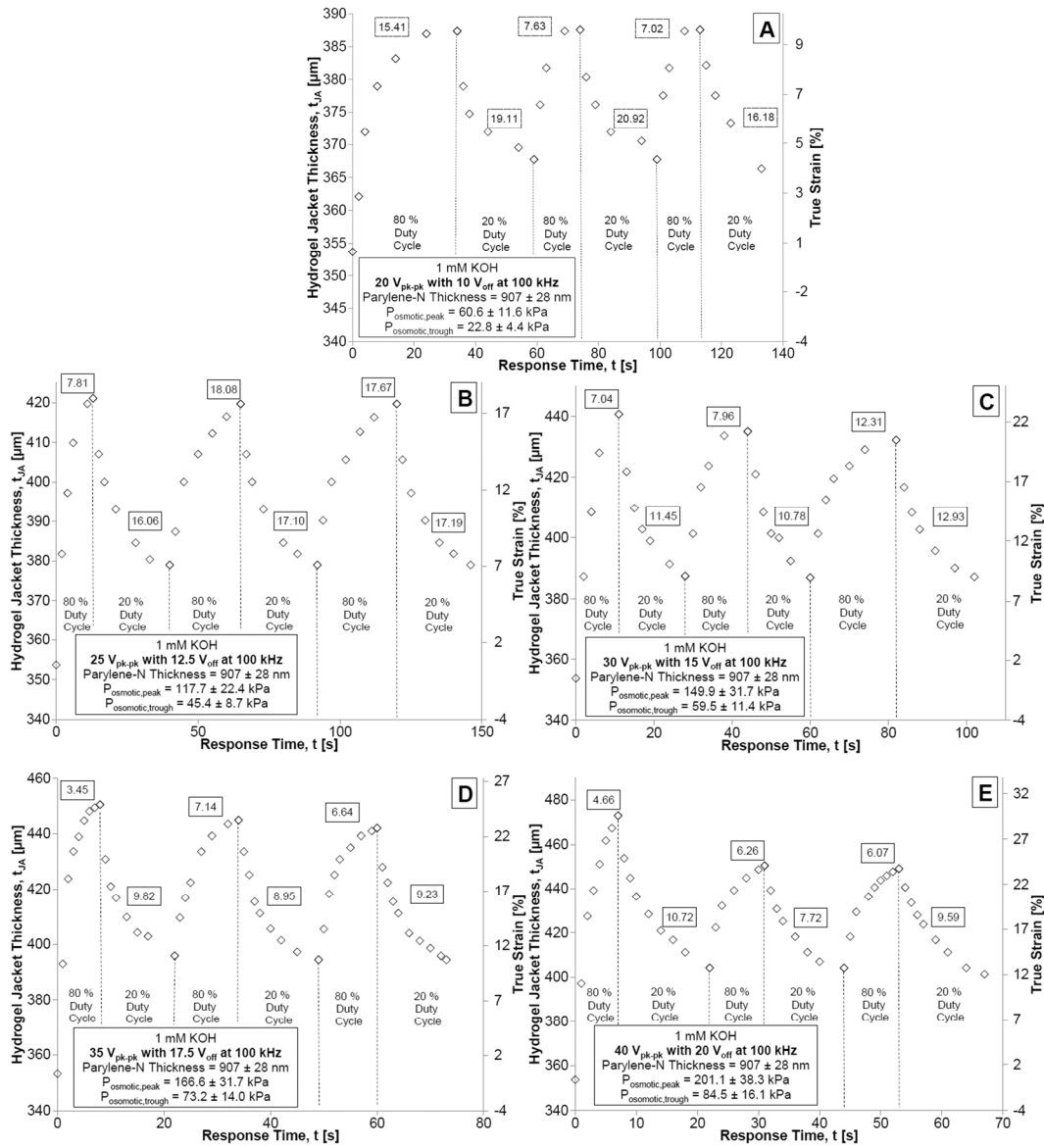
Figure 7.4: Electrical hydrogels on dielectrics cyclical actuation examining three cycles of actuation. The duty cycle was cycled between 80 % and 20 % for a total three cycles. The boxed numbers beside each curve represent the rise time constants for each transition. The $P_{osmotic}$ shown represent the maximum and minimum pressures over the entire three cycles. The electric potential were (a) 20 $V_{pk\text{-}pk}$ with 10 V_{off} (b) 25 $V_{pk\text{-}pk}$ with 12.5 V_{off} (c) 30 $V_{pk\text{-}pk}$ with 15 V_{off} (d) 35 $V_{pk\text{-}pk}$ with 17.5 V_{off} (e) 40 $V_{pk\text{-}pk}$ with 20 V_{off}.

239
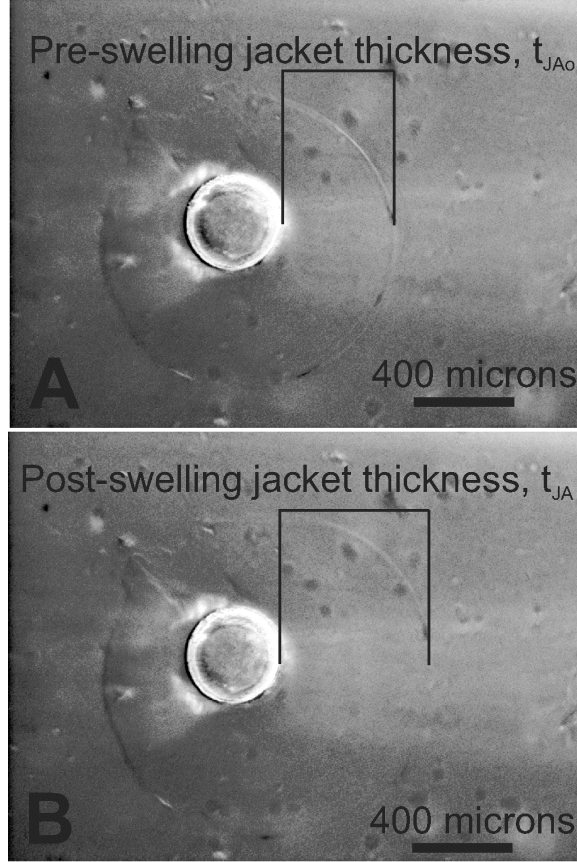
Figure 7.5: Micrograph of a hydrogel between an anode and cathode (not shown) as (a) equilibrated in 1 KOH (b) asymmetrically swollen towards the anode.

not uniform around the hydrogel. In addition, for the electric fields applied a slight deswelling was observed on the cathode side of the hydrogel. This deswelling was due to the electric field causing a slight decrease in the osmotic pressure on the hydrogels cathode side, similar to the behavior previously shown numerically [34]. Reversing the electric field polarity (switching the anode and cathode), would have caused the hydrogel to swell to the new-anode side and deswell on the old-anode side. This was also previously shown numerically by our group for a square hydrogel configuration with coplanar electrodes [34].

Please note that error bars are not shown in Figure 7.4 and other subsequent figures because the data represents one trial only. This was due to the highly labor-intensive process of extracting data from the still-photo images. To examine the repeatability of the electrical actuation, an additional sample was actuated at 25 V_{pk-pk}, as seen in Figure 7.6. The

sample had a maximum true strain of 16.8 %, with rise and fall times between 16-20 s and 18-23 s, respectively. The peak and trough osmotic pressures were 113.9±216 kPa and 53.0±10.1 kPa, respectively. Comparatively the maximum true strain response between the two samples differed by ~0.6 %. The average rise times differed by 3.4 s, which could be attributed to the new samples larger initial jacket thickness causing longer diffusion pathways. In general the system response characteristics appeared to be repeatable provided the initial states of the hydrogel and fabricated dielectric thicknesses were close.
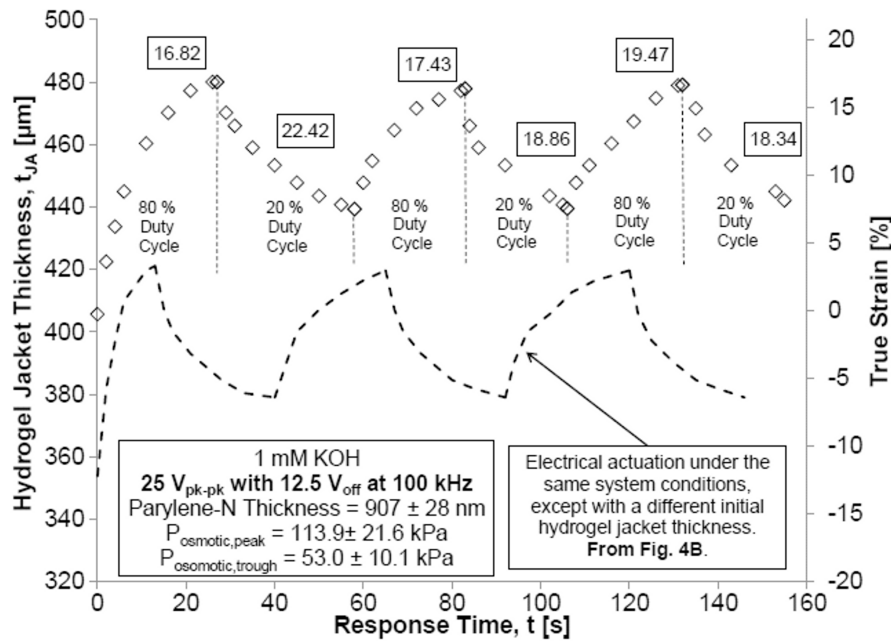
Figure 7.6: Examining the repeatability of electrical hydrogels on dielectrics cyclical actuation. The dashed (---) line represents data outlined in Figure 7.4(b), as compared to a new sample cyclically actuated with the same system characteristics. The inset parameters and true strain secondary y-axis refer to the new sample.

While increased electric field increased the true strain response, it was observed that the peak-to-trough true strain response plateaued at higher applied voltages, as seen in Figure 7.7. In addition, the difference between the peak strains at each particular cycle increased as the electric potential was increased. Therefore, for peristaltic pumping applications, the cyclical actuation would be maximized and further electric field increases would have insignificant effect. This plateau region occurs as

the peak and trough deformations begin to increase at the same rate when electric potential was increased. In addition, the error in the peak-to-trough true strain averaged over three cycles was largest at 40 V_{pk-pk}, thus cycle-to-cycle strain has the highest variability at the highest applied electric potential. It should be highlighted that the results of Figure 7.4 were from one sample that was repeatedly tested at increasing electric potentials, thus displaying the robustness of the hydrogel actuator and the Parylene-N film.

In general, increasing the applied electric potential decreased both the rise time and fall times of hydrogel swelling and deswelling, respectively, shown in Figure 7.8. Deswelling fall times were reduced from 18.7±2.4 s to 9.3±1.5 s, as the electric potential was increased from 20 V_{pk-pk} to 40 V_{pk-pk}. Swelling rise times were more complex, as initially rise times rose between 20 V_{pk-pk} and 25 V_{pk-pk}, but subsequently fell from 14.5±5.8 s to 5.7±0.9 s between 25 V_{pk-pk} and 40 V_{pk-pk}. The initial increase in rise times could be explained by the increased swelling strain response requiring more time to reach equilibrium, as relatively the magnitude of strain was increased. Afterwards, the strain responses still increased but the induced osmotic pressure was large enough to compensate for the increased strain and rise times were decreased. For all electric potentials applied the deswelling fall times were slower than the swelling rise times. Slower fall times were expected because with an 80 % duty cycle, swelling was a result of applying an increased osmotic pressure, while at 20 % duty cycle this osmotic pressure was decreased significantly and elastic restoring forces from the hydrogel polymer network aided deswelling.

The EHOD sample in Figure 7.4 was cycled 15 times in total, or 3 cycles at each electric potential examined. At potentials ≥ 30 V_{pk-pk} a decrease in deformation in this sample was observed for successive cycles. Two major effects could have caused this: electrical breakdown of the dielectric at higher applied potential or fatigue of the hydrogel sample. At higher voltages the dielectric could be undergoing partial breakdown,

reducing its quality and subsequently decreasing the amount of electric field transmitted through it. The hydrogel could also be undergoing fatigue, since deformation occurs in the non-linear regime. Performing a fatigue analysis up to 100 cycles could be used to examine which factor was most dominant in deformation decline. Theoretically nothing limits the number of
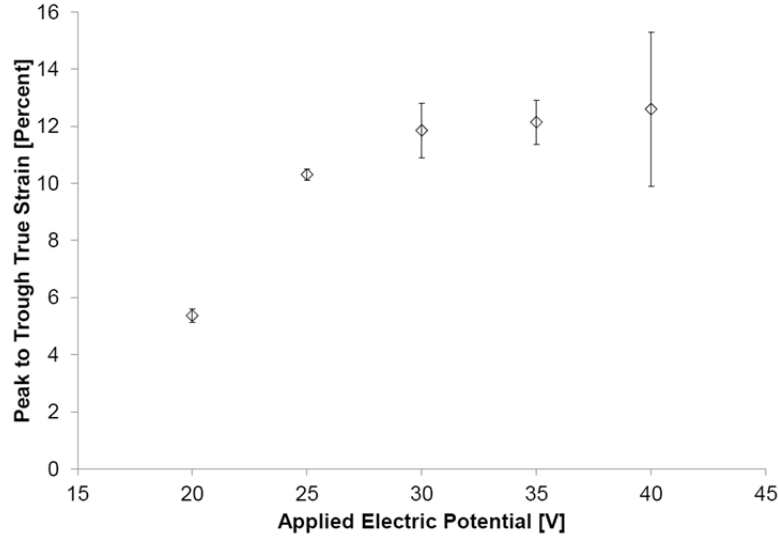
Figure 7.7: Electrical hydrogels on dielectrics peak to trough true strain response from an applied electric potential between 20 V_{pk-pk} to 40 V_{pk-pk}. Each point has an average and standard deviation based off the three peaks or troughs observed during electrical actuation.
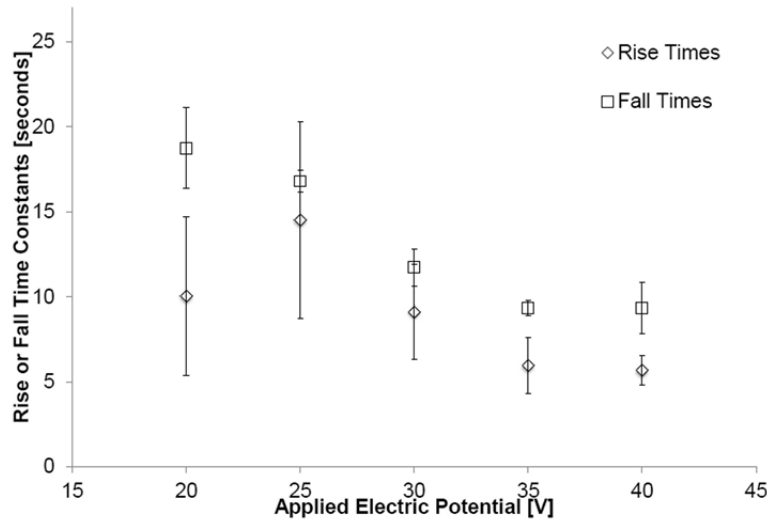
Figure 7.8: Electrical hydrogels on dielectrics rise times and fall times due to an 80 % or 20 % duty cycle, respectively, for applied electric potentials from 20 V_{pk-pk} to 40 V_{pk-pk}. Each point has an average and standard deviation based off the three peaks or troughs observed during electrical actuation.

243

cycles a hydrogel can actuate; however, the fatigue of the system would need to be examined thoroughly to understand practical limits on cyclical actuation. To the author's knowledge, cyclical actuation of hydrogels, of any geometries or configurations, has only been demonstrated up to five cycles of actuation; therefore, further work is needed to examine many cycles of actuation to examine performance stability for applications such as micropumping or multiuse microvalves.

The closest electrically activated hydrogel-based system for comparison was developed by Bassetti *et al.* [13]. This system had the same HEMA-AA hydrogel composition and very similar dimensions. For Bassetti *et al.*'s applied electric potential of 20 V DC the hydrogel deformed 120 µm in ~1 s. Factoring in losses through the Parylene-N layer and duty cycle manipulation; those results can be compared with this work's 35 V_{pk-pk} deformation of 97.3 µm and 4 s rise time. The results are similar, with deviations in response time being attributed to Bassetti *et al.*'s use of a stronger 50 mM potassium buffer flowing through the microchannel at 0.5 ml/min, which would have enhanced mobile ion flux. The difference in deformations could be attributed to higher osmotic pressures established due to the stronger buffer solution or differences in the hydrogel's mechanical properties.

Comparing the electrically actuated system to other hydrogel-based systems highlights this system's enhanced performance. Kim *et al.* performed pH-based cycling of a hydrogel rod with a critical dimension of 2 mm, and found a typical cycle time of ~ 2 hours [6]. De *et al.* performed pH-based cycling of cylindrical 150 µm diameter hydrogels, and found a typical cycle time of ~28 minutes [8]. Richter *et al.* thermally cycled 135±15 µm spherical particles, observing valve switching times from 35 to 5 s depending on the ratio of particle volume to chamber volume [9]. The hydrogel's within this work were ~1100 µm in diameter when swollen with a ~400 µm interior post, thus significant room exists to further scale down these hydrogels to optimize response time for a specific application.

Previously, macroscale large aspect ratio rectangular prisms or cylindrical rods were electrically actuated cyclically for applications as artificial muscles or fingers. However, these systems were open to atmosphere to ventilate bubbles generated by electrolysis. Some researchers observed irreproducible actuation with 3V applied where bending angle or contraction was irregular or systematically declined [18, 19], while others achieved reproducible cyclical bending with 15 V applied and response times on the order of seconds [35]. The system described in this work had a reproducible response at applied voltages up to 40 V_{pk-pk} with response times on the order of seconds.

The pressure generated by this system was also of a magnitude useful for 3D microfluidic regulation. Liu *et al.* developed a 3D pH-based microvalve that had a maximum 185 μm of deformation, which translated into ~56 kPa of pressure applied to a flexible membrane [7]. The maximum osmotic pressure developed in this work was 201.1±38.3 kPa at 40 V_{pk-pk} with corresponding maximum deformation of 119 μm, which if harnessed appropriately could be applied in a configuration similar to Liu *et al.*

There was ~27 % applied electric potential attenuated within the Parylene-N dielectric layer coating the electrodes [23], further optimization of this layer could significantly enhance actuation performance. Figure 7.9 shows a micrograph of Parylene-N deposited on the surface of a gold electrode, which displays non-uniformity over the surface. Areas of larger thickness would attenuate the electric field even more than analytically calculated, while areas of lower thickness would be more susceptible to electric breakdown. The film in Figure 7.9 was deposited at 35 vacuum units, while previous attempts were deposited at 75 vacuum units but the films were found to breakdown at larger applied electric potentials or with repeated testing. One method to further improve performance would be fabrication of ultrathin Parylene-N layers, which are uniformly closed and able to withstand breakdown. Rapp *et al.* [36] fabricated Parylene-C layers

which were closed down to 35 nm. Experiments would need to be undertaken to determine if Parylene-N could have the same closed structure at similar thicknesses. Parylene-C was previously attempted here too, but its dielectric breakdown threshold and sensitivity to frequency were inadequate compared to Parylene-N. Another method to improve actuation performance would be to substitute the Parylene-N layer with another dielectric material of similar or better dielectric properties, that can be fabricated thinner. Low voltage electrowetting-on-dielectric researchers have been exploring this problem through the use of multilayer systems [37, 38]. Specifically, Lin *et al.* developed a system combining a 120 nm thick sputtered insulator of tantalum pentoxide (Ta_2O_5) with a 200 nm thick Parylene-C coating and a 70 nm hydrophobic coating CYTOP, which still had an acceptable breakdown voltage of 60 V [39]. Further optimization of the EHOD system would bring performance closer to electrical hydrogel actuation without dielectrics, as shown in the next section.

The apparent power required for this system's operation can be estimated based off a similar system, one that had a thinner 648±11 nm Parylene-N layer [23]. This system had the same geometries; however, for all cases in the work presented here the AC frequency was 100 kHz with a 907±28 nm Parylene-N layer. Operating at 80 % duty cycle the apparent power of this system at 40 V_{pk-pk} and 20 V_{pk-pk} could be estimated at ~1.79 mVA and ~0.45 mVA, respectively. The exact apparent power value would be slightly lower, due to the increased thickness from the literature's work compared to the thickness implemented here. An increase in thickness was shown to increase the impedance of the system, and hence decrease apparent power. Operating at 20 % duty cycle would require ~12.5 % of the apparent power, as the V_{rms} would be reduced by half.
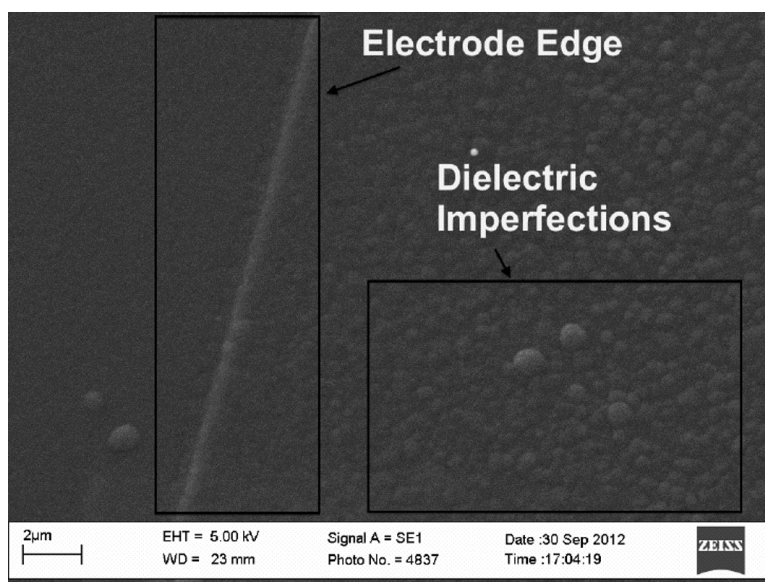
Figure 7.9: Parylene-N vapor deposited on a gold electrode, showing surface roughness that promote attenuation or the applied electric field. The measured thickness was 907±28nm, but observations show increased surface variations that could be larger than this measured error.

Also, operating at lower frequencies was shown to significantly reduce power consumption, and still provided a measure of actuation even though electrostatic shielding effects were still present [23]. The system examined here could be cyclically actuated using lower frequencies, provided the specific application was achieved with less than optimal actuation pressures and deformations.

As previously mentioned, the hydrogel jacket thickness was measured from post to hydrogel-electrolyte interface, which could have induced a measurement error into the data. Within this work, measurement error was quantified as the visible thickness of the hydrogel-electrolyte interface itself, thus at 1 mM, 5 mM, and 50 mM, the measurement error was ±10 µm and at 500 mM or as-fabricated ±5 µm (due to a sharper boundary edge). This error was factored into the error in hydration, storage modulus, and osmotic pressure. An alternative technique for strain measurements could have been microscopic particle image velocimetry [40], but these particles must not influence polymerization or materials properties. Future work will examine out-of-

plane deformation employing a laser doppler vibrometer to increase accuracy.

7.3.3 Electric Hydrogel without Dielectrics

For comparative purposes hydrogels were electrically actuated without dielectric coated electrodes, and instable and stable actuations were found to exist. The system required modifications to the previous experimental set-up: electrolyte was continually flowed down the microchannel to wash away generated bubbles, the anode was positioned downstream so no protons generated contacted the hydrogel, and electrolyte concentrations stronger than 1 mM were used to allow higher storage modulus hydrogels. In addition, platinum electrodes were used instead of chrome-gold electrode so that no electrochemical degradation of the electrodes occurred during actuation.

Figure 7.10 shows the unstable cyclical actuation of hydrogels without dielectrics at applied electric potentials of 10 V_{pk-pk} and 25 V_{pk-pk}. The unstable deformation was a result of bubbles within the microchannel, both: decreasing the applied electric field influencing the hydrogel-electrolyte system and inhibiting the generation of a larger osmotic pressure at the hydrogel-electrolyte interface. Figure 7.11 shows an electrically stimulated hydrogel with a microchannel full of bubbles as they were washed through the channel. In Figure 7.11 there was a minimum amount of bubbles stuck or surrounding the hydrogel, because of the channel flow. Contrary to the hydrogel shown in Figure 7.5 the EFSH in Figure 7.11 experienced swelling on both the anode and the cathode side of the hydrogel. This cathode side swelling occurred because the applied electric field was strong enough to cause an increase in the osmotic pressure, whereas in the EHOD case the hydrogel experienced a slight cathode-side deswelling.
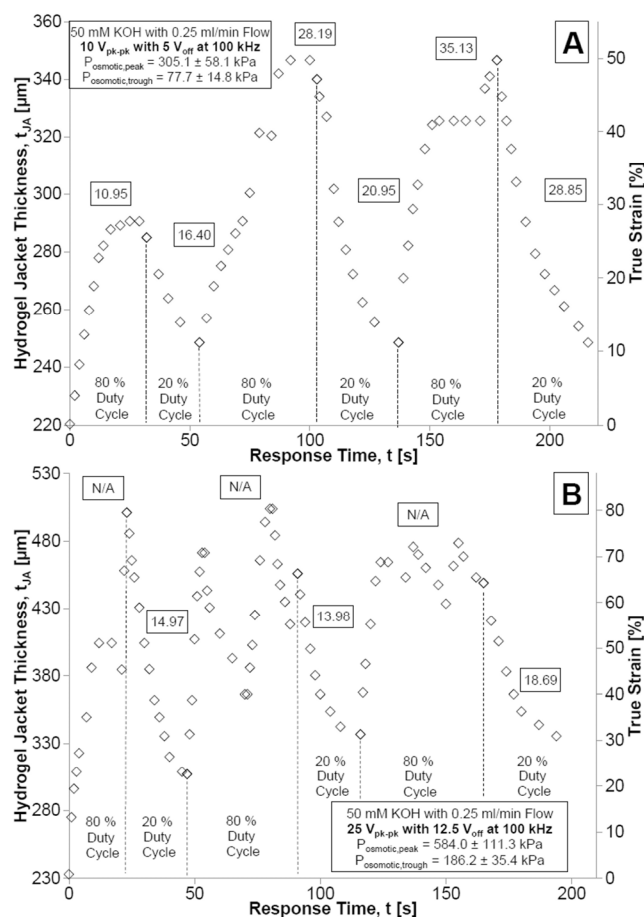
Figure 7.10: Unstable cyclical actuation of electrical hydrogels without dielectrics. The applied electric potential was (a) 10 V_{pk-pk} with 5 V_{off} (b) 25 V_{pk-pk} with 12.5 V_{off}.

Comparing the results of Figure 7.10(A) with Figure 7.4(B) highlights the significant increase in both the strain response and the osmotic pressures generated with no dielectric. At 25 V_{pk-pk}, not employing a dielectric layer increased the electrically induced osmotic pressure generated by ~396 % and subsequent true strain by ~370 %, even though the response was highly unstable. This contrast highlights how the system with dielectric coated electrodes could be improved, should the dielectric layer be optimized to maximize the transmission of the applied electric field. These two systems were also actuated in difference electrolyte concentrations. The stronger concentration, as in Figure 7.9(A), had a lower chemical equilibrium osmotic pressure of 361.4±78.5 kPa compared to the 1 mM osmotic pressure of 635.9±128.8 kPa. Hence an applied
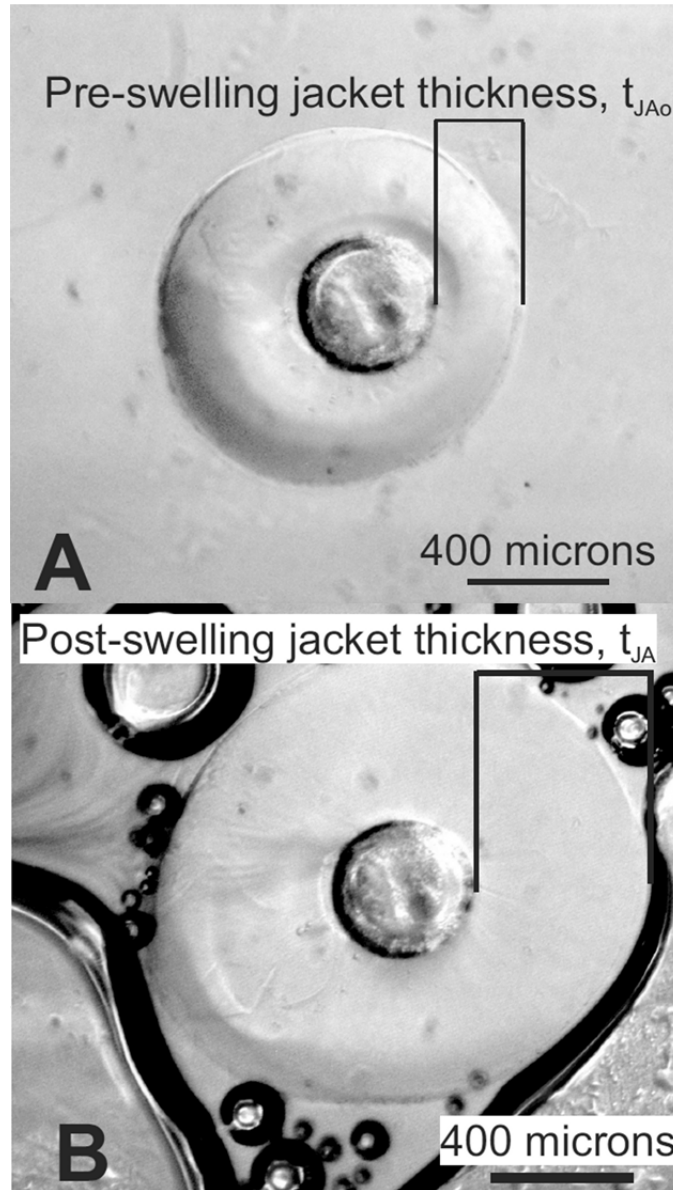
Figure 7.11: Electrically stimulated hydrogel without dielectric coated electrodes (a) at equilibrium (b) actuated showing electrolyte flowing through the microchannel washing away the bubbles and bubbles surrounding the hydrogel.

electric field would modify the lower pressure to a larger extent; however, this effect would be minimal compared to the extra electric field applied to the system by actuating without a dielectric layer.

Two modifications were made to achieve stable electrical actuation without dielectrics: reduction of the electrolyte concentration to 5 mM as less electrolysis occurs at lower concentrations, and decreasing the rate of electrolysis that does occur by applying a maximum electric potential of 10

V_{pk-pk}. Stable cyclical actuation can be seen in Figure 7.12, with applied electric potentials of 5 V_{pk-pk} and 10 V_{pk-pk}. Applied electric potentials larger than 10 V_{pk-pk} were attempted but the osmotic pressures generated were large enough to cause rupture of the hydrogel, as reducing the electrolyte concentration from 50 mM to 5 mM decreased the storage modulus, seen in Figure 7.3.

Figure 7.13 shows the rise times, fall times, and true strain results observed for stable cyclical hydrogel actuation without dielectric coated electrodes. True strain was moderately increased with increased electric potential, but more significant was the reduction in both the rise times and fall times during actuation. The decreased rise times were a direct result of larger osmotic pressure being generated, while the decreased fall times were due to a larger elastic restoring force caused by the hydrogels higher relative strain.

Cyclical actuation was performed for 4 and 5 cycles, seen in Figure 7.12(A) and Figure 7.12(B), respectively, which was higher than the 3 cycles for EHOD. This was to examine hydrogel fatigue after one or two more cycles. The samples did experience some decrease in deformation, but this was not significant even though the true strain response was over 40 %. Therefore the decrease in deformation observed for EHOD samples could be due to the presence of more induced defects in the dielectric layer. However, a thorough fatigue analysis of the hydrogel and dielectric layer would be needed to quantify any performance degradation.

Overall, cyclical actuation of hydrogels without the use of dielectric coated electrodes provided larger true strains and osmotic pressures than the system employing dielectric coated electrodes. However, these systems are highly unstable and required specific configurations for continued operation. Should an appropriate configuration be found for a microvalve or micropump application the system would still require an external syringe pump to flow electrolyte down the microchannel. This external component (and associated power requirements) significantly

251
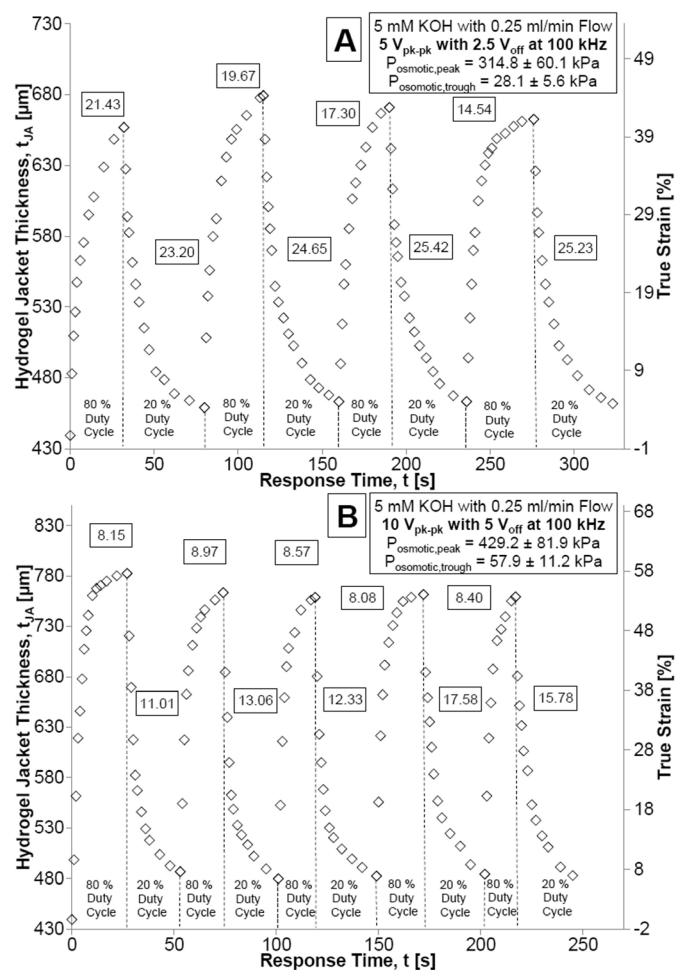
Figure 7.12: Stable cyclical actuation of electric hydrogels without dielectrics. The applied electric potential was (a) 5 V_{pk-pk} with 2.5 V_{off} (b) 10 V_{pk-pk} with 5 V_{off}.
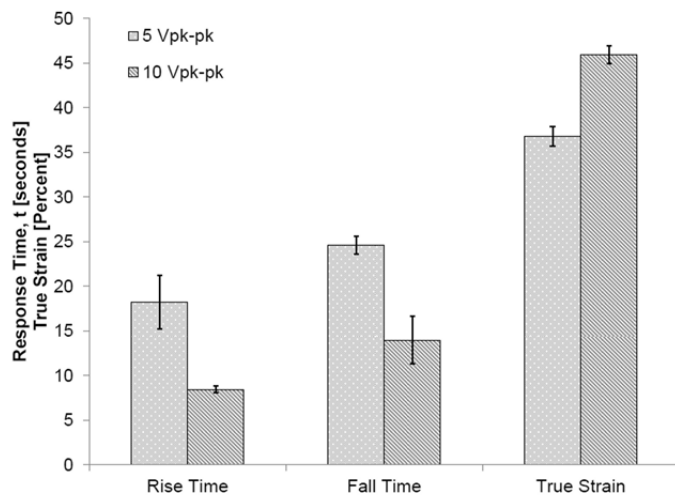
Figure 7.13: Average rise times, fall times, and true strain for stable cyclical electrical hydrogel actuation without dielectric coated electrodes, due to an 80 % duty cycle induced swelling or 20 % duty cycle induced deswelling at 5 or 10 V_{pk-pk}. Each bar is an average of all cycles observed.

hampers the systems portability and thus the compatibility with a full lab-on-a-chip device. Unless the intended application can support these external components, optimization of the system employing dielectric coated electrodes would move its performance closer to the performance specifications outlined in this section.

7.4   Conclusions and Future Work

The results presented within this work demonstrate the viability of cyclical microactuation of hydrogels employing dielectric coated electrodes at various applied electric potentials. The response time of the system was on the order of seconds, much faster than non-electrical hydrogel stimulation and comparable with other electrical stimulation. The main system described here does not suffer from electrolysis of electrolyte or require any external components for operation (other than an electrical power supply), thus it could be integrated directly into lab-on-a-chip systems for microfluidic regulation.

Cycling the duty cycle between 80 % and 20 % was shown to be an effective method to control the hydrogel's actuation response. Duty cycles between 99% and 1 %, and anything in between, could theoretically be employed to induce actuation. However, duty cycles should be large enough to ensure that an electric field strong enough be applied to actuate the hydrogel. The duty cycles chose here were the limits of the electrical equipment available.

Comparing the systems with and without dielectric coated electrodes shows the difference in osmotic pressure and deformation developed. This comparison highlights the future performance potential of the EHOD system, provided the dielectric layer can be optimized to minimize any electric field attenuation.

Actuation of the cylindrical hydrogel between coplanar electrodes would always generate asymmetrical actuation towards the anode. Symmetrical actuation could be induced by modifying the electrode

253

configuration to include a circular anode surrounding the hydrogel, with a small interior cathode aligned to the hydrogel center. Employing dielectric coated electrodes allows this enhancement, whereas before the hydroxide generated at the cathode would deswell the hydrogel.

The pressures generated at the higher applied voltages were also comparable with pH-based 3D microvalve configurations. Thus, hydrogels in this system to be used for out-of-plane actuation by deforming a flexible membrane to inhibit fluid flow. Multiple single cells could also be aligned over a microchannel, and operated with a cascading electrical signal, to generate peristaltic pumping.

References

[1] P. Mitchell, "Microfluidics - downsizing large-scale biology," *Nature Biotechnology,* vol. 19, pp. 717-721, Aug 2001.

[2] L. Gervais, N. de Rooij, and E. Delamarche, "Microfluidic Chips for Point-of-Care Immunodiagnostics," *Advanced Materials,* vol. 23, pp. H151-H176, Jun 24 2011.

[3] K. W. Oh and C. H. Ahn, "A review of microvalves," *Journal of Micromechanics and Microengineering,* vol. 16, pp. R13-R39, May 2006.

[4] B. D. Iverson and S. V. Garimella, "Recent advances in microscale pumping technologies: a review and evaluation," *Microfluidics and Nanofluidics,* vol. 5, pp. 145-174, Aug 2008.

[5] D. J. Beebe, J. S. Moore, J. M. Bauer, Q. Yu, R. H. Liu, C. Devadoss*, et al.,* "Functional hydrogel structures for autonomous flow control inside microfluidic channels," *Nature,* vol. 404, pp. 588-590, Apr 6 2000.

[6] S. J. Kim, S. J. Park, and S. I. Kim, "Properties of smart hydrogels composed of polyacrylic acid/poly(vinyl sulfonic acid) responsive to external stimuli," *Smart Materials & Structures,* vol. 13, pp. 317-322, Apr 2004.

[7] R. H. Liu, Q. Yu, and D. J. Beebe, "Fabrication and characterization of hydrogel-based microvalves," *Journal of Microelectromechanical Systems,* vol. 11, pp. 45-53, Feb 2002.

[8] S. K. De, N. R. Aluru, B. Johnson, W. C. Crone, D. J. Beebe, and J. Moore, "Equilibrium swelling and kinetics of pH-responsive hydrogels: Models, experiments, and simulations," *Journal of Microelectromechanical Systems,* vol. 11, pp. 544-555, Oct 2002.

[9] A. Richter, D. Kuckling, S. Howitz, T. Gehring, and K. F. Arndt, "Electronically controllable microvalves based on smart hydrogels: Magnitudes and potential applications," *Journal of Microelectromechanical Systems,* vol. 12, pp. 748-753, Oct 2003.

[10] A. Richter, S. Klatt, G. Paschew, and C. Klenke, "Micropumps operated by swelling and shrinking of temperature-sensitive hydrogels," *Lab on a Chip,* vol. 9, pp. 613-618, 2009.

[11] S. R. Sershen, G. A. Mensing, M. Ng, N. J. Halas, D. J. Beebe, and J. L. West, "Independent optical control of microfluidic valves formed from optomechanically responsive nanocomposite hydrogels," *Advanced Materials,* vol. 17, pp. 1366-1368, Jun 6 2005.

[12] N. S. Satarkar, W. L. Zhang, R. E. Eitel, and J. Z. Hilt, "Magnetic hydrogel nanocomposites as remote controlled microfluidic valves," *Lab on a Chip,* vol. 9, pp. 1773-1779, 2009.

[13] M. J. Bassetti, A. N. Chatterjee, N. R. Aluru, and D. J. Beebe, "Development and modeling of electrically triggered hydrogels for microfluidic applications," *Journal of Microelectromechanical Systems,* vol. 14, pp. 1198-1207, Oct 2005.

[14] R. P. Hamlen, C. E. Kent, and S. N. Shafer, "Electrolytically Activated Contractile Polymer," *Nature,* vol. 206, pp. 1149-1150, 1965.

[15] T. Tanaka, I. Nishio, S. T. Sun, and S. Uenonishio, "Collapse of Gels in an Electric-Field," *Science,* vol. 218, pp. 467-469, 1982.

[16]   T. Shiga and T. Kurauchi, "Deformation of Polyelectrolyte Gels under the Influence of Electric-Field," *Journal of Applied Polymer Science,* vol. 39, pp. 2305-2320, Jun 5 1990.

[17]   M. Doi, M. Matsumoto, and Y. Hirose, "Deformation of Ionic Polymer Gels by Electric-Fields," *Macromolecules,* vol. 25, pp. 5504-5511, Sep 28 1992.

[18]   S. J. Kim, H. I. Kim, S. J. Park, I. Y. Kim, S. H. Lee, T. S. Lee*, et al.*, "Behavior in electric fields of smart hydrogels with potential application as bio-inspired actuators," *Smart Materials & Structures,* vol. 14, pp. 511-514, Aug 2005.

[19]   E. A. Moschou, M. J. Madou, L. G. Bachas, and S. Daunert, "Voltage-switchable artificial muscles actuating at near neutral pH," *Sensors and Actuators B-Chemical,* vol. 115, pp. 379-383, May 23 2006.

[20]   M. L. O'Grady, P. L. Kuo, and K. K. Parker, "Optimization of Electroactive Hydrogel Actuators," *Acs Applied Materials & Interfaces,* vol. 2, pp. 343-346, Feb 2010.

[21]   G. H. Kwon, G. S. Jeong, J. Y. Park, J. H. Moon, and S. H. Lee, "A low-energy-consumption electroactive valveless hydrogel micropump for long-term biomedical applications," *Lab on a Chip,* vol. 11, pp. 2910-2915, 2011.

[22]   G. H. Kwon, Y. Y. Choi, J. Y. Park, D. H. Woo, K. B. Lee, J. H. Kim*, et al.*, "Electrically-driven hydrogel actuators in microfluidic channels: fabrication, characterization, and biological application," *Lab on a Chip,* vol. 10, pp. 1604-1610, 2010.

[23]   J. R. Saunders and W. Moussa, "AC Frequency-based Electrical Stimulation of Hydrogel Microactuators Employing Parylene-N Coated Electrodes," *Sensors and Actuators B: Chemical,* vol. 182, pp. 761-773, June 2013.

[24]   T. B. Jones, M. Gunji, M. Washizu, and M. J. Feldman, "Dielectrophoretic liquid actuation and nanodroplet formation," *Journal of Applied Physics,* vol. 89, pp. 1441-1448, Jan 15 2001.

[25]   V. Mukundan, P. Ponce, H. E. Butterfield, and B. L. Pruitt, "Modeling and characterization of electrostatic comb-drive actuators in conducting liquid media," *Journal of Micromechanics and Microengineering,* vol. 19, Jun 2009.

[26]   S. C. System, "Parylene Electrical Properties," ed. Indianapolis, IN.

[27]   J. C. McDonald, D. C. Duffy, J. R. Anderson, D. T. Chiu, H. K. Wu, O. J. A. Schueller*, et al.*, "Fabrication of microfluidic systems in poly(dimethylsiloxane)," *Electrophoresis,* vol. 21, pp. 27-40, Jan 2000.

[28]   R. D. Tacito and C. Steinbruchel, "Fine-line patterning of parylene-n by reactive ion etching for application as an interlayer dielectric," *Journal of the Electrochemical Society,* vol. 143, pp. 1974-1977, Jun 1996.

[29]   D. Biswal and J. Z. Hilt, "Analysis of Oxygen Inhibition in Photopolymerizations of Hydrogel Micropatterns Using FTIR Imaging," *Macromolecules,* vol. 42, pp. 973-979, Feb 24 2009.

[30]   J. R. Saunders, S. Abu-Salih, T. Khaleque, S. Hanula, and W. A. Moussa, "Modeling Theories of Intelligent Hydrogel Polymers," *Journal of Computational and Theoretical Nanoscience,* vol. 5, pp. 1942-1960, 2008.

[31]   O. Okay and S. Durmaz, "Charge density dependence of elastic modulus of strong polyelectrolyte hydrogels," *Polymer,* vol. 43, pp. 1215-1221, Feb 2002.

[32] J. R. Saunders and W. Moussa, "Dynamic mechanical properties and swelling of UV-photopolymerized anionic hydrogels," *Journal of Polymer Science Part B: Polymer Physics,* vol. 50, pp. 1198-1208, Aug 15 2012.

[33] H. Li, T. Y. Ng, Y. K. Yew, and K. Y. Lam, "Modeling and simulation of the swelling behavior of pH-stimulus-responsive hydrogels," *Biomacromolecules,* vol. 6, pp. 109-120, Jan-Feb 2005.

[34] J. R. Saunders, S. Abu-Salih, and W. A. Moussa, "Parametric Chemo-Electro-Mechanical Modeling of Smart Hydrogels," *Journal of Computational and Theoretical Nanoscience,* vol. 5, pp. 1961-1975, Oct 2008.

[35] S. J. Kim, S. G. Yoon, and S. I. Kim, "Effect of the water state on the electrical bending behavior of chitosan/poly(diallyidimethylammonium chloride) hydrogels in NaCl solutions," *Journal of Polymer Science Part B: Polymer Physics,* vol. 42, pp. 914-921, Mar 1 2004.

[36] B. E. Rapp, A. Voigt, M. Dirschka, and K. Lange, "Deposition of ultrathin parylene C films in the range of 18 nm to 142 nm: Controlling the layer thickness and assessing the closeness of the deposited films," *Thin Solid Films,* vol. 520, pp. 4884-4888, May 31 2012.

[37] H. Liu, S. Dharmatilleke, D. K. Maurya, and A. A. O. Tay, "Dielectric materials for electrowetting-on-dielectric actuation," *Microsystem Technologies-Micro-and Nanosystems-Information Storage and Processing Systems,* vol. 16, pp. 449-460, Mar 2010.

[38] H. Moon, S. K. Cho, R. L. Garrell, and C. J. Kim, "Low voltage electrowetting-on-dielectric," *Journal of Applied Physics,* vol. 92, pp. 4080-4087, Oct 1 2002.

[39] Y. Y. Lin, R. D. Evans, E. Welch, B. N. Hsu, A. C. Madison, and R. B. Fair, "Low voltage electrowetting-on-dielectric platform using multi-layer insulators," *Sensors and Actuators B-Chemical,* vol. 150, pp. 465-470, Sep 21 2010.

[40] B. D. Johnson, D. J. Beebe, and W. Crone, "Effects of swelling on the mechanical properties of a pH-sensitive hydrogel for use in microfluidic devices," *Materials Science & Engineering C-Biomimetic and Supramolecular Systems,* vol. 24, pp. 575-581, Jun 1 2004.

Chapter 8

General Discussion and Conclusions

8.1 Overview and Summary

This thesis presents the successful development of an electrically stimulated hydrogel microactuator that can be cyclically actuated by employing AC frequencies and Parylene-N coated electrodes. During this development various interconnected novel achievements were demonstrated, which include:

- The first effective cyclical microactuation of hydrogels through the application of pulse width modulation at increasing electric field magnitudes to generate a maximum true strain of ~27% with response times less than 10 seconds. This work was reviewed and disseminated in the Journal of Microelectromechanical Systems [1].

- Analytical prediction of the previously unknown characteristic AC frequency to promote maximum electrical hydrogel actuation, and subsequent successful prototype demonstration of microactuation between frequencies of 10 Hz to 100 kHz. This work was reviewed and disseminated in Sensors and Actuators B: Chemical [2].

- Characterization of the HEMA-AA hydrogel's dynamic mechanical properties between cyclically straining frequencies of 0.1 to 10 Hz, and with a wide variety of fabrication parameters. This investigation quantified a large range of storage moduli from ~10 kPa to ~1.7

MPa. This work was reviewed and disseminated in the Journal of Polymer Science B: Polymer Physics [3].

- The first numerical investigation of the hydrogel's response to a reversed electric field polarity. The examination focused on the electrical and chemical field dynamics that occur during chemical or electrical stimulation, which underlie the normally observable deformation. This work was reviewed and disseminated in the Journal of Computational and Theoretical Nanoscience [4].

- In parallel to the aforementioned major achievements the hydrogel microactuator had its electrically induced osmotic pressure analytically calculated [1], the microactuator system had its impedance and apparent power characterized [2], and the general morphology of the fabricated hydrogels was investigated [3].

Demonstration of cyclical electrical hydrogel microactuation was performed by employing duty cycles of 20 % and 80 % at electric field magnitudes up to 20 kV/m [1]. These conditions generated a maximum true strain response of ~27 % with rise and fall response times under 10 seconds. Upon further investigation a plateau in the peak-to-trough true strain response was also observed at higher applied electric fields, as the absolute maximum and minimum deformation began increasing together at the same rate. Comparing the system with Parylene-N coated electrodes to that without Parylene-N highlighted the differing performance, as the maximum true strain response peaked above 50 % at a fraction of the applied electric field.

The characteristic AC actuation frequency was analytically predicted by modeling the entire hydrogel-electrolyte-dielectric system's capacitance [2]. The overall capacitance was primarily a function of the electrolyte regions, hydrogel regions, and dielectric layers, while the characteristic frequency was dominated by the dielectric layer over the electrodes. The characteristic frequency was investigated at varying electrolyte

concentration and dielectric thicknesses, and operational regions were identified where experimental microactuation was possible.

The swelling true strain and response time of the hydrogel microactuator, as a function of the applied AC frequency, was characterized for two systems, one below and one above the characteristic frequency [2]. It was demonstrated that operating above this frequency provided adequate performance for microactuation. In addition, it was observed that the hydrogel still underwent swelling at lower frequencies, displaying that even a minimal AC frequency will partially disturb the induced electric double layer and its electrostatic shielding effects. These less-optimum actuation states could be beneficial for ultra-lower power operation, as it was found that apparent power has a minimum between 1 to 10 kHz.

To examine the effect of cyclical deformation on the hydrogel's dynamic mechanical properties the relationship between storage modulus and loss modulus was examined for a range of testing and fabrication conditions [3]. The degree of hydrogel swelling was shown to significantly affect this relationship, causing a higher loss modulus with increased swelling. However, the storage modulus of all hydrogels tested was dominant over loss modulus effects, generally by one order of magnitude. The tested hydrogel also had their morphology examined through scanning electron microscopy to observe the changes in the hydrogel's morphology as a result of the various environment and fabrication conditions.

The theoretical basis for cyclical electrical hydrogel actuation was also initially examined through numerical modeling of the chemo-electro-mechanical response [4]. This numerical modeling investigated chemical swelling, electrical swelling, and reversed electric field polarity induced cyclical actuation. The response was shown to be theoretically fully reversible, with the deformation performance and response kinetics dominated by the magnitude of electric fields and hydrogel critical

260

dimensions, respectively. This modeling also provided insight into the transient chemical and electric field dynamics that were responsible for generating the osmotic pressure.

To provide a knowledgebase background for the works above two reviews of research literature were collaboratively performed. One examined the equations systems available for numerical modeling of chemical and electrically stimulated microscale hydrogels-based systems [5], and is available in Appendix A-1. Another overviewed the different actuation mechanisms for stimuli sensitive hydrogels, their mechanical characterization, and the different prototype systems hydrogel's have been incorporated within [6].

8.2   Future Work

The demonstrated successful electrical stimulation of hydrogel microactuators, without the negative effects of electrolyte electrolysis and electrochemical reactions, provides multiple new research pathways. These pathways can be developed to optimize the current system or apply the developed principles to new systems.

I.   Symmetric Swelling. Throughout this work the hydrogel underwent asymmetric swelling towards the anode. The configuration of the examined system could potentially be modified to promote symmetric radial swelling and deswelling. This could be performed by using a circular outer electrode surrounding a cylindrical hydrogel, combined together with a circular inner electrode positioned at the center of the hydrogel. This could potentially generate an osmotic pressure symmetrically around the hydrogel, and hence cause symmetric deformation. In addition, this electrode configuration would have a shorter electrode gap causing higher electric fields than generated in this work with the same electric

261

potential range. These higher electric fields would further promote a higher strain response and shorter response times.

II. Dielectric Coatings. The dielectric layer implemented within the experimental studies was Parylene-N, which was deposited between 300 nm to 1 µm. Further optimization of this dielectric layer could significantly enhance performance, as contrasted by experiments in Chapter 7. A uniform and defect-free Parylene-N layer of 100 nm thickness would be preferential to reduce the characteristic actuation frequency and reduce electric field losses. This Parylene-N thickness has been previously fabricated in literature, but its microfabrication was not achievable in this work. Furthermore, it has been demonstrated for electrowetting on dielectric systems that alternative dielectric materials are available which uniformly cover electrodes at thicknesses of <100 nm. Incorporation of one of these alternative dielectrics within the system could potentially replace Parylene-N to provide lower characteristic frequencies and improve actuator performance. This reduction in the characteristic frequency would also extend the range of electrolyte concentrations that could be used within the system.

III. New Hydrogel Materials. A significant number of electrically stimulated hydrogel compositions were previously tested. While the majority is not amenable to photopolymerization, those that are could provide alternative material compositions for substitution in the system examined here. A better hydrogel material would be one that can withstand larger induced osmotic pressures without rupture, operate in air at relatively low applied electric potentials, or perhaps be electrically active in both alkaline and acidic solutions. However, should a better alternative be found, it would also need to have its dynamic

mechanical properties characterized to further perform any analytical analysis or numerical modeling.

IV. Out-of-plane Actuation. The system examined in this work was mechanically constrained to in-plane actuations. This system could be modified to produce out-of-plane actuations by replacing one constraining surface with a flexible membrane. Upon electrical stimulation the hydrogel experiences multidirectional osmotic pressure, which would then deform the flexible membrane. This technique was previously implemented for pH stimulated hydrogels for microvalving and for thermosensitive hydrogel for microvalving and micropumping. This configuration would require an appropriate balance between the membrane's elastic restoring force and the applied pressure from the hydrogel to generate an adequate magnitude of actuation. This configuration could also build off the aforementioned future research pathways to produce a microactuator with highly competitive performance.

References

[1]   J. R. Saunders and W. Moussa, "Cyclical Electrical Stimulation of Hydrogel Microactuators Employing Parylene-N Coated Electrodes," *Journal of Microelectromechanical Systems,* Accepted and In Press, pp. 1-13, 2013. DOI: 10.1109/JMEMS.2013.2268382

[2]   J. R. Saunders and W. Moussa, "AC frequency-based electrical stimulation of hydrogel microactuators employing Parylene-N coated electrodes," *Sensors and Actuators B: Chemical,* vol. 182, pp. 761-773, June 2013.

[3]   J. R. Saunders and W. Moussa, "Dynamic mechanical properties and swelling of UV-photopolymerized anionic hydrogels," *Journal of Polymer Science Part B: Polymer Physics,* vol. 50, pp. 1198-1208, 2012.

[4]   J. R. Saunders, S. Abu-Salih, and W. A. Moussa, "Parametric Chemo-Electro-Mechanical Modeling of Smart Hydrogels," *Journal of Computational and Theoretical Nanoscience,* vol. 5, pp. 1961-1975, Oct 2008.

[5]   J. R. Saunders, S. Abu-Salih, T. Khaleque, S. Hanula, and W. A. Moussa, "Modeling Theories of Intelligent Hydrogel Polymers," *Journal of Computational and Theoretical Nanoscience,* vol. 5, pp. 1942-1960, 2008.

[6]   T. Khaleque, S. Abu-Salih, J. R. Saunders, and W. Moussa, "Experimental Methods of Actuation, Characterization and Prototyping of Hydrogels for BioMEMS/NEMS Applications," *Journal of Nanoscience and Nanotechnology,* vol. 11, pp. 2470-2479, Mar 2011.

Appendix A-1

Modeling Theories of Intelligent Hydrogel Polymers[1]

A-1.1 Introduction

Numerical modeling of the volume transition mechanism of the intelligent polyelectrolyte hydrogels has recently received a lot of interest from researchers. The drive to reduce the cost associated with and time required for prototyping and optimization has caused this interest. Multiple theoretical models are available for numerical simulations, with the predominant models for simulating hydrogels being presented here. The papers is outlined as follows, a brief review of hydrogel composition, stimulation methods, swelling/deswelling mechanisms, and applications is given in Section A-1.1. In Section A-1.2, the numerical models based on the theories of thermodynamics, multiphasic mixtures, transport, and molecular dynamics are discussed. The review is then concluded in Section A-1.3.

A-1.1.1 Hydrogel Composition

Hydrogels are composed of a three dimensional cross-linked polymer network. The polymer chains are interconnected through crosslinks and are immersed in aqueous solution [1, 2]. The polymer

---

[1] A version of this chapter has been published. Saunders, Abu-Salih, Khaleque, Hanula, Moussa 2008. Journal of Computational and Theoretical Nanoscience. 5(11): 1942-1960.

network may be hydrophilic and/or hydrophobic [3]. The hydrophilic components cause the hydrogel to swell, whereas the hydrophobic components control the swelling of the gel as well as the mechanical properties [4]. Temperature sensitive hydrogels are characterized by the presence of hydrophobic components, and the swelling/deswelling of temperature sensitive hydrogels can be varied by changing the ratio of hydrophobic and hydrophilic components [5, 6]. There are generally ionizable basic or acidic groups attached to these polymer chains, with some of these ionizable groups dissociating completely and others dissociating partially in solutions [1, 7]. Anionic hydrogels have negative ions which are bound to the polymer network, shown in Figure A-1.1, while cationic hydrogels have fixed positive ions, seen in Figure A-1.2, and neutral hydrogels contain the same amount of both positive and negative fixed ions. It is generally assumed that neutral hydrogels have a nearly identical concentration distribution of fixed ions throughout the polymer matrix. Hydrogels are considered super absorbent because they can absorb large amounts of surrounding water or solvent upon stimulation. The amount of water absorbed by the hydrogel depends on the balance between the stimuli induced osmotic pressure and the inherit elastic restoring force of the polymer network. For large values of elastic restoring force the gel absorbs, comparatively, less water than for lower values. The composition of hydrogels varies with the polymerization monomer composition that are used to fabricate hydrogels [8]. The most general structure of a hydrogel consists of backbone monomer, crosslinking co-monomer, electrolyte co-monomer, and solvent [9]. Based on the types of bonding that exists between the polymer chains, hydrogels can be classified as physical gels or chemical gels. In physical gels the polymer chains are held together via polymer chain entanglement or non-covalent bond with the attractive forces induced by the hydrogen bonding or hydrophobic forces. In chemical gels the polymer chains are bound to each other by covalent bonds [8].
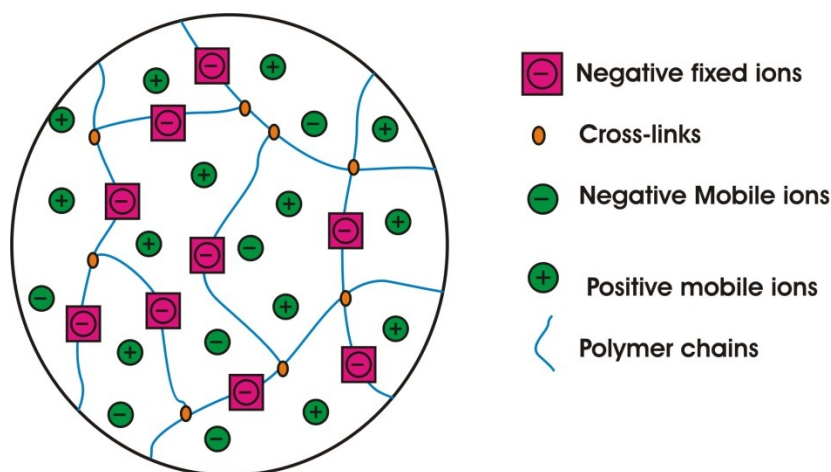
Figure A-1.1: Structure of an anionic hydrogel
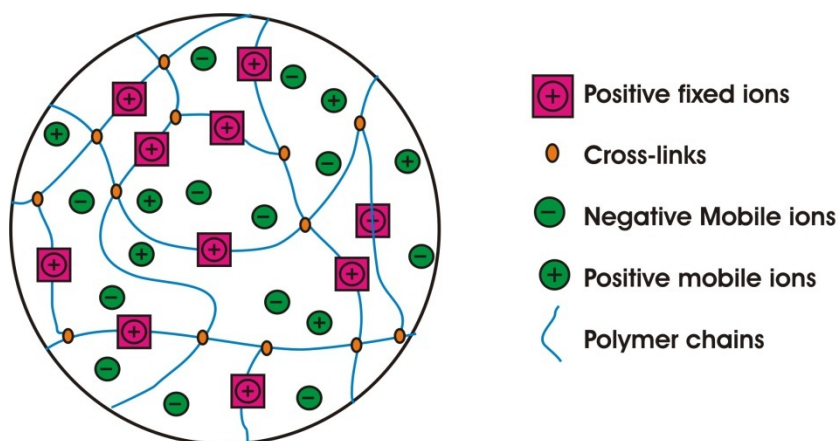
Figure A-1.2: Structure of a cationic hydrogel

A-1.1.2   Hydrogel Stimulation Methods

Hydrogels react to a wide range of external stimuli, including but not limited to pH [10], temperature [11], solvent composition [12], enzymes [13], electric fields [14], and light [3]. A volume change, in the form of volume expansion or contraction, is usually accompanied by these stimuli methods. The elapsed time for volume transition significantly depends on the stimulation methods, from milliseconds with electrical stimulation [15] to hours using visible light [3]. The stimulus is usually only mechanism that facilitates the volume transition of the hydrogel structure. In other words, an electric field will cause a pH gradient to be established, which will cause osmotic pressure to buildup on the hydrogel's boundary

267

surfaces, leading to a volume transition. Each specific stimulation method has a different mechanism leading to the hydrogel volume transition response, with the most common mechanisms being discussed in the following section.

A-1.1.3   Hydrogel Swelling/Deswelling Mechanism

Hydrogels react to a variety of external stimulus, with each stimulus invoking a different mechanism causing the phenomena of volume transition. This section reviews the stimulation methods of pH, electric field, temperature, visible light, and grafted enzymes, and their associated mechanism for volume transition.

The swelling and deswelling of hydrogels due to a pH change is reversible and repeatable [10, 16-18]. pH sensitive hydrogels have either acidic and/or basic groups bound to their polymer chains, referred to herein as cationic and anionic hydrogels, respectively. At high pH the acidic groups of anionic hydrogels deprotonate and at low pH the basic groups protonate [18, 19]. As the pH of the surrounding solvent changes, an ion concentration gradient is established between the inside and outside of the gel. This gradient causes diffusion of mobile ions into and out of the hydrogel, and most importantly causes an osmotic pressure to be established on the surface of the hydrogel. This osmotic pressure, expanding or compressing the hydrogel, causes the desired volume transition. Anionic hydrogels swell at high pH, with the ionic composition depicted in Figure A-1.3, while cationic hydrogels swell at low pH [10, 20]. Swelling of the hydrogel induces elastic restoring forces within the polymer network, which eventually balances the osmotic pressure, resulting in an equilibrium gel state. The degree of swelling/deswelling within a hydrogel depends on the osmotic pressure generated, induced by the concentration gradient of mobile ions, and the elastic restoring force. This restoring elastic force plays a significant role for balancing the osmotic pressure in order to place the hydrogel in an equilibrium state [1, 7].
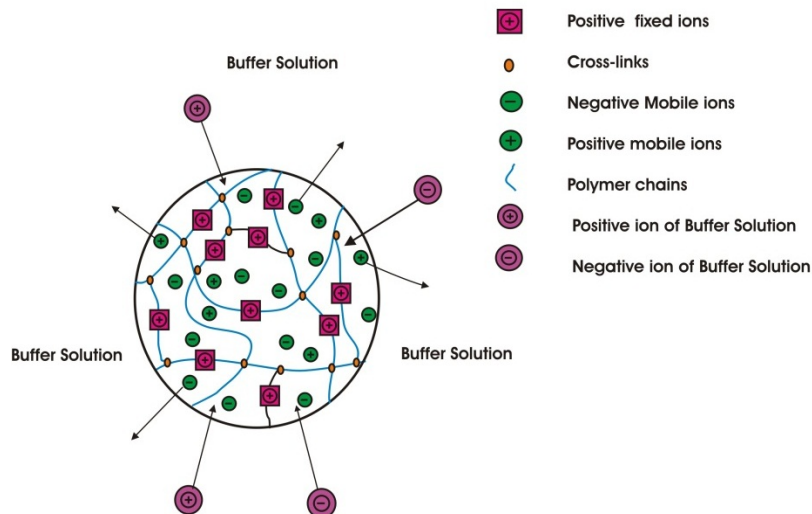
Figure A-1.3: Hydrogel swelling mechanism due to chemical (pH) stimulation.

Hydrogels swell, shrink, and bend in response to electrical stimulus using a very similar mechanism as that described for pH stimulus. The major difference, and advantage, between electrical and pH stimulations is that in the former one the electrical field migrate the mobile ions to set-up a ion concentration gradient through hydrogel and solution mediums [14, 15, 21, 22]. This ionic migration diffusion is much faster than the unforced diffusion based processes that depend on the pH difference between the interior and exterior of the hydrogel structure. The ionic gradients established can also be much larger than that provided by pH stimulation [23], which causes a larger osmotic pressure to be established resulting in faster response times [15]. In addition, reversing the polarity of the electric field reverses the concentration gradients, and subsequently causes the osmotic pressures previously established to act in the opposite direction. This easy and fast switching of a hydrogels volume transition can be exploited for a variety of applications.

Temperature sensitive hydrogels contain both hydrophobic and hydrophilic groups bound to their network. They undergo volume changes (swelling/deswelling) either at lower critical solution temperature (LCST) or upper critical solution temperature (UCST) [6, 16, 24, 25]. Temperature sensitive hydrogels are classified as negatively temperature sensitive,

269

positively temperature sensitive and thermally reversible hydrogels [6, 16, 25]. Negatively temperature sensitive hydrogels deswell as the temperature of their buffer increases above the LCST. On the other hand, positively temperature sensitive hydrogels deswell as the temperature decreases below the UCST [5, 6, 16, 25]. The degree of temperature sensitivity of hydrogels depends on the temperature dependency of the hydrogen bonding and hydrophobic interactions. In case of lower temperatures within negatively temperature sensitive hydrogels the hydrogen bonding of water molecules is strong near the hydrophobic polymer chains. This lowers the mixing free energy and increases the solubility of polymer chains in water, and as a result the hydrogel swells. But, at higher temperatures the hydrogen bond becomes weak and the hydrophobic interaction is dominant and the gel shrinks [10, 26, 27]. Also as the temperature increases the hydrophilic/hydrophobic balance of the polymer network is disturbed, leading to dehydration and the gel shrinks [5].

Light sensitive hydrogels are classified as UV light sensitive and visible light sensitive hydrogels [3, 6]. Some UV light sensitive hydrogels contain a UV light ionizable molecule, leuco cyanide [3, 6, 28]. Upon irradiation of UV light the leuco cyanide ionizes and cyanide ions cause an increase in osmotic pressure and the gel swells. Visible light sensitive hydrogels contain chromophore, and when exposed to visible light the chromophore absorbs light and then dissipates as heat. As a result the temperature of the gel increases which results deswelling of the gel similar to the temperature sensitive hydrogels [3, 29, 30].

Enzymes have also been grafted onto the hydrogel's polymer backbone, which act to catalyze the breakdown of specific molecules. This breakdown changes the internal equilibrium inside the hydrogel causing stimulation. For example, the detection of a lethal organophosphorus (OP) pesticide using hydrogels bonded with organophosphorus hydrolase (OPH) enzyme has been studied [13]. The

270

OPH breaks down OP into ionic compounds and a pH change occurs after which the hydrogel undergoes measured phase transition with incredible sensitivity.

A-1.1.4 Hydrogel Applications

Hydrogels have been implemented in a diverse range of applications suitable to utilize their unique properties. The ability of hydrogels to adsorb large volumes of surrounding solvent that is coupled with their response to the pH, electrical, or temperature stimulation, encouraged researchers to implement these hydrogel materials in microvalves and micropumps devices. In addition, due to the large percentage of solvent retention surrounding an interior polymer matrix, degradable hydrogels are suitable hosts for the growth or regeneration of tissues. These hydrogels can also encapsulate drugs for site specific delivery. Moreover, the ability to fabricate hydrogels stimulated by biological or inorganic molecules allows them to sense a very wide range of materials with increasing sensitivity.

Hydrogels have been found to act as chemo-electro-mechanical actuators, as they simulate the behavior of muscles [31, 32]. One of the first microvalve designs incorporating hydrogels was published by Beebe *et al..* A three-dimensional pH sensitive hydrogel microvalve which was isolated from the regulated fluid, and an in-plane pH sensitive hydrogel microvalve was proposed for fluidic regulation [33]. An anatomic venous valve was mimicked, and contributed to a pH responsive bi-strip in-flow hydrogel microvalve [34]. A temperature sensitive and electronically controllable in-flow hydrogel microvalve was studied by Richter *et al.* [35] who later developed an automatic microvalve based on the original design [36]. Lee *et al.* designed a pH sensitive hydrogel used as a microvalve and pH feedback sensor, which allowed for fluidic based regulation of pH [37]. Optically sensitive hydrogels were fabricated and used as an in-flow T-valve composed of gold colloid/nanoshell particles which responded to specific wavelengths of light [38]. A microvalve incorporated into a

cassette for DNA detection and amplification [39] using a thermally-activated in-plane hydrogel microvalve was designed by Wang *et al.* with a swollen hydrogel controlling fluidic movement [40]. There are many more different microvalves based on resistance based valves, hydrogel jacket valves, hybrid hydrogel membrane valves, electrically triggered valves, and biomimetic valves [41]. A pH and temperature sensitive hydrogel was used as a clutch mechanism for the control of a micromixer driven by an external rotating magnetic field, which was further engineered to act as a rotary micropump [42]. Moreover, pH and electrically stimulated hydrogel micropumps have also been developed for fluidic movement at the microscale. One configuration was created by Eddington and Beebe incorporating an array of pH sensitive hydrogels. These cylindrical hydrogels swell and deflect a thin membrane building up channel pressure, which is subsequently released through the deactivation of a pH sensitive hydrogel microvalve [43]. Two hydrogel check valves used in conjunction with a pneumatic actuator have been completed by Kim *et al.* which acts like a micropump, and allows delicate biological material such as fibroblast cells to be pumped [44]. In addition to valves and pump, and due to the locomotive action of hydrogels, there are biologically inspired hydrogels which have path-controlled linear locomotion, which mimic snake like or snail like movements [45].

Hydrogels unique structure also lend themselves to drug delivery applications, regeneration and growth of tissues, and formation of unique bio-active hydrogel hybrids. Hydrogels have aided in regeneration and repair of tissues through drug delivery to the eye [46], lungs [47], skin [48, 49], neurons [50-52], bone [53], and cartilage [54]. Another drug delivery technique incorporates a hydrogel shell immunologically isolating donor islet cells, which then may be used as replacement therapy for Type I Diabetes [55, 56]. Biocompatible and biodegradable [53] hydrogels have also been engineered as scaffold material. Through a synergy of drug delivery and cell adhesion markers [57], hydrogels imitate the real extra-

272

cellular matrix of tissue [58]. Skeletal [53, 59], nerve [60], and cartilage tissue [61] have been regenerated successfully using various 3-D scaffold systems. The evolution of computer aided 3-D organ printing [62] is now a first step for engineered tissues which could be used to replace or repair failing organs. For a review of 3-D skeletal tissue organ printing incorporating hydrogels (see Fedorovich, N. E. et. al. 2007) [63]. Some interesting organs that have been grown are implantable bio-artificial livers [64] and cardiac muscle tissue [65]. Hydrogels have also been utilized as an antibacterial material through the fabrication of a hybrid hydrogel, which incorporated different sizes of silver nanoparticles [66]. A thorough review on composite aqueous microgels was written by Pich and Adler, and gives an overview of recent advances in synthesis, characterization and applications [67]. Many stimuli-sensitive microgels can self-assemble with custom tailored properties and synthetic and biological molecules, a comprehensive review has been written by Xu and Kopecek [68].

In addition to hydrogels uses as actuating components or as components for biological regeneration and repair, hydrogels have interested researchers as components within sensing systems. Hydrogels are unique in that they react, through swelling or deswelling, to a range of external stimuli. A hydrogel can be fabricated to respond to a wide variety of stimulus. A reversibly antigen-responsive hydrogel [69], responds to various buffer solutions in response to a specific antigen and its corresponding antibody grafted to the polymer network. Microcantilevers have also had their surfaces functionalized using hydrogels for high sensitivity pH measurements [70]. Humidity actuated sensors [71] have been fabricated, some in the microscale with reversible switching responses on the order of 60 ms [72]. A fluorescent thin-film hydrogel incorporating a two-component sensing system based on viologen boronic acid and a fluorescent dye, immobilized in a hydrogel, measure fluorescence via fiber optics in order to sense glucose concentration [73]. Enzymatic breakdown of specific molecules allow for the detection of a

lethal organophosphorus (OP) pesticide. Hydrogels bonded with organophosphorus hydrolase (OPH) enzyme break down OP into ionic compounds and a pH change occurs after which the hydrogel undergoes measured volume change which can be measured with incredible sensitivity [13]. There are many more applications for bioresponsive hydrogel that are reviewed thoroughly by Ulijn *et al.* [74].

A-1.2 Hydrogel Theory

The four models reviewed for simulating the swelling/deswelling phenomena of polyelectrolyte hydrogels are thermodynamics, multiphasic mixture, transport, and molecular dynamics, which are discussed in the following sections 2.1, 2.2, 2.3, and 2.4, respectively.

A-1.2.1 Thermodynamic Models

During the last three decades many thermodynamic models were proposed to predict the swelling and deswelling response of ionic hydrogel polymers. In these models the total free energy of the polymer-solvent systems is mainly assumed to be the sum of: mixing, elastic and ionic free energies. Where, mixing free energy is due to the mixing process of the hydrogel network chains with the solvent molecules, the elastic free energy is a contribution due to the elastic response of the network chains, and the free ionic energy emanates from the attachment of charged ions to the network chains [11, 75-83]. Most of these thermodynamic models are based on the Flory's work [75, 77] and are proposed with the following assumptions [75, 77, 84]:

- The total free energy is assumed to be linear with the independent mixing, elastic and ionic free energies.
- The network chains are weakly crosslinked and therefore the Gaussian model [75] can be implemented in the elastic free energy contribution.

- The elongation and contraction of a single chain is assumed to be proportional to the expansion and contraction of the overall hydrogel structure, the so called affine assumption.

- The mobile and fixed ions confined in the hydrogel structure together affect and determine the ionic free energy of the system.

- In most thermodynamic models the osmotic pressure is assumed to be dependent on the concentration difference of the ionic species inside and outside the hydrogel.

The chemo-electro-mechanical responses (swelling and deswelling) of hydrogels is enforced and determined by the so called osmotic pressure, which is related to the change of the total free energy and is given by [75, 84]

$$\pi_{tot} = -\frac{\partial \psi_{tot}}{\partial V} = \pi_{mix} + \pi_{ela} + \pi_{ion} \tag{A-1.1}$$

where V is the hydrogel volume. π_{mix}, π_{ela} and π_{ion} are the osmotic pressures associated to the change in the mixing, elastic and ionic free energies, respectively. The osmotic pressure π_{mix} is given by the Flory-Huggins polymer solution theory as [75]:

$$\pi_{mix} = -\frac{RT}{V_1}\left(\ln(1-\phi) + \phi + \chi\phi^2\right) \tag{A-1.2}$$

where R, T, V_1 and χ are the universal gas constant, temperature, molar volume of the solvent, and the polymer-solvent interaction parameter, respectively. ϕ is the volume fraction of the hydrogel and therefore $1-\phi$ is the volume fraction of the solvent. The polymer is considered to be quite soluble when χ is less than 0.5 and insoluble when χ is greater than 0.5. χ can be related to the solubility parameter difference between polymer and solvent and so can be estimated from tables [75] and used to design a gel with actuator properties in any solvent combination. The interaction hydrogel-solvent parameter χ assumed to be dependent on the composition as well as on the temperature (at constant pressure) in

order to capture the volume transition of hydrogel [75, 77, 85]. For this end χ is appropriately expressed empirically by [75, 77]

$$\chi = \chi_1 + \chi_2 \phi + \chi_3 \phi^2 + \cdots \tag{A-1.3}$$

where the constants χ_i are function of temperature. In general, the third and higher order terms are neglected and the previous equation is reduced to the following linear relation [77]

$$\chi = \chi_1 + \chi_2 \phi \tag{A-1.4}$$

In order to satisfy the critical condition for neutral hydrogel volumes transition, i.e. swelling and deswelling, the two parameters χ_1 and χ_2 should be equal to 1/2 and 1/3, respectively.

The osmotic pressure related to the elastic free energy is given by [75, 77, 84]

$$\pi_{ela} = -\frac{RT}{V_1} N_c^{-1} \left(\phi^{\frac{1}{3}} \phi_0^{\frac{2}{3}} - \frac{\phi}{2} \right) \tag{A-1.5}$$

where N_c and ϕ_0 are the average number of segments in the network chain and the polymer volume fraction at the initial state, respectively. The elastic free energy that gives rise to the elastic part of the osmotic pressure is based on the Gaussian chain model that is derived from the rubber elasticity theory. The Gaussian model is a simple model and can be easily employed in thermodynamic models, but applicable only for hydrogels which are not highly crosslinked. In case of highly crosslinked hydrogels the non-Gaussian model should be used [86-88]. Several expressions for describing the volume transition of non-Gaussian polymer network have been proposed in the literature [81, 86, 89-91].

The osmotic pressure that is derived from the contribution of the ionic groups to the change in the total free energy is given by [75, 84]

$$\pi_{ion} = \frac{fRT}{\overline{V}_r} \phi \tag{A-1.6}$$

where f and $\overline{V}_r$ are the charge density of the hydrogel and the molar volume of the polymer monomer. The linear relation of the total osmotic

276

pressure expression with the ionic group term is valid when the number of ionic groups on each network chain is small [75, 77]. In the presence of salt buffer the osmotic pressure is modified to include the effect of non-uniform distribution of the mobile ions. The osmotic pressure term which includes such effect is given by [92, 93]

$$\pi_{electrolet} = 2(K-1)V_1 C_{salt}$$

(A-1.7)

where C_{salt} is the concentration of the salt and K is the Donnan coefficient of the mobile ions inside and outside the hydrogel. This Donnan coefficient is calculated by

$$K\left(K + \frac{f\phi}{\bar{V}_r C_{salt}}\right) - 1 = 0$$

(A-1.8)

The total osmotic pressure is the sum of Eqs. A-1.2 to A-1.7 and is equal to zero at the equilibrium steady-state.

$$\ln(1-\phi) + \phi + \chi\phi^2 + N_C^{-1}\left(\phi^{\frac{1}{3}}\phi_0^{\frac{2}{3}} - \frac{\phi}{2}\right) - 2(K-1)V_1 C_{salt} - V_1\frac{f}{\bar{V}_r}\phi = 0 \quad \text{(A-1.9)}$$

The volume fraction ϕ at the equilibrium state is calculated using the previous equation. The model of equilibrium swelling behavior of copolymer hydrogels containing monoprotic acid moieties was proposed by Caykara *et al.* [80, 94, 95].

The equilibrium swelling model of Flory is based on the Flory-Rehner equation and the osmotic pressure which is calculated from the difference of the concentration of mobile ions due to the ionic charges using the Donnan theory [75-77, 92, 96, 97]. However this model was criticized by Katchalsky and Michaeli [98], who claimed that the electrostatic interactions between charged ions have a significant contribution on the swelling behavior of ionic gel and should not be ignored. This electrostatic interaction term in the free energy was taken into account by Fomenko *et al.* [99, 100].

Although Flory's theory was criticized by researchers such as Hasa and Ilavsky [101-104] many studies have proposed osmotic pressure in

which the electrostatic repulsive force was not considered [105]. The effect of the charge distribution on the swelling behavior of ionic gels was investigated by Ogawa *et al.* and they concluded that their results could not be explained in term of osmotic pressure [105]. However, Baek *et al.* proposed a model in which the osmotic pressures concept and the electrostatic interaction are replaced with a specific form of the free energy of the system. This specific term includes the free energy changes due to the change of the concentration of ionic species [96, 106]. The free energy of polyampholytic hydrogels that were considered by English E. Antony consist of four terms: mixing, elastic, translation and coulombic free energies [76]. However Kramarteno et al. added the free energy gained from ion pairing and the combinatorial entropy of distribution of counterions between three possible states [107]. In some other models the free energy of the system assumed to a probability distribution function of different states [108].

Despite of the simplicity of thermodynamic equilibrium models they still do not give good quantitative results [7]; however, they do allow qualitative insight into hydrogels behavior, as shown in Table A-1.1. Most of these thermodynamic models rely on the assumption that different terms of free energies are independent. This summation relation is questionable because all the energy terms depend on the configuration of mesh chain, and therefore, should be connected by the nature of the hydrogel structure. In addition, many of the input parameters in the model are difficult to be determined experimentally and are often adjusted to fit the hydrogel equilibrium behavior. Most of the thermodynamic models are formed to capture the equilibrium steady state; therefore, they are not employed to predict the transient chemo-electro-mechanical response of hydrogels. Furthermore, the thermodynamic model does not inherently simulate very large deformations of hydrogels, due to the Gaussian chain model employed. Researchers looking for microscale simulation of

hydrogel volume transition are suggested to review other numerical models.

Table A-1.1: Advantages and disadvantages of the thermodynamics model for simulating hydrogel volume transition.

	Qualitative Agreement	Quantitative Agreement	Min. Scale Modeled	Transient Analysis	Equilibrium Analysis	Large Deformations
Thermo-dynamics	Yes	No	Macroscale	No	Yes	??

A-1.2.2 Multiphasic Mixture Theory

Multiphasic mixture models assume that the physical environment examined can be divided into two or more phases, each with its own specific governing equations. These multiple phases include; an incompressible solid phase, an incompressible fluidic phase, and an ionic phase which consist of anions and cations. To define the transient volume transition of polyelectrolyte hydrogels a triphasic mixture theory was formulated. Triphasic mixture theory was derived from biphasic mixture theory [109-116]. Biphasic mixture theory was formulated to study the volume transition of articular cartilage, and does not include an ionic phase. The base biphasic confined compression model [110] was systematically modified to include; non-linear permeability [109], non-linear strain dependant permeability [111], unconfined compression [112], the effect of concentrations [113], and unconfined compression including the effects of concentration and creep [114]. The biphasic model was then examined using finite element analysis for linear confined compression [115] and then later for non-linear confined compression including strain-dependent permeability [116]. However, these biphasic models were not adequate for examining articular cartilage when the total solute concentration within the tissue was allowed to change. Therefore, a third phase was introduced to include the contributions of miscible solutes (mobile cations and anions, and fixed anions or cations) within the solid and liquid phases [117], which became the basis for triphasic mixture theory.

Triphasic mixture theory incorporates the contributions from an incompressible solid, an incompressible fluid, and miscible solutes (mobile and fixed anions and/or cations), and was first formulated by Lai *et al*. [117]. The first triphasic model examined equilibrium free and confined swelling where Donnan osmotic pressure and bulk chemical expansion contributed to swelling. This initial model was then expanded to include transient swelling, with the capability of predicting all field variables within the articular cartilage when subjected to either a mechanical and/or a chemical load [118]. Lai *et al*.'s triphasic theory was implemented to examine; a 1-D steady permeation of hydrated tissue subjected to an applied mechanical pressure and/or osmotic pressure [119], 1-D ion-induced deformation of soft charged tissue using a simplified version of Lai *et al*.'s equations [120], unconfined compression of an intervertebral disc using finite elements [121], the swelling of soft tissues modeled as poroelastic materials [122], multivalent ionic phases [123], stress-relaxation behavior of hydrated charged tissue in a 1-D confined compression state [124], 1-D confined compression of charged hydrated tissue using a simplified triphasic theory which expresses the ionic concentrations and chemical expansion stress as a function of the chemical energy and electrostatic energy [125], respectively, 1-D finite element confined compression and free swelling model using modified electrochemical/chemical potentials [126], the mechano-electrokinetic behavior of charged hydrated tissues with multi-electrolytes resulting from mechanochemical, electrochemical, and electrical forces [127], 1-D steady state and transient mechano-electrochemical behavior of charged hydrated soft tissue accounting for streaming and diffusion potential [128], three 2-D plain strain models using radial basis functions to solve the triphasic governing equations [129], 2-D steady state behavior of a hydrogel strip subjected to an external electric field [130], the effect of fixed charge density and tissue hydration on the permeability and creep behavior of cartilaginous tissues [131], an unconfined compression model

280

which explicitly incorporates the fixed charge density, diffusion potential and streaming potential [132], and dynamic unconfined compression of charged soft tissue containing uncharged solutes [133].

Li *et al.* [134, 135] composed a comprehensive triphasic mixture theory based on the previous theories by Lai *et al.* [118, 128], Mow *et al.* [124], Hon *et al.* [125], Gu *et al.* [123, 127], Sun *et al.* [126], and Zhou *et al.* [130]. Li *et al.*'s triphasic mixture theory mathematically formulated the constitutive governing equations for charged hydrated tissues and hydrogels which included three distinct phases. These three phases include: a solid phase, an interstitial liquid phase, and an ionic species phase denoted by s, w, and k (k = 1, 2, ... , n_f , where n_f is the total number of mobile ionic species considered), respectively. Li *et al.*'s model assumes that ions flow, osmosize, and redistribute within porous media that is subjected to an externally applied electric field. The governing equations are derived starting with the saturation condition:

$$\phi^s + \phi^w + \sum_{k=1}^{n_f} \phi^k = 1 \qquad \text{(A-1.10)}$$

where ϕ^α (α = s, w, k) are the volume fractions of the solid polymer network, miscible liquid phase, and ionic species, respectively, and n_f is the total number of mobile ionic species. Since ϕ^+ and ϕ^- are small in magnitude compared to ϕ^s and ϕ^w the saturation condition can be written as $\phi^s + \phi^w = 1$. In addition, assuming infinitesimal deformation [130] we obtain:

$$\phi^w = 1 - \frac{\phi_0^s}{1 + tr(\mathbf{E})} \qquad \text{(A-1.11)}$$

where ϕ_0^s is the solid phase volume fraction at the reference configuration and **E** is the elastic strain vector of the solid phase.

The law of conservation of mass requires that the velocities of the solid, liquid, and ionic phases must satisfy the continuity equation:

$$\frac{\partial \rho^\alpha}{\partial t} + \nabla \cdot \left(\rho^\alpha v^\alpha \right) = 0 \tag{A-1.12}$$

where t is time, ρ^α is the apparent mass density of phase α, and u^α is the velocity vector of phase α. The apparent mass density ρ^α of the solid and liquid phases (α = s,w) are equal to $\rho_T^\alpha \phi^\alpha$, where ρ_T^α is the true mass density of phase α. The apparent mass density of the ionic species is given by $\rho^k = \rho_T^k \phi^k = c^k M_k \phi^w$, where c^k and M_k are the concentration and molar weight of the kth ionic species, respectively. Eqn. A-1.12 can then be rewritten as follows:

$$\frac{\partial \phi^\alpha}{\partial t} + \nabla \cdot \left(\phi^\alpha v^\alpha \right) = 0 \tag{A-1.13}$$

Through the summation of Eqn. A-1.13, and by substituting in the saturation condition we obtain:

$$\nabla \cdot \left[\phi^w \left(v^s - v^w \right) \right] = \nabla \cdot v^s \tag{A-1.14}$$

The fixed charges on the polymer backbone must also satisfy the law of conservation of mass, given by:

$$\frac{\partial c^f}{\partial t} + \nabla \cdot \left(c^f v^s \right) = 0 \tag{A-1.15}$$

where c^f is given by:

$$c^f = \frac{c_0^f}{\left(1 + \dfrac{tr(\mathbf{E})}{\phi_0^w} \right)} \tag{A-1.16}$$

where c_0^f and ϕ_0^w are the concentration of fixed charges and the water volume fraction at the reference configuration, respectively.

Now the momentum equations for the mixture, water, and ionic phases are given by Eqns. A-1.17, A-1.18, and A-1.19, respectively, as follows:

$$\nabla \cdot \boldsymbol{\sigma} = 0 \tag{A-1.17}$$

282

$$-\rho^w \nabla \mu^w + f_{ws}\left(v^s - v^w\right) + \sum_{k=1}^{n_f} f_{wk}\left(v^k - v^w\right) = 0 \tag{A-1.18}$$

$$-\rho^k \nabla \mu^k + f_{ks}\left(v^s - v^k\right) + f_{kw}\left(v^w - v^k\right) + \sum_{j=1(j\neq k)}^{n_f} f_{kj}\left(v^j - v^k\right) = 0 \tag{A-1.19}$$

where $\boldsymbol{\sigma}$ is the mixture stress vector, μ^α is the chemical potential of phase α (w or k), $f_{\alpha\beta}$ is the frictional coefficient between α and β phases. The frictional coefficient $f_{\alpha\beta}$ is equal to $f_{\beta\alpha}$. In addition, the frictional coefficients f_{sk} and f_{kj} can be neglected in comparison with the frictional coefficients f_{ws} and f_{wk} [130]. Through the summation of Eqns. A-1.18 and A-1.19, we obtain

$$f_{ws}\left(v^s - v^w\right) = \sum_{\alpha=w,k} \rho^\alpha \nabla \mu^\alpha \tag{A-1.20}$$

The constitutive equations for the mixture, water, and ionic phases are given by Eqns. A-1.21, A-1.22, and A-1.23, respectively, as follows:

$$\boldsymbol{\sigma} = -p\mathbf{I} + \lambda_s tr(\mathbf{E})\mathbf{I} + 2\mu_s \mathbf{E} \tag{A-1.21}$$

$$\mu^w = \mu_0^w + \frac{1}{\rho^w}\left[p - RT\sum_{k=1}^{n_f} \Phi^k c^k + B_w tr(\mathbf{E})\right] \tag{A-1.22}$$

$$\mu^k = \mu_0^k + \frac{RT}{M^k}\ln\left(\gamma_k c^k\right) + \frac{z^k F\psi}{M^k} \tag{A-1.23}$$

where p is the osmotic pressure, μ_0^α is the chemical potential of phase α at the reference configuration, R is the universal gas constant, T is the absolute temperature, B_w is the coupling coefficient, F is Faraday's constant, ψ is the electric potential, Φ^k is the osmotic coefficient of the kth ion, γ_k is the activity coefficient of ion k, and z^k is the valence of the kth ion. λ_s and μ_s are the Lame coefficients of the solid matrix.

Now by substituting Eqns. A-1.22 and A-1.23 into Eqn. A-1.20, we obtain:

$$f_{ws}\left(v^s - v^s\right) = \phi^w\left[\nabla p + RT\nabla\sum_k\left(1-\Phi^k\right)c^k + F\nabla\psi\sum_k z^k c^k + B_w\nabla tr(\mathbf{E})\right] \quad \text{(A-1.24)}$$

and by implementing Eqn. A-1.14, we can obtain the displacement of the solid phase, u^s, as follows:

$$\nabla\frac{\partial u^s}{\partial t} = \nabla\left[\frac{\left(\phi^w\right)^2}{f_{ws}}\left(\nabla p + RT\nabla\sum_{k=1}^{n_f}\left(1-\Phi^k\right)c^k + F\sum_{k=1}^{n_f} z^k c^k\nabla\psi + B_w\nabla tr(\mathbf{E})\right)\right] \quad \text{(A-1.25)}$$

The diffusion equation for ionic species k is given by:

$$\frac{\partial c^k}{\partial t} = -\nabla J^k + r_k \quad \text{(A-1.26)}$$

where J^k is the flux of ionic species k, r_k is the source term from the chemical reaction of molecules. Typically the flux of an ionic species k can be expressed by:

$$J^k = -D_k\nabla c^k - \frac{F}{RT}z^k D_k c^k\nabla\psi + c^k\nabla v \quad \text{(A-1.27)}$$

Substituting Eqn. A-1.27 into A-1.26, and neglecting the chemical reaction term, we obtain the convection-diffusion to determine the ionic concentration c^k:

$$\nabla\left(D_k\nabla c^k\right) + \frac{Fz^k}{RT}\nabla\left(D_k c^k\nabla\psi\right) = \frac{\partial c_k}{\partial t} + \nabla\left(c^k\nabla v\right)$$
$$\left(k = 1,2,\cdots,n_f\right) \quad \text{(A-1.28)}$$

The convection-diffusion equation relies on the determination of the electric potential throughout the domains, which is given by the Poisson equation:

$$\nabla^2\psi = -\frac{F}{\varepsilon_r\varepsilon_0}\sum_{k=1}^{n_f}\left(z^k c^k + z^f c^f\right) \quad \text{(A-1.29)}$$

where ε_r and ε_0 represent the relative permittivity and permittivity of free space, respectively.

Overall, the triphasic mixture model composed by Li *et al.* consists of the momentum equation, Eqn. A-1.17, complemented by the constitutive equation, Eqn. A-1.21 to determine the solid matrix displacement, the continuity equation to calculate the osmotic pressure, Eqn. A-1.25, the convection diffusion equation for determination of the ionic concentrations Eqn. A-1.28, and the Poisson equation, Eqn. A-1.29, used to calculate the electric potential distribution.

The constitutive equation set derived by Li *et al.* have been; implemented to study 1-D swelling of a hydrogel strip subjected to an external electric field [136], reformulated to account for large deformations within a finite element model studying articular cartilage curling [137], extended to study 2-D steady-state swelling of a hydrogel subjected to an external electric field [138], and non-dimensionalized and expanded to simulate the 1-D transient swelling of a hydrogel strip within an electric field [139, 140].

Multiphasic mixture models give good qualitative and quantitative agreement with experimental results, as highlighted in Table A-1.2, with some characteristic numerical verification experiments performed by Sun *et al.* [126] and Gu *et al.* [131]. In addition, mixture theory has successfully modeled macroscale hydrogels undergoing transient chemo-electro-mechanical response to stimulus. However, since infinitesimal deformation was assumed to formulate the model, the model is inherently limited in simulating the very large deformations that some hydrogels experience.

Table A-1.2: Advantages and disadvantages of the thermodynamics and multiphasic models for simulating hydrogel volume transition.

	Qualitative Agreement	Quantitative Agreement	Min. Scale Modeled	Transient Analysis	Equilibrium Analysis	Large Deformations
Thermo-dynamics	Yes	No	Macroscale	No	Yes	??
Multiphasic Mixtures	Yes	Yes	Macroscale	Yes	Yes	One Model

A-1.2.3 Transport Models

Transport equations for numerically modeling chemically and electrically stimulated polyelectrolytes were first implemented by Grimshaw *et al.* [141] to study the swelling of polymethacrylic acid (PMMA) membranes. Chu *et al.* used simple transport equations to model the behavior of pH stimulated hydrogels [7]. Wallmersperger *et al.* also used simple transport equations to model the transient behavior of electrical and ionic properties within a hydrogel [142], extending the model later to include the structural forces applied to the hydrogel membrane [9]. A coupled chemo-electro-mechanical (deemed MECpH) was composed by Li *et al.* [143-145] to simulate hydrogels swelling. The MECpH model was later implemented using the Meshless Hermite-Cloud Method [146] by; Li *et al.* [147] to determine the influence of buffer concentration of the equilibrium swelling, Wang *et al.* [148] to model a cylindrical hydrogel within a microchannel, and Ng *et al.* [149] to investigate how the initial-fixed charge density effects equilibrium swelling of a hydrogel. The MECpH model was later reformulated by Lam *et al.* [150] to account for large deformations and electrical stimulus.

A comprehensive transport model for pH stimulated hydrogels was composed by De *et al.* [1, 19], and furthered for electrically stimulated hydrogels by Bassetti *et al.* [15], the composite of which is presented here. The models composed by De *et al.* and Bassetti *et al.* were based on the previous work of Nussbaum [151], Grimshaw [152], Grimshaw *et al.* [141], Chu *et al.* [7], Wang *et al.* [153], and Wallmersperger *et al.* [142].

Poisson's equation governs the applied electric field, and ensures that contributions from mobile and fixed ions are accounted for

$$\nabla \cdot \left(\varepsilon_0 \varepsilon_e \nabla \bar{\psi} \right) = -F \left(\sum_{k=1}^{N} \overline{c}_k z_k + \overline{c}_f z_f \right)$$
(A-1.30)

where ε_0 and ε_e are the dielectric constant of vacuum and the effective dielectric constant of the hydrogel, respectively. $\bar{\psi}$ is the intermembrane electric potential, F is the Faraday constant, $\overline{c}_k$ is the intermembrane (hydrogel interior) concentration of the kth ionic species, z_k is the valence of the kth ionic species, $\overline{c}_f$ is the intermembrane concentration of the fixed ions, and z_f is the valence of the fixed ions. The $^-$ denotes a quantity within the hydrogel membrane. The effective dielectric constant of the hydrogel can be determined using the following equation [154]:

$$\varepsilon_e = \frac{\varepsilon_p + \varepsilon_w - \phi \left(\varepsilon_p - \varepsilon_w \right)}{\varepsilon_p + \varepsilon_w + \phi \left(\varepsilon_p - \varepsilon_w \right)} \varepsilon_p$$
(A-1.31)

where ε_p is the dielectric constant of the polymer, ε_w is the dielectric constant of water, and ϕ is porosity of the hydrogel. The concentration of the fixed ions is given by [155]:

$$\overline{c}_f = \frac{1}{H} \frac{c_{mo}^s K_A}{(K_A + \overline{c}_H)}$$
(A-1.32)

where H is the hydration of the hydrogel, c_{mo}^s is the initial concentration of the fixed ionic groups in the dry gel, and K_A is the dissociation constant of the fixed acidic groups.

The distribution of all the ionic species within the hydrogel and surrounding fluid can be determined with the following chemical field equations. The continuity equation governs the flux of ionic species throughout the hydrogel membrane and surrounding solution, and is given for the hydrogel by:

$$\frac{\partial\left(H\overline{c}_k\right)}{\partial t} = -\left(1+H\right)\nabla\cdot\Gamma_k \tag{A-1.33}$$

where the flux, Γ_k, of the kth ionic species is given by:

$$\Gamma_k = \phi\left[-\overline{D}_k\nabla\cdot\overline{c}_k - z_k\overline{\mu}_k\overline{c}_k\nabla\cdot\overline{\psi}\right] + \overline{c}_k\overline{U} \tag{A-1.34}$$

where $\overline{D}_k$ is the intermembrane diffusivity of the kth ionic species, $\overline{\mu}_k$ is the intermembrane ionic mobility of the kth ionic species, and $\overline{U}$ is the area-averaged fluid velocity through the hydrogel relative to the hydrogel's polymer network. The porosity of the hydrogel is given by [155]:

$$\phi = \frac{H}{1+H} \tag{A-1.35}$$

The intermembrane diffusivity can be determined from the diffusivity in aqueous solution using Eqn. A-1.36, as follows [155, 156]:

$$\frac{\overline{D}_k}{D_k} = \left(\frac{H}{2+H}\right)^2 \tag{A-1.36}$$

From the ionic mobility in aqueous solution the diffusivity can be calculated using the Einstein relationship [157], developed from Einstein's work on Brownian motion :

$$D_k = \frac{\mu_k RT}{F} \tag{A-1.37}$$

where μ_k is the ionic mobility of the kth ionic species in aqueous solution, R is the universal gas constant, and T is temperature. By combining Eqns. A-1.33 and A-1.34, the intermembrane flux of the kth ionic species can be evaluated by:

$$\frac{\partial\left(H\overline{c}_k\right)}{\partial t} = -\left(1+H\right)\nabla\cdot\left(\phi\left[-\overline{D}_k\nabla\cdot\overline{c}_k - z_k\overline{\mu}_k\overline{c}_k\nabla\cdot\overline{\psi}\right] + \overline{c}_k U\right) \tag{A-1.38}$$

The consideration of hydrogen ions requires some special modifications to Eqn. A-1.38, as hydrogen ions are also found bound to

the migrating buffer ions and bound to the acidic groups on the polymer chain backbone. The continuity equation for hydrogen ions is given below:

$$\frac{\partial \left(H\overline{c}_H + H\overline{c}_H^b + H\overline{c}_{HB} \right)}{\partial t} = -\left(1 + H \right) \nabla \cdot \left(\Gamma_H + \Gamma_{HB} \right) \qquad \text{(A-1.39)}$$

where $\overline{c}_H$ is the intermembrane concentration of hydrogen ions, $\overline{c}_H^b$ is the intermembrane concentration of hydrogen ions bound to the fixed acidic group found on the polymer chain backbone, $\overline{c}_{HB}$ is the intermembrane concentration of hydrogen ions bound to the migrating buffer ions, and Γ_{HB} is the flux of the intermembrane hydrogen ions bound to the buffer ions. The concentration of hydrogen ions bound to the fixed acidic groups can be evaluated using:

$$\overline{c}_H^b = \frac{\overline{c}_T \overline{c}_H}{K_B + \overline{c}_H} \qquad \text{(A-1.40)}$$

where $\overline{c}_T$ is the total concentration of buffer ions found within the hydrogel, given by the total concentration of mobile buffer ions plus the buffer ions bound to the hydrogen ions ($\overline{c}_T = \overline{c}_B + \overline{c}_{HB}$), while K_B is the dissociation constant of buffer. The intermembrane concentration of hydrogen ions bound to the fixed acidic groups can be determined by:

$$\overline{c}_{HB} = \frac{\overline{c}_{mo}^s}{H} \left(\frac{\overline{c}_H}{K_A + \overline{c}_H} \right) \qquad \text{(A-1.41)}$$

The intermembrane flux of the hydrogen ions bound to the buffer ions is proportional to the flux of the hydrogen ions, as governed by the following:

$$\Gamma_{HB} = \frac{\overline{D}_{HB}}{\overline{D}_H} \frac{\overline{c}_T}{K_B + \overline{c}_H} \Gamma_H \qquad \text{(A-1.42)}$$

where $\overline{D}_{HB}$ is the intermembrane diffusivity of the hydrogen ions bound to the migrating buffer ions, and Γ_{HB} is the flux of hydrogen ions bound to the migrating buffer ions. Combining Eqns. A-1.39 and A-1.34 with Eqns. A-

1.42, A-1.40, and A-1.41 yields the continuity equation for intermembrane hydrogen ions:

$$\frac{\partial\left[H\overline{c}_H + \frac{H\overline{c}_T\overline{c}_H}{K_B + \overline{c}_H} + \frac{\overline{c}_{mo}^s\overline{c}_H}{K_A + \overline{c}_H} \right]}{\partial t} =$$

$$-(1+H)\nabla\cdot\left[\left(1+\frac{\overline{D}_{HB}}{\overline{D}_H}\frac{\overline{c}_T}{K_B+\overline{c}_H}\right)\left(\phi\left(-\overline{D}_k\nabla\overline{c}_k - z_k\overline{\mu}_k\overline{c}_k\nabla\cdot\overline{\psi}\right)+\overline{c}_kU\right)\right] \quad \text{(A-1.43)}$$

The structural equations dictating the displacement of the hydrogel polymer network are obtained by starting with the equations of motion:

$$\rho\frac{\partial^2 u}{\partial t^2} + f\frac{\partial u}{\partial t} = \nabla\cdot\sigma + \rho b \quad \text{(A-1.44)}$$

where ρ is the density of the hydrogel, u is the calculated displacement of the polymer network, f is the viscous damping parameter between the polymer network and the solution, σ is the stress tensor, and b is the body forces acting on the hydrogel. Generally the body forces acting upon and the frictional forces within the hydrogel are neglected. In addition, the displacement of the hydrogel occurs much quicker than the flux of the mobile ions; therefore, the inertial terms are not dominant and motion can be considered quasi-static, and the structural field can be given by:

$$\nabla\cdot\sigma = 0 \quad \text{(A-1.45)}$$

Isolating the x-component of Eqn. A-1.45 yields:

$$\frac{\partial\sigma_{xx}}{\partial x} + \frac{\partial\tau_{xy}}{\partial y} = 0 \quad \text{(A-1.46)}$$

where σ_{xx} is the normal stress on the x-plane in the x-direction and τ_{xy} is the shear stress on the x-plane in the y-direction. For a plane strain condition, the x-component of the normal stress can be given by:

$$\sigma_{xx} = \frac{E}{(1+v)(1-2v)}\left[(1-v)\frac{\partial u_x}{\partial x} + v\frac{\partial u_y}{\partial y}\right] - \left(P_{osmotic} + \sigma_{electrostatic}\right) \quad \text{(A-1.47)}$$

where E is Young's Modulus of the hydrogel, υ is Poisson's Ratio of the hydrogel, u_x is the x-component of the polymer network displacement, u_y is the y-component of the polymer network displacement, $P_{osmotic}$ is the osmotic pressure, $\sigma_{electrostatic}$ is the electrostatic stress. The shear stress of the x-component is given by:

$$\tau_{xy} = G\left[\frac{\partial u_x}{\partial y} + \frac{\partial u_y}{\partial x}\right] \tag{A-1.48}$$

where G is the shear modulus of the hydrogel. Combining Eqns. A-1.46, A-1.47, and A-1.48 gives the x-component of the mechanical field equations as follows:

$$0 = \frac{E(1-\nu)}{(1+\nu)(1-2\nu)}\frac{\partial^2 u_x}{\partial x^2} + \frac{E\nu}{(1+\nu)(1-2\nu)}\frac{\partial^2 u_y}{\partial x\partial y} + G\left[\frac{\partial^2 u_y}{\partial x^2} + \frac{\partial^2 u_x}{\partial x\partial y}\right] - \frac{\partial\left[P_{osmotic} + \sigma_{electrostatic}\right]}{\partial x} \tag{A-1.49}$$

The osmotic pressure can be calculated using the calculated concentrations from the chemical field equations:

$$P_{osmotic} = RT\sum_{k=1}^{n}\left(\overline{c}_k - c_k^0\right) \tag{A-1.50}$$

where *n* is the number of mobile ionic species contributing to the osmotic pressure, $\overline{c}_k$ is the intermembrane concentration of the *k*th mobile ionic species, c_k^0 is the extramembrane concentration of the *k*th mobile ionic species. The electrostatic stress can be determined using the following [154]:

$$\sigma_{electrostatic} = k_0\nabla\cdot\left(\varepsilon_e\nabla\psi\right)\begin{pmatrix} 1 & 0 \\ 0 & 1 \end{pmatrix} \tag{A-1.51}$$

where k_0 is a material property dependent on the distribution of fixed charges within the polymer network and the network's geometry. The Young's Modulus of the hydrogel polymer network also varies with changing hydration and shear modulus as follows [158]:

$$E = \frac{E_o(1+H_o)^{\frac{1}{3}}}{(1+H)^{\frac{1}{3}}} + \Delta E \tag{A-1.52}$$

where E_o and H_o are the initial Young's Modulus and hydration, respectively, of the hydrogel. ΔE is the change in Young's Modulus associated with a change in the shear modulus, and is calculated from the following:

$$\Delta E = \frac{\Delta G}{2(1+\upsilon)} \tag{A-1.53}$$

where ΔG is the change in the Shear Modulus of the hydrogel due to a changing hydration or a varying electric field, and is given by the following:

$$\Delta G = \frac{9}{4}\left(\frac{1}{1+H}\right)\varepsilon_e\varepsilon_0\kappa^2\left(\nabla\bar{\psi}\right)^2 \tag{A-1.54}$$

where κ is the Clausius-Mossotti function [159], which is a function of the relative dielectric constant of the polymer matrix and solvent. The hydration of the hydrogel can be determined by the following equation:

$$H = \frac{V_f}{V_s} = \frac{V_t - V_s}{V_s} = \varepsilon_x + \varepsilon_y + \varepsilon_x\varepsilon_y \tag{A-1.55}$$

where V_f, V_s, V_t are the volume of fluid, solid, and total volume, respectively, within the hydrogel polymer network. ε_x and ε_y are the x- and y-components of strain within the hydrogel polymer network. The density of the hydrogel can be determined from the following [160, 161]:

$$\rho = \left(\frac{1}{1+H}\right)^2\rho_{so} + \frac{H}{1+H}\rho_w \tag{A-1.56}$$

where ρ_{so} and ρ_w are the density of the undeformed solid gel and the density of water, respectively.

Overall, the transport equations composed of the work by De *et al.* and Bassetti *et al.* consist of; Poisson's equation, Eqn. A-1.30, to determine the electric field distribution of the hydrogel and surrounding solute, the Nernst-Planck equation, Eqns. A-1.38 and A-1.43, to calculate

the ionic concentrations within the hydrogel and surrounding solute, and the equations of motion, Eqn. A-1.49, to evaluate the hydrogel's displacements. These three governing equations are directly coupled and are complemented by the appropriate supplementary equations.

Transport models have been found to accurately model the qualitative and quantitative behavior of hydrogels subjected to both chemical and electrical stimulation, as displayed in Table A-1.3. A few characteristic experiments carried out on hydrogels were performed by Grimshaw *et al.* [141], De *et al.* [1, 19], and Bassetti *et al.* [15]. In addition, transport models have been validated [15], to accurately simulate the behavior of microscale hydrogels subjected to an external electrical field. This highlights the diversity of using transport theory, and allows researchers simulating hydrogels on the microscale to accurately design and optimize their devices. Furthermore, both the transient and equilibrium responses of hydrogels can be simulated for hydrogels undergoing very large deformations. Transport theory incorporates many material non-linearities that help account for large deformation of the hydrogel's polymer network.

Table A-1.3: Advantages and disadvantages of the thermodynamics, multiphasic, and transport models for simulating hydrogel volume transition.

	Qualitative Agreement	Quantitative Agreement	Min. Scale Modeled	Transient Analysis	Equilibrium Analysis	Large Deformations
Thermo-dynamics	Yes	No	Macroscale	No	Yes	??
Multiphasic Mixtures	Yes	Yes	Macroscale	Yes	Yes	One Model
Transport	Yes	Yes	Microscale	Yes	Yes	Yes

A-1.2.4 Molecular Simulations

Molecular simulations are an excellent complement to micro and macroscale simulations and experiments, giving atomistic insight into hydrogel swelling and deswelling. Many variations of molecular models exist for simulating the interactions within a hydrogel. Models pertaining to

the swelling and deswelling of hydrogels were examined and are outlined below.

A Gibbs-ensemble molecular dynamics (MD) simulation was executed to study the swelling of a model network in contact with three coarse-grained solvents (s1, s6, s12) within the high pressure regime at supercritical temperatures [162]. It was found that the swelling ratio of the model network is decreased when the chain length of the solvent increases.

A discontinuous MD model was combined with the MC simulation technique to study the swelling of athermal, continuous-space, near-perfect, trifunctional polymer network immersed in an athermal hard-sphere solvent [163]. This novel theory performed extremely well at predicting the gel packing fraction at swelling equilibrium, and fairly well at predicting the solvent fraction. This model implemented a simple theoretical approach which captured the main features of gel swelling.

Nick and Suter combined Widom's particle-insertion method with the thermodynamic-integration approach within MD simulations to determine the excess chemical potential of water in dense, amorphous polymer BPA-PC and PVA microstructures [164]. This method was found to be applicable for calculation of the excess chemical potential in water for a variety of polymers, allowing for an estimate of the polymer's water sorption behavior.

Lu and Hentschke performed a MD-Widom test particle simulation investigating swelling of a polymer network contacting a Lennard-Jones one-site solvent under subcritical and supercritical conditions, which simultaneously calculated the particle motion and solvent particle concentration [165]. Increasing temperature or pressure under subcritical conditions causes the polymer network to shrink; under intermediate supercritical conditions the swelling ratio obtains a maximum, which shifts to higher supercritical temperature and pressures with the increase of

temperature or pressure; under the highest supercritical conditions the network swells monotonically with increasing temperature and pressure.

Gilra *et al.* used Monte Carlo simulation incorporating the 3-D bond fluctuation model to examine the deformation of end-linked polymer networks where uniaxial expansion and contraction was induced by varying the wall-polymer potential [166]. At high volume fractions the network and athermal linear chain P-V behaviors were similar; in addition at large deformations the elastic chain dimensions were non-Gaussian and Gaussian in the direction of and perpendicular to, respectively, the direction of deformation.

A MD-particle-transfer method was employed to study the swelling of a model polymer network by a short chain solvent, which utilized Rosenbluth's sampling method to determine the solvent chemical potentials [167]. The Flory-Huggins mean field model was implemented to extend the available model data, whose data can be implemented beyond or between simulation results; however, for the larger solvents studied model improvement could be required.

Lu *et al.* concluded a series of papers by examining the swelling of polymer networks with varying cross-link densities in contact with a one-site or six-site solvent through the implementation of MD utilizing the Widom test particle and Rosenbluth sampling for calculating solvent chemical potential [168]. For all cross-link densities the one-site solvent was in excellent qualitative agreement with theory, while the chain-like solvent only had partial qualitative agreement.

Monte Carlo simulations were performed on a cross-linked polyelectrolyte gel composed of a charged defect-free network represented by explicit counterions and linked charged beads[169]. For the polyelectrolyte gel, non-ionic polymer gel, and several partially or fully degraded gels the pressure-density relationships were determined, and the polyelectrolyte gel showed a large swelling capacity.

Cross-linked polyelectrolyte gels were investigated by means of MC simulations which incorporated charged defect-free 3-D polymer networks with diamond-like topology and explicit counterions [170]. An increase in the volume was observed by; increasing chain stiffness, decreasing cross-linking density, and increasing charge density; while an equilibrium volume decrease was observed when monovalent counterions were exchanged for divalent ions. The affine assumption was found to have only limited validity, while the Gaussian chain approximation was never fulfilled for polyelectrolyte gels.

Brownian-dynamics simulation methods were combined with different scaling arguments to determine the effect of an electric field on charged polyelectrolyte chains, which include the effects of counterion condensation and PE collapse [171]. Condensed counterions were dragged along the polyelectrolyte chains at low electric field strength, while at high field strength the condensed counterions started to glide along the chain contributing to the overall conduction.

A 'two-box-particle-transfer' 3-D MD simulation was performed to determine the swelling of a polyelectrolyte gel accounting for counterions and a Stockmayer solvent [172]. The simulation showed that the maximum swelling ratio was a function of charge of the network bead, due to the two opposing forces of electrostatic repulsion and network conformational entropy. This observed effect could be reduced if the dipole moment of the Stockmayer fluid was increased.

A course-grained model of a polyelectrolyte network with annealed permanent tetrafunctional cross-linked sites was examined to determine the structure and properties using MC simulations [173]. A strong dependence on the strength of electrostatic interactions was exhibited in the pressure-density relationships, while a discontinuous volume change was observed when the electrostatic interactions are strong.

The distributions of counterions around a flexible polyelectrolyte chains was examined using Langevin dynamics to determine the effect of

296

vary salt concentration, polymer concentration, and counterion valence [174]. The radius of gyration and net polymer charge decreased with increasing salt concentration or polymer concentration. The distributions of counterions surrounding the polymer chain are presented for both monovalent and divalent counterions.

A MD model with bead-spring chains and explicit counterions was used to simulate polyelectrolytes in near-Θ-solvent, for both fully and partially charged chains with varying monomer concentration covering the dilute and semidilute regimes [175]. Scaling theory agreed excellently with simulation results where the chain experienced the strongest stretching, in the middle of the chain. Whereas, scaling theory didn't agree with simulation results near the chain ends where fluctuations are important and the strong stretching approximation breaks down.

Molecular dynamics of multi-chain polyelectrolyte systems in salt-free solutions with explicit counterion consideration was employed to determine the osmotic coefficient and counterion distribution functions [176]. The osmotic coefficient decreased non-monotonically with increasing polymer concentration in agreement with the two-zone model, for both flexible and rodlike polyelectrolytes.

Monte Carlo simulations were performed to determine the swelling behavior of polyelectrolyte gels at varying permittivities, and with or without short-range attraction [177]. Volume transitions occur at critical values of permittivity and short-range attraction, with the collapse being due to a change in the enthalpy-entropy balance and the attraction between beads of a network, respectively.

A coarse-grained MD model using scaling arguments was employed to investigate the equilibrium swelling behavior of a polyelectrolyte composed of a bead-spring defect-free diamond shaped network [178]. Network strands formed a straight linear sequence of blobs, from which a universal scaling relation was derived to determine the end-to-end distance of network chains.

297

The swelling transition of charged hydrogels was examined when varying the solution salt concentration, hydrogel cross-link density, and with the addition of pendant PEG side chains [179]. The degree of swelling was found to be quite sensitive to the suspension pH, vary non-monotonically with solution salt concentration, and increase with the addition of PEG chains. The transition pH was found the be effected by decreasing the subchain length and/or salt concentration.

A MD-MC hybrid technique was implemented where the explicit solvent was subjected to the particle transfer step of Gibbs ensemble-Monte Carlo, to analyze the swelling behavior of a tightly meshed polymer network with varying fluid composition, temperature, and pressure [180]. Bulk results for the separation factor and swelling ration were insensitive to bulk solvent composition at the highest, but not lowest, temperature considered. Higher concentrations of the smaller solvent species were found inside the network, but with increasing temperature this effect was diminished.

Large-scale MD simulations were performed on a polyelectrolyte defect-free network close to the transition point in good solvent and without an added salt [181]. The final hydrogel shape was determined by the maximum elongation of the network strands and the renormalized amount of charges on these strands.

A cooperative motion algorithm was employed to determine the configuration of a polyelectrolyte chain with counterions and added salt on a face-centered cubic lattice [182]. A sharp decrease in the mean radius of gyration and the mean end-to-end distance was observed at a relatively low concentration of monovalent salt, which was accompanied by a drop in the effective mean charge per monomer and the system's inner energy.

A charged polyelectrolyte brush with added salt and under a moderate electrostatic coupling strength was examined using MD simulations [183]. As the salt concentration decreased so too did the brush thickness, obeying a weak power law.

Discontinuous volume phase transitions of a highly-charged polyelectrolyte with defect-free tetrafunctional crosslinks was examined using molecular dynamic simulations [184]. The observed osmotic pressure depended significantly on the strength of the electrostatic interactions, with strong interactions causing a volume transition to occur.

The effect of salt valence and a reduced temperature on a single polyelectrolyte chain was examined using a co-operative motion algorithm [185]. For a fixed salt cation concentration and temperature, the chain becomes more compact as salt valence increases, with condensation being dominated by multivalent ions with a charge opposite of the monomer.

Monte Carlo simulations were performed to model a salt-free polyelectrolyte system to determine the osmotic pressure [186]. In dilute and concentrated solutions the osmotic coefficient decreased and increased, respectively, with increasing concentration. The model's results are in qualitative agreement, but underestimate the osmotic pressure in dilute solutions.

Several peripherally substituted [6.3.1] helicenses were investigated to determine their viability as linear actuators utilizing MD calculations [187]. The potential for a reversible chemically driven molecular actuator was confirmed based on MD results.

A molecular dynamics model incorporating both the viscous and stochastic forces was utilized to obtain osmotic coefficients of neutral or non-neutral polyampholyte chains with varying segment size and charge sequences [188]. In addition, this work develops a molecular thermodynamics model by extending the chemical association theory of polyelectrolytes solutions to that of polyampholyte solutions. The thermodynamic model's predicted osmotic coefficients were in agreement with computed coefficients for neutral polyampholytes in weak or strong columbic coupled systems. For higher monomer valence and non-neutral polyampholyte models MD and model osmotic coefficients had a slight

deviation, with further improvements for the thermodynamic model proposed.

Molecular dynamics simulations were performed to examine the structure and peculiar swelling behavior of a novel hydrogel prepared with scleroglucan and borax, a hydrogel suitable for drug delivery [189]. The most probable assembly of the polymer network was proposed, both in the presence and absence of the three model drugs tested; theophylline, Vitamin B12, and Myoglobin. The peculiar swelling behavior was explained by the ability to preserve ordered configurations in aqueous media.

A coarse-grained MD simulation was performed to investigate the interactions of an anionic polyelectrolyte with monomeric and dimeric cationic surfactants [190]. The polyelectrolyte-surfactant mixture evolved with time into a micellar complex of increasing size, with the equilibrium complex size becoming larger with higher surfactant concentration. The observed electrostatic and hydrophobic interaction played where dominant in the formation of a micellar complex.

A Brownian dynamics simulation, incorporating a course-grained bead-spring chain model with explicit counterions, was used to analyze the nonlinear shear rheology in relation to shear rate, Bjerrum length, and concentration of polyelectrolytes in dilute solutions [191]. It was observed that the ion cloud around the polyelectrolyte chain deforms under flow, causing a significant increase in viscosity as concentration increases.

The behavior of dilute polyelectrolyte solutions under elongational flow was examined using a bead-and-spring model and the Brownian dynamics simulation technique incorporating hydrodynamic interactions [192]. The relaxation time was found to be dependent on the ionic solution's strength. The Deborah number at which the coil-stretch transition occurred was determined; in addition, the power law relationship relating the critical elongation rate with the polyelectrolyte molecular weight was examined.

300

The mechanical and transport properties of a double network PEO-PAA hydrogel with 76 %wt water content was examined using atomistic MD simulations [193]. The salvation of the polymer network was enhanced for the DN in comparison with either component as a single network (SN), while the diffusion of solutes was decreased due to the smaller effective mesh size. Above ~100% strain the stress of the DN was much higher than the sum of each component within a SN.

Molecular dynamic simulations very accurately depict the molecular interactions between the polymer chains, fixed bonds on these chains, and water or solvent molecules. Some of these simulations results can be scaled up, but these results can also give researchers insight into their micro or macroscale simulations regarding the accuracy of using certain governing and supplementary equations. However, mostly the scale of the structures analyzed are small compared to those being fabricated, making the results hard to utilize for prototype design and optimization. In addition, large simulations are very computationally expensive, and most require access to cluster computing resources.

Various types of molecular models have been employed to accurately describe the qualitative and quantitative swelling and deswelling of polyelectrolyte hydrogels, with some characteristic advantages and disadvantages shown in Table A-1.4. These molecular numerical models offer complementing insights to experiments performed on polyelectrolyte hydrogels. Some molecular models are able to determine the transient hydrogel behavior, while others are only interested in the equilibrium behavior. Generally, molecular models provide accurate insight at the atomistic scale; however, some numerical models employ scaling arguments to extend their solutions to the micro and macroscale, and in some cases the large deformation of a polyelectrolyte chain can be observed. A major disadvantage of molecular models is the large computational facilities required for some of the simplest models, with larger models desiring cluster computer resources.

Table A-1.4: Advantages and disadvantages of the thermodynamics, multiphasic, transport and molecular models for simulating hydrogel volume transition.

	Qualitative Agreement	Quantitative Agreement	Min. Scale Modeled	Transient Analysis	Equilibrium Analysis	Large Deformations
Thermo-dynamics	Yes	No	Macroscale	No	Yes	??
Multiphasic Mixtures	Yes	Yes	Macroscale	Yes	Yes	One Model
Transport	Yes	Yes	Microscale	Yes	Yes	Yes
Molecular	Yes	Yes	Atomistic	Some	Yes	No

A-1.3 Conclusions

Four numerical models for the simulation of the swelling and deswelling phenomena associated with polyelectrolyte hydrogels were reviewed. The thermodynamic model provides good qualitative agreement with experimental results, but still required some adjusting of critical parameters to match data. Multiphasic models provide both qualitative and quantitative agreement with experiments, and can examine both equilibrium and transient volume transition. Multiphasic models do have the limitation of small deformations and neglects the transient behavior of some critical parameters. Transport models are robust in their ability to accurately model the qualitative and quantitative behavior of both equilibrium and transient hydrogel volume transition. The transport model does not have many limitations, and currently describes microscale hydrogels with high accuracy. Molecular dynamic simulations accurately describe microscale and nanoscale hydrogel volume transition; however, are currently limited in their ability to model larger hydrogel structures. Numerical modeling of hydrogel phenomena can currently be performed with multiple various methods, providing a promising avenue for researchers wanting to bypass high prototyping and optimization costs.

References

[1]   S. K. De, N. R. Aluru, B. Johnson, W. C. Crone, D. J. Beebe, and J. Moore, "Equilibrium swelling and kinetics of pH-responsive hydrogels: Models, experiments, and simulations," *Journal of Microelectromechanical Systems,* vol. 11, pp. 544-555, Oct 2002.

[2]   A. N. Chatterjee, Q. Yu, J. S. Moore, and N. R. Aluru, "Mathematical modeling and simulation of dissolvable hydrogels," *Journal of Aerospace Engineering,* vol. 16, pp. 55-64, Apr 2003.

[3]   K. Al-Aribe, G. K. Knopf, and A. S. Bassi, "Photo-responsive hydrogel for controlling flow on a microfluidic chip," in *Photonics North 2006*, 2006, p. 63432R.

[4]   Y. L. Zhang, C. Y. Won, and C. C. Chu, "Synthesis and characterization of biodegradable network hydrogels having both hydrophobic and hydrophilic components with controlled swelling behavior," *Journal of Polymer Science Part a-Polymer Chemistry,* vol. 37, pp. 4554-4569, Dec 15 1999.

[5]   W. Xue, I. W. Hamley, and M. B. Huglin, "Rapid swelling and deswelling of thermoreversible hydrophobically modified poly(N-isopropylacrylamide) hydrogels prepared by freezing polymerisation," *Polymer,* vol. 43, pp. 5181-5186, Sep 2002.

[6]   Y. Qui and K. Park, "Environment-Sensitive Hydrogels for drug delivery," *Advanced Drug Delivery,* vol. 53, pp. pp. 321-339, 2001.

[7]   Y. Chu, P. P. Varanasi, M. J. Mcglade, and S. Varanasi, "Ph-Induced Swelling Kinetics of Polyelectrolyte Hydrogels," *Journal of Applied Polymer Science,* vol. 58, pp. 2161-2176, Dec 19 1995.

[8]   A. S. Hoffman, "Hydrogels for biomedical applications," *Bioartificial Organs Iii: Tissue Sourcing, Immunoisolation, and Clinical Trials,* vol. 944, pp. 62-73, 2001.

[9]   T. Wallmersperger, B. Kroplin, and R. W. Gulch, "Coupled chemo-electro-mechanical formulation for ionic polymer gels - numerical and experimental investigations," *Mechanics of Materials,* vol. 36, pp. 411-420, May 2004.

[10]   J. Zhang and N. A. Peppas, "Synthesis and characterization of pH- and temperature-sensitive poly(methacrylic acid)/poly(N-isopropylacrylamide) interpenetrating polymeric networks," *Macromolecules,* vol. 33, pp. 102-107, Jan 11 2000.

[11]   W. Xue, S. Champ, and M. B. Huglin, "Network and swelling parameters of chemically crosslinked thermoreversible hydrogels," *Polymer,* vol. 42, pp. 3665-3669, APR 2001.

[12]   A. G. Didukh, R. B. Koizhaiganova, G. Khamitzhanova, L. A. Bimendina, and S. E. Kudaibergenov, "Stimuli-sensitive behaviour of novel betaine-type polyampholytes," *Polymer International,* vol. 52, pp. 883-891, Jun 2003.

[13]   M. Zourob, K. G. Ong, K. F. Zeng, F. Mouffouk, and C. A. Grimes, "A wireless magnetoelastic biosensor for the direct detection of organophosphorus pesticides," *Analyst,* vol. 132, pp. 338-343, 2007.

[14]   S. Sun and A. F. T. Mak, "The dynamical response of a hydrogel fiber to electrochemical stimulation," *Journal of Polymer Science Part B-Polymer Physics,* vol. 39, pp. 236-246, Jan 15 2001.

[15] M. J. Bassetti, A. N. Chatterjee, N. R. Aluru, and D. J. Beebe, "Development and modeling of electrically triggered hydrogels for microfluidic applications," *Journal of Microelectromechanical Systems,* vol. 14, pp. 1198-1207, Oct 2005.

[16] S. J. Kim, S. J. Park, and S. I. Kim, "Properties of smart hydrogels composed of polyacrylic acid/poly(vinyl sulfonic acid) responsive to external stimuli," *Smart Materials & Structures,* vol. 13, pp. 317-322, Apr 2004.

[17] M. Lei, A. Salim, R. Siegel, and B. Ziaie, "A Hydrogel-actuated microvalve for smart flow control," in *Conference Proceedings IEEE Eng. Med. Biol. Soc.*, 2004.

[18] R. H. Liu, Q. Yu, and D. J. Beebe, "Fabrication and characterization of hydrogel-based microvalves," *Journal of Microelectromechanical Systems,* vol. 11, pp. 45-53, Feb 2002.

[19] S. K. De and N. R. Aluru, "A chemo-electro-mechanical mathematical model for simulation of pH sensitive hydrogels," *Mechanics of Materials,* vol. 36, pp. 395-410, May 2004.

[20] B. Kim, K. La Flamme, and N. A. Peppas, "Dynamic swelling Behavior of pH-sensitive anionic hydrogels used for protein delivery," *Journal of Applied Polymer Science,* vol. 89, pp. 1606-1613, Aug 8 2003.

[21] T. Shiga and T. Kurauchi, "Deformation of Polyelectrolyte Gels under the Influence of Electric-Field," *Journal of Applied Polymer Science,* vol. 39, pp. 2305-2320, Jun 5 1990.

[22] Y. Osada, J. P. Gong, and Y. Tanaka, "Polymer gels (Reprinted from Functional Monomers and Polymers, pg 497-528, 1997)," *Journal of Macromolecular Science-Polymer Reviews,* vol. C44, pp. 87-112, Feb 2004.

[23] S. J. Kim, H. I. Kim, S. J. Park, I. Y. Kim, S. H. Lee, T. S. Lee*, et al.*, "Behavior in electric fields of smart hydrogels with potential application as bio-inspired actuators," *Smart Materials & Structures,* vol. 14, pp. 511-514, Aug 2005.

[24] H. Li, X. G. Wang, Z. J. Wang, and K. Y. Lam, "Multiphysics modelling of volume phase transition of ionic hydrogels responsive to thermal stimulus," *Macromolecular Bioscience,* vol. 5, pp. 904-914, Sep 16 2005.

[25] R. Masteikova, Z. Chalupova, and Z. Sklubalova, "Stimuli-sensitive hydrogels in controlled and sustained drug delivery," *Medicina (Kaunas),* vol. 39, pp. 19-24, 2003.

[26] V. Ozturk and O. Okay, "Temperature sensitive poly(N-t-butylacrylamide-co-acrylamide) hydrogels: synthesis and swelling behavior," *Polymer,* vol. 43, pp. 5017-5026, Aug 2002.

[27] L. Yin, Z. Yuan, and L. H. He, "Model development and numerical simulation of temperature-sensitive hydrogels," *Computational Materials Science,* vol. 31, pp. 299-308, Nov 2004.

[28] A. Mamada, T. Tanaka, D. Kungwatchakun, and M. Irie, "Photoinduced Phase Transition of gels," *Macromolecules,* vol. 23, pp. 1517-1519, 1990.

[29] A. Suzuki, T. Ishii, and Y. Maruyama, "Optical switching in polymer gels," *Journal of Applied Physics,* vol. 80, pp. 131-136, Jul 1 1996.

[30] A. Suzuki and T. Tanaka, "Phase-Transition in Polymer Gels Induced by Visible-Light," *Nature,* vol. 346, pp. 345-347, Jul 26 1990.

[31] T. F. Otero and J. M. Sansinena, "Soft and wet conducting polymers for artificial muscles," *Advanced Materials,* vol. 10, pp. 491-494, Apr 16 1998.

[32] T. F. Otero, S. Villanueva, M. T. Cortes, S. A. Cheng, A. Vazquez, I. Boyano, *et al.*, "Electrochemistry and conducting polymers: soft, wet, multifunctional and biomimetic materials.," *Synthetic Metals,* vol. 119, pp. 419-420, Mar 15 2001.

[33] D. J. Beebe, J. S. Moore, J. M. Bauer, Q. Yu, R. H. Liu, C. Devadoss, *et al.*, "Functional hydrogel structures for autonomous flow control inside microfluidic channels," *Nature,* vol. 404, pp. 588-590, Apr 6 2000.

[34] Q. Yu, J. M. Bauer, J. S. Moore, and D. J. Beebe, "Responsive biomimetic hydrogel valve for microfluidics," *Applied Physics Letters,* vol. 78, pp. 2589-2591, Apr 23 2001.

[35] A. Richter, D. Kuckling, S. Howitz, T. Gehring, and K. F. Arndt, "Electronically controllable microvalves based on smart hydrogels: Magnitudes and potential applications," *Journal of Microelectromechanical Systems,* vol. 12, pp. 748-753, Oct 2003.

[36] A. Richter, S. Howitz, D. Kuckling, and K. F. Arndt, "Influence of volume phase transition phenomena on the behavior of hydrogel-based valves," *Sensors and Actuators B-Chemical,* vol. 99, pp. 451-458, May 1 2004.

[37] S. H. Lee, D. T. Eddington, Y. M. Kim, W. S. Kim, and D. J. Beebe, "Control mechanism of an organic self-regulating microfluidic system," *Journal of Microelectromechanical Systems,* vol. 12, pp. 848-854, Dec 2003.

[38] S. R. Sershen, G. A. Mensing, M. Ng, N. J. Halas, D. J. Beebe, and J. L. West, "Independent optical control of microfluidic valves formed from optomechanically responsive nanocomposite hydrogels," *Advanced Materials,* vol. 17, pp. 1366-1368, Jun 6 2005.

[39] J. Wang, Z. Y. Chen, P. L. A. M. Corstjens, M. G. Mauk, and H. H. Bau, "A disposable microfluidic cassette for DNA amplification and detection," *Lab on a Chip,* vol. 6, pp. 46-53, 2006.

[40] J. Wang, Z. Y. Chen, M. Mauk, K. S. Hong, M. Y. Li, S. Yang, *et al.*, "Self-actuated, thermo-responsive hydrogel valves for lab on a chip," *Biomedical Microdevices,* vol. 7, pp. 313-322, Dec 2005.

[41] D. T. Eddington and D. J. Beebe, "Flow control with hydrogels," *Advanced Drug Delivery Reviews,* vol. 56, pp. 199-210, Feb 10 2004.

[42] A. K. Agarwal, S. S. Sridharamurthy, D. J. Beebe, and H. R. Jiang, "Programmable autonomous micromixers and micropumps," *Journal of Microelectromechanical Systems,* vol. 14, pp. 1409-1421, Dec 2005.

[43] D. T. Eddington and D. J. Beebe, "A valved responsive hydrogel microdispensing device with integrated pressure source," *Journal of Microelectromechanical Systems,* vol. 13, pp. 586-593, 2004.

[44] J. Kim, J. Baek, K. Lee, Y. Park, K. Sun, T. Lee, *et al.*, "Photopolymerized check valve and its integration into a pneumatic pumping system for biocompatible sample delivery," *Lab on a Chip,* vol. 6, pp. 1091-1094, 2006.

[45] S. M. Liang, J. Xu, L. H. Weng, L. N. Zhang, X. L. Guo, and X. L. Zhang, "Biologically inspired path-controlled linear locomotion of polymer gel in air," *Journal of Physical Chemistry B,* vol. 111, pp. 941-945, Frb 8 2007.

[46] R. T. Pijls, S. Lindemann, R. M. M. A. Nuijts, G. W. Daube, and L. H. Koole, "Pradofloxacin release from the OphthaCoil: a new device for sustained delivery of drugs to the eye," *Journal of Drug Delivery Science and Technology,* vol. 17, pp. 87-91, Jan-Feb 2007.

[47]   J. Wu, W. Wei, L. Y. Wang, Z. G. Su, and G. H. Ma, "A thermosensitive hydrogel based on quaternized chitosan and poly(ethylene glycol) for nasal drug delivery system," *Biomaterials,* vol. 28, pp. 2220-2232, Apr 2007.

[48]   T. P. Amadeu, A. B. Seabra, M. G. de Oliveira, and A. M. A. Costa, "S-nitrosoglutathione-containing hydrogel accelerates rat cutaneous wound repair," *Journal of the European Academy of Dermatology and Venereology,* vol. 21, pp. 629-637, May 2007.

[49]   A. B. Seabra, E. Pankotai, M. Feher, A. Somlai, L. Kiss, L. Biro*, et al.*, "S-nitrosoglutathione-containing hydrogel increases dermal blood flow in streptozotocin-induced diabetic rats," *British Journal of Dermatology,* vol. 156, pp. 814-818, May 2007.

[50]   S. F. C. Jessica O. Winter, Joseph F. Rizzo III,, "Neurotrophin-eluting hydrogel coatings for neural stimulating electrodes," *Journal of Biomedical Materials Research Part B: Applied Biomaterials,* vol. 81B, pp. 551-563, 2007.

[51]   J. Piantino, J. A. Burdick, D. Goldberg, R. Langer, and L. I. Benowitz, "An injectable, biodegradable hydrogel for trophic factor delivery enhances axonal rewiring and improves performance after spinal cord injury," *Experimental Neurology,* vol. 201, pp. 359-367, Oct 2006.

[52]   C. E. Schmidt and J. B. Leach, "Neural tissue engineering: Strategies for repair and regeneration," *Annual Review of Biomedical Engineering,* vol. 5, pp. 293-347, 2003.

[53]   D. A. Wang, C. G. Williams, F. Yang, N. Cher, H. Lee, and J. H. Elisseeff, "Bioresponsive phosphoester hydrogels for bone tissue engineering," *Tissue Engineering,* vol. 11, pp. 201-213, Jan 2005.

[54]   K. Na, S. Kim, D. G. Woo, B. K. Sun, H. N. Yang, H. M. Chung*, et al.*, "Synergistic effect of TGF beta-3 on chondrogenic differentiation of rabbit chondrocytes in thermo-reversible hydrogel constructs blended with hyaluronic acid by in vivo test," *Journal of Biotechnology,* vol. 128, pp. 412-422, Feb 1 2007.

[55]   J. L. Wyman, S. Kizilel, R. Skarbek, X. Zhao, M. Connors, W. S. Dillmore*, et al.*, "Immunoisolating pancreatic islets by encapsulation with selective withdrawal," *Small,* vol. 3, pp. 683-690, Apr 2007.

[56]   G. M. Cruise, O. D. Hegre, D. S. Scharp, and J. A. Hubbell, "A sensitivity study of the key parameters in the interfacial photopolymerization of poly(ethylene glycol) diacrylate upon porcine islets," *Biotechnology and Bioengineering,* vol. 57, pp. 655-665, Mar 20 1998.

[57]   K. H. Park, K. Na, and H. M. Chung, "Enhancement of the adhesion of fibroblasts by peptide containing an Arg-Gly-Asp sequence with poly(ethylene glycol) into a thermo-reversible hydrogel as a synthetic extracellular matrix," *Biotechnology Letters,* vol. 27, pp. 227-231, Feb 2005.

[58]   K. Na, D. W. Kim, and K. H. Park, "Certification of fibroblast cell adhesion and spreading mediated by Arg-Gly-Asp (RGD) sequence on thermo-reversible hydrogel," *Journal of Microbiology and Biotechnology,* vol. 11, pp. 922-927, Dec 2001.

[59]   F. P. Luyten, F. Dell'Accio, and C. De Bari, "Skeletal tissue engineering: opportunities and challenges," *Best Practice & Research Clinical Rheumatology,* vol. 15, pp. 759-769, 2001/12 2001.

[60]   K. H. Park and K. Yun, "Immobilization of Arg-Gly-Asp (RGD) sequence in a thermosensitive hydrogel for cell delivery using pheochromocytoma cells

(PC12)," *Journal of Bioscience and Bioengineering,* vol. 97, pp. 374-377, Jun 2004.

[61]   P. C. Elisseeff J, Yang F,Sharma B, "Advances in skeletal tissue engineering with hydrogels," *Orthod Craniofacial Res.,* vol. 8, pp. 150-161, 2005.

[62]   V. Mironov, T. Boland, T. Trusk, G. Forgacs, and R. R. Markwald, "Organ printing: computer-aided jet-based 3D tissue engineering," *Trends in Biotechnology,* vol. 21, pp. 157-161, Apr 2003.

[63]   N. E. Fedorovich, J. Alblas, J. R. de Wijn, W. E. Hennink, A. J. Verbout, and W. J. A. Dhert, "Hydrogels as extracellular matrices for skeletal tissue engineering: state-of-the-art and novel application in organ printing," *Tissue Engineering,* vol. 13, pp. 1905-1925, Aug 2007.

[64]   X. H. Wang, Y. N. Yan, F. Lin, Z. Xiong, R. D. Wu, R. J. Zhang*, et al.*, "Preparation and characterization of a collagen/chitosan/heparin matrix for an implantable bioartificial liver," *Journal of Biomaterials Science-Polymer Edition,* vol. 16, pp. 1063-1080, 2005.

[65]   L. Hecker and R. K. Birla, "Engineering the heart piece by piece state of the art in cardiac tissue engineering," *Regenerative Medicine,* vol. 2, pp. 125-144, Mar 2007.

[66]   Y. M. Mohan, K. Lee, T. Premkumar, and K. E. Geckeler, "Hydrogel networks as nanoreactors: A novel approach to silver nanoparticles for antibacterial applications," *Polymer,* vol. 48, pp. 158-164, Jan 5 2007.

[67]   A. Z. Pich and H. J. P. Adler, "Composite aqueous microgels: an overview of recent advances in synthesis, characterization and application," *Polymer International,* vol. 56, pp. 291-307, Mar 2007.

[68]   C. Y. Xu and J. Kopecek, "Self-assembling hydrogels," *Polymer Bulletin,* vol. 58, pp. 53-63, Jan 2007.

[69]   T. Miyata, N. Asami, and T. Uragami, "A reversibly antigen-responsive hydrogel," *Nature,* vol. 399, pp. 766-769, Jun 24 1999.

[70]   J. Z. Hilt, A. K. Gupta, R. Bashir, and N. A. Peppas, "Ultrasensitive biomems sensors based on microcantilevers patterned with environmentally responsive hydrogels," *Biomedical Microdevices,* vol. 5, pp. 177-184, Sep 2003.

[71]   R. A. Barry and P. Wiltzius, "Humidity-sensing inverse opal hydrogels," *Langmuir,* vol. 22, pp. 1369-1374, Jan 31 2006.

[72]   A. Sidorenko, T. Krupenkin, A. Taylor, P. Fratzl, and J. Aizenberg, "Reversible switching of hydrogel-actuated nanostructures into complex micropatterns," *Science,* vol. 315, pp. 487-490, Jan 26 2007.

[73]   P. Thoniyot, F. E. Cappuccio, S. Gamsey, D. B. Cordes, R. A. Wessling, and B. Singaram, "Continuous glucose sensing with fluorescent thin-film hydrogels. 2. Fiber optic sensor fabrication and in vitro testing," *Diabetes Technology & Therapeutics,* vol. 8, pp. 279-287, Jun 2006.

[74]   R. V. Ulijn, N. Bibi, V. Jayawarna, P. D. Thornton, S. J. Todd, R. J. Mart*, et al.*, "Bioresponsive hydrogels," *Materials Today,* vol. 10, pp. 40-48, APR 2007.

[75]   P. J. Flory, *Principles of polymer chemistry*. Ithaca, N.Y.: Cornell University Press, 1953.

[76]   A. E. English, S. Mafe, J. A. Manzanares, X. H. Yu, A. Y. Grosberg, and T. Tanaka, "Equilibrium swelling properties of polyampholytic hydrogels," *Journal of Chemical Physics,* vol. 104, pp. 8713-8720, Jun 1 1996.

[77]   B. Erman and P. J. Flory, "Critical Phenomena and Transitions in Swollen Polymer Networks and in Linear Macromolecules," *Macromolecules,* vol. 19, pp. 2342-2353, Sep 1986.

[78]   M. Annaka, M. Tokita, T. Tanaka, S. Tanaka, and T. Nakahira, "The gel that memorizes phases," *Journal of Chemical Physics,* vol. 112, pp. 471-477, Jan 1 2000.

[79]   T. Caykara and I. Aycicek, "pH-responsive ionic poly(N,N-diethylaminoethyl methacrylate-co-N-vinyl-2-pyrrolidone) hydrogels: Synthesis and swelling properties," *Journal of Polymer Science Part B-Polymer Physics,* vol. 43, pp. 2819-2828, Oct 1 2005.

[80]   T. Caykara and M. Dogmus, "Swelling-shrinking behavior of poly(acrylamide-co-itaconic acid) hydrogels in water and aqueous NaCl solutions," *Journal of Macromolecular Science-Pure and Applied Chemistry,* vol. A42, pp. 105-111, Jan 2005.

[81]   A. J. Galli and W. H. Brumage, "The Freely Jointed Chain in Expanded Form," *Journal of Chemical Physics,* vol. 79, pp. 2411-2418, 1983.

[82]   A. R. Khokhlov and E. Y. Kramarenko, "Collapse of a Polymer Gel Induced by Complex-Formation with Linear-Polymers," *Makromolekulare Chemie-Theory and Simulations,* vol. 2, pp. 169-177, Mar 1993.

[83]   A. R. Khokhlov and E. Y. Kramarenko, "Polyelectrolyte/Ionomer Behavior in Polymer Gel Collapse," *Macromolecular Theory and Simulations,* vol. 3, pp. 45-59, Jan 1994.

[84]   S. N. Wu, H. Li, J. P. Chen, and K. Y. Lam, "Modeling investigation of hydrogel volume transition," *Macromolecular Theory and Simulations,* vol. 13, pp. 13-29, Jan 12 2004.

[85]   T. Hino and J. M. Prausnitz, "Molecular thermodynamics for volume-change transitions in temperature-sensitive polymer gels," *Polymer,* vol. 39, pp. 3279-3283, Jun 1998.

[86]   N. A. Peppas, *Hydrogels in medicine and pharmacy*. Boca Raton, Fla.: CRC Press, 1986.

[87]   N. A. Peppas and R. S. Langer, *Biopolymers II*. Berlin ; New York: Springer-Verlag, 1995.

[88]   N. A. Peppas, R. S. Langer, and S. Amselem, *Biopolymers I*. Berlin ; New York: Springer-Verlag, 1993.

[89]   J. Kovac, "Modified Gaussian Model for Rubber Elasticity," *Macromolecules,* vol. 11, pp. 362-365, 1978.

[90]   N. Gundogan, D. Melekaslan, and O. Okay, "Swelling and elasticity of poly (N-isopropylacrylamide-co-4-vinyl benzene sulfonic acid sodium salt) hydrogels," *Journal of Applied Polymer Science,* vol. 94, pp. 135-141, Oct 5 2004.

[91]   S. Durmaz, S. Fank, and O. Okay, "Swelling and mechanical properties of solution-crosslinked poly(isobutylene) gels," *Macromolecular Chemistry and Physics,* vol. 203, pp. 663-672, Mar 15 2002.

[92]   O. Okay, S. Durmaz, and B. Erman, "Solution cross-linked poly(isobutylene) gels: Synthesis and swelling behavior," *Macromolecules,* vol. 33, pp. 4822-4827, Jun 27 2000.

[93]   O. Okay and S. B. Sariisik, "Swelling behavior of poly(acrylamide-co-sodium acrylate) hydrogels in aqueous salt solutions: theory versus experiments," *European Polymer Journal,* vol. 36, pp. 393-399, Feb 2000.

[94]   T. Caykara, U. Bozkaya, and O. Kantoglu, "Network structure and swelling behavior of poly(acrylamide/crotonic acid) hydrogels in aqueous salt solutions," *Journal of Polymer Science Part B-Polymer Physics,* vol. 41, pp. 1656-1664, Jul 15 2003.

[95]   T. Caykara and M. Dogmus, "The effect of solvent composition on swelling and shrinking properties of poly(acrylamide-co-itaconic acid) hydrogels," *European Polymer Journal,* vol. 40, pp. 2605-2609, Nov 2004.

[96]   S. Baek and A. R. Srinivasa, "Modeling of the pH-sensitive behavior of an ionic gel in the presence of diffusion," *International Journal of Non-Linear Mechanics,* vol. 39, pp. 1301-1318, Oct 2004.

[97]   E. D. Oliveira, A. F. S. Silva, and R. F. S. Freitas, "Contributions to the thermodynamics of polymer hydrogel systems," *Polymer,* vol. 45, pp. 1287-1293, Feb 15 2004.

[98]   A. Katchalsky and I. Michaeli, "Polyelectrolyte Gels in Salt Solutions," *Journal of Polymer Science,* vol. 15, pp. 69-86, 1955.

[99]   A. Fomenko, H. Pospisil, Z. Sedlakova, J. Plestil, and M. Ilavsky, "Phase transition in swollen gels - Part 32. Temperature transition in charged poly(N-isopropylmethacrylamide) hydrogels in water and aqueous NaCl solutions," *Physical Chemistry Chemical Physics,* vol. 4, pp. 4360-4367, 2002.

[100]   A. Fomenko, Z. Sedlakova, and M. Ilavsky, "Phase transition in swollen gels - 30. Temperature-induced phase transition in positively charged poly(N-isopropylacrylamide) hydrogels in water and aqueous NaCl solutions," *Polymer Bulletin,* vol. 47, pp. 367-374, Dec 2001.

[101]   M. Ilavsky, E. Talasova, and K. Dusek, "Photo-Elastic Behavior of Swollen Networks of Polymethacrylic Acid," *European Polymer Journal,* vol. 16, pp. 191-199, 1980.

[102]   J. Hasa, M. Ilavsky, and K. Dusek, "Deformational, Swelling, and Potentiometric Behavior of Ionized Poly(Methacrylic Acid) Gels .1. Theory," *Journal of Polymer Science Part B-Polymer Physics,* vol. 13, pp. 253-262, 1975.

[103]   M. Ilavsky, J. Plestil, and K. Dusek, "The Photo-Elastic Behavior and Small-Angle X-Ray-Scattering of Ionized Gels of Co-Polymers of 2-Hydroxyethyl Methacrylate with Methacrylic-Acid," *European Polymer Journal,* vol. 16, pp. 901-907, 1980.

[104]   M. Ilavsky, J. Hasa, and K. Dusek, "Photoelastic Behavior of Poly(Normal-Alkyl Acrylate) Networks in Rubbery State," *Journal of Polymer Science Part C-Polymer Symposium,* pp. 239-256, 1975.

[105]   K. Ogawa, Y. Ogawa, and E. Kokufuta, "Effect of charge inhomogeneity of polyelectrolyte gels on their swelling behavior," *Colloids and Surfaces a-Physicochemical and Engineering Aspects,* vol. 209, pp. 267-279, Sep 25 2002.

[106]   S. Baek and A. R. Srinivasa, "Diffusion of a fluid through an elastic solid undergoing large deformation," *International Journal of Non-Linear Mechanics,* vol. 39, pp. 201-218, Mar 2004.

[107]   E. Y. Kramarenko, A. R. Khokhlov, and K. Yoshikawa, "A three-state model for counterions in a dilute solution of weakly charged polyelectrolytes," *Macromolecular Theory and Simulations,* vol. 9, pp. 249-256, Jun 28 2000.

[108]   Y. B. Huang, I. Szleifer, and N. A. Peppas, "A molecular theory of polymer gels," *Macromolecules,* vol. 35, pp. 1373-1380, Feb 12 2002.

[109]   W. M. Lai and V. C. Mow, "Drag-Induced Compression of Articular-Cartilage during a Permeation Experiment," *Biorheology,* vol. 17, pp. 111-123, 1980.

[110] V. C. Mow, S. C. Kuei, W. M. Lai, and C. G. Armstrong, "Biphasic Creep and Stress-Relaxation of Articular-Cartilage in Compression - Theory and Experiments," *Journal of Biomechanical Engineering-Transactions of the Asme,* vol. 102, pp. 73-84, 1980.

[111] W. M. Lai, V. C. Mow, and V. Roth, "Effects of Non-Linear Strain-Dependent Permeability and Rate of Compression on the Stress Behavior of Articular-Cartilage," *Journal of Biomechanical Engineering-Transactions of the Asme,* vol. 103, pp. 61-66, May 1981.

[112] C. G. Armstrong, W. M. Lai, and V. C. Mow, "An Analysis of the Unconfined Compression of Articular-Cartilage," *Journal of Biomechanical Engineering-Transactions of the Asme,* vol. 106, pp. 165-173, 1984.

[113] Y. Lanir, "Biorheology and Fluid Flux in Swelling Tissues .1. Bicomponent Theory for Small Deformations, Including Concentration Effects," *Biorheology,* vol. 24, pp. 173-187, 1987.

[114] Y. Lanir, "Biorheology and Fluid Flux in Swelling Tissues .2. Analysis of Unconfined Compressive Response of Transversely Isotropic Cartilage Disk," *Biorheology,* vol. 24, pp. 189-205, 1987.

[115] R. L. Spilker, J. K. Suh, and V. C. Mow, "Linear Biphasic finite element analysis of the unconfined compression of articular cartilage," in *Winter Anual meeting of the american society of mechanical engineers*, New York, NY, 1987, pp. 49-50.

[116] R. L. Spilker, "Finite element formulation of the non-linear biphasic model for articular cartilage and hydrated soft tissues including strain-dependent permeability," in *Symposium in Computational Methods in Bioengineering*, Chicago, Il, 1988, pp. 81-92.

[117] W. M. Lai, "Triphasic theory for articular cartilage swelling and donnan osmotic pressure," *American Society of Mechanical Engineers,* vol. 98, pp. 33-36, 1989.

[118] W. M. Lai, J. S. Hou, and V. C. Mow, "A Triphasic Theory for the Swelling and Deformation Behaviors of Articular-Cartilage," *Journal of Biomechanical Engineering-Transactions of the Asme,* vol. 113, pp. 245-258, Aug 1991.

[119] W. Y. Gu, W. M. Lai, and V. C. Mow, "Transport of Fluid and Ions through a Porous-Permeable Charged-Hydrated Tissue, and Streaming Potential Data on Normal Bovine Articular-Cartilage," *Journal of Biomechanics,* vol. 26, pp. 709-723, Jun 1993.

[120] T. G. Myers, G. K. Aldis, and S. Naili, "Ion-Induced Deformation of Soft-Tissue," *Bulletin of Mathematical Biology,* vol. 57, pp. 77-98, JAN 1995.

[121] H. Snijders, J. M. Huyghe, and J. D. Janssen, "Triphasic Finite-Element Model for Swelling Porous-Media," *International Journal for Numerical Methods in Fluids,* vol. 20, pp. 1039-1046, Apr 30 1995.

[122] B. R. Simon, J. P. Liable, D. Pflaster, Y. Yuan, and M. H. Krag, "A poroelastic finite element formulation including transport and swelling in soft tissue structures," *Journal of Biomechanical Engineering-Transactions of the Asme,* vol. 118, pp. 1-9, Feb 1996.

[123] W. Y. Gu, W. M. Lai, and V. C. Mow, "A mixture theory for charged-hydrated soft tissues containing multi-electrolytes: Passive transport and swelling behaviors," *Journal of Biomechanical Engineering-Transactions of the Asme,* vol. 120, pp. 169-180, Apr 1998.

[124] V. C. Mow, G. A. Ateshian, W. M. Lai, and W. Y. Gu, "Effects of fixed charges on the stress-relaxation behavior of hydrated soft tissues in a confined

compression problem," *International Journal of Solids and Structures,* vol. 35, pp. 4945-4962, Dec 1998.

[125] Y. C. Hon, M. W. Lu, W. M. Xue, and X. Zhou, "A new formulation and computation of the triphasic model for mechano-electrochemical mixtures," *Computational Mechanics,* vol. 24, pp. 155-165, Sep 1999.

[126] D. N. Sun, W. Y. Gu, X. E. Guo, W. M. Lai, and V. C. Mow, "A mixed finite element formulation of triphasic mechano-electrochemical theory for charged, hydrated biological soft tissues," *International Journal for Numerical Methods in Engineering,* vol. 45, pp. 1375-1402, Aug 10 1999.

[127] W. Y. Gu, W. M. Lai, and V. C. Mow, "Transport of multi-electrolytes in charged hydrated biological soft tissues," *Transport in Porous Media,* vol. 34, pp. 143-157, Mar 1999.

[128] W. M. Lai, V. C. Mow, D. D. Sun, and G. A. Ateshian, "On the electric potentials inside a charged soft hydrated biological tissue: Streaming potential versus diffusion potential," *Journal of Biomechanical Engineering-Transactions of the Asme,* vol. 122, pp. 336-346, Aug 2000.

[129] Y. C. Hon, M. W. Lu, W. M. Xue, and X. Zhou, "Numerical algorithm for triphasic model of charged and hydrated soft tissues," *Computational Mechanics,* vol. 29, pp. 1-15, Jul 2002.

[130] X. Zhou, Y. C. Hon, S. Sun, and A. F. T. Mak, "Numerical simulation of the steady-state deformation of a smart hydrogel under an external electric field," *Smart Materials & Structures,* vol. 11, pp. 459-467, Jun 2002.

[131] W. Y. Gu and H. Yao, "Effects of hydration and fixed charge density on fluid transport in charged hydrated soft tissues," *Annals of Biomedical Engineering,* vol. 31, pp. 1162-1170, Nov 2003.

[132] D. D. Sun, X. E. Guo, M. Likhitpanichkul, W. M. Lai, and V. C. Mow, "The influence of the fixed negative charges on mechanical and electrical behaviors of articular cartilage under unconfined compression," *Journal of Biomechanical Engineering-Transactions of the Asme,* vol. 126, pp. 6-16, Feb 2004.

[133] H. Yao and W. Y. Gu, "Physical signals and solute transport in cartilage under dynamic unconfined compression: Finite element analysis," *Annals of Biomedical Engineering,* vol. 32, pp. 380-390, Mar 2004.

[134] H. Li, J. Chen, and K. Y. Lam, "Multiphysical modeling and meshless simulation of electric-sensitive hydrogels," *Journal of Polymer Science Part B-Polymer Physics,* vol. 42, pp. 1514-1531, Apr 15 2004.

[135] H. Li, Z. Yuan, K. Y. Lam, H. P. Lee, J. Chen, J. Hanes*, et al.*, "Model development and numerical simulation of electric-stimulus-responsive hydrogels subject to an externally applied electric field," *Biosensors & Bioelectronics,* vol. 19, pp. 1097-1107, Apr 15 2004.

[136] J. Chen, H. Li, and K. Y. Lam, "Transient simulation for kinetic responsive behaviors of electric-sensitive hydrogels subject to applied electric field," *Materials Science & Engineering C-Biomimetic and Supramolecular Systems,* vol. 25, pp. 710-712, Dec 2005.

[137] Y. Chen, X. Chen, and T. Hisada, "Non-linear finite element analysis of mechanical electrochemical phenomena in hydrated soft tissues based on triphasic theory," *International Journal for Numerical Methods in Engineering,* vol. 65, pp. 147-173, Jan 8 2006.

311

[138]   J. Chen and G. Ma, "Modelling deformation behavior of polyelectrolyte gels under chemo-electro-mechanical coupling effects," *International Journal for Numerical Methods in Engineering,* vol. 68, pp. 1052-1071, 2006.

[139]   H. Li, J. Chen, and K. Y. Lam, "Transient simulation of kinetics of electric-sensitive hydrogels," *Biosensors & Bioelectronics,* vol. 22, pp. 1633-1641, Mar 15 2007.

[140]   H. Li, J. Chen, and K. Y. Lam, "A transient simulation to predict the kinetic behavior of hydrogels responsive to electric stimulus," *Biomacromolecules,* vol. 7, pp. 1951-1959, Jun 2006.

[141]   P. E. Grimshaw, J. H. Nussbaum, A. J. Grodzinsky, and M. L. Yarmush, "Kinetics of Electrically and Chemically-Induced Swelling in Polyelectrolyte Gels," *Journal of Chemical Physics,* vol. 93, pp. 4462-4472, Sep 15 1990.

[142]   T. Wallmersperger, B. Kroplin, J. Holdenried, and R. W. Gulch, "A Coupled Multi-Field-Formulation for Ionic Polymer Gels in Electric Fields," in *Smart Structures and Materials 2001: Electroactive Polymer Actuators and Devices*, 2001, pp. 264-275.

[143]   H. Li, Y. Yew, K. Y. Lam, and T. Ng, "Numerical Simulation of Hydrogel-Based pH-responsive Biosensors in BioMEMS," in *Design, Test, Integration & Packaging of MEMS/MOEMS*, Cannes-Mandelieu, 2003, pp. 218-222.

[144]   H. Li, Y. Yew, K. Y. Lam, and T. Ng, "Numerical simulation of pH-stimuli responsive hydrogel in buffer solutions," *Colloids and Surfaces a-Physicochemical and Engineering Aspects,* vol. 249, pp. 149-154, Nov 30 2004.

[145]   H. Li, T. Y. Ng, Y. K. Yew, and K. Y. Lam, "Modeling and simulation of the swelling behavior of pH-stimulus-responsive hydrogels," *Biomacromolecules,* vol. 6, pp. 109-120, Jan-Feb 2005.

[146]   H. Li, T. Y. Ng, J. Q. Cheng, and K. Y. Lam, "Hermite-Cloud: a novel true meshless method," *Computational Mechanics,* vol. 33, pp. 30-41, Dec 2003.

[147]   H. Li, Y. K. Yew, T. Y. Ng, and K. Y. Lam, "Meshless steady-state analysis of chemo-electro-mechanical coupling behavior of pH-sensitive hydrogel in buffered solution," *Journal of Electroanalytical Chemistry,* vol. 580, pp. 161-172, Jun 15 2005.

[148]   Q. X. Wang, H. Li, and K. Y. Lam, "Meshless simulation of equilibrium swelling/deswelling of PH-sensitive hydrogels," *Journal of Polymer Science Part B-Polymer Physics,* vol. 44, pp. 326-337, Jan 15 2006.

[149]   T. Y. Ng, H. Li, Y. K. Yew, and K. Y. Lam, "Effects of initial-fixed charge density on pH-sensitive hydrogels subjected to coupled pH and electric field stimuli: A meshless analysis," *Journal of Biomechanical Engineering-Transactions of the Asme,* vol. 129, pp. 148-155, Apr 2007.

[150]   K. Y. Lam, H. Li, T. Y. Ng, and R. M. Luo, "Modeling and simulation of the deformation of multi-state hydrogels subjected to electrical stimuli," *Engineering Analysis with Boundary Elements,* vol. 30, pp. 1011-1017, Nov 2006.

[151]   J. H. Nussbaum, "Electric Field Control of Mechanical and Electrochemical Properties of Polyelectrolyte Gel Membranes," Degree of Doctor of Science, Department of Electrical Engineering and Computer Science, Massachusetts Institute of Technology, 1986.

[152]   P. E. Grimshaw, "Electrical control of solute transport across polyelectrolyte membranes," Doctor of Philosophy, Department of Electrical Engineering and Computer Science, Massachusetts Institute of Technology, 1989.

[153] C. J. Wang, Y. Li, and Z. B. Hu, "Swelling kinetics of polymer gels," *Macromolecules,* vol. 30, pp. 4727-4732, Aug 11 1997.

[154] S. Nemat-Nasser and J. Y. Li, "Electromechanical response of ionic polymer-metal composites," *Journal of Applied Physics,* vol. 87, pp. 3321-3331, Apr 1 2000.

[155] J. H. Nussbaum, "Electric field control of mechanical and electrochemical properties of polyelectrolyte gel membranes," Ph.D. / Sc.D., Electrical Engineering and Computer Science, Massachusetts Institute of Technology, 1986.

[156] J. S. Mackie and P. Meares, "The Diffusion of Electrolytes in a Cation-Exchange Resin Membrane .1. Theoretical," *Proceedings of the Royal Society of London Series a-Mathematical and Physical Sciences,* vol. 232, pp. 498-509, 1955.

[157] A. Einstein, "Investigations on the Theory of the Brownian Movement," *Dover Publications,* vol. 2007, 1905.

[158] O. Okay and S. Durmaz, "Charge density dependence of elastic modulus of strong polyelectrolyte hydrogels," *Polymer,* vol. 43, pp. 1215-1221, Feb 2002.

[159] T. B. Jones, *Electromagnetics of Particles*. New York: Cambridge University Press, 1995.

[160] D. S. Chandrasekharaiah and L. Debnath, *Continuum Mechanics*. San Diego: Academic Press Inc., 1994.

[161] D. Hariharan and N. A. Peppas, "Swelling of Ionic and Neutral Polymer Networks in Ionic-Solutions," *Journal of Membrane Science,* vol. 78, pp. 1-12, Mar 25 1993.

[162] E. M. Aydt and R. Hentschke, "Swelling of a model network: A Gibbs-ensemble molecular dynamics study," *Journal of Chemical Physics,* vol. 112, pp. 5480-5487, Mar 22 2000.

[163] N. R. Kenkare, C. K. Hall, and S. A. Khan, "Theory and simulation of the swelling of polymer gels," *Journal of Chemical Physics,* vol. 113, pp. 404-418, Jul 1 2000.

[164] B. Nick and U. W. Suter, "Solubility of water in polymers - atomistic simulations," *Computational and Theoretical Polymer Science,* vol. 11, pp. 49-55, 2001.

[165] Z. Y. Lu and R. Hentschke, "Swelling of a model polymer network by a one-site solvent: Computer simulation and Flory-Huggins-like theory," *Physical Review E,* vol. 6305, pp. 1-8, May 2001.

[166] N. Gilra, A. Z. Panagiotopoulos, and C. Cohen, "Monte Carlo simulations of polymer network deformation," *Macromolecules,* vol. 34, pp. 6090-6096, AUG 14 2001.

[167] Z. Y. Lu and R. Hentschke, "Computer simulation study on the swelling of a model polymer network by a chainlike solvent," *Physical Review E,* vol. 65, pp. 1-7, Apr 2002.

[168] Z. Y. Lu and R. Hentschke, "Swelling of model polymer networks with different cross-link densities: A computer simulation study," *Physical Review E,* vol. 66, pp. 1-8, Oct 2002.

[169] S. Schneider and P. Linse, "Swelling of cross-linked polyelectrolyte gels," *European Physical Journal E,* vol. 8, pp. 457-460, Aug 2002.

[170] S. Schneider and P. Linse, "Monte Carlo simulation of defect-free cross-linked polyelectrolyte gels," *Journal of Physical Chemistry B,* vol. 107, pp. 8030-8040, Aug 14 2003.

[171] R. R. Netz, "Polyelectrolytes in electric fields," *Journal of Physical Chemistry B,* vol. 107, pp. 8208-8217, Aug 14 2003.

[172]   Z. Y. Lu and R. Hentschke, "Computer simulation study on the swelling of a polyelectrolyte gel by a Stockmayer solvent," *Physical Review E,* vol. 67, pp. 1-7, Jun 2003.

[173]   Q. L. Yan and J. J. de Pablo, "Monte Carlo simulation of a coarse-grained model of polyelectrolyte networks," *Physical Review Letters,* vol. 91, pp. 1-4, Jul 4 2003.

[174]   S. Liu, K. Ghosh, and M. Muthukumar, "Polyelectrolyte solutions with added salt: A simulation study," *Journal of Chemical Physics,* vol. 119, pp. 1813-1823, Jul 15 2003.

[175]   Q. Liao, A. V. Dobrynin, and M. Rubinstein, "Molecular dynamics simulations of polyelectrolyte solutions: Nonuniform stretching of chains and scaling behavior," *Macromolecules,* vol. 36, pp. 3386-3398, May 6 2003.

[176]   Q. Liao, A. V. Dobrynin, and M. Rubinstein, "Molecular dynamics simulations of polyelectrolyte solutions: Osmotic coefficient and counterion condensation," *Macromolecules,* vol. 36, pp. 3399-3410, May 6 2003.

[177]   S. Schneider and P. Linse, "Discontinuous volume transitions in cross-linked polyelectrolyte gels induced by short-range attractions and strong electrostatic coupling," *Macromolecules,* vol. 37, pp. 3850-3856, May 18 2004.

[178]   B. A. Mann, R. Everaers, C. Holm, and K. Kremer, "Scaling in polyelectrolyte networks," *Europhysics Letters,* vol. 67, pp. 786-792, Sep 2004.

[179]   J. Ostroha, M. Pong, A. Lowman, and N. Dan, "Controlling the collapse/swelling transition in charged hydrogels," *Biomaterials,* vol. 25, pp. 4345-4353, Aug 2004.

[180]   E. Oyen and R. Hentschke, "Computer simulation of polymer networks: Swelling by binary Lennard-Jones mixtures," *Journal of Chemical Physics,* vol. 123, pp. 1-8, Aug 1 2005.

[181]   B. A. Mann, C. Holm, and K. Kremer, "Swelling of polyelectrolyte networks," *Journal of Chemical Physics,* vol. 122, pp. 1-14, Apr 15 2005.

[182]   J. Klos and T. Pakula, "Lattice Monte Carlo simulations of a charged polymer chain: Effect of valence and concentration of the added salt," *Journal of Chemical Physics,* vol. 122, pp. 1-7, Apr 1 2005.

[183]   N. A. Kumar and C. Seidel, "Polyelectrolyte brushes with added salt," *Macromolecules,* vol. 38, pp. 9341-9350, Nov 1 2005.

[184]   D. W. Yin, Q. L. Yan, and J. J. de Pablo, "Molecular dynamics simulation of discontinuous volume phase transitions in highly-charged crosslinked polyelectrolyte networks with explicit counterions in good solvent," *Journal of Chemical Physics,* vol. 123, pp. 1-9, Nov 1 2005.

[185]   J. Klos and T. Pakula, "Monte Carlo simulations of a polyelectrolyte chain with added salt: Effect of temperature and salt valence," *Journal of Chemical Physics,* vol. 123, pp. 1-8, Jul 8 2005.

[186]   R. Chang and A. Yethiraj, "Osmotic pressure of salt-free polyelectrolyte solutions: A Monte Carlo simulation study," *Macromolecules,* vol. 38, pp. 607-616, Jan 25 2005.

[187]   P. Rempala and B. T. King, "Simulation of actuation by polymeric polyelectrolyte helicenes," *Journal of Chemical Theory and Computation,* vol. 2, pp. 1112-1118, Jul 11 2006.

[188]   J. Feng, H. Liu, and Y. Hu, "Molecular dynamics simulations of polyampholyte solutions: osmotic coefficient," *Molecular Simulation,* vol. 32, pp. 51-57, Jan 2006.

[189] A. Palleschi, T. Coviello, G. Bocchinfuso, and F. Alhaique, "Investigation on a new scleroglucan/borax hydrogel: Structure and drug release," *International Journal of Pharmaceutics,* vol. 322, pp. 13-21, Sep 28 2006.

[190] Y. Xu, J. Feng, H. Liu, Y. Hu, and J. Jiang, "Molecular dynamics simulation of polyelectrolyte with oppositely charged monomeric and dimeric surfactants," *Molecular Simulation,* vol. 33, pp. 261-268, 2007.

[191] C. Stoltz, J. J. de Pablo, and M. D. Graham, "Simulation of nonlinear shear rheology of dilute salt-free polyelectrolyte solutions," *Journal of Chemical Physics,* vol. 126, pp. 1-15, Mar 28 2007.

[192] R. Pamies, J. G. H. Cifre, and J. G. De la Torre, "Brownian dynamics simulation of polyelectrolyte dilute solutions: Relaxation time and elongational flow," *Journal of Polymer Science Part B-Polymer Physics,* vol. 45, pp. 714-722, Mar 15 2007.

[193] S. S. Jang, W. A. Goddard, and M. Y. S. Kalani, "Mechanical and transport properties of the poly(ethylene oxide)-poly(acrylic acid) double network hydrogel from molecular dynamic simulations," *Journal of Physical Chemistry B,* vol. 111, pp. 1729-1737, Feb 22 2007.

Appendix A-2

Safety and Supplier Information for Chemicals and Materials

Material	Company	Product Number	MSDS
2-Hydroxyethyl Methacrylate	Sigma-Aldrich	477028-100ml	http://www.sigmaaldrich.com/catalog/product/aldrich/477028?lang=en&region=CA
Acrylic Acid	Fisher Scientific	AC16425-0010	http://www.fishersci.ca/viewmsds.do?catNo=AC16425O010
ethylene glycol dimethacrylate	Sigma-Aldrich	335681-100ml	http://www.sigmaaldrich.com/catalog/product/aldrich/335681?lang=en&region=CA
2,2-dimethoxy-2-phenylacetophenone	Sigma-Aldrich	196118-50g	http://www.sigmaaldrich.com/catalog/product/aldrich/196118?lang=en&region=CA
polydimethylsiloxane	Andarr Industries	Slygard 184	http://www.dowcorning.com/applications/search/default.aspx?R=131EN
potassium hydroxide	Sigma-Aldrich	P5958	http://www.sigmaaldrich.com/catalog/product/sial/p5958?lang=en&region=CA
isobornyl acrylate	Sigma-Aldrich	392103-100ml	http://www.sigmaaldrich.com/catalog/product/aldrich/392103?lang=en&region=CA
tetraethylene glycol dimethacrylate	Sigma-Aldrich	86680-100ml	http://www.sigmaaldrich.com/catalog/product/aldrich/86680?lang=en&region=CA
Acetone	Sigma-Aldrich	320110-1L	http://www.sigmaaldrich.com/catalog/product/sial/320110?lang=en&region=CA
Isopropanol Alcohol	Sigma-Aldrich	AC18413-0025	http://www.sigmaaldrich.com/catalog/product/aldrich/w292907?lang=en&region=CA
tricholorol(1,1,2,2-perfluorooctyl)silane	Sigma-Aldrich	448931-10g	http://www.sigmaaldrich.com/catalog/product/aldrich/448931?lang=en&region=CA

Appendix A-3

Matlab Code for Characteristic Frequency Analysis

```
%%%%%%%%%%%%%%%%%%%%%%%%%%%%%%%%%%%%%%%%%%%%%%%%%%%%%%%%%%%%%%%%%%%%%%%%%
%%%%%                     Appendix A-2                      %%%%%
%%%%%     Characteristic AC Frequency for Electrical Actuation  %%%%%%
%%%%%            Developed by: Joseph Ryan Charles Saunders     %%%%%%
%%%%% Inputs: Electrolyte Concentration and Dielectric Thickness %%%%%%
%%%%%    Outputs: Characteristic Frequency and Voltage Loss      %%%%%%
%%%% This analytical coding was developed to evaluate the system  %%%%%
%%%% characteristic frequency that would minimize electrostatic   %%%%%
%%%% shielding. The results plotted below have been presented in  %%%%%
%%%% chapter 6 of Saunders' PhD thesis and within a publication   %%%%%
%%%% in Sensors and Actuators B: Chemical.                        %%%%%
%%%%%%%%%%%%%%%%%%%%%%%%%%%%%%%%%%%%%%%%%%%%%%%%%%%%%%%%%%%%%%%%%%%%%%%%%

%%% System Constants %%%%
F=96485;                  %[C/mol]     Faraday's Constant
T=298;                    %[K]         Temperature
R=8.314;                  %[JK/mol]    Ideal Gas Constant
e=1.602E-19;              %[C]         Elementary Charge
kb=1.381E-23;             %[J/K]       Boltzmann Constant
eo=8.854E-12;             %[C/Vm]      Permittivity of Free Space
Na=6.022E23;              %[atoms/mol] Avogadro's Number
diffH=9.31E-9;            %[m2/s]      Hydrogen : Diffusivity
diffK=1.96E-9;            %[m2/s]      Potassium : Diffusivity
diffOH=5.26E-9;           %[m2/s]      Hydroxide : Diffusivity
eD=2.65;                  %[unitless]  Parylene-N : Relative Permittivity
eS=5;                     %[unitless]  Stern Layer : Relative Permittivity
eM=78;                    %[unitless]  Water : Relative Permittivity
eP=5.6;                   %[unitless]  Polymer : Relative Permittivity
%%%%%%%%%%%%%%%%%%%%%%%%%%

%%%%%%%%%%%%%%%%%%%%%%%%%%
%%%%% Channel Height %%%%%
%%%%%%% (7,7) Matrix %%%%%
%%%%%%%% [meter] %%%%%%%%%
h_chan(1,1:7)=50E-6;      %
h_chan(2,1:7)=150E-6;     %
h_chan(3,1:7)=254E-6;     %
h_chan(4,1:7)=350E-6;     %
h_chan(5,1:7)=450E-6;     %
h_chan(6,1:7)=550E-6;     %
h_chan(7,1:7)=650E-6;     %
%%%%%%%%%%%%%%%%%%%%%%%%%%

%%%%%%%%%%%%%%%%%%%%%%%%%%
%%%%% Electrode Gap %%%%%
%%%%%%% (7,7) Matrix %%%%
%%%%%%%% [meter] %%%%%%%%
EG(1:7,1)=100E-6;         %
EG(1:7,2)=500E-6;         %
EG(1:7,3)=1000E-6;        %
EG(1:7,4)=1500E-6;        %
EG(1:7,5)=2000E-6;        %
EG(1:7,6)=2500E-6;        %
EG(1:7,7)=3000E-6;        %
%%%%%%%%%%%%%%%%%%%%%%%%%%
```

```matlab
%%%%%%%%%%%%%%%%%%%%%%%%%%%%%%%%%%%
%%%% Geometric System Properties %%%%
%%%%%%%%%%% [meter] %%%%%%%%%%%%%%%%
%%% Rows: Constant % Col: Constant %%
%%%%%%%%% (7,7) Matrix %%%%%%%%%%%%%%
tS(1:7,1:7)=5E-10;                  % Stern Layer : Thickness
EW(1:7,1:7)=100E-6;                 % Electrode : Width
EL(1:7,1:7)=1.05E-3;                % Electrode : Length
WH(1:7,1:7)=1E-3;                   % Hydrogel : Width
%%%%%%%%%%%%%%%%%%%%%%%%%%%%%%%%%%%

%%%%%%%%%%%%%%%%%%%%%%%%%%%%%%%%%%%%%%%%%%%%%%%%%
%%%%%%%%%%%%%% Effective Electrode Width %%%%%%%%%%%%
%%%%%%%%%%%%%%%%%%%%%%%%% [meter^2] %%%%%%%%%%%%%%%%%%%%%
%%%%%%%%%%%%%%%%%%%%%%%%%%%%%%%%%%%%%%%%%%%%%%%%%
EW_Eff=(EG/2).*((1+(h_chan./(EG/2)).^2).^0.5-1);    % Effective Width
EW_InEff=abs(EW-EW_Eff);                            % Ineffective Width
%%%%%%%%%%%%%%%%%%%%%%%%%%%%%%%%%%%%%%%%%%%%%%%%%

%%%%%%%%%%%%%%%%%%%%%%%%%%%%%%%%%%%
%%%%%%%%% Electrode Areas %%%%%%%%%%%%
%%%%%%%%% [meters squared] %%%%%%%%%%%
%%%%%%%%%%%%%%%%%%%%%%%%%%%%%%%%%%%
A_Eff=EW_Eff(3,4).*EL;              % Total Effective Area
A_InEff=(EW(1,1)-EW_Eff(3,5)).*EL;  % Total Ineffective Area
A_Eff_H=EW_Eff(3,5).*WH;            % Effective Area to Hydrogel
%%%%%%%%%%%%%%%%%%%%%%%%%%%%%%%%%%%

%%%%%%%%%%%%%%%%%%%%%%%%%%%%%%%%%%%%%%%%
%%%%%%%%%%%%%%% Hydrogel Properties %%%%%%%%%%%%%%
%%%%%%%%%%%%%%%%%%%% [unitless] %%%%%%%%%%%%%%%%%%
H=2;                                           % Hydration
por=H/(1+H);                                   % Porosity
eH=eP*(eP+eM-por*(eP-eM))/(eP+eM+por*(eP-eM));  % Relative Permittivity
%%%%%%%%%%%%%%%%%%%%%%%%%%%%%%%%%%%%%%%%%%%%%%%

%%%%%%%%%%%%%%%%%%%%%%%%%%%%%%%%%%%
%%% Parylene-N Thickness [meter] %%%%
% Rows: Constant; Columns: Variable %
%%%%%%%%%%% (7,7) Matrix %%%%%%%%%%%%
tD(1,1:7)=100E-9;                   %
tD(2,1:7)=250E-9;                   %
tD(3,1:7)=500E-9;                   %
tD(4,1:7)=1E-6;                     %
tD(5,1:7)=2E-6;                     %
tD(6,1:7)=5E-6;                     %
tD(7,1:7)=10E-6;                    %
%%%%%%%%%%%%%%%%%%%%%%%%%%%%%%%%%%%

%%%%%%%%%%%%%%%%%%%%%%%%%%%%%%%%%%%
%%%%%% Electrolyte Concentration %%%%
%%%%%%%%%%%%%%%% [mol/L] %%%%%%%%%%%%%
conc(1:7,1)=1E-3;                   %
conc(1:7,2)=5E-3;                   %
conc(1:7,3)=1E-2;                   %
conc(1:7,4)=5E-2;                   %
conc(1:7,5)=1E-1;                   %
conc(1:7,6)=5E-1;                   %
conc(1:7,7)=1;                      %
cK(1:7,1:7)=2;                      % Potassium Concentration in Hydrogel
cOH(1:7,1:7)=0.2;                   % Hydroxide Concentration in Hydrogel
cF(1:7,1:7)=1.8;                    % Hydrogel's Fixed Ion Concentration
%%%%%%%%%%%%%%%%%%%%%%%%%%%%%%%%%%%

%%%%%%%%%%%%%%%%%%%%%%%%%%%%%%%%%%%
%%%% Conductivity & Debye Length %%%%
ElecCond=(F^2/(R*T)).*(1000*diffK.*conc+1000*diffOH.*conc); % [S/m] Media
ElecCond_H=(F^2/(R*T))*(1000*diffK.*cK+1000*diffOH.*cOH); % [S/m] Hydrogel
```

318

```
tDL=sqrt(eM*eo*kb*T./(2000*(e^2).*Na.*conc));    % [m] Debye Length
%%%%%%%%%%%%%%%%%%%%%%%%%%%%%%%%%%%%%%


%%%%%%%%%%%%%%%%%%%%%%%%%%%%%%%%%%%%%%%%
%%%%%%%%%% System Capacitance %%%%%%%%%%
%%%%%%%%%%%%%%%%% [F] %%%%%%%%%%%%%%%%%%
%%%% Rows: Constant % Col: Variable  %%%%
% For more information on capacitive   %%
% pathways, see Figures in Chapter 6   %%
%%%%%%%%%%%%%%%%%%%%%%%%%%%%%%%%%%%%%%%%
%%%%%%%%%%%%% --- CTeq1 --- %%%%%%%%%%%%
%%%%%%%%%%%%% --- Cxeq11 --- %%%%%%%%%%%
C_D1=eD*eo*200E-9*EL./EG(1,5);         % Dielectric Layer
C_xeq11=C_D1;                          % Pathway Total Capacitance
%%%%%%%%%%%%%%%%%%%%%%%%%%%%%%%%%%%%%%%%
%%%%%%%%%%%%% --- Cxeq12 --- %%%%%%%%%%%
R_M2=(2*3.14156./WH)*(ElecCond.*reallog(1+2.*EW_Eff(3,5)./(EG(1,5)-
WH(1,1))+sqrt((1+2*EW_Eff(3,5)./(EG(1,5)-WH(1,1))).^2-1))).^-1; % [Ohms] Media
Resistance
R_H=(2*3.14156./WH)*(ElecCond_H.*reallog(1+2.*EW_Eff(3,5)./WH(1,1)+sqrt((1+2*EW_Ef
f(3,5)./WH(1,1)).^2-1))).^-1; % [Ohms] Hydrogel Resistance
C_D2=eD*eo*A_Eff_H./tD;                % Dielectric Layer
C_S2=eS*eo*A_Eff_H./tS;                % Media Stern Layer
C_DL2=eM*eo*A_Eff_H./tDL;              % Media Debye Layer
C_SH=eS*eo.*WH.*h_chan(3,1)./tS;       % Hydrogel Stern Layer
C_DLH=eM*eo.*WH.*h_chan(3,1)./tDL;     % Hydrogel Debye Layer
C_M2=(2/3.14159)*eM*eo.*WH.*reallog(1+2.*EW_Eff(3,5)./(EG(1,5)-
WH(1,1))+sqrt((1+2*EW_Eff(3,5)./(EG(1,5)-WH(1,1))).^2-1));   % Bulk Media
C_H=(2/3.14159)*eH*eo.*WH.*reallog(1+2.*EW_Eff(3,5)./WH(1,1)+sqrt((1+2*EW_Eff(3,5)
./WH(1,1)).^2-1));                     % Hydrogel
C_EINT=(1./C_DL2+1./C_S2+1./C_D2).^-1;  % Electrode Interface
C_HINT=(1./C_SH+1./C_DLH).^-1;         % Hydrogel Interface
C_HTOT=(2./C_HINT+1./C_H).^-1;         % Total Hydrogel
C_xeq12=(2./C_D2+2./C_S2+2./C_DL2+2./C_DLH+2./C_SH+2./C_M2+1./C_H).^-1;    %
Pathway Total Capacitance
%%%%%%%%%%%%%%%%%%%%%%%%%%%%%%%%%%%%%%%%
%%%%%%%%%%%%% --- Cxeq13 --- %%%%%%%%%%%
R_M3=h_chan(3,1)./(ElecCond.*EL.*EW_InEff(3,4)); % [Ohms] Resistance Media
C_D3=eD*eo*A_InEff./tD;                    % Dielectric Layer
C_S3=eS*eo*A_InEff./tS;                    % Stern Layer
C_DL3=eM*eo*A_InEff./tDL;                  % Debye Layer
C_M3=eM*eo*A_InEff./h_chan(3,1);           % Bulk Media
C_TOP=(2/3.14159)*eP*eo.*EL.*reallog(1+2.*EW_InEff(3,4)./EG(1,5)+sqrt((1+2*EW_InEf
f(3,4)./EG(1,5)).^2-1));  % Top of Microchannel
C_xeq13=(1./C_TOP+2./C_D3+2./C_S3+2./C_DL3+2./C_M3).^-1;               %
Total Pathway Capacitance
%%%%%%%%%%%%%%%%%%%%%%%%%%%%%%%%%%%%%%%%
C_Teq1=C_xeq11+C_xeq12+C_xeq13;        % Total Pathway Capacitance
%%%%%%%%%%%%%%%%%%%%%%%%%%%%%%%%%%%%%%%%


%%%%%%%%%%%%%%%%%%%%%%%%%%%%%%%%%%%%%%%%
%%%%%%%%%%%%% --- CTeq2 --- %%%%%%%%%%%%
%%%%%%%%%%%%% --- Cxeq21 --- %%%%%%%%%%%
C_xeq21=C_D1;                          % Total Pathway Capacitance
%%%%%%%%%%%%%%%%%%%%%%%%%%%%%%%%%%%%%%%%
%%%%%%%%%%%%% --- Cxeq22 --- %%%%%%%%%%%
R_M22=(2*3.14156./EL)*(ElecCond.*reallog(1+2.*EW_Eff(3,5)./EG(1,5)+sqrt((1+2*EW_Ef
f(3,5)./EG(1,5)).^2-1))).^-1; % [Ohms] Media Resistance
C_D22=eD*eo*A_Eff./tD;                 % Dielectric Layer
C_S22=eS*eo*A_Eff./tS;                 % Stern Layer
C_DL22=eM*eo*A_Eff./tDL;               % Debye Layer
C_M22=(2/3.14159)*eM*eo.*EL.*reallog(1+2.*EW_Eff(3,5)./EG(1,5)+sqrt((1+2*EW_Eff(3,
5)./EG(1,5)).^2-1));          % Bulk Media
C_INT=(1./C_DL22+1./C_S22+1./C_D22).^-1;% Electrode Interface
C_xeq22=(2./C_D22+2./C_S22+2./C_DL22+1./C_M22).^-1;        % Total Pathway
Capacitance
%%%%%%%%%%%%%%%%%%%%%%%%%%%%%%%%%%%%%%%%
%%%%%%%%%%%%% --- Cxeq23 --- %%%%%%%%%%%
C_xeq23=(2./C_D3+2./C_S3+2./C_DL3+2./C_M3+1./C_TOP).^-1;  % Total Pathway
Capacitance
%%%%%%%%%%%%%%%%%%%%%%%%%%%%%%%%%%%%%%%%
```

```matlab
C_Teq2=C_xeq21+C_xeq22+C_xeq23;          % Total Pathway Capacitance
%%%%%%%%%%%%%%%%%%%%%%%%%%%%%%%%%%%%%%%


%%%%%%%%%%%%%%%%%%%%%%%%%%%%%%%%%%%%%%%
%%%%%%%%%%%%% Total Capacitance %%%%%%%%%%
%%%%%%%%%%%%%%%%%%%%%%%%%%%%%%%%%%%%%%%
C_TOTAL=C_Teq1+2*C_Teq2;                  % Total System Capacitance
%%%%%%%%%%%%%%%%%%%%%%%%%%%%%%%%%%%%%%%


%%%%%%%%%%%%%%%%%%%%%%%%%%%%%%%%%%%%%%%
%%%%%%%%%%%%% Time Constants %%%%%%%%%%%%%
%%%%%%%%%%%% [seconds] %%%%%%%%%%%%%%%%
tc_EINT=R_M2.*C_EINT;                     % Electrode Interface
tc_HINT=R_M2.*C_HINT;                     % Hydrogel Interface
tc_M2=R_M2.*C_M2;                         % Bulk Media
tc_H=R_H*C_H;                             % Hydrogel
tc_tot=(2./tc_EINT+2./tc_HINT+2./tc_M2+1./tc_H).^-1; % System Total
%%%%%%%%%%%%%%%%%%%%%%%%%%%%%%%%%%%%%%%


%%%%%%%%%%%%%%%%%%%%%%%%%%%%%%%%%%%%%%%
%%%%%%% Characteristic Frequencies %%%%%
%%%%%%%%%%%% [cycles/second] %%%%%%%%%%%%
cf_EINT=2./(2*pi*tc_EINT);                % Electrode Interface
cf_HINT=2./(2*pi*tc_HINT);                % Hydrogel Interface
cf_M2=2./(2*pi*tc_M2);                    % Media
cf_H=1./(2*pi*tc_H);                      % Hydrogel
%%%%%%%%%%%%%%%%%%%%%%%%%%%%%%%%%%%%%%%


%%%%%%%%%%%%%%%%%%%%%%%%%%%%%%%%%%%%%%%
%%%% Voltage Lost through Dielectric %%%%
Vapp(1:7,1)=5;                            %
Vapp(1:7,2)=10;                           %
Vapp(1:7,3)=20;                           %
Vapp(1:7,4)=30;                           %
Vapp(1:7,5)=40;                           %
Vapp(1:7,6)=50;                           %
Vapp(1:7,7)=60;                           %
V_Ratio=((C_D2/2)./(C_D2/2+C_M2));        % [Unitless] Voltage Ratio
V_M=Vapp.*V_Ratio;                        % [V] Voltage across media
V_D=(Vapp-V_M)./2;                        % [V] Voltage across Dielectric
D=275590551;                              % [V/m] Dielectric Strength
V_Break=D.*tD;                            % [V] Breakdown Threshold
%%%%%%%%%%%%%%%%%%%%%%%%%%%%%%%%%%%%%%%


%%%%%%%%%%%%%%%%%%%%%%%%%%%%%%%%%%%%%%%%%%
%%%%%%%%%%%  FIGURE PLOTTING   %%%%%%%%%%%%
clear figure(1)                           %
clear figure(2)                           %
clear figure(3)                           %
clear figure(4)                           %
clear figure(5)                           %
clear figure(6)                           %
clear figure(7)                           %
clear figure(8)                           %
clear figure(9)                           %
%%%%%%%%%%%%%%%%%%%%%%%%%%%%%%%%%%%%%%%%%%


%%%%%%%%%%%%%%%%%%%%%%%%%%%%%%%%%%%%%%%%%%%%%%%%%%%%%%%%%%%%%%
%%%%%%%%%%%%%%%%% Plot of the Effective Electrode Width %%%%%%%%%%%%%%%%%
figure(1)                                                    %
grid off;                                                    %
hold on;                                                     %
figure(1)                                                    %
plot(h_chan(:,1),EW_Eff(:,3),':k+','LineWidth',2.5,'MarkerSize',10);   %
plot(h_chan(:,1),EW_Eff(:,4),'--ks','LineWidth',2.5,'MarkerSize',10);   %
plot(h_chan(:,1),EW_Eff(:,5),'-ko','LineWidth',2.5,'MarkerSize',10);   %
xlabel('Channel Height [μm]','FontSize',20);                 %
ylabel('Effective Electrode Width [μm]','FontSize',20);      %
set(gca,'FontSize',16,...                                    %
    'Yscale', 'linear', 'Xscale','linear',...                %
```

```matlab
    'XTick',50E-6:1E-4:6E-4,'XTickLabel',50:100:600,...          %
    'YTick',0:25E-6:350E-6,'YTickLabel',0:25:350,...             %
    'XLim',[50E-6 400E-6]);                                      %
legend('1000 µm','1500 µm','2000 µm','location','best');         %
hold off                                                         %
%%%%%%%%%%%%%%%%%%%%%%%%%%%%%%%%%%%%%%%%%%%%%%%%%%%%%%%%%%%%%%%%%%%


%%%%%%%%%%%%%%%%%%%%%%%%%%%%%%%%%%%%%%%%%%%%%%%%%%%%%%%%%%%%%%%%%%%
%%%%%%%%%%%%% Plot of the System's Characteristic Frequencies%%%%%%%%%%%%%
figure(2);                                                       %
grid off;                                                        %
hold on;                                                         %
plot(conc(1,:),cf_EINT(1,:),'-.k+','LineWidth',2.5,'MarkerSize',10);   %
plot(conc(1,:),cf_EINT(4,:),'--ks','LineWidth',2.5,'MarkerSize',10);   %
plot(conc(1,:),cf_EINT(7,:),'-ko','LineWidth',2.5,'MarkerSize',10);    %
xlabel('Electrolyte Concentration [M]','FontSize',20);           %
ylabel('Characteristic Frequency [Hz]','FontSize',20);           %
set(gca,'FontSize',16,...                                        %
    'Yscale', 'log', 'Xscale','log',...                          %
    'YLim',[1E3 1E9]);                                           %
legend('100 nm','1 µm','10 µm','location','best');               %
hold off                                                         %
                                                                 %
figure(3)                                                        %
grid off                                                         %
hold on                                                          %
plot(tD(:,1),cf_EINT(:,1),'-.k+','LineWidth',2.5,'MarkerSize',10);    %
plot(tD(:,1),cf_EINT(:,3),'--ks','LineWidth',2.5,'MarkerSize',10);    %
plot(tD(:,1),cf_EINT(:,4),':ko','LineWidth',2.5,'MarkerSize',10);     %
plot(tD(:,1),cf_EINT(:,7),'-kd','LineWidth',2.5,'MarkerSize',10);     %
xlabel('Dielectric Thickness [m]','FontSize',20);                %
ylabel('Characteristic Frequency [Hz]','FontSize',20);           %
set(gca,'FontSize',16,...                                        %
    'Yscale', 'log', 'Xscale','log',...                          %
    'YLim',[1E3 1E9]);                                           %
legend('1 mM','10 mM','50 mM','1 M','location','best');          %
hold off                                                         %
%%%%%%%%%%%%%%%%%%%%%%%%%%%%%%%%%%%%%%%%%%%%%%%%%%%%%%%%%%%%%%%%%%%


%%%%%%%%%%%%%%%%%%%%%%%%%%%%%%%%%%%%%%%%%%%%%%%%%%%%%%%%%%%%%%%%%%%
%%%%%%%%%%%%%%%%%%% Plot of the System's Time Constants %%%%%%%%%%%%%%%%%%%
figure(4);                                                       %
grid off;                                                        %
hold on;                                                         %
plot(conc(1,:),tc_HINT(4,:),'k:.','LineWidth',2.5,'MarkerSize',10);   %
plot(conc(1,:),tc_EINT(4,:),'k:','LineWidth',2.5,'MarkerSize',10);    %
plot(conc(1,:),tc_H(4,:),'k-.','LineWidth',2.5,'MarkerSize',10);      %
plot(conc(1,:),tc_M2(4,:),'k--','LineWidth',2.5,'MarkerSize',10);     %
plot(conc(1,:),tc_tot(4,:),'k-','LineWidth',2.5,'MarkerSize',10);     %
xlabel('Electrolyte Concentration [M]','FontSize',20);           %
ylabel('Time Constant [s]','FontSize',20);                       %
set(gca,'FontSize',16,...                                        %
    'Yscale', 'log', 'Xscale','log');                            %
legend('Hydrogel Interface','Electrode
Interface','Hydrogel','Media','Total','location','best'); %
%%%%%%%%%%%%%%%%%%%%%%%%%%%%%%%%%%%%%%%%%%%%%%%%%%%%%%%%%%%%%%%%%%%


%%%%%%%%%%%%%%%%%%%%%%%%%%%%%%%%%%%%%%%%%%%%%%%%%%%%%%%%%%%%%%%%%%%
%%%% Plot of the Voltage Through Dielectric, Media & Breakdown Voltage %%%
figure (5)                                                       %
grid off                                                         %
hold on                                                          %
plot(tD(:,1),V_Break(:,4),'-k+','LineWidth',2.5,'MarkerSize',10);      %
plot(tD(:,1),V_D(:,2),':ks','LineWidth',2.5,'MarkerSize',10);          %
plot(tD(:,1),V_D(:,3),'-.ko','LineWidth',2.5,'MarkerSize',10);         %
plot(tD(:,1),V_D(:,4),'k:.','LineWidth',2.5,'MarkerSize',10);          %
plot(tD(:,1),V_D(:,5),'--kx','LineWidth',2.5,'MarkerSize',10);         %
xlabel('Dielectric Thickness [µm]','FontSize',20);               %
ylabel('Voltage Across Dielectric [V]','FontSize',20);           %
set(gca,'FontSize',16,...                                        %
```

```matlab
    'Yscale', 'linear', 'Xscale','linear',...              %
    'XLim',[0 1E-5], 'YLim',[0 200]);                      %
legend('Breakdown Voltage','10V','20V','30V','40V','location','best');   %
                                                           %
figure (6)                                                 %
grid off                                                   %
hold on                                                    %
plot(tD(:,1),V_M(:,2),':k+','LineWidth',2.5,'MarkerSize',10);   %
plot(tD(:,1),V_M(:,3),'-.ks','LineWidth',2.5,'MarkerSize',10);  %
plot(tD(:,1),V_M(:,4),'--ko','LineWidth',2.5,'MarkerSize',10);  %
plot(tD(:,1),V_M(:,5),'-kd','LineWidth',2.5,'MarkerSize',10);   %
xlabel('Dielectric Thickness [µm]','FontSize',20);         %
ylabel('Voltage Across Media [V]','FontSize',20);          %
set(gca,'FontSize',16,...                                  %
    'Yscale', 'linear', 'Xscale','linear',...              %
    'XTick',0:0.5E-6:3E-6,'XTickLabel',0:0.5:3,...         %
    'XLim',[0 3E-6], 'YLim',[0 40]);                       %
legend('10V','20V','30V','40V','location','best');         %
%%%%%%%%%%%%%%%%%%%%%%%%%%%%%%%%%%%%%%%%%%%%%%%%%%%%%%%%%%%%%%%%%%%%%%%%

%%%%%%%%%%%%%%%%%%%%%%%%%%%%%%%%%%%%%%%%%%%%%%%%%%%%%%%%%%%%%%%%%%%%%%%%
%%%%%%%%%%%%%%% Plot of the System's Capacitances  %%%%%%%%%%%%%%%%%%%%%
figure(7)                                                  %
grid off                                                   %
hold on                                                    %
plot(tD(:,1),C_EINT(:,1),':.k','LineWidth',2.5,'MarkerSize',10);    %
plot(tD(:,1),C_HTOT(:,1),':ks','LineWidth',2.5,'MarkerSize',10);    %
plot(tD(:,1),C_M2(:,1),'-.k+','LineWidth',2.5,'MarkerSize',10);     %
plot(tD(:,1),C_xeq12(:,1),'-kd','LineWidth',2.5,'MarkerSize',10);   %
plot(tD(:,1),C_xeq13(:,1),'--kx','LineWidth',2.5,'MarkerSize',10);  %
xlabel('Dielectric Thickness [m]','FontSize',20);          %
ylabel('Capacitance [F]','FontSize',20);                   %
set(gca,'FontSize',16,...                                  %
    'Yscale', 'log', 'Xscale','log',...                    %
    'YLim',[1E-15 2E-11]);                                 %
legend('Electrode Interface','Total -
Hydrogel','Media3','xeq12','xeq13','location','best'); %
hold off                                                   %
                                                           %
figure(8)                                                  %
grid off                                                   %
hold on                                                    %
plot(tD(:,1),C_xeq12(:,1),':k+','LineWidth',2.5,'MarkerSize',10);   %
plot(tD(:,1),C_Teq2(:,1),'-.ks','LineWidth',2.5,'MarkerSize',10);   %
plot(tD(:,1),C_Teq1(:,1),'--ko','LineWidth',2.5,'MarkerSize',10);   %
plot(tD(:,1),C_TOTAL(:,1),'-kd','LineWidth',2.5,'MarkerSize',10);   %
xlabel('Dielectric Thickness [m]','FontSize',20);          %
ylabel('Capacitance [F]','FontSize',20);                   %
set(gca,'FontSize',16,...                                  %
    'Yscale', 'log', 'Xscale','log',...                    %
    'YLim',[1E-14 1E-12]);                                 %
legend('xeq12','Teq2','Teq1','Total Capacitance','location','best');   %
hold off                                                   %
%%%%%%%%%%%%%%%%%%%%%%%%%%%%%%%%%%%%%%%%%%%%%%%%%%%%%%%%%%%%%%%%%%%%%%%%

%%%%%%%%%%%%%%%%%%%%%%%%%%%%%%%%%%%%%%%%%%%%%%%%%%%%%%%%%%%%%%%%%%%%%%%%
%%%%%%%%%%%%%%%%%%%% Plot of the Electric Conductivity %%%%%%%%%%%%%%%%%%%%
figure(9)                                                  %
grid off                                                   %
hold on                                                    %
[AX,H1,H2]=plotyy(conc(1,:),ElecCond(1,:),conc(1,:),tDL(1,:),'loglog');   %
set(H1,'LineStyle','--','LineWidth',2.5,'Color','k');      %
set(H2,'LineStyle',':','LineWidth',2.5,'Color','k');       %
set(get(AX(1),'Ylabel'),'String','Electric Conductivity [S/m]',
'FontSize',20,'Color','k') %
set(get(AX(2),'Ylabel'),'String','Debye Length [m]', 'FontSize',20,'Color','k') %
xlabel('Electrolyte Concentration [M]','FontSize',20)      %
%%%%%%%%%%%%%%%%%%%%%%%%%%%%%%%%%%%%%%%%%%%%%%%%%%%%%%%%%%%%%%%%%%%%%%%%

%%%%%%%%%%%%%%%%%%% END OF FILE || Thank You, Good Night  %%%%%%%%%%%%%%%
```

322